Impact of Soil Moisture-Atmosphere Interactions on the Development of Extreme Weather in the Western Mediterranean

Zur Erlangung des akademischen Grades eines
DOKTORS DER NATURWISSENSCHAFTEN
von der KIT-Fakultät für Physik des
Karlsruher Instituts für Technologie (KIT)

genehmigte

DISSERTATION

von

M.Sc. Sebastian Helgert
aus Fulda

Tag der mündlichen Prüfung:	03.05.2019
Referent:	Prof. Dr. Christoph Kottmeier
Korreferent:	Prof. Dr. Joaquim Pinto

Abstract

The Western Mediterranean (WMed) region is frequently affected by weather extremes such as heat waves and droughts in summer and heavy precipitation events (HPEs) and flash floods mostly in autumn. Both dry and wet extremes lead to damages which cost billions of euros and frequently cause human fatalities. The projected climate change indicates a considerable increase in the frequency and intensity of such extremes in this region. Therefore, a better prediction of these phenomena is essential in order to develop strategies for the prevention and the adaptation of the Mediterranean society and infrastructure to such hazards in a changing climate.

The WMed is a transitional region between dry subtropical and wet mid-latitude climates, where soil moisture (SM) is a crucial component controlling the partitioning of surface heat fluxes over land. This region is prone to extreme weather events due to its complex physiographic terrain which is characterised by strong ocean-land-atmosphere interactions. Due to its long-term memory SM variability affects the near-surface conditions that can favour extreme events on different time scales.

However, the contribution of SM-atmosphere interactions to the initiation and evolution of extremes in the complex terrain of the WMed is still not fully understood due to the lack of adequate SM observations and the inaccurate modelling representation of SM feedbacks with the atmosphere. Thus, the aim of this thesis is to assess the relevance of SM-atmosphere interactions for the development of extremes in the WMed and to gain better process understanding about SM feedbacks. A multi-scale modelling approach using the model of the Consortium for Small-scale Modeling (COSMO) was carried out at spatial scales of convection-permitting ($\sim$3 km) and convection-parametrised ($\sim$7 km) resolutions and at temporal scales ranging from hours up to several months. This approach encompasses the most relevant scales of the involved processes. The analysis is divided into three main parts. In the first part, the autumn period 2012 was selected to analyse wet extremes. For this period the Special Observation Period 1 (SOP1) campaign of the HYdrological cycle in the Mediterranean EXperiment (HyMeX) provides unprecedented observational data sets with a focus on wet extremes. In the second part, state-of-the-art 1 km satellite-derived surface soil moisture (SSM) observations from the Soil Moisture and Ocean Salinity (SMOS) mission were used for the first time to initialise the COSMO model in order to improve the initial SM status. Extreme heat waves in the summer of 2003 and 2015 were investigated in the third part of the analysis. All seasonal simulations were performed with a convection-permitting resolution over large domains containing the entire WMed and for the study of dry periods extending to continental Europe. Various experiments were conducted with physically-based extreme values of initial SM to investigate the sensitivity of the atmospheric conditions on extreme SM conditions.

In autumn 2012, the representation of precipitation timing and of intensity in the WMed corresponds well between the seasonal convection-permitting simulation and the observations. In this respect, the representation of the higher resolution is more accurate than in the coarser convection-parametrised simulation. In this period, wet and dry SM initial conditions in the COSMO model induce a positive SM-atmosphere coupling with seasonal mean changes in near-surface heat fluxes, atmospheric moisture and instability. In the wet initial SM scenario the modified atmospheric conditions cause a positive SM-precipitation feedback with an increase in mean moist convection and low-cloud cover which leads to an increase in seasonal mean precipitation of about +25 % in semi-arid regions. Depending on the regional climate conditions the effects of the initial SM conditions on extreme precipitation varies. The wet initial SM scenario leads to an increase in the frequency and intensity of daily extreme precipitation events in semi-arid regions while the dry initial SM scenario causes higher hourly precipitation rates and an increase in extreme precipitation in moderately humid regions.

Four HPEs were selected during autumn 2012 to test the realistic initialisation with 1 km SMOS-L4 3.0 SSM data. For this purpose, a SMOS-L4 SM profile product was created by applying a cumulative density function (CDF)-matching bias correction and an exponential filter. The implementation of this product for SM initialisation in COSMO improves the representation of all selected HPEs with an optimal time of realistic SMOS initialisation of 3 days in advance.

The dry summer seasons in 2003 and 2015 reveal a strong response of seasonal mean atmospheric conditions to the modified initial SM in spring with feedback mechanisms on temperature, precipitation and the large-scale conditions. The reduction of initial SM in the whole investigation domain results in a seasonal mean increase in maximum temperature of about +2.5 °C in the Iberian Peninsula (IP) subdomain and about +4 °C in the Central Europe (ME) subdomain. The temperature increase is double the existing observed temperature anomaly in both years. At the same time, the seasonal mean decrease in precipitation is about 40 % in both regions. The extent of the temperature and precipitation differences originating from remote sources reaches 30 % and 50 %, respectively. Analyses of dry extreme indices demonstrate that the SM-atmosphere interactions induced by a dry SM initialisation in spring lead to an increase in the number of hot days and the heat wave duration by a factor of 3 in the ME subdomain and by a factor of 1.5 in the IP subdomain. Contrariwise, wet SM spring conditions reduce the number of hot days and the duration of heat waves by about 50 %.

This thesis demonstrates the potential of combining state-of-the-art observations and high-resolution modelling to improve the understanding of SM-atmosphere interactions and feedbacks in the WMed. The importance of local and remote SM-atmosphere interactions for the development of heat waves and HPEs in the WMed and continental Europe is highlighted in seasonal convection-permitting simulations. The presented high-resolution realistic SM initialisation and modelling are expected to have real applicability for future weather to climate modelling in order to improve the prediction uncertainties of extremes in the WMed and Europe.

Zusammenfassung

Die Region des westlichen Mittelmeeres ist häufig von Wetterextremen wie Hitzewellen und Dürren im Sommer sowie Starkniederschlagsereignissen und Sturzfluten vorwiegend im Herbst betroffen. Beide Arten von Extremwetterereignissen führen zu milliardenschweren Schäden und fordern oftmals eine hohe Anzahl von Todesopfern. Durch den prognostizierten Klimawandel wird eine deutliche Zunahme der Häufigkeit und Intensität derartiger Wetterextreme in dieser Region erwartet. Eine verbesserte Vorhersage dieser Wetterphänomene ist unerlässlich zur Entwicklung von Präventions- und Anpassungsmaßnahmen für die Gesellschaft und Infrastruktur im Mittelmeerraum hinsichtich des sich verändernden Klimas und der damit einhergehenden Gefahren.

Das Gebiet des westlichen Mittelmeeres ist eine Übergangsregion zwischen trockenem subtropischem und feuchtem gemäßigtem Klima, in der die Bodenfeuchte eine entscheidende Kontrollfunktion für die Aufteilung der Oberflächenwärmeflüsse über Land einnimmt. Die Region ist aufgrund ihres komplexen physiographischen Geländes, das durch starke Wechselwirkungen zwischen Land, Ozean und Atmosphäre gekennzeichnet ist, anfällig für extreme Wetterereignisse. Aufgrund des „Langzeitgedächtnisses“ des Bodens werden die atmosphärischen Bedingungen in der planetaren Grenzschicht durch die Variabilität der Bodenfeuchte beeinflusst. Dies kann Wetterextreme auf verschiedenen Zeitskalen begünstigen.

Da geeignete Beobachtungen zur Bodenfeuchte fehlen und die Rückkopplungen zwischen Bodenfeuchte und Atmosphäre nur unzureichend in Modellen repräsentiert werden, ist der Einfluss der Wechselwirkungen zwischen Bodenfeuchte und Atmosphäre auf die Initiierung und Entwicklung von Wetterextremen für das komplexe Gebiet des westlichen Mittelmeeres bislang nur unzureichend erforscht. Das Ziel dieser Arbeit ist es daher, die Relevanz dieser Wechselwirkungen auf die Entstehung von Wetterextremen im westlichen Mittelmeer zu bewerten und ein verbessertes Prozessverständnis über Bodenfeuchterückkopplungen zu erlangen. Hierfür wird ein multiskaliger Modellierungsansatz mit dem regionalen "Consortium for Small-scale Modeling (COSMO)"−Modell auf verschiedenen räumlichen Skalen mit und ohne Konvektionsparametrisierung und zeitlichen Skalen von einigen Stunden bis zu mehreren Monaten durchgeführt.

Die Analyse gliedert sich in drei Hauptteile. Im ersten Teil wird die Herbstperiode 2012 herangezogen, um Niederschlagextreme zu untersuchen. Für diesen Zeitraum liefert eine Messkampagne im Rahmen des HyMeX-Programmes eine beachtliche Anzahl an Beobachtungsdatensätzen, schwerpunktmäßig für Niederschlagsextreme. Zur Verbesserung der Initialisierung der Bodenfeuchte werden im zweiten Teil der Analyse erstmals neuartige 1 km satellitengestützte Beobachtungen der oberflächennahen Bodenfeuchte der "Soil Moisture and Ocean Salinity (SMOS)" Mission verwendet. Im dritten Abschnitt der

Untersuchung stehen extreme Hitzewellen in den Sommerperioden 2003 und 2015 im Fokus. Alle saisonalen Simulationen wurden in einer konvektionserlaubenden Modellauflösung für ein großflächiges Untersuchungsgebiet ausgeführt, welches das gesamte westliche Mittelmeer umfasst und für die Betrachtung von Hitzeperioden zusätzliche Gebiete in Kontinentaleuropa beinhaltet. Um die Sensitivität der atmosphärischen Bedingungen in Hinblick auf extreme Bodenfeuchtebedingungen zu erforschen, wurden verschiedene Bodenfeuchteinitialisierungsexperimente mit bodenspezifischen Extremwerten durchgeführt.

Bei der Untersuchung von Niederschlagsextremen im westlichen Mittelmeer im Herbst 2012 stimmen Zeitpunkt und Intensität der Niederschläge in der saisonalen Simulation ohne Konvektionsparametrisierung gut mit den Beobachtungsdaten überein und werden besser repräsentiert als in der Simulation mit Konvektionsparametrisierung. In diesem Zeitraum bewirken feuchte und trockene Anfangsbedingungen der Bodenfeuchte einen positiven Rückkopplungseffekt zwischen Bodenfeuchte und Atmosphäre, einhergehend mit saisonalen Durchschnittsänderungen in den oberflächennahen Wärmeflüssen, in der atmosphärischen Feuchtigkeit und der Stabilität der Atmosphäre. Die Betrachtung des Anfangsszenarios mit höherer Bodenfeuchte zeigt, dass die veränderten atmosphärischen Bedingungen zu einer Zunahme der durchschnittlichen feuchten Konvektion und der niedrigen Bewölkung führen und dies eine positive Niederschlagsrückkopplung induziert. Der Anstieg der durchschnittlichen saisonalen Niederschläge beläuft sich auf bis zu +25 % in semiariden Regionen. Der Einfluss des anfänglichen Bodenfeuchteszenarios auf extreme Niederschläge variiert in Abhängigkeit von den regionalen Klimabedingungen. Das Szenario mit höherer Bodenfeuchte führt zu einer Zunahme der Häufigkeit und Intensität der täglichen extremen Niederschlagsereignisse in semiariden Regionen, während das trockene Bodenfeuchteszenario höhere stündliche Niederschlagsraten und eine Zunahme der Extremniederschläge in mäßig feuchten Regionen verursacht.

Vier Starkniederschlagsereignisse wurden innerhalb der Herbstperiode 2012 ausgewählt, um die realistische Initialisierung mit 1 km satellitengestützten oberflächennahen SMOS-L4 Bodenfeuchtedaten zu testen. Hierfür wurde die systematische Abweichung zwischen Modell- und Satellitendaten korrigiert und durch Anwendung eines Exponentialfilters ein Bodenfeuchte-Profilprodukt erstellt. Die Implementierung dieses Produktes für die Bodenfeuchteinitialisierung verbessert die Modelldarstellung aller ausgewählten Starkniederschlagsereignisse, wobei der optimale Zeitpunkt der realistischen Initialisierung 3 Tagen vor dem Auftreten des Extremereignisses liegt.

In den trockenen Sommerperioden 2003 und 2015 zeigen die durchschnittlichen saisonalen atmosphärischen Bedingungen eine starke Reaktion auf die modifizierten Anfangsbedingungen der Bodenfeuchte im Frühjahr. Diese gehen mit Rückkopplungsmechanismen auf die Temperatur, den Niederschlag und die großskaligen Wetterbedingungen einher. Die Reduzierung der anfänglichen Bodenfeuchte im gesamten Untersuchungsgebiet führt zu einem saisonalen mittleren Anstieg der Maximaltemperatur um etwa +2.5 °C in der Region der Iberischen Halbinsel und um etwa +4 °C in Mitteleuropa. Der Temperaturanstieg entspricht einer Verdopplung der bestehenden beobachteten Temperaturanomalien in beiden

Jahren. Gleichzeitig beträgt die saisonale mittlere Abnahme der Niederschläge in beiden Regionen circa 40 %. Temperatur- und Niederschlagsunterschiede, bedingt durch nicht-lokale Quellen, leisten einen Beitrag von 30 % bzw. 50 %. Analysen von Temperaturextremindizes zeigen, dass die durch eine trockene Bodenfeuchteinitialisierung im Frühjahr induzierten Wechselwirkungen zwischen Bodenfeuchte und Atmosphäre zu einer Erhöhung der Anzahl der heißen Tage und einem Anstieg der Dauer von Hitzewellen um den Faktor 3 in Mitteleuropa und um den Faktor 1,5 in der Region der Iberischen Halbinsel führen. Im Gegensatz dazu reduzieren Anfangsbedingungen mit höherer Bodenfeuchte im Frühjahr die Anzahl der heißen Tage und die Dauer der Hitzewellen um etwa 50 %.

Die Ergebnisse dieser Arbeit demonstrieren, dass die Kombination von neuartigen Beobachtungen mit einer hochauflösenden Modellierung ein immenses Potenzial für ein verbessertes Verständnis der Wechselwirkungen zwischen Bodenfeuchte und Atmosphäre sowie Rückkopplungseffekten im Bereich des westlichen Mittelmeeres aufweist. Wie groß die Bedeutung dieser lokalen und nicht-lokalen Wechselwirkungen für die Entwicklung von Hitzewellen und Starkniederschlagsereignissen ist, wird in den saisonalen Simulationen ohne Konvektionsparametrisierung verdeutlicht. Die in dieser Arbeit angewendete hochauflösende realistische Initialisierung der Bodenfeuchte und konvektionserlaubende Modellierung kann die Vorhersageunsicherheiten von Extremwetterereignissen in der Wetter- und Klimamodellierung im westlichen Mittelmeer und Europa künftig verbessern.

Contents

1. Introduction and Motivation

The Mediterranean basin is unique because of its geographical position which brings hot and dry conditions in summer due to the position of the descending branch of the Hadley circulation and mild and wet winters due to prevailing westerlies in this season (Bolle, 2003). The particularity of the Mediterranean region is that the Mediterranean Sea is almost completely surrounded by land, with many sharp orographic features and distinct water basins, gulfs, islands and peninsulas of various sizes (Lionello, 2006). The Mediterranean Sea covers about 2.5 million km^2 (42 %) of the total Mediterranean basin (6 million km^2; 10°W-40°E, 28N°-47°N) and has an exceptionally long coastline of 46,000 km (Bolle, 2003). The hydrological Mediterranean basin comprises 21 main river catchments with an area of 1.7 million km^2. The remaining land parts consist of small and medium size watersheds associated with small rivers that originate from the surrounding mountains (Drobinski and Ducrocq, 2008). The soils within these catchments have a large diversity, resulting from differences in local climatic conditions, landscape, vegetation and the long-term influence of human activities (Zdruli et al., 2011). The Mediterranean region is affected by an intense air-sea exchange associated with intense wind flows caused by orography in response to the large-scale forcing (e.g., Mistral, Bora, Scirocco). The orography and thermal contrasts in this region can induce deep cyclogenesis (e.g., Genoa cyclogenesis) and occasional stationary pressure systems such as the Iberian thermal low (Ducrocq et al., 2010). Furthermore, the Mediterranean region is a transition zone between dry and wet climates, in which soil conditions and particularly the land-atmosphere coupling play a central role since evapotranspiration is limited by soil moisture (SM) availability. SM controls the partitioning of incoming radiation into latent and sensible heat fluxes through evapotranspiration processes at the land surface and allocates the precipitation into runoff, subsurface flow and infiltration (GOSIC, 2018). In this way, SM anomalies have strong effects on the land energy and water balances (Seneviratne and Stöckli, 2008).

These complex physiographic conditions result in many interactions and feedbacks between the ocean-land-atmosphere processes which influence the Mediterranean climate and its associated high-impact weather events (Ducrocq et al., 2010). The Mediterranean climate is characterised by high daily and seasonal variability with frequent long drought periods in summer followed by very intense precipitation events in autumn and winter. The Western Mediterranean (WMed: Iberian Peninsula, Mediterranean Maghreb states, Southern France, Italy and the coast around the Adriatic Sea) is particular prone to wet extremes during autumn, such as heavy precipitation events (HPEs) and flash floods. Most of these events are usually caused by mesoscale convective systems (MCSs) (Houze, 2004) and they are supported by the warm sea surface temperature (SST) in autumn which peaks of in September. One of the

main precursors of HPEs is the low-level moisture supply which has to ascend rapidly, e.g. by low-level convergence. Depending on the synoptic conditions, evaporation from the Mediterranean Sea itself can account for 60 % of the moisture supply of such systems (Duffourg and Ducrocq, 2013). However, Winschall et al. (2014) concluded that the Mediterranean Sea is only one of several moisture sources for the development of extreme precipitation for all seasons. Further important moisture sources are remote areas such as the Atlantic and the Tropics as well as land evapotranspiration from Africa and Europe. Intense surface evaporation anomalies advected from these remote regions often provide the additional moisture supply for extraordinary precipitation events in the WMed (Pinto et al., 2013; Winschall et al., 2014).

In the last autumn season 2018 several such devastating HPEs -with total rainfall amounts of more than 300 mm per day and more than 40 dead people in Spain (Oct 9, 2018; Oct 12-18, 2018), Southern France (Oct 15, 2018) and Italy (Oct 29 until Nov 03, 2018)- have demonstrated the high socio-economic vulnerability to high-impact events in this region. As most of the 466 million people in the Mediterranean region live concentrated in cities near the coast, human society and infrastructure are highly vulnerable to extreme events. In addition to these HPEs this region frequently suffers from heat waves and droughts. European heat waves and the drought from July to August 2003 alone caused 70,000 fatalities and led to total losses of 14,000 million US$ (Munich RE NatCatSERVICE, 2019). The Mediterranean has been identified as one of the main ”hot-spot” regions of climate change, where a particularly strong intensification of weather extremes is expected (Giorgi, 2006; Giorgi et al., 2011). The Fifth Assessment Report (AR5) of the Intergovernmental Panel on Climate Change (IPCC) confirmed a high confidence in observed increases in dry extremes like heat waves and droughts as well as in extreme precipitation in the Mediterranean in recent decades (Hartmann et al., 2013). Global and regional climate models project an increase in heat extremes which comes along with reduced mean precipitation, soil moisture and evapotranspiration in the Mediterranean area (Fischer and Schär, 2010; Orlowsky and Seneviratne, 2012). Despite an expected decrease in mean precipitation in the Mediterranean, several studies show an increase in observed extreme precipitation (Alpert, 2002; van den Besselaar et al., 2012; Blanchet et al., 2018; Ribes et al., 2018). Some future projections indicate an increase in extreme precipitation associated with longer dry spells (Sillmann et al., 2013; Hertig et al., 2014; Paxian et al., 2015) with varying impacts for the different regions of the Mediterranean basin (Beaulant et al., 2011; Hertig et al., 2014; Rajczak and Schär, 2017; Drobinski et al., 2018; Tramblay and Somot, 2018).

The SM-climate interactions contribute significantly to extreme temperatures as shown by sensitivity studies of SM indicating that up to 40 % of the signal of the major summer European heat waves of recent decades have been attributed to SM anomalies (Jaeger and Seneviratne, 2011). In the Mediterranean region the future projections indicate that the changes in SM account for about 25 % of the projected change of extreme temperatures (Seneviratne et al., 2013). In this context, the long-term “memory” of SM (Koster and Suarez, 2001) regarding dry and wet anomalous conditions in deeper soil layers plays an important role in forcing atmospheric processes over land (Wang et al., 2010) and leads to land-

atmosphere feedbacks in a wide range of spatial and temporal scales (Schär et al., 2004; Koster et al., 2004; Hohenegger et al., 2009; Seneviratne et al., 2010; Taylor et al., 2011; Miralles et al., 2018). Observational and modelling studies have demonstrated an important impact of SM on the evolution of near-surface air temperature (Jaeger and Seneviratne, 2011; Hirschi et al., 2014; Schwingshackl et al., 2017) and on the formation of precipitation (Koster et al., 2004; Taylor et al., 2012a; Guillod et al., 2015). In this regard, the sign of the SM-precipitation feedback is still an open question: past results have shown that direct effects of moisture recycling lead to a positive feedback (Eltahir and Bras, 1996), whereas other studies concluded that indirect effects dealing with the dynamics through the impact on the planetary boundary layer, modification of mesoscale circulation patterns or the influences from remote SM could lead to either positive or negative feedbacks (Schär et al., 1999; Seneviratne et al., 2010; Taylor et al., 2012a; Lorenz et al., 2016). Furthermore, Vautard et al. (2007) and Zampieri et al. (2009) showed that Mediterranean drought conditions in spring and early summer precede to anomalous hot summer temperatures contributing to the development of extreme heat in continental Europe in the 10 hottest summers between 1948 and 2005. The drier air from Southern Europe is transported northwards by occasional southern winds and establishes two main SM feedbacks, which amplify the warming signal: higher sensible heat emissions and favoured upper-air anticyclonic circulations (Zampieri et al., 2009).
Although SM can have an impact on the representation of HPEs in the WMed, the scientific community has paid less attention to this issue since an adequate representation of SM observations and SM-atmosphere interactions in models was not available. Up to now, the inaccurate representation of SM-precipitation feedbacks and SM initialisation remain a source of uncertainty in weather and climate models. Further limitations are the missing representation of fine-scale processes. A more accurate representation of SM-atmosphere interactions in models combined with high-resolution observations of SM is necessary to close this representation gap and enables the quantification of the SM-atmosphere interactions in this region.
However, obtaining accurate global observations of soil moisture is extremely complicated because of its high spatial and temporal variability. This is especially evident for point-scale in-situ measurements, which can provide important information for a limited area, but are not suitable for regional or global observations. Therefore, new satellite-based remote sensing observations of active and passive microwave sensors can fill the gap of lacking adequate SM observations. This data source has the unique advantage of transmitting global information of the spatio-temporal variation of surface soil moisture (SSM) (Petropoulos et al., 2018). As the first mission of its kind the Soil Moisture and Ocean Salinity (SMOS) mission measures in the most promising wavelength of microwaves at low frequencies of the L-Band (1-2 GHz), because the emissivity of the wet soil is strong in this wavelength. The microwave signal is not influenced by clouds or the atmosphere and it penetrates vegetation (Kerr et al., 2010, 2012). Since 2010 the passive L-band radiometer onboard the SMOS satellite has been observing the SSM in a soil depth of approximately 5 cm with a spatial resolution of 40-50 km in a revisit time of 3 days.

The potential to improve the temperature skill using satellite-based SSM information to initialise a regional climate model (∼50 km) was demonstrated by Bisselink et al. (2011). In this study an exponential filter methodology of Wagner et al. (1999) was applied to estimate the profile of SM due to the fact that SM measurements from satellites are limited to a soil depth of 2-5 cm. In addition, the assimilation of SMOS-Level 2 (∼30 km) data into global land surface models lead to an improved status of SM and other land surface variables (Blankenship et al., 2016; de Lannoy and Reichle, 2016).
Nevertheless, a high-resolution land surface analysis in the order of 1-10 km is necessary to capture heterogeneity on native scales of land-atmosphere interactions (Piles et al., 2011; Dirmeyer and Halder, 2016). Therefore, various downscaling techniques based on complementarity and interchangeability between earth observation data have been developed in recent years to estimate high-resolution SSM (Piles et al., 2016). These methods disaggregate passive microwave SSM to higher spatial or temporal resolutions using the synergy of visible, infrared and thermal information. Such semi-empirical methods are used by Piles et al. (2011, 2014) to derive SSM in a 1 km resolution from the combination of high-accuracy SMOS brightness temperatures with high-resolution information of the land surface temperature (LST) and the normalised difference vegetation index (NDVI) from the Moderate Resolution Imaging Spectroradiometer (MODIS). In the most recent update, version 3.0 (SMOS-L4 3.0), LST from ERA-interim was introduced to obtain data even on cloudy days (Piles et al., 2015). This implementation significantly increases the availability of data and improves the estimation of SSM data compared to older versions (Khodayar et al., 2019).
In addition, the HYdrological cycle in the Mediterranean EXperiment (HyMeX) program, in line with the aim of understanding weather extremes in the WMed region, provides unprecedented observational data sets within the conducted Special Observation Period 1 (SOP1) campaign from September 5 to November 6, 2012 on the wet extreme phenomena in the WMed. These novel observation data of SMOS and HyMeX give new opportunities for improving the SM initial status of model simulation and for the validation of the modelling results.

This PhD thesis addresses the issue of remaining uncertainties in the weather to seasonal prediction of dry and wet extremes related to the inadequate representation of initial SM, SM-atmosphere interactions and their feedback mechanisms in the WMed. The novelty of this study is to use the synergy of a multi-temporal and multi-spatial approach with the Consortium for Small-scale Modeling (COSMO) model (Schaettler et al., 2014) and state-of-the-art satellite-derived SSM observations as well as in-situ measurements from the HyMeX campaign to assess SM-atmosphere interactions. For the first time, the COSMO model is initialised with the novel state-of-the-art 1 km disaggregated satellite-derived SSM to improve the initial SM representation. Also innovative is the seasonal convection-permitting modelling (∼3 km) domain size of the whole WMed for the wet autumn period 2012 and even up to continental Europe for the dry summer periods in 2003 and 2015. These investigation domains allow the analysing of local and remote SM-atmosphere interactions and feedbacks within the Western Mediterranean and

towards the surrounding areas of continental Europe with an unprecedented high spatial resolution. The importance of investigating such SM-atmosphere interactions in convection-permitting simulations is emphasised in the outlook of several recent studies (Stéfanon et al., 2014; Prein et al., 2015; Dirmeyer and Halder, 2016; Sillmann et al., 2017). By utilising these new approaches within this thesis, a better understanding of the impact of SM on atmospheric processes, the sign of SM-atmosphere feedbacks and the quantification of the involved processes are assessed. The objectives and scientific questions investigated in this thesis are as follows:

1. Assessment of the relevance of SM-atmosphere interactions for the development and occurrence of extreme weather phenomena in the WMed region.
    - *What is the impact of SM conditions on the chain of atmospheric processes leading to heavy precipitation?*
    - *How do the extreme dry and wet SM initialisations influence the seasonal mean precipitation and the extreme rainfall events?*
    - *What is the sign of possible SM-precipitation feedbacks? Does this sign depend on the model resolution?*

    These questions are answered in Chapter 5 analysing the sensitivity of WMed heavy precipitation to extreme SM initialisation in autumn 2012. Furthermore, the SM-precipitation feedbacks in convection-permitting and convection-parametrised model resolutions are discussed.

2. Investigation of the impact of realistic initialisation with high resolution satellite-derived SSM observations on the numerical weather prediction modelling of extreme precipitation.
    - *What is the added value of a bias-corrected, high-resolution SM profile derived from SMOS 1 km data compared to the standard SM model representation?*
    - *Does a realistic SM initialisation lead to an improved modelling of extreme precipitation events?*
    - *How are the atmospheric processes leading to convective precipitation influenced by high-resolution realistic SM initialisation?*

    These questions are addressed in Chapter 6, which presents a novel strategy to initialise the COSMO model with 1 km SMOS-L4 3.0 and assesses the application of 1 km SMOS-L4 initialisation for different HPEs in autumn 2012. In order to understand the modification of the triggering processes of convective precipitation in a case study, a heavy rainfall event is analysed in detail and processes are examined and assessed.

3. Improvement of the understanding of the local and remote effects of WMed SM-atmosphere interactions on the development of heat waves in continental Europe.

   - *Which kind of local and remote SM feedbacks between southwestern Europe and Central Europe could be found in convection-permitting simulations?*
   - *How pronounced are the effects of spring SM deficit on the development of heat waves in the WMed and continental Europe?*

   These questions are examined in Chapter 7. The sensitivity of WMed SM-atmosphere interactions in convection-permitting model resolutions to different initial SM conditions are analysed for the hot summers of 2003 and 2015.

This thesis is structured in eight chapters: Chapter 2 describes the theoretical background of the characteristics and the climate of the Mediterranean region, of atmospheric convection and the current state of scientific knowledge about SM-atmosphere interactions. Chapter 3 introduces the limited-area numerical weather prediction model COSMO and the used observational data sets. The considered investigation domains, the time periods and the statistical methods are presented in Chapter 4. Chapters 5-7 analyse the raised scientific questions. Finally, Chapter 8 summarises the main conclusions of this thesis.

2. The Continental Components of the Water Cycle in the Mediterranean

The water transport within the water cycle from one reservoir to another takes place by evaporation processes of water from the land and sea surface in the atmosphere, by condensation processes from water vapour to clouds and finally by precipitation back to the surface. Thereby the water cycle connects different climate system components: ocean, land and atmosphere. Within the continental branch of the water cycle the soil moisture-atmosphere interactions are of particular interest. This chapter focuses on the most important processes involved in these interactions which lead to feedback of soil moisture to temperature and precipitation. In this context, the role of soil moisture for the water and energy balance at the surface and the energy transfer from the surface to the atmosphere by atmospheric convection is presented. The basic concepts of moist convection, atmospheric stability and convective indices are introduced. Moreover, an overview about the climate and characteristics of the Mediterranean region is given and finally the definitions of extremes in the Western Mediterranean and their projected future changes are described.

At the beginning of this thesis the terminology of coupling, feedback and interaction is explained to avoid confusion about their slightly different meaning. The concept of coupling is based on the degree to which one variable/climate system component controls another one (Seneviratne et al., 2010). For example, in Fig. 2.4b the one-way coupling between soil moisture and evapotranspiration is shown by a blue arrow, in which an increase in soil moisture leads to a higher evapotranspiration rate. The concept of feedback bases on a two-way coupling between two variables/climate system components. Negative feedback occurs, for example, when the higher evapotranspiration rate described above, induced by a positive soil moisture anomaly, leads to a reduction of this original wet SM anomaly (Fig. 2.4b). The term "interaction" is generally used to describe the sum of all relationships and processes involved without reference to the direction of causality (Seneviratne et al., 2010). The concept of soil moisture-atmosphere interactions includes the chain of processes and variables in the atmosphere that are influenced by a change in soil moisture.

2.1. Climate and Characteristics of the Mediterranean Region

The Mediterranean area has been identified as one of the most sensitive regions to climate change in the world (Giorgi, 2006). A high sensitivity of the Mediterranean hydrological cycle in respect to climate change can be explained by its transitional location between temperate climate in the mid-latitudes

and hotter-drier North African climate and its specific physiographic features (Thiébault et al., 2016). The unique character of this region results from an almost enclosed Mediterranean Sea, surrounded by high mountain ridges and highly urbanised coastal areas. Together with distinct islands, peninsulas and many regional river catchments, seas and basins these features lead to complex interactions and feedbacks between ocean-atmosphere-land processes. The sharp orographic features cause sharper climatic features than expected without their existence (Lionello, 2006). About 60 % of the Mediterranean region (10°W-40°E, 28N°-47°N) consists of land areas where SM plays a central role for surface-atmosphere interactions and the hydrological response during flood events (Drobinski et al., 2014). For heat wave phases Stéfanon et al. (2014) showed the dependence of soil moisture-atmosphere responses on different terrains in the northwestern Mediterranean. In the plains soil moisture deficit influences the boundary layer by less evapotranspiration and higher sensible heat fluxes with a positive feedback due to the increase in the temperature. On the other hand, the higher sensible heat fluxes induced by a soil moisture deficit above the mountain terrains reinforce slope winds and sea-breeze. These strengthened mesoscale circulations generate wind convergence and foster the advection of moist air from remote regions which contribute to enhance vertical motion and favour convection initiation and precipitation. Moreover, the interplay between geographical characteristics of the Mediterranean region and large-scale forcing modify atmospheric circulation which leads to mesoscale features and several cyclogenesis mechanisms such as the Genoa low (Trigo et al., 2002) or the Iberian Peninsula thermal low (Hoinka and Castro, 2003).

The Mediterranean region is defined as the land around the Mediterranean Sea that has a climate that is characterised by mild wet winters and warm to hot, dry summers (Lionello, 2006). Figure 2.1 shows the domain of the Mediterranean region with its surface relief, the most important mountain ranges and major rivers. The Mediterranean is located on three continents (Europe, Africa and Asia) and reaches its maximum altitude of 4800 m in the Alps. The shallow submarine ridge between Sicily and Tunisia divides the Mediterranean region into the Western Mediterranean (WMed) and the Eastern Mediterranean (Drobinski and Ducrocq, 2008).

The Mediterranean climate has a strong seasonal variability in temperature and precipitation with long drought periods in summer, followed by intense rainfall events in autumn (WMed) and winter. In addition, there is a large south-north gradient of meteorological parameters within the Mediterranean. In summer, the mean surface air temperature in the Mediterranean region ranges from 15.5 °C (±5 °C) in the European highlands up to 32.5 °C (±10 °C) in the North African coastal zone. In winter it ranges from 2.5 °C (±2.5 °C) in the European highlands up to 15 °C (±5 °C) over the Mediterranean Sea (Bolle, 2003). In addition, spatial and temporal variability of total annual precipitation is high ranging from mean values below 200 mm/year in North Africa to 2000 mm/year over the Alps (Xoplaki et al., 2004). Precipitation in the winter half-year accounts for between 30 % and 80 % of the total annual precipitation.

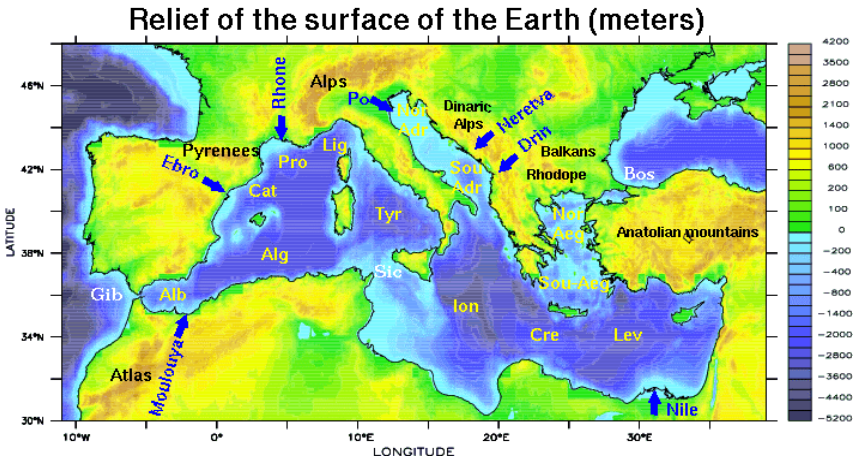

Figure 2.1.: Relief of the Mediterranean region. The black names indicate the names of the mountain ranges and the blue arrows and names illustrate the major rivers. The Mediterranean basin can be defined between longitudes 10°W-40°E and latitudes between 28°N-47°N [Adopted from Drobinski and Ducrocq (2008)].

The high spatial and temporal variability of the seasonal mean temperature and precipitation conditions in the Mediterranean is influenced by both mid-latitudes and tropical climate variability. The northwestern Mediterranean in particular is affected by the southeastern edge of the North Atlantic storm tracks in the cold wet season and is highly sensitive to interannual displacement of the path of mid-latitude cyclones which is associated with the North Atlantic Oscillation (NAO) phase. The winter precipitation in the WMed is anti-correlated with the NAO. On the contrary, the Eastern Mediterranean shows teleconnections with the El Nino Southern Oscillation (ENSO), which play an important role for the winter rainfall. Furthermore, the southeast Mediterranean is influenced by tropical and subtropical systems. In the summer, the Hadley cell moves northward leading to predominantly anticyclonic conditions and the advection of moisture from the Atlantic to the Mediterranean is weak. The weather regimes in the southeast Mediterranean summer are also linked to the Asian and the African monsoons (Lionello, 2006).
The land components of the water cycle in the Mediterranean exhibit a strong annual variation. Fig. 2.2 shows the domain-average values (10°W-40°E, 28°N-47°N) for precipitation (P), the evaporation (E) and the differences of P-E separately for land and sea areas of the Coupled Model Intercomparison Project Phase 3 (CMIP3) (Mariotti et al., 2008). In the Mediterranean continental water cycle, P reaches the annual maximum of about 1.4 mm/d in November and the minimum of about 0.6 mm/d in July. In May, the land evaporation has its maximum of approx. 1.5 mm/d due to the higher solar insolation in the summer half year and a still sufficient soil water availability, which is a limited factor in the following summer months. The minimum in E of around 0.6 mm/d is reached in November. From March to August a negative effective precipitation rate (P-E) over land is observed with a negative maximum of approx. -0.6 mm/d in June. In contrast, an annual maximum evaporation rate of about 4 mm/d is reached over the sea in the autumn by combination of warm sea surface temperature (SST) with stronger advection of cold, drier air masses in autumn which results in a higher evaporation compared to summer (Mariotti et al., 2002). Furthermore, a negative effective precipitation rate (P-E) is observed over the sea through-

out the year.

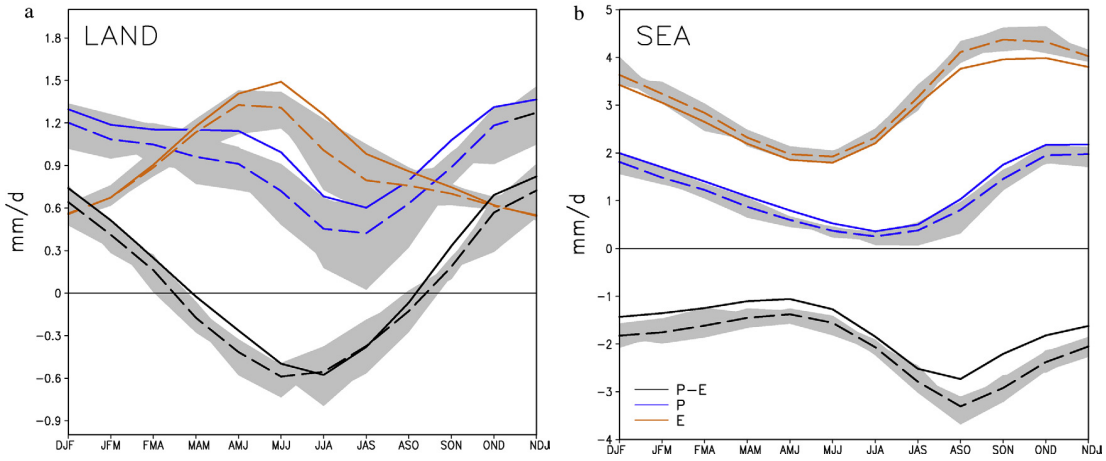

Figure 2.2.: Mediterranean water cycle for land a) and sea b) in 2070–2099 (dashed) compared to the 1950–2000 period (solid) based on an average of CMIP3 model simulations. The brown lines show the seasonal cycles of evaporation (E), the blue lines the precipitation (P) and the black lines the precipitation minus evaporation (P-E). For each, grey shading depicts the envelope of individual model anomalies [Adopted from Mariotti et al. (2008)].

Since precipitation is the main driver in the land surface hydrological cycle, changes of P also have strong impact on other hydrological components. Future projections suggest a change in the Mediterranean water cycle by the end of the 21st century (Fig. 2.2 (Mariotti et al., 2008)). The projected changes in precipitation over land areas are about -15 % compared to 1950-2000 which induce drier soil conditions. This reduction in precipitation and the increase in soil aridity leads to a reduction in summer land evaporation of -10 %. Moreover, the effective land precipitation (P-E) decreases by about 20 % in both summer and winter season. As a result, a 5 % decrease in total soil moisture and a 15-30 % decrease in total runoff is predicted (Mariotti et al., 2015). Future projections over the Mediterranean Sea indicate a further loss of fresh water (P-E) due to decrease in precipitation and increased evaporation due to warming. This projected decline in fresh water in the Mediterranean Sea is reinforced by a reduction in river runoff from the surrounding land areas (Mariotti et al., 2008).

2.2. Soil Moisture-Atmosphere Interactions

Soil moisture (SM) has a regulatory function for evapotranspiration and acts as the main moisture source for the atmosphere in the continental branch of hydrological cycle (Seneviratne et al., 2010). The soil moisture has a “memory” of wet and dry anomalies caused by conditions that are long forgotten by the atmosphere (Koster and Suarez, 2001). In this way, SM is one of the major “slow” drivers of the climate system (Seneviratne et al., 2006a) and is a key aspect for land-atmosphere interactions on different temporal and spatial scales, ranging from daily to climate and from local to global. Several recent studies have shown that soil moisture-climate feedbacks are responsible for a significant part of the simulated

changes in climate projections (Seneviratne et al., 2006a; Jaeger and Seneviratne, 2011; Boberg and Christensen, 2012; Seneviratne et al., 2013). On decadal time scales, the initial conditions of SM have an important impact on the water cycle components depending on the regional characteristics (Khodayar et al., 2015; Breil and Schädler, 2017). In addition, events such as droughts, floods or summer heat waves could be maintained or amplified by SM anomalies on seasonal scale extremes (Beljaars et al., 1996; Fischer et al., 2007a; Zampieri et al., 2009; Saini et al., 2016). Since SM anomalies in the deep soil layers persist for several months, these anomalies have a significant implication for seasonal prediction (Ferranti and Viterbo, 2006; Seneviratne et al., 2006a). Finally, initial soil moisture strongly influences the boundary layer characteristics on weather time scales (Zhou and Geerts, 2013; Dirmeyer and Halder, 2016).

The influence of soil moisture on the surface climate is most pronounced in transitional climate regions, where evapotranspiration is strongly dependent on soil moisture. Due to the impact of evapotranspiration on the partitioning of the incoming energy in latent and sensible heat fluxes, soil moisture further affects processes determining albedo, air temperature, boundary-layer stability and precipitation (Seneviratne et al., 2010). In the following, the definition of SM and its coupling with evapotranspiration in the energy and water balances is described. Soil moisture is defined as the amount of water stored in the unsaturated soil zone and is often given by the volumetric soil moisture:

$$\theta = \frac{V_{H_2O}}{V} \tag{2.1}$$

where V is the soil volume and V_{H_2O} is the volume of water in the soil. θ has the unit ${m^3}_{H_2O}/{m^3}_{soil}$. The hydrological cycle on land can be described by the land surface water budget (Seneviratne et al., 2010):

$$\frac{dS}{dt} = P - E - R_s - R_g \tag{2.2}$$

where $\frac{dS}{dt}$ is the change of the surface soil layer water storage, P corresponds to the precipitation, E is the evapotranspiration and R_s is the surface runoff and R_g is the drainage. The term dS/dt includes the soil moisture but also contains other forms of water storage such as surface water, snow and ice cover and ground water. Furthermore, the soil moisture influences the energy balance for the same surface layer:

$$\frac{dH}{dt} = R_n - L_0 - H_O - G \tag{2.3}$$

where dH/dt is the change of energy within the surface soil layer, R_n is the net radiation, H_0 is the sensible heat flux, L_0 is the latent heat flux and G is the ground heat flux to deeper layers. The net radiation R_n is given by:

$$R_n = SW_{in} - SW_{out} + LW_{in} - LW_{out} \tag{2.4}$$

where SW_{in} and SW_{out} are the incoming and outgoing shortwave radiation and LW_{in} and LW_{out} are the incoming and outgoing longwave radiation.

Soil moisture-evapotranspiration coupling

The equations 2.1-2.4 are used in a conceptual framework to describe evapotranspiration as a function of soil moisture (Seneviratne et al., 2010). A distinction is made between an energy-limited and soil moisture-limited evapotranspiration regime (Fig. 2.3). The energy-limited evapotranspiration regime corresponds to soil moisture values above a given critical soil moisture value θ_{CRIT}, where the evaporative fraction $EF = L_0/R_n$ is independent of soil moisture. The soil moisture limited evapotranspiration regime is below the θ_{CRIT} and in this regime the soil moisture impacts the climate system via evapotranspiration processes. Another important threshold is the wilting point θ_{WILT}, at which no soil moisture can be extracted from the soil by plants. In this regard, three climate/soil moisture regimes are defined to describe the impact of SM on evapotranspiration variability (Koster et al., 2004). In the wet ($\theta > \theta_{CRIT}$) and dry ($\theta < \theta_{WILT}$) climate regime SM does not impact the evapotranspiration variability, whereas in a third transitional climate regime ($\theta_{WILT} \leqq \theta \leqq \theta_{CRIT}$) the variability of evapotranspiration is strongly limited. The Mediterranean is a region with such a transitional regime between wet and dry climate, in which a strong soil moisture-atmosphere coupling is possible (Seneviratne et al., 2010).

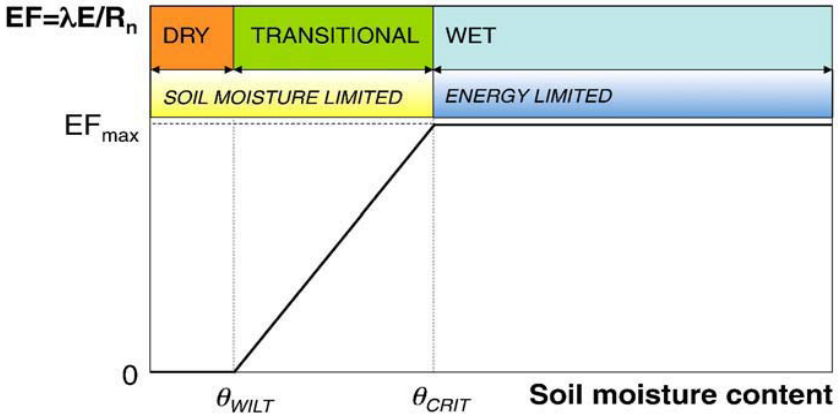

Figure 2.3.: Conceptual framework for the dependence of evapotranspiration on soil moisture. θ_{WILT} is the wilting point and θ_{CRIT} is the critical soil moisture point. EF denotes the evaporative fraction and EF_{max} is its maximal value [Adopted from Seneviratne et al. (2010)].

Soil moisture-temperature feedback mechanism

The effect of soil moisture on near-surface conditions is related to changes in air-temperature. When SM limits the latent heat flux more energy is available for sensible heat flux which leads to an increase in the near-surface temperature (Seneviratne et al., 2010). Such soil moisture-temperature interactions can be relevant for the development of dry extremes like hot temperatures and heat waves (Fischer et al., 2007a,b; Jaeger and Seneviratne, 2011; Stéfanon et al., 2014; Schwingshackl et al., 2017)).

In Fig. 2.4a the possible soil moisture-temperature feedback mechanisms are illustrated (Seneviratne et al., 2010). A decrease in soil moisture leads to a decrease in evapotranspiration (A) and an increase in sensible heat flux and finally to an increase in temperature (B). These couplings are indicated by positive

red arrows. The blue arrows show two negative couplings which induce a possible positive feedback (C). A higher temperature leads to an increase in evapotranspiration and then again to higher evapotranspiration rates which induces a further decrease in soil moisture. The IPCC AR4 land-atmosphere coupling diagnostics (Seneviratne et al., 2006b) identify the Mediterranean region as a hot spot region of strong soil moisture-atmosphere interaction related to temperature.

Soil moisture-precipitation feedback mechanism

The discussion about the soil moisture-precipitation feedbacks and its possible sign has been going on for several years. Soil moisture-precipitation feedback can be caused by direct and indirect effects. In general, the local sources of atmospheric moisture leading to precipitation are: the local evapotranspiration and the external advection of moisture (Bisselink and Dolman, 2008). In the 1990s the concept of "precipitation recycling" was predominant. In this concept local soil moisture contributes to precipitation via surface turbulent fluxes (Entekhabi et al., 1992; Eltahir and Bras, 1996). The recent study by van der Ent et al. (2010) showed that over the Mediterranean land about 40-70 % of terrestrial evaporation returns as precipitation. Over the Iberian Peninsula Rios-Entenza and Miguez-Macho (2014) found that 30-60 % of the precipitation are originated from "precipitation recycling" in the month of May in the years 2000 to 2010. Moreover, Thiébault et al. (2016) concluded that evapotranspiration over land accounts for 50 % to 80 % of the total annual rainfall over the Mediterranean land areas and is therefore a key process in the annual continental hydrological cycle.

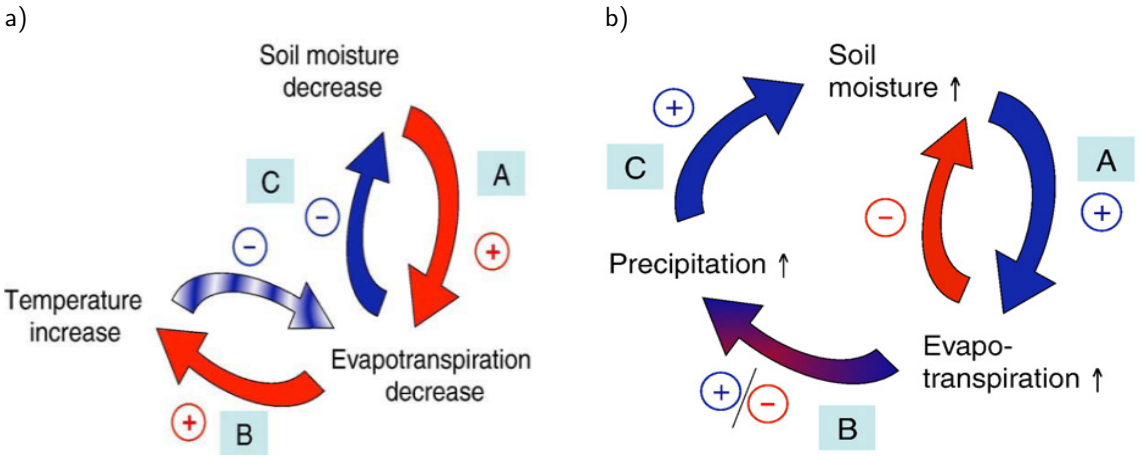

Figure 2.4.: a) Processes that contribute to the SM-temperature feedback mechanism. Red arrows indicate processes leading to drying/warming in response to a negative SM anomaly and blue arrows denote potential negative feedbacks. Relationship (A) relates to the link between SM and evapotranspiration, (B) between evapotranspiration and sensible heat flux and (C) relates to a potential positive feedback. b) Processes that contribute to soil moisture-precipitation feedback mechanism. Blue arrows represent positive soil moisture feedbacks and red arrows indicate potential negative feedbacks. (A) is the relationship between SM and evapotranspiration anomalies, (B) the relationship between evapotranspiration and subsequent precipitation anomalies and (C) the relationship between precipitation and SM anomalies [Adapted from Seneviratne et al. (2010)].

In addition to the direct effect, indirect interactions due to the boundary-layer characteristics, mesoscale circulations and the remote soil moisture status also play an important role in the soil moisture-precipitation feedback (Schär et al., 1999; Hohenegger et al., 2009; Seneviratne et al., 2010; Wang et al., 2010; Taylor et al., 2011; Guillod et al., 2015; Lorenz et al., 2016). In these studies, the decisive aspect for understanding the soil moisture-precipitation interactions depends more on the impact of soil moisture anomalies on the boundary-layer stability and precipitation formation than on the absolute moisture input by modified evapotranspiration.

Figure 2.4b provides an overview of possible SM-precipitation feedbacks. The positive blue arrows indicate processes leading to positive soil moisture feedbacks and the negative red arrows illustrate the potential of negative feedback to weaken the original soil moisture anomaly (Seneviratne et al., 2010). The coupling between higher soil moisture leading to higher evapotranspiration (A) is favoured for the mentioned transitional regime between wet and dry climates. On the other hand, increasing evapotranspiration may result in a negative coupling to the original wet soil moisture anomaly with a decrease in the available soil moisture. The relationship between a higher evapotranspiration rate and an increase in precipitation is the most uncertain relationship in the soil moisture-precipitation feedback due to the high number of involved processes (B). A possible positive sign of soil moisture feedback results from the influence of SM in the energy (Eq. 2.3) and the water balances (Eq. 2.2). In the latter case, the direct effect of "precipitation recycling" induces a positive feedback in which wet soil moisture leads to more precipitation. In addition, Eltahir (1998) showed the influence of wet soils on the surface energy by reducing the surface albedo and the Bowen ratio which lead to an enhancement of net solar and terrestrial radiation (Eq. 2.4). Consequently, a higher total flux of heat from the surface to the boundary layer creates more moist static energy and local convective storms lead to more precipitation (Eltahir, 1998). On the other hand, some studies suggest negative feedbacks due to complexity of the processes involved with different temporal and spatial scales. For example, deep convection and cloud formation can be triggered if stronger daytime heating over dry soils induces vigorous thermals which break through the stable layer at the top of the boundary layer (Hohenegger et al., 2009). Finally, in the SM-precipitation feedback loop in Fig. 2.4b higher precipitation leads to an increase in soil moisture which is a positive feedback.

The coexistence of opposite feedback signs within the same region is shown by Guillod et al. (2015). In their study afternoon precipitation events occur preferentially during wet and heterogeneous soil moisture conditions while being located over comparatively drier patches. They concluded that positive temporal coupling might enhance the persistence of precipitation while negative spatial coupling tends to regionally homogenised land surface conditions. The current study of Yang et al. (2018) additionally supported the idea that positive and negative SM-precipitation feedbacks appear simultaneously over land. In this regard, positive feedbacks occur mainly in transitional regions while negative feedbacks appear in extreme dry and wet regions.

2.3. Atmospheric Convection

Modified surface conditions due to a soil moisture anomaly affect the atmosphere conditions via atmospheric instability and convection. Thereby the modified energy signal at surface is transported horizontally and vertically into the troposphere. Convection is a process of energy transfer which is from the meteorology point of view an exchange of heat and moisture from the surface to the atmosphere and from the equator to polar regions. Therefore, a variety of forms of atmospheric convection exist with different spatial and temporal scales. Atmospheric convection is strongly influenced by the phase changes of water (Emanuel, 1994). A differentiation is made between dry and humid atmospheric convection. Furthermore, atmospheric convection is distinguished between free and forced convection processes. Free or buoyant convection is predominantly vertical motion driven by buoyancy forces arising from a static instability of a hydrostatic equilibrium. In contrast, the forced convection is caused by some dynamical mechanisms of frontal lifting, orographic lifting or induced by vertical motion by surface wind convergence. These convective processes are governed by fundamental equations of motion and thermodynamics and are based on physical principles like the conservation of momentum, energy and mass. In the following the concept of an air parcel is used to consider convective processes. This concept is fundamental to explain stability processes of an isolated body of density to its environment. The environment is defined as the air surrounding of the parcel.

Dry convection

In the dry convection the relative humidity within a parcel is below 100 % in which no phase transition from water vapour to liquid water takes place. To describe the buoyancy-induced motion in the atmosphere the vertical moment equation of an ideal fluid is considered:

$$\frac{dw}{dt} = \frac{1}{\overline{\rho}} \frac{\partial p'}{\partial z} - g\left(\frac{\rho'}{\overline{\rho}}\right) \tag{2.5}$$

where w is the vertical motion, z is the atmospheric height and g is the gravitation acceleration. The density ρ and pressure p are divided in a mean value $(\overline{\rho}, \overline{p})$ and the deviation value to the standard value of pressure and density (ρ', p'). The first term on the right side refers to the nonhydrostatic pressure gradient acceleration which arises from dynamical effects of forced momentum changes (Emanuel, 1994). The second term is the buoyancy acceleration which represents the action of gravity on density anomalies:

$$B \equiv -g\left(\frac{\rho'}{\overline{\rho}}\right) \tag{2.6}$$

Furthermore, the state of the dry system can be described by the potential temperature θ. The potential temperature is the temperature which an air parcel would have at some given temperature T and pressure

p if it is adiabatically expanded or compressed to a reference pressure p_0. Adiabatic processes are reversible processes in which no heat is exchanged with the surroundings. θ is defined as:

$$\theta \equiv T\left(\frac{p_0}{p}\right)^{\frac{R}{c_p}} \tag{2.7}$$

where p_0 is the reference pressure (typically 1000 hPa), $R = 287.15\ Jkg^{-1}K^{-1}$ is the gas constant and $c_p = 1005\ Jkg^{-1}K^{-1}$ is the specific heat at constant pressure.
The rate of decrease of temperature with height due to the expansion and cooling of lifted air is given by the lapse rate of temperature. For an atmosphere in which potential temperature is constant the dry adiabatic is defined as follow:

$$\Gamma_d \equiv \frac{dT}{dz} = \frac{g}{c_p} \tag{2.8}$$

Moist convection

In Mediterranean land areas soil moisture is an important moisture and instability source for moist convection. In general, moist convection is essential in the earth system because the condensation of saturated water vapour in an air mass allows the formation of clouds and precipitation. In this regard, clouds occur when the air is cooled to the dewpoint and cloud droplets grow by condensation of water vapour on cloud condensation nuclei. The growth of these cloud droplets to rain drops is caused by complex microphysic processes including different phases of clouds, the Bergeron-Findeisen process, collision and coalescence processes. With respect to convective clouds it can be distinguished between shallow and deep convection, whereby more available convective energy can lead to higher convective clouds. The shallow convection clouds have a height of 1-2 km within the atmospheric boundary layer while deep moist convection clouds reach a vertical extent of 10-15 km. Deep convection is accompanied with hazardous weather phenomena such as heavy precipitation, flash floods, tornados or wind gusts.
The difference between moist convection and dry convection is that saturation is reached. The change in the phase of water is often accompanied with the release of latent heat which affects the dynamics but already the presence of water vapour can be critical to the buoyancy acceleration (Holton and Hakim, 2013). The equation of state for moist air is given by:

$$p = \rho R_d T_v \tag{2.9}$$

where R_d is the dry air gas constant and T_v is the virtual temperature representing the temperature dry air would have if its pressure and density are equal to those of moist air:

$$T_v = \frac{T}{1 - \frac{e}{p}\left(1 - \frac{R_d}{R_v}\right)} \tag{2.10}$$

where R_v is the gas constant of water vapour and e is the vapour pressure. Hereby is $T_v \geq T$ and the difference is in an order of a few degrees but small differences decide upon an air parcel being stable or

unstable (Holton and Hakim, 2013). When a moist air parcel ascends adiabatically it expands and cools, thereby the relative humidity (RH) increases and can reach saturation. RH is given by the water vapor pressure e and the saturated water vapor pressure e_s:

$$RH = 100 \times \frac{e}{e_s} \tag{2.11}$$

To facilitate the considering of the parcel dynamics in a moist atmosphere the equivalent potential temperature θ_e is used (Holton and Hakim, 2013):

$$\theta_e \approx \theta exp\Big(\frac{L_c q_s}{c_p T}\Big) \tag{2.12}$$

where L_c is the latent heat of vaporisation, $q_s = 0.622\frac{e}{p-e}$ is the saturation mixing ratio. θ_e is the potential temperature that an air parcel would have if all its moisture condensed and fell out and the air parcel is compressed adiabatically to a pressure level of 1000 hPa. Thereby the released latent heat raises the temperature of the air parcel. The equivalent potential temperature is a measure for the temperature and humidity in the atmosphere.

Parallel to the dry adiabatic lapse rate the moist adiabatic lapse rate (pseudo-adiabatic lapse rate) can be formulated as follows:

$$\Gamma_s \equiv \frac{dT}{dz} = \Gamma_d \frac{[1 + \frac{L_c q_s}{RT}]}{[1 + \varepsilon \frac{L_C^2 q_s}{c_p R T^2}]} \tag{2.13}$$

with ε=0.622 as the ratio of the molecular weight of water to that of dry air. The pseudo-adiabatic lapse rate Γ_s is always less than the adiabatic lapse rate Γ_d ($\sim 10\, Kkm^{-1}$). Γ_s values range from $\sim 4\, Kkm^{-1}$ in warm, humid air masses in the lower troposphere up to about $6-7\, Kkm^{-1}$ in the midtroposphere (Holton and Hakim, 2013).

Atmospheric stability

The atmospheric stability can be influenced by initial soil moisture. In this respect, for example Schär et al. (1999) showed that wet soils imply the build-up of a shallow boundary layer with high values of low-level moist heat and moisture concentrated in a comparatively small volume of air. These processes provide a source of convective instability.

The parcel method is used to describe the stability of the atmosphere leading to convection. In this method the air parcel undergoes a vertical displacement from an equilibrium level. The air parcel follows the dry and wet adiabatic lapse rate depending on saturation is either reached or not reached. The difference in the lapse rate of the air parcel with the atmospheric lapse rate (γ) of the environment determines the stability of the air parcel. The potential temperature is a function of height and the following different kinds of instabilities can be distinguished:

1. **Absolutely stable** $\gamma < \Gamma_d \quad \frac{\partial \theta}{\partial z} > 0$
   An air parcel is colder than its environment and no lifting forced on the parcel is induced. If the parcel is perturbed it returns to its initial point.

2. **Absolutely unstable** $\gamma > \Gamma_d \quad \frac{\partial \theta}{\partial z} < 0$
   The atmospheric lapse rate is greater than the dry-adiabatic lapse rate. The temperature of the air parcel is warmer than the environment which leads to further acceleration of a vertically displaced air parcel in the direction of displacement.

3. **Potentially unstable** $\frac{\partial \theta_e}{\partial z} < 0$
   The potential instability also called convective instability is the state of an unsaturated atmospheric layer or column of air with upward-decreasing θ_e. The air mass is stable to unsaturated vertical displacement until a lifted air mass is completely saturated. Then the lifted air mass will become unstable. At this point the atmospheric lapse rate exceeds the moist adiabatic lapse rate.

4. **Conditionally unstable** $\Gamma_d > \gamma > \Gamma_s \quad \frac{\partial \theta_{es}}{\partial z} < 0$
   The state of an unsaturated atmospheric layer is conditionally unstable when its lapse rate is less than the dry-adiabatic lapse rate but greater than the moist-adiabatic lapse rate. Under such conditions the atmospheric layer is locally stable to the displacement of an unsaturated air parcel but once the air parcel becomes saturated the conditions become unstable. The saturated equivalent potential θ_{es} is considered in conditional instability. In this case, the necessary condition is that the air parcel reaches the level of free convection (LFC). Differences between potential and conditional instability can be summarised that only if the vertical displacement is sufficient enough and a potentially unstable layer or parcel is lifted to saturation it will become conditionally unstable (ZAMG, 2007).

For an illustration of the conditional instability the Skew-T-Lop p (Fig. 2.5) is a useful “pseudo-adiabatic thermodynamic diagram". The Skew-T-Lop p provides an information about the profile of temperature, pressure and dewpoint for a given time. The structure of the diagram shows horizontal isobars as a vertical coordinate with a logarithmic scale and skewed isothermal lines at 45° to the plot. The dry and moist adiabats are represented as slight curve lines sloping from the lower right to the upper left. For conditional instability sufficient moisture and/or forcing lifting are necessary to produce this instability. In Fig. 2.5 a surface-based parcel is lifted with the lapse rate Γ_d until it reaches saturation at the lifting condensation level (LCL). With saturation the air parcel follows the moist adiabatic curve Γ_s and if the air parcel is lifted to the level of free convection (LFC) where the air parcel rises without any external forcing process. At this point the temperature of the air parcel becomes warmer than the environment temperature by release of latent heat. The parcel rises until buoyancy returns to zero at the so-called level

of neutral buoyancy (LNB). The integrated buoyancy between the LFC and the LNB is termed as the convective available potential energy (CAPE) and is given by (Holton and Hakim, 2013):

$$CAPE = g \cdot \int_{zLFC}^{zLNB} \left(\frac{T_{parcel} - T_{env}}{T_{env}} \right) dz \tag{2.14}$$

where T_{parcel} is the virtual temperature of the parcel, T_{env} is the virtual temperature of the environment and zLNB and zLFC are the heights of LFC and LNB. CAPE is an index describing the maximum amount of potential energy which is available in an air parcel for convection in J/kg. A further index for quantification of atmospheric inhibition is the convective inhibition (CIN) (Markowski and Richardson, 2010). This index represents the required energy (J/kg) of a synoptic or mesoscale force to lift an air parcel adiabatically to the LFC. In the Skew-T-Lop CIN is illustrated by the integrated negative buoyancy below the origin level of the air parcel and the LFC (Kirshbaum et al., 2018).

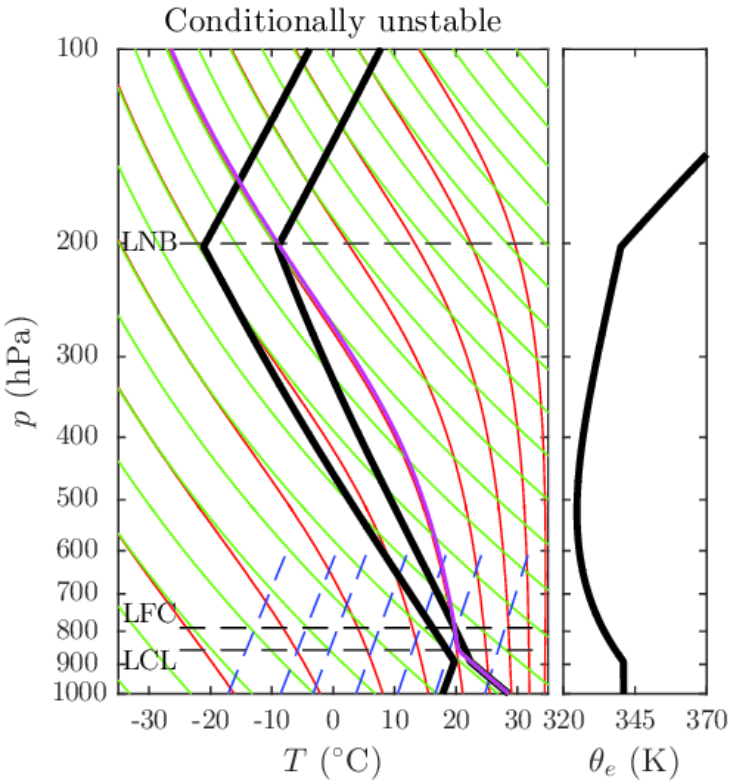

Figure 2.5.: The left figure illustrates the Skew-T/log-P diagram for a conditionally unstable environment. The thick black lines indicate the temperature T (right) and the dewpoint temperature T_d (left) of the environment. The lines show in green the dry adiabats, in red the moist adiabats and the dashed blue lines show the T_d profiles of air with different saturation mixing ratios. The thick magenta line presents the path of adiabatically lifted surface-based parcel. On the right side the corresponding vertical profile of θ_e is shown. The illustration is extracted from Kirshbaum et al. (2018).

2.4. Dry and Wet Extremes in the Mediterranean

The Mediterranean region is affected by all main natural risks associated with the water cycle. These include wet extremes such as heavy precipitation events and flash floods as well as dry extremes such as heat waves and droughts (Thiébault et al., 2016). Extremes are by definition rare events which are often characterised by large spatial and temporal variability. However, some seasons are identified to be prone for extremes, e.g. the autumn season for wet extremes in the WMed and the summer season for dry extremes. In these seasons the following extreme phenomena are investigated:

Dry extremes:

- **Heat wave**: A range of weather-related and bioclimatic definitions of heat wave have been developed with regard to their impact on natural and social systems or on human health (Stefanon et al., 2012). In this work, the Jaeger and Seneviratne (2011) heat wave criterion of the 90th percentile of the domain-average maximum temperature (long-term: 1961-1990) for at least two consecutive days is adapted. The studies of Lorenz et al. (2010) and Stefanon et al. (2012) highlighted the impact of soil moisture on the persistence of heat waves and its soil moisture-temperature response in Europe and the northwestern Mediterranean.

- **Drought**: The definition of drought is diverse depending on the regions, needs and disciplinary approaches. To facilitate the discussion about drought definitions, it can be categorised into four general types: Meteorological/climatological, agricultural, hydrological and socioeconomic droughts. The first three types are defined by physical, hydrometeorological or biological parameters while the fourth describes the impacts of drought on society (American Meteorological Society (AMS), 2019). In this thesis only a meteorological drought is considered which is defined as an unusual period of abnormally dry weather with a precipitation deficit persisting for a timescale longer than a month. Corresponding drought periods in the investigation domains are identified with the effective drought index (EDI). Spinoni et al. (2015) investigated the biggest drought events in Europe from 1950-2012 and showed the highest drought frequency, duration and severity in the 1990s and 2000s for the Mediterranean area. The influence of spring and summer soil moisture deficit for the development of droughts and heat waves is demonstrated in several studies (Vautard et al., 2007; Fischer et al., 2007a; Zampieri et al., 2009; García-Herrera et al., 2010). For the record-breaking drought in summer 2003 over the European continent, García-Herrera et al. (2010) identified three main contributing factors: blocking episode, soil moisture deficit and high sea surface temperature. In this regard, Ferranti and Viterbo (2006) and Fischer et al. (2007a) showed the sensitivity of this exceptional drought to soil water initial conditions. Without soil moisture anomalies the summer heat wave would be potentially reduced up to 40 %. Moreover, positive feedbacks of SM could be found on continental-scale circulation. A recent paper of Ionita et al. (2017) pointed out that five of the six hottest summers since 1950 in Europe occurred after the year 2000. They ranked

the summers 1972, 2003, 2010 and 2015 as both extreme hot and dry periods. For the selected summers 2003 and 2015 a detail description will be given in Chapter 7.1.

Wet extremes: The definition of wet extremes depends on the specific physiographic conditions of a location:

- In the Western Mediterranean **heavy precipitation events (HPEs)** are characterised by a rainfall amount of more than 100 mm/d which are typically generated by orographic precipitation, frontal systems or mesoscale convective systems (MCSs) (Ducrocq et al., 2014). The WMed including eastern Spain, southern France, northwestern Italy and northern Africa is prone for HPEs due to the interplay between the dominant atmospheric low-level flow circulation pattern and the complex relief and orientation of mountains at the coast (Jansa et al., 2014; Ducrocq et al., 2014; Khodayar et al., 2016a). The main ingredients for the initiation of deep convection leading to such HPEs are: a trigger mechanism, sufficient low-level atmospheric moisture, conditional instability and large-scale lifting and/or low-level convergence (Doswell et al., 1998; Khodayar et al., 2018). The involved atmospheric processes caused HPEs working at different atmospheric scales such as local convection, upper synoptic-scale-level troughs and mesoscale convective systems (Dayan et al., 2015). The main water sources contributing to Mediterranean HPEs are the Mediterranean Sea, the North Atlantic and the African and the Mediterranean land surfaces (Duffourg and Ducrocq, 2013; Pinto et al., 2013; Winschall et al., 2014; Khodayar et al., 2018). In this respect, local moisture sources are transported in the low troposphere in time scales about 1-2 days and remote sources are transported in time scales of about 2-10 days. Winschall et al. (2014) concluded that the water supply from remote intense evapotranspiration anomalies is essential for the occurrence of HPEs. In this context, soil moisture can play a key role as a moisture source for evapotranspiration anomalies or in the modification of latent and sensible heat fluxes generating conditionally instability. These processes are important for the triggering of deep convection.

- A specific kind of HPEs are the **flash floods** caused by short-lasting heavy rainfall systems that produce more than 100 mm rainfall amount in a time period of less than one hour up to 24 h. The affected areas are often limited to a few hundred square kilometres and are associated with a rapid hydrological response in discharge with a delay of less than 6 hours (Gaume et al., 2016). These disastrous flash-floods are more frequently in the Western Mediterranean (WMed), especially in Spain and Italy, than in the rest of Europe (Llasat et al., 2010; Gaume et al., 2016). Flash floods are often associated with MCSs lasting several hours stationary on one location (Bluestein and Jain, 1985). Some examples of dramatic flash-flood events in the WMed occurred in Vaison-la-Romaine in September 1992 with about 300 mm in 4 h (Sénési et al., 1996), in Liguria in October and November 2011 with about 500 mm in 6-12 h (Silvestro et al., 2012; Rebora et al., 2013) or in Valencia in November 1987 with about 800 mm in 24 h (Romero et al., 2000). The land use,

soil type and the initial soil moisture affect the responses of watershed to such flash floods in the WMed (Tramblay et al., 2011; Gaume et al., 2016).

Trends in wet and dry extremes

Until the end of the 21st century the temperature in the Mediterranean land areas are projected to increase between +3 °C and +7 °C. At the same time the mean annual precipitation is expected to decrease about -10 %, with summer rainfall reducing 50 % in the Eastern Mediterranean, Spain and Italy (Alpert et al., 2013). This decrease in projected mean precipitation is accompanied by an increase in daily extreme rainfall (95th percentile) of about +10 % (Thiébault et al., 2016). Especially in the Western Mediterranean (South France or North Italy) the increase of extreme precipitation can exceed +20 % until the end of the twenty-first century (Tramblay and Somot, 2018). This positive sign of projected extreme precipitation values arises from a combination of (a) drying associated with a poleward shift of the circulation in the WMed and a decrease in land evaporation and (b) an increase of precipitative water content in the atmosphere due to a higher sea evaporation rate (Pfahl et al., 2017). Another main driver of extreme precipitation is the low-level instability which in a changing climate can be influenced by higher differential heating between sea/land surface and the low troposphere which in turn influences the vertical potential instability (Tramblay and Somot, 2018).

The IPCC report (Christensen et al., 2013) emphasised the possible amplification of temperature extremes by changes in soil moisture. The Mediterranean region is identified as one of the hot spots of change in heat extremes associated with a reduction of precipitation, soil moisture and evapotranspiration (Giorgi, 2006). A high consistency between different regional climate model projections is found, showing the change in heat wave patterns in this region (Orlowsky and Seneviratne, 2012). Lorenz et al. (2016) concluded that a projected drying trend in soil moisture in the Mediterranean leads to an increase in intensity, frequency and duration of temperature extremes by the end of the 21st century. In the Mediterranean region the changes of SM in the CMIP5 projections are accounts for about 25 % of the projected change in extreme temperature at the end of the 21th century (Seneviratne et al., 2013).

3. Model Setup and Observational Data Sets

This chapter presents the COSMO model and the observational data sets that are used to analyse the Western Mediterranean SM-atmosphere interactions. The basic model equations, the main physical parameterisations and the necessary initial and boundary conditions of COSMO are described in Sec. 3.1. The lower boundary conditions at surface of the COSMO model are provided by the multi-layer soil and vegetation model TERRA-ML which parameterises the land surface processes. Soil moisture derived from the satellite mission SMOS and the new downscaled 1 km SMOS-L4 SSM product are described in Sec. 3.2. Finally, Sec. 3.3 introduces observation data sets for the validation of the model results and the remote sensing measurements of the SMOS mission.

3.1. COSMO Model

The Consortium for Small-scale Modeling (COSMO) is a non-hydrostatic atmospheric prediction model for a limited-area. COSMO is based on the primitive thermo-hydrodynamical equations describing compressible flows in a moist atmosphere. The equations are formulated in terrain following height coordinates with rotated geographical coordinates without any scale approximation. The model is designed to represent processes in the meso-β and meso-γ scale (2-200 km). Important physical processes on subgrid-scale have to be parametrised because not all spatial and temporal scales of the atmospheric processes can be resolved by the weather and climate models like COSMO. For specific events COSMO simulations are performed with the numerical weather prediction (NWP) version and on seasonal scale with the climate version (CLM). The COSMO-NWP and COSMO-CLM have the same dynamics, numerics and parameterisations but COSMO-CLM requires additional variables in the initial and boundary conditions, as e.g. plant characteristics and sea surface temperatures are not kept constant in the COSMO-CLM. In this work, the COSMO-NWP version 5.01 (Schaettler et al., 2014) is used, with the corresponding version CLM-5.00 for the climate mode.

3.1.1. Model Equations and Physical Parameterisations

To describe the atmospheric flow, the atmosphere is considered as a multicomponent continuum of dry air, water vapour, liquid and solid water in an ideal mixture (Doms and Baldauf, 2018). The basic model equations are based on the conservation of heat, mass and momentum, the gravity force and Coriolis force as well as phase changes of water. For the calculation of the atmospheric state, the meteorology variables of wind velocity $\vec{v} = (u, v, w)$, density ρ, pressure p, temperature T and the specific humidity q

have to be solved numerically with five coupled partial differential equations.
The first basic model equation named *Navier-Stokes equation* predicts the changes in the wind fields:

$$\rho \frac{dv}{dt} = -\nabla p + \rho \vec{g} - 2\Omega \times (\rho \vec{v}) - \nabla \vec{\tau} \tag{3.1}$$

where, ρ is the density, p the pressure and $\vec{v}$ the wind vector. The first term on the right side expresses the pressure gradient force, the second term stands for the gravitational force with the gravity acceleration $\vec{g}$. The third term describes the Coriolis force with the angular velocity of the earth rotation Ω and the last term presents the friction forces with the stress tensor $\vec{\tau}$.
The second basic model equation is the *continuity equation* which describes the conservation of mass:

$$\frac{d\rho}{dt} = -\rho \nabla \cdot \vec{v} \tag{3.2}$$

The third *prognostic equation of humidity* is given by:

$$\rho \frac{dq^x}{dt} = -\nabla \cdot J^x + I^x \tag{3.3}$$

where x represents a specific constituent of the mixture (d=dry air, v=water vapour, l= liquid water or f for solid frozen state). Further $dq^x = \rho^x/\rho$ is the mass fraction of constituent x and J^x denotes the diffusion flux and I^x stands for the sources/sinks of moisture.

The fourth differential equation is *the prognostic equation for temperature*, which represents the thermodynamic processes:

$$\frac{\partial T}{dt} + \vec{v} \cdot \nabla p = \frac{1}{\rho c_{pd}} (\frac{\partial p}{\partial t} + \vec{v} \cdot \nabla p) + Q_T \tag{3.4}$$

where Q_T is the diabatic heating due to evaporation and radiation processes and c_{pd} is the specific heat capacity of constant pressure.

The diagnostic *equation of state* describes the density of moist air which is derived by the ideal gas law:

$$\rho = \frac{p}{R_d(1 + (\frac{R_v}{R_d} - 1)q^v - q^l - q^f)T} \tag{3.5}$$

with R_v and R_d as the gas constant for water vapour and dry air. Further q^v is the specific humidity in the atmosphere and q^l presents the water content and q^f is the ice content.

Transformation of COSMO coordinate system

These basic mathematical equations are converted into a realistic description of coordinates in the earth system. For this purpose, spherical coordinates with the longitude λ coordinate, latitude φ coordinate and the terrain-following vertical coordinate ζ are used. In addition, the coordinate system is rotated to

overcome numerical problems due to convergence of the meridians in high geographical latitudes. In the new rotated coordinate system, the equator and the main meridian intersect at the centre of the model domain. The terrain-following ζ coordinate simplifies the numerical solution of the equation at the upper and lower boundaries. The lower boundary is the surface of the orography and the upper boundary of the atmosphere ($\sim 22\,km$) is a plane surface. Further details can be found in Doms and Baldauf (2018).

Time discretisation and grid structure

The basic partial differential equations Eq. 3.1-3.4 must be resolved numerically with a finite difference method. Therefore, the atmosphere is divided into finite numbers of grid points (i, j, k) where i corresponds to the λ-direction, j to the φ-direction and k to the ζ-direction. Every grid point represents the center of the elementary rectangular grid volume with the side length $\Delta\lambda, \Delta\varphi, \Delta\zeta$. The wind vectors u, v and w are set halfway between the grid-box faces ($\lambda_{i\pm1/2}, \varphi_{j\pm1/2}, \zeta_{k\pm1/2}$). For the spatial discretisation a three-dimensional Arakawa-C/Lorenz grid is used (Fig. 3.1) where the model variables T, p or q^x are defined in the center of the grid box and the normal velocity components are defined on the corresponding box faces. In vertical direction the upper boundary layer is set a half level above the uppermost model layer and the lower boundary is half a level below the first model layer.

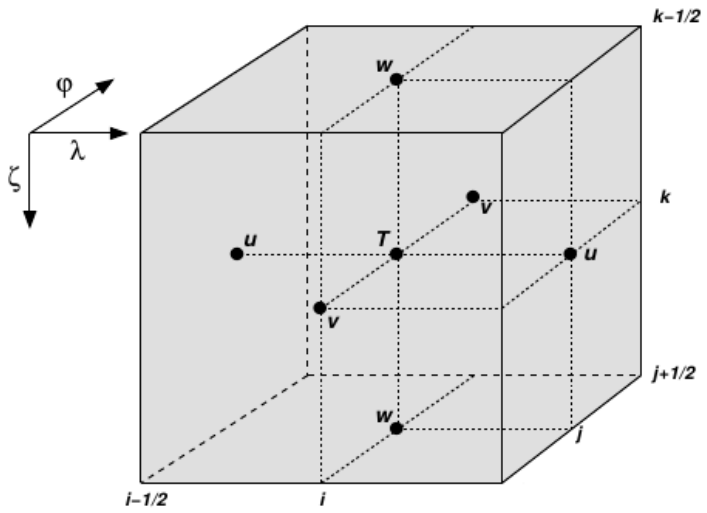

Figure 3.1.: A grid box volume $\Delta V = \Delta\zeta\Delta\lambda\Delta\varphi$ showing the Arkawa-C/Lorenz staggering of the dependent model variables. The figure is extracted from Schaettler et al. (2014).

The time integration is also divided into discrete steps by using a fix timestep Δt. To improve the numerical efficiently, the prognostic equations use a time splitting technique to separate fast processes (related to acoustic and gravity wave modes) from slower varying modes of motions in the prognostic equations. For this time discretisation, the 3rd order Runge-Kutta time stepping scheme is applied (Wicker and Skamarock, 2002).

Physical parameterisation

Atmospheric processes cover a wide range of spatial and temporal scales, including molecular to planetary horizontal scales and time scales from seconds up to years. The space and time resolutions in the atmospheric model are limited, therefore important parts of the model physics cannot be resolved by the model grid of the basic equations. Parameterisation for molecular processes such as radiation, cloud microphysics and laminar transport in the immediate vicinity of surface boundaries as well as for processes of turbulence and convection must be defined. Parameterisation is based on a simple modelling method that replaces processes on the sub-grid scale or complex processes. An overview of the most important physical parameterisation in COSMO is given below, more details can be found in Doms et al. (2011).

Turbulence parameterisation

The atmospheric *subgrid-scale turbulence parameterisation* consists of the prognostic turbulent kinetic energy (TKE) closure at 2.5-Level (Mellor and Yamada, 1982) which includes the effects from the subgrid-scale condensation and from the thermal circulation. The turbulent fluxes near the surface lead to an exchange of processes of momentum, heat and humidity between the atmosphere and soil. A *surface layer parameterisation* uses a surface layer scheme for the TKE where the lowest model layer is divided into a laminar-turbulent layer, a roughness layer and the Prandtl layer (Heise, 2002).

Parameterisation of radiative transfer

The radiation scheme according to Ritter and Geleyn (1992) solves the δ two-stream version of the radiative transfer equation. The scheme describes the radiative effects of scattering, absorption and emission by cloud droplet, aerosol and gases in each part of the spectrum. Three shortwave and five longwave spectral intervals are considered (Schaettler et al., 2014).

Cloud and precipitation parameterisation

The basic parameterisation scheme for the formation of grid-scale clouds and precipitation employs the Kessler-type bulk formulation which categorises various cloud and precipitation particles into broad groups of water substance. The precipitation formation includes the determination of water vapour, cloud water, cloud ice, rain and snow and its three-dimensional transport in different precipitation phases is considered in the microphysic parameterisation. The subgrid-scale clouds are determined by an empirical function which depends on relative humidity and height (Schaettler et al., 2014).

Moist convection parameterisation

A great variety of convective clouds exists in the atmosphere. Convection is a sub-grid scale phenomenon which cannot be calculated explicitly and therefore has to be parameterised. The cumulus convection has a large impact on the vertical structure of temperature and moisture fields in the atmosphere. This kind of convection acts on horizontal scales smaller than 3 km and must be parameterised in large-scale or

mesoscale models due to its significantly coarser spatial resolutions. In convection-permitting simulations on scales of $\leq$3 km the cumulus or deep convection parameterisation is turned off and only shallow convection parameterisation is required. In this thesis, the standard cumulus convection parameterisation scheme of Tiedtke (1989) is used for the simulations in (deep) convection-parameterised scales. In the mass flux scheme of Tiedtke (1989) some basic effects of moist convection are parameterised such as the diabatic heating due to the release of latent heat which results from cloud condensation and from the formation and evaporation of precipitation. Furthermore, the convection parameterisation represents the vertical transport of heat, moisture and momentum in cumulus via updrafts and downdrafts. Disadvantages of the deep convection parameterisation are the fact that these parameterised processes lead to a stabilisation and thus distort the original thermally unstable stratification. Moreover, influence to mesoscale circulations is neglected in the parameterisation and processes due to organised convection are not represented in the moisture budget of the parameterisation (Doms et al., 2011).

3.1.2. Initial and Boundary Data

A limited-area model (like COSMO) requires initial and boundary data from a coarse-grid driving model. The forcing data is interpolated in a preprocessing step with an interpolation program called "int2lm". To solve the prognostic differential equations the following interpolated initial and boundary data are necessary:

1. The atmosphere state is represented by the *atmospheric variables*: the wind field $\vec{v}$, the temperature T, the surface pressure field and the different terms of q^x.

2. *External surface parameters* provide information about the lower boundary of the domain. The variables are the height of surface topography, the geopotential of surface, the fraction of land in each grid cell, the land soil type and the roughness length z_0. In this thesis the external data sets are chosen from the Global Land One-km Base Elevation (GLOBE) for orography, the Global Land Cover 2000 (GLC2000) for land use and the Harmonised World Soil Database (HWSD) for the soil types. The climate mode simulations demand additional information about the plant cover, the leaf area index, root depth and the ozone contents.

3. The *surface variables* at the lower boundary are the temperature and water content of snow surface, the water content of interception water and the temperature and the specific water vapour content at the surface. For the climate mode, the surface temperature of water is also required.

4. The *soil variables* for the multi-layer soil model are temperature and water content in different soil layers and the density and the freshness of snow.

Nesting strategy

In this study two nesting steps are performed. The analysis data of the operational atmospheric Integrated Forecasting System (IFS) model is used (Owens and Hewson, 2018). This analysis product provides the best gridded estimate of the state of the atmosphere (best fit to observations). The spatial resolution is 0.25°(∼30 km) and boundary conditions are updated every 6 hours at the four main synoptic hours 00, 06, 12 and 18 UTC. The initial and boundary data from IFS data are interpolated to the first nest of 0.0625°(∼7 km), abbreviated as COSMO-7km. The second nest is chosen so that deep convection is calculated explicitly with a horizontal grid resolution of 0.025° (∼2.8 km), abbreviated as COSMO-2.8 km. The initial and boundary data originate from COSMO-7km. The nesting of a high-resolution limited area model in a low-resolution driving model causes numerical problems at lateral boundary conditions. These problems are related to a non-unique information transfer between the models at the boundaries, due to differences in the spatial resolution and the use of different sets of model equations (Doms and Baldauf, 2018). In order to minimise possible perturbations, the relaxation boundary condition of Davies (1976) is used for the one-way nesting. A relaxation zone is considered in which the variables of the high-resolution model are gradually modified to merge them with the driving model variables (Doms and Baldauf, 2018). In this investigation the domains are chosen so that there is enough relaxation between the coarser domain and finer domain (at least 8 grid points).

This dynamical downscaling approach for the Western Mediterranean (WMed) is illustrated in Fig. 3.2. The simulation domain of the COSMO-7km (magenta colour) is larger for the WMed to avoid the described numerical problems related to lateral boundary conditions. The green box indicates the domain of the nested COSMO-2.8km simulation. The latter domain is simultaneous with the investigation domain of the WMed in which SM-atmosphere interactions and feedbacks are considered.

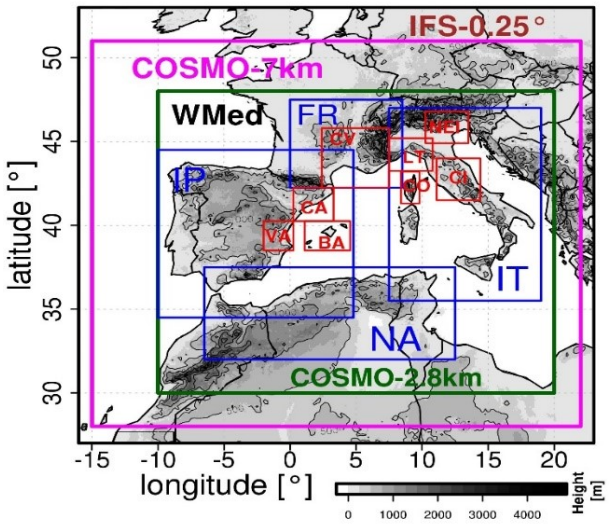

Figure 3.2.: Investigation and simulation domains in WMed. The magenta box shows the WMed simulation domain of the COSMO-7km and the green box of the COSMO-2.8km. The blue boxes are in this thesis regionally defined subdomains and the red boxes are the target areas of HyMeX. The grey scale indicates the orography.

The main difference in the model setup of COSMO-7km and COSMO-2.8km is summarised in Tab. 3.1. Both model resolutions have the same time integration, turbulence and radiation scheme. Differences can be seen in COSMO-2.8km simulation with a higher number of vertical levels and the smaller time steps to ensure stability criteria of horizontal and vertical advection. The main difference between both resolutions is that in the convection parameterisation in the COSMO-2.8km deep convection is explicitly calculated and only shallow convection is parameterised (convection-permitting) instead of the parameterisation of shallow and deep convection in the COSMO-7km (convection-parameterised).

Table 3.1.: Characteristics of different model resolution settings of COSMO-7km and COSMO-2.8km.

	COSMO-7km	COSMO-2.8km
Horizontal resolution	0.0625°	0.025°
Driving data	IFS	COSMO-7km
Number of vertical levels	40	50
Time steps	60s	20s
Time integration scheme	3rd Runge-Kutta time stepping	3rd Runge-Kutta time stepping
Turbulence scheme	1D TKE closure	1D TKE closure
Convection parameterisation	Tiedtke deep and shallow convection	Tiedtke shallow convection and explicit calculation of deep convection
Cloud physics parameterisation	Basic bulk microphysics for precipitation formation	Basic bulk microphysics for precipitation formation
Radiation	δ two-stream radiation scheme	δ two-stream radiation scheme

3.1.3. The Multi-Layer Soil and Vegetation Model TERRA-ML

The Soil Vegetation Atmosphere Transfer (SVAT) multi-layer model TERRA-ML (Grasselt et al., 2008) calculates the soil moisture and temperature in different soil layers. The uppermost soil layer provides the temperature and specific humidity conditions at the ground for the calculation of the surface flux formulation in the atmospheric part of the COSMO model. For these quantities TERRA-ML solves simultaneously the equations of the thermal and hydrological processes in the soil. Parameters such as the heat and water storage capacity depend strongly on the soil type, therefore the soil model distinguishes between five soil types and three special soil types namely ice, rock and peat. The spatial distribution of soil types is given by the HWSD dataset and a soil type within a grid point is represented for the whole soil column depth. For this work the standard 8-layer structure with the half-level layer depths of 0.005, 0.02, 0.06, 0.18, 0.54, 1.62, 4.86, 14.58 m is selected. Fig. 3.3 shows this layer structure in which the depths of main levels (layer centers) are given by $z_{m,k} = 0.5 \cdot (z_{h,k} + z_{h,k-1})$ with $k = 1, 2 \ldots ke_{soil,th} + 1$, where $z_{h,0} = 0$. The vertical water transport is determined by the water budget in each layer which depends on the boundary values at the upper and lower boundary of the soil layer, the water extraction by evapotranspiration, gravitational and capillary transport and the runoff formation. In TERRA-ML no lateral transport is considered and the vertical transport of water is calculated for all soil types except of ice and rock.

The soil model has precipitation as an input variable which is first accumulated in the interception store. If the maximum of the interception store capacity is exceeded, the surplus of water can further infiltrate into the soil. Surface runoff is generated if the infiltration rate is lower than the precipitation rate. The maximal infiltration rate depends on the field capacity of the corresponding soil type. Ground runoff is created when the soil water content reaches the field capacity of the corresponding soil type. In the following an overview of the most important thermal and hydrological processes and the coupling between soil and atmosphere is given, further details can be found in Doms et al. (2011).

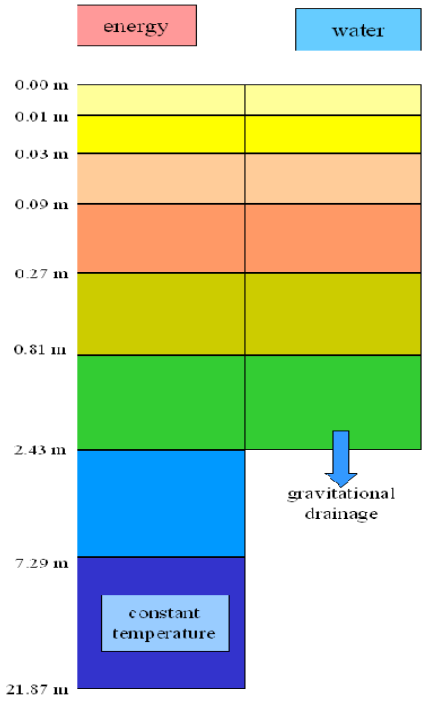

Figure 3.3.: Layer structure of the TERRA-ML model (Doms et al., 2011).

Soil temperature

The soil temperature is predicted with the heat conduction equation for all active soil layers:

$$\frac{\partial T_{SO}}{\partial t} = \frac{1}{\rho c}\frac{\partial}{\partial z}\left(\lambda \frac{\partial T_{SO}}{\partial z}\right) \tag{3.6}$$

where T_{SO} is the soil temperature, ρc represents the volumetric heat capacity and λ the heat conductivity. The volumetric heat capacity takes the heat capacity of dry soil, of water and of ice into account whereas an average soil water content is assumed for heat conductivity. The lowest soil layer (>7 m) is prescribed with a climatology temperature that is given by a boundary value. In the upper boundary the soil temperature interacts with the radiation and the sensible and latent heat fluxes, as shown in Fig. 3.4b.

Hydrological processes

The hydrology part of the soil model determines the liquid water content in different water reservoirs and in the soil. To calculate the *vertical soil water transport* the equation of liquid water budget is solved (Fig. 3.4a):

$$\frac{\partial w_l}{\partial t} = \frac{1}{\rho_w}\frac{\partial F}{\partial z} \tag{3.7}$$

where ρ_w is the density of water and w_l is the fractional water content $w_l = \frac{W_l}{\Delta z}$. The vertical water transport due to gravity and capillary forces is described by the general Richard equation (Hillel, 1980) for soil water flux F:

$$F = -\rho_w \Big[-D_w(w_l)\frac{\partial w_l}{\partial z} + K_w(w_l) \Big] \tag{3.8}$$

The parameterisation of hydraulic diffusivity $D_w(w_l)$ and hydraulic conductivity $K_W(w_l)$ after Rijtema (1969) depends on the water content and the soil type. The solution of the Richards equation is conducted for the active layers up to a depth of 4 m. In the lowest two layers only downward, gravitational transport is considered.

The *runoff* from soil layer k is built if the total water content w_k of a layer exceeds the field capacity w_{FC} and the divergence of the fluxes F is negative:

$$R_k = \frac{w_k - w_{FC}}{w_{PV} - w_{FC}} \Big(\frac{\partial F}{\partial z}\Big)_k \Delta z_k \tag{3.9}$$

The soil type depends on the volume of voids w_{PV} and the field capacity w_{FC} which are shown in Tab. 3.2.

Table 3.2.: Soil type dependent values of the volume of voids w_{PV}, the field capacity w_{FC} and the permanent wilting point w_{PWP} are used in the TERRA-ML model (extracted from Doms et al. (2011)).

soil type	ice	rock	sand	sandy loam	loam	loamy clay	clay	peat
volume of voids w_{PV}	-	-	0.364	0.445	0.445	0.475	0.507	0.863
field capacity w_{FC}	-	-	0.196	0.260	0.340	0.370	0.463	0.763
permanent wilting point w_{PWP}	-	-	0.042	0.100	0.110	0.185	0.257	0.265

TERRA-ML has no explicit vegetation layer but *evapotranspiration* processes are calculated by parameterisation of evaporation from the interception reservoir, from the snow reservoir, from the bare soil of the uppermost soil layer as well as from the plant transpiration. For all components of the total evapotranspiration the potential evaporation E_{pot} is included:

$$E_{pot}(T_{sfc}) = \rho C_q^d |v_h| (q^v - Q^v(T_{sfc})) \tag{3.10}$$

where T_{sfc} is the temperature of the respective surface, q^v the specific humidity, C_q^d the bulk-aerodynamical coefficient for turbulent moisture transfers at the surface and Q^v is the saturation of specific humidity.

The *evaporation rate of bare soil* is defined by the minimum potential evaporation at surface temperature and the maximum moisture flux through the surface that the soil can sustain (Dickinson, 1984). The

evaporation rate of the interception storage follows the same principle.

For the *plant transpiration parameterisation* it is assumed that the moisture flux between the plant foliage and the air inside of the canopy is equal to the flux between the air inside and the air above the canopy. Moreover, the foliage temperature has the same temperature as the surface. With these simplifications the plant transpiration (Dickinson, 1984) is given by:

$$T_r = \sigma_f \cdot E_{pot}(T_{sfc}) r_a (r_a + r_f)^{-1} \tag{3.11}$$

with the resistances of atmosphere r_a and foliage r_f. σ_f describes the fraction area covered by plants in relation to interception and snow fraction. Further derivation can be found in Doms et al. (2011).

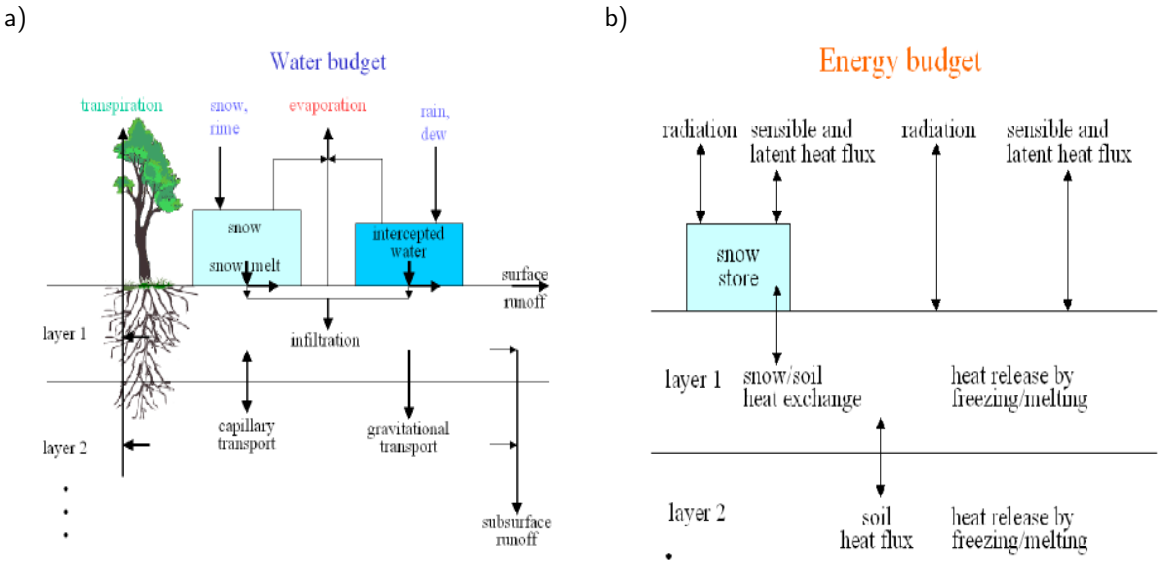

Figure 3.4.: a) Hydrologic and b) energetic processes which are considered in the soil model TERRA-ML (Doms et al., 2011).

Coupling between soil and atmosphere

The equations 3.6-3.11 determine the soil temperature and soil moisture in all soil layers. Thereby the uppermost soil layer is coupled with the atmosphere. The soil temperature interacts with the atmosphere via the sensible heat flux:

$$H_0 = -\rho c_h^d |v_h| (\theta \pi_{sfc} - T_{sfc}) \tag{3.12}$$

where $|v_h|$ is the absolute wind speed in the lowest atmospheric grid level above the surface, T_{sfc} is the ground temperature and c_h^d is the bulk-aerodynamical transfer coefficient for turbulent heat exchange. θ and π_{sfc} are the potential temperature at the lowest grid level above the earth surface and the scaled pressure at the ground.

The latent heat flux is influenced by the total evapotranspiration:

$$L_0 = -\rho c_q^d |v_h| (q_v - q_{sfc}) \tag{3.13}$$

with q_v as the specific humidity of the lowest grid level above ground and q_{sfc} is the sum of evaporation of bare soil, the interception store and the transpiration.

3.2. Satellite-Derived SMOS 1 km Disaggregated SSM

Soil moisture is recognised by the World Meteorological Organisation (WMO) as an essential climate variable (ECV) because of its significant impacts on global water, energy and biogeochemical cycle (Srivastava et al., 2016). The observation of soil moisture is a challenge due to its high variability in space and time. In-situ observations give an accurate measurement of near-surface and root-zone soil moisture, but are limited to specific locations and are unable to represent SM on a large-scale. For this reason, satellite-based observation is the only possibility for an adequate temporal and spatial measurement of global surface soil moisture. In the last decades remote sensing of microwave detection has been successfully proven to be an adequate method to estimate soil moisture from dielectric properties of soil which is based on land surface emissivity (Mohanty et al., 2017). Various low frequencies in the X-, C- and L-band have been used to detect bare or vegetated surface soil moisture (SSM). The most promising soil moisture retrieval in the X- and C-band are derived from the Advanced Microwave Scanning Radiometer - Earth Observing System (AMSR-E) on-board of the Aqua satellite (Owe et al., 2008) and the Advanced SCATterometer (ASCAT) on-board of the Metop satellite (Naeimi et al., 2009). However, these wavelengths are not optimal to measure soil moisture remotely as their retrievals are only sensitive to a shallow soil layer and are significantly influenced by vegetation cover (Panciera et al., 2014). For this reason, two new missions in the most promising L-band microwave length have been launched in recent years to enhance the global monitoring of SSM (Kerr et al., 2012). The first mission that measures soil moisture with the L-band microwave radiometry is the European Space Agency's (ESA) Soil Moisture and Ocean Salinity (SMOS) mission. This mission was launched in November 2009 followed by the second Soil Moisture Active Passive mission (SMAP) which was launched in January 2015 (Entekhabi et al., 2014). Besides these single-sensor products the ESA Climate Change Initiative (CCI) generates a multi-decadal, global satellite-observed SSM data set in a spatial resolution of 0.25°, based on the combination of existing active and passive microwave sensors (Dorigo et al., 2017).
The data of the SMOS mission is chosen in this thesis because in the last years great efforts have been made in the development of the SMOS algorithms and related products (González-Zamora et al., 2015; Khodayar et al., 2019). In this regard, several validation studies (Sanchez et al., 2012; González-Zamora et al., 2015; Piles et al., 2014; Khodayar et al., 2019) showed good agreement of satellite-derived SSM SMOS products in the area of interest over the Iberian Peninsula and the period of interest in 2012 including the HyMeX SOP1 period. The advantages of SMOS are presented in the next subsection. In addition, the new 1 km downscaled SMOS-L4 3.0 is presented in the following, which is used for the realistic SM initialisation of COSMO.

3.2.1. SMOS Satellite Mission

The scientific aim of the SMOS mission is to achieve a direct and robust quantity to estimate SSM over the land surface with a desired accuracy of 0.04 m^3/m^3. SMOS provides a multi-angular dual polarised brightness temperature T_B over the globe in a horizontal resolution of about 40 km. SSM is measured in a sun synchronous orbit twice per day, one in the ascending pass (6 am) and one in the descending pass (6 pm), for both passes with a revisit time of 3 days at the equator. The SMOS satellite carries a single payload: the Microwave Imaging Radiometer using an Aperture Synthesis (MIARS) instrument. MIARS is a 2-D interferometric radiometer which measures the emitted radiation of the earth's surface in the microwave L-Band (1.4 GHz, 21 cm) to retrieve the moisture content from the dielectric constant in the first few centimetres of soil (Kerr et al., 2010).

The measured passive microwave L-band signal is mainly a function of SSM, vegetation opacity and effective surface temperature. This wavelength penetrates well through the atmosphere and vegetation up to a biomass of 5 kg/m. Previous satellite-derived SSM instruments in higher microwave frequencies ∼6-7 GHz (AMSR-E) (Brocca et al., 2011) or active instruments like ASCAT (Naeimi et al., 2009) have the disadvantage that the frequency of these instruments are stronger influenced by vegetation and surface roughness than SMOS. Another advantage of SMOS is the capability of multi angular measurements. Classical conical scan radiometers such as the AMSR-E and SMAP have the best fully polarised measurements for a given point but simultaneous retrievals of several surface variables are not possible (Kerr et al., 2012). Further data sources are necessary to obtain information of such variables as the surface temperature or the vegetation opacity. Since SMOS has fully polarised measurements of 160 angular surface soil moisture and the vegetation opacity are derived directly. A challenge in the microwave L-band is the effect of unwanted man-made radio frequency interferences (RFI). Furthermore, the spatial resolution is limited because it is proportional to the antenna diameter and inversely proportional to the wavelength. For this reason, MIARS requires an antenna diameter of 8 m at a wavelength of 21 cm and a polar orbiting height of 750 km which was a technical challenge until the last decade (Kerr et al., 2010).

A soil moisture retrieval algorithm determines swath-based soil moisture and other geophysical products from the multi-angular brightness temperatures T_B of the Level 1 product. This algorithm is based on an iterative approach which aims to minimising the cost function. The main component of this cost function is the sum of the squared weighted difference between measured and modelled T_B data for a variety of different incidence angles (Kerr et al., 2012). The Level 2 algorithm finds the best set of parameters which drive directly the T_B model and thus minimises the cost function. In addition, auxiliary data are required for the derivation of SSM such as the static data of non or slowly time varying quantities like soil texture, land use and topographical index. Further types are dynamic time dependent auxiliary data like snow, frozen rain, liquid rain and temperature which are obtained by forecasts. SSM is retrieved over relatively large and inhomogeneous areas with a large variety of surface types, whereby SSM is only meaningful for certain surface types. To facilitate the retrieval process, only the dominant part within

a pixel is retrieved and the other contributors are described by predetermined reference values (Kerr et al., 2012). The target area is decomposed in 4 km cells which is the resolution of the land use data. The fractions of the main surface categories are distinguished according to low vegetation, forest areas, barren soils, water bodies, urban areas and permanent ice and snow. A decision tree is used to select the dominant fraction for the retrieval algorithm. The output Level 2 product contains SSM, vegetation opacity, estimated dielectric constants of any surface, T_B computed at 42.5° and quality indices.

3.2.2. High-Resolution Downscaled L4-Product

Despite the enhancement of SMOS algorithm and its products the spatial resolution of SMOS-L2 ($\sim$15 km) and SMOS-L3 ($\sim$25 km) is insufficient for regional and local studies requiring horizontal scales of 1-10 km (Piles et al., 2016). For this purpose, Piles et al. (2011, 2014) presented a new downscaling approach to estimate multi-resolution SSM from the combination of SMOS-L2 data and visible-to-infrared observations from Moderate Resolution Imaging Spectroradiometer (MODIS) onboard of the Terra/Aqua satellites. This downscaling approach merges high-sensitive but low-resolution SMOS polarimetric observations with fine-scale but low-sensitive MODIS data. The low orbiting satellites SMOS, Terra and Aqua have different local equatorial crossing times but they can be combined with the assumption that soil moisture patterns are spatially persistent for a few hours before and after SMOS-L2 overpass (Piles et al., 2014). For the morning pass, the SMOS-L2 ascending (6 am) pass is combined with Terra/Aqua descending passes at 1:30 pm/1:30 am. In the afternoon pass the SMOS-L2 descending pass (6 pm) is merged with the Terra/Aqua ascending passes at 10:30 am/10:30 pm.

The downscaling algorithm is based on a linear linking model that combines SMOS-L2 T_B and MODIS NDVI and MODIS LST to derive fine-scale soil moisture. Theoretical and experimental studies have demonstrated that there can be a unique relationship between SSM, NDVI and LST for a given region under specific climatic conditions and land surface types (Piles et al., 2011). Piles et al. (2014) showed an improvement in fine-scale SSM estimates, including polarimetric and multi-angular information. The resulting linking formula is applied for two scales represented: the scale of SMOS (40 km) and of MODIS (1 km).

$$s_m = a_0 + a_1 \cdot T_n + a_2 \cdot F_N + \sum_{i=1}^{3} a_{3i} \cdot T_{BH\theta_i N} + \sum_{i=1}^{3} a_{4i} \cdot T_{BV\theta_i N} \tag{3.14}$$

where s_m stands for soil moisture, T_N and F_N are normalised LST and NDVI, $T_{BH\theta_i N}$ and $T_{BV\theta_i N}$ are the normalised horizontally and vertically polarised T_B at different incidence angles. T_N and F_N are linearly aggregated to the low-spatial resolution of 40 km and $T_{BH\theta_i N}$ and $T_{BV\theta_i N}$ are resampled to the high-spatial resolution of 1 km. The model is first applied to the low-resolution to estimate the model fitting coefficients a_k and then these coefficients are used to obtain the disaggregated soil moisture at high-resolution. Validation with ground-based observation in Piles et al. (2014) revealed that the downscaling method improves the spatial representation of SMOS-L2 SSM estimates while maintaining temporal correlation and root mean squared differences in comparison to in-situ observations. Furthermore, the

downscaled maps capture the soil moisture dynamics of land uses except for irrigate crops.
The created downscaled 1 km SMOS-L4 2.0 product is made available by the Barcelona Expert Center (BEC) in two products per day in an ascending and a descending orbit for the years 2010 to 2018. A limitation of the SMOS-L4 2.0 product is the lack of information on cloudy days which reduces the data availability of this product significantly. To overcome the limitation, a new version of the SMOS-L4 product has been developed that implements ERA-Interim LST data into the MODIS LST/NDVI space. This so-called "all weather" version (hereafter SMOS-L4 3.0) has the advantage that it does not depend on cloud coverage anymore. Therefore, validation with in-situ observations shows an improvement in SMOS-L4 3.0 SSM representation in frequency and the accuracy of SSM measurement compared to the previous SMOS-L4 2.0 product (Piles et al., 2015). The novel 1 km disaggregated SMOS-L4 3.0 SSM product is developed and recently released by the SMOS-BEC. This product is exclusively available for the Iberian Peninsula, South France and North Morocco (34N-45N, 10W-5E). With the fine resolution of the SMOS-L4 3.0 SSM product it is possible to adequately characterise SM spatio-temporal variability (Khodayar et al., 2019) which is necessary to analyse SM-related fine-scale processes at the surface and their interactions with the atmosphere.

3.3. Observational Data

This section describes the observational data sets used for comparison with model simulation results and remote sensing data to verify their accuracy. Some of these observations are taken from the HyMeX database for the analysis of the SOP1 period in autumn 2012. In addition, three available ground-based SM networks in the study area are presented for the validation of the results of 1 km SMOS-L4 3.0 SSM data. Finally, satellite data from CMORPH and ground-based gridded E-OBS data are used to examine the results of simulated precipitation and temperatures in WMed and Europe.

3.3.1. HyMeX Data Base

The HYdrological cycle in the Mediterranean EXperiment (HyMeX) program is a jointed international collaboration to advance the knowledge about the Mediterranean water cycle and thus to improve the processed-based and regional climate modelling (Drobinski et al., 2014). HyMeX offers a unique opportunity to enhance the capabilities to predict high impact weather such as heavy precipitation events (HPEs) or flash floods. A multiscale data modelling approach is pursued with large field experiments for process and predictability studies about specific areas embedded in a 10-year period of data collection over the Mediterranean basin. The experiment is divided in a long-term observation period, two enhanced observation periods and two special observations periods (SOPs). The first field experiment took place in the SOP1 period in the northwestern Mediterranean from September 5 to November 6, 2012. During this period about 20 intense weather events were identified by more than 200 research instruments in intense observation periods (IOPs) (Ducrocq et al., 2014).

The collected unprecedented data set for this region is available in the HyMeX data base (`http://mistrals.sedoo.fr/HyMeX/`) and can be used to investigate the interactions and feedbacks between different components of the hydrological cycle during heavy precipitation and flash floods. Within the data base a high-density and quality-check rain gauge network is provided over France, Italy, Spain and further WMed countries. In this thesis hourly and daily rainfall accumulations of rain gauges are used to analyse precipitation in the HyMeX domain for the considered periods of the September 1, 2012 until November 31, 2012 (SON).

3.3.2. Ground-Based SM Networks

In the investigation domain of the downscaled SMOS-L4 SSM product (Fig. 3.5) three in-situ soil moisture networks exist, namely REMEDHUS (Martínez-Fernández and Ceballos, 2005), SMOSMANIA (Albergel et al., 2008) and the Valencia Anchor Station (VAS) (López-Baeza et al., 2003). These SM ground-based networks are used for validation of the SMOS-L4 3.0 SSM product. The main characteristics of these ground-based networks are described below.

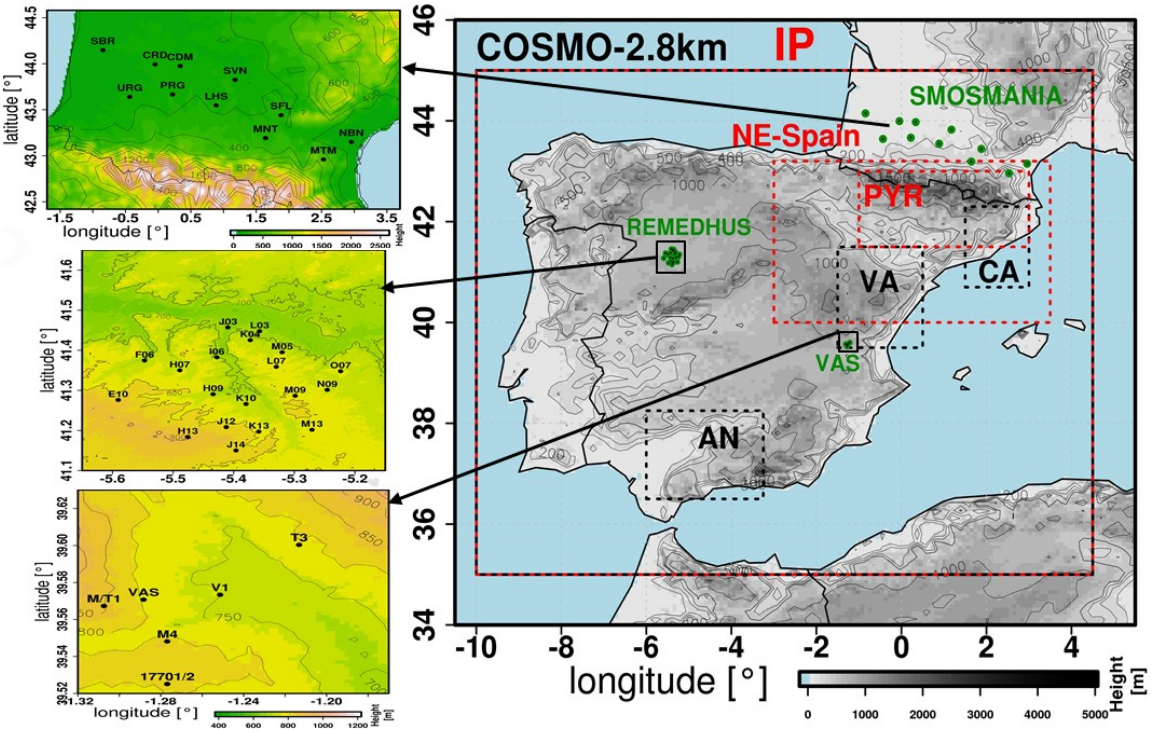

Figure 3.5.: Investigation and simulation domains for the SMOS initialisation with in-situ observations networks. Target areas of different heavy precipitation events (HPEs) are indicated in dotted boxes. The underlying orography is shown in grey colours and contour lines (right panel). The three in-situ networks SMOSMANIA, REMEDHUS and VAS are presented on the left side (underlying orography in coloured contour). The red dotted boxes show the IP, the Northeast (NE)-Spain and the Pyrenees (PYR) investigation domains of the HPE on the Sept 9, 2012.

REMEDHUS

The REMEDHUS network consists of 23 automatic soil moisture monitoring stations with hydro probes which measure hourly the near-surface SM at a soil depth of 5 cm. The main land use is agricultural with rainfed cereals (78 %), irrigated crops (5%), perennial vineyards (3 %) and forest-pasture areas (13 %) (Sanchez et al., 2012). The stations are located in the central Duero basin in Spain on an area of 1300 km^2 (41.1° to 41.5°N and 5,1° to 5.7°W) in relatively flat terrain (700-900 m above sea level). The area has a continental semi-arid Mediterranean climate with an average annual precipitation of 385 mm and a mean temperature of 12 °C (Sanchez et al., 2012; González-Zamora et al., 2015). The network has been used for many validation exercises of SMOS products (Sanchez et al., 2012; Petropoulos et al., 2014; Piles et al., 2014; González-Zamora et al., 2015; Piles et al., 2016). In this thesis, 19 of 23 stations are selected for the year 2012 after a quality check of the data availability.

SMOSMANIA

SMOSMANIA is a long-term data acquisition network to observe soil moisture in the southwestern France (Calvet et al., 2007; Albergel et al., 2008). Twenty-one stations of the existing RADOME (Réseau d'Acquisition de Données d'Observations Météorologique), the automatic weather station network of Météo-France were chosen for the SMOSMANIA project. Since January 2007 SM has been measured by ThetaProbe ML2x of Delta-T Devices at four soil depths of 5, 10, 20, 30 cm with a time step of 12 min. Soil characteristics for 12 investigated stations distinguish between clay and sand fraction, organic matter and bulk density which are listed in Albergel et al. (2008). On the basis of a quality check of data availability of the stations and the size of SMOS-L4 3.0 SSM domain, 11 stations are selected in this investigation. The stations follow a Mediterranean-Atlantic transect and are located in flat areas with the highest station at 538 m.

VAS

The Valencia Anchor Station (VAS) site was established in December 2001 as a Calibration/Validation (CAL/SLA) site for different low-resolution Earth Observation data products (López-Baeza et al., 2003). The VAS site covers a 50x50 km^2 domain in eastern Spain with reasonably homogeneous and mostly flat conditions (750-900 m). The main land cover type is vineyard (56 %), followed by trees, shrubs, forests, industrial and urban cover types (Juglea et al., 2010). The climate in this area varies between semi-arid to dry-sub-humid with a mean temperature between 12 °C-14 °C and annual mean precipitation of about 450 mm. A soil moisture network of eight ThetaProbe ML2x soil moisture stations has been installed in a 10x10 km^2 domain (39.52°-39.62°N, 1.2°-1.32°W) about 80 km from the city of Valencia. SM is measured in the first 5 cm of soil in a time step of 10 min.

3.3.3. CMORPH Satellite Data

The Climate prediction center MORPHing technique (CMORPH) data product is a half-hourly global precipitation (60°N-60°S) derived exclusively from passive microwave satellite estimates the features of which are propagated by motion vectors derived from geostationary satellite infrared data (Joyce et al., 2004). The passive microwave rainfall is derived from the low-orbits instruments: Special Sensor Microwave Imager (SSM/I), the Tropical Rainfall Measuring Mission (TRMM), the Advanced Microwave Sounding Unit (AMSU) and AMSR-E. The shape and intensity of the precipitation features are modified during the time between two microwave sensor scans by performing a time-weighted linear interpolation. The result is a spatial and temporal complete microwave-derived precipitation analysis independent from the infrared temperature field. The original product has a spatial resolution of 0.07°($\sim$8 km) and is available for the years 1998 until present. Validation with rain gauge observation and different satellite products show good performance of the high-resolution CMORPH product (Habib et al., 2012; Stampoulis et al., 2013; Furl et al., 2018). Stampoulis et al. (2013) concluded in their investigation of HPEs in the Mediterranean that CMOPRH-8km has a better error statistic than other satellite-based precipitation products, although the high-precipitation rates are underestimated, especially in convective storms.

3.3.4. E-OBS Gridded Data Set

The E-OBS data set (Haylock et al., 2008) provides daily gridded precipitation and temperature data for the European land grid points (25°N-75°N, 40W-75°E). In this work the daily maximum and mean temperature are taken from version 17.0 (`https://www.ecad.eu`) which covers in a regular grid of 0.25 °($\sim$25 km) the time period from 1950 until 2017. Depending on the time period more than 2000 stations are used to generate this gridded data set. The interpolation process is divided into three steps. In a first step, the monthly precipitation sums and the monthly mean temperature are interpolated using three-dimensional thin-plate splines. The daily anomalies are interpolated applying the universal Kriging method for precipitation and the Kriging with an external drift for temperature. Finally, both monthly and daily estimates are combined. The daily uncertainty strongly depends on the season and the number of contributing observations. In addition, the spatial interpolation has a large impact on the magnitude of extremes, especially for smoothing of extremes in the interpolation of daily anomalies.

4. Methodology

This chapter presents the methodology that is applied to study the role of soil moisture-atmosphere interactions on the development of extremes in the WMed. Given that the involved processes act on different temporal and spatial scales, the focus of this thesis is on the analysis of different timescales from hourly up to several months and different spatial scales from 2 km up to about 2000 km. In Sec. 4.1 a multiscale modelling strategy with the COSMO model is developed to capture atmospheric processes on these different scales. Sec. 4.2 introduces the concept of artificial and realistic SM initialisation experiments. Based on these different initial SM experiments, knowledge should be gained about the sensitivity of convective processes to initial SM in the WMed. In Sec. 4.3 relevant indices are described to select favourable time periods for the application of the SM initial experiments. Finally, the main statistical tools for the analysis of this work are presented.

4.1. Multi-Scale Modelling Approach

The recent study of Sillmann et al. (2017) highlighted that the development of extreme events depends on the initial state, large-scale processes and local-to-regional feedbacks. The relative importance of these factors for short- and long-duration extreme events is shown in Fig. 4.1. Sillmann et al. (2017) concluded that one of the essential contributors to understand the evolution of extreme events is the initial soil moisture state and its local-to-regional feedback processes on drought events. In addition, they emphasised the urgent need of better observations and higher model resolutions for an enhanced understanding and prediction of short- and long-duration extreme events.

For this purpose, a multiscale modelling approach is applied to understand the role of SM variability and its coupling to the atmosphere leading to the development of extremes across temporal and spatial scales. On the temporal scale, seasonal simulations are considered to examine the impact of long-term memory of SM perturbation on the evolution of heavy precipitation (HP) and heat waves. On the event scales of about 1-5 days, the influence of SM initialisation with state-of-the-art satellite-derived SM observations (realistic initialisation) on the representation of heavy precipitation events (HPEs) should be assessed. Another novelty feature of the applied approach is the analysis of high-resolution convection-permitting seasonal simulation for a large domain of the WMed (Fig. 3.2) and continental Europe (Fig. 7.2). With these investigation domain sizes including the different types of mesoscale (mesos $\alpha - \gamma$: 2-2000 km) and temporal scales of hours up to several months a variety of important atmospheric phenomena such as convective systems, heat waves and droughts can be studied.

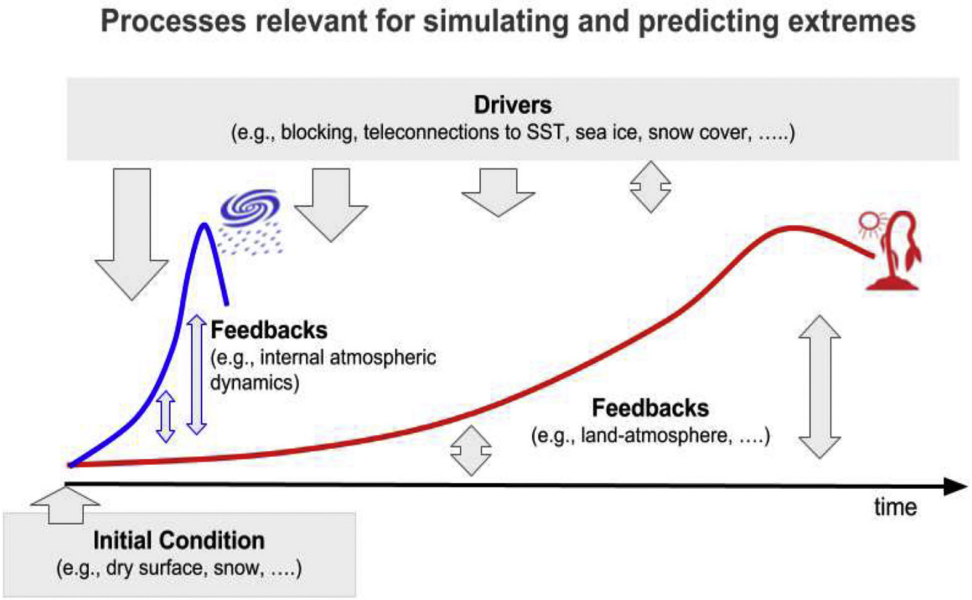

Figure 4.1.: The conceptual scheme of Sillmann et al. (2017) illustrates the relevance factors of the development of extreme events. The blue colour indicates feedbacks for short-duration events such as convective storms and the red colour for long-duration events such as heat waves or droughts.

For the analysis of local and regional processes the WMed is divided in regional subdomains of France (FR), Italy (IT), Iberian Peninsula (IP) and North Africa (NA) (blue boxes in Fig. 3.2). The names do not represent the political borders of the countries. A description of characteristics of the defined regional subdomains is given in Chapter 5.1. Moreover, the HyMeX target areas during SOP1 are considered: Valencia (VA), Catalonia (CA), Baleric Islands (BA), Cévennes-Vivarais (CV), Corsica (CO), Liguria-Tuscany (LT), North-Eastern Italy (NEI) and Central Italy (CI). All these areas have particular geographical, topographical and climatological characteristics. An example of such regional features is the distribution in soil types within the WMed in Fig. 4.2 and Tab. 4.1. Within the WMed the dominant soil type is loam with 61 %, followed by clay loam (13 %) and sand (11 %).

Table 4.1.: Percentage of different COSMO soil types and sea amount in the WMed domain.

Domain	ice	rock	sand	sandy loam	loam	clay loam	clay	peat	sea
WMed [%]	0	0	8	11	61	13	7	0	41
NA [%]	0	0	3	6	55	25	11	0	31
IT [%]	0	0	12	14	59	10	6	0	51
IP [%]	0	0	10	12	59	10	9	0	50
FR [%]	0	0	13	17	47	13	8	0	13

In the regional subdomains, the percentage of soil types can be varied. For example, in the IP and IT domain the percentage of loam is high with about 60 % while the amounts of clay loam is lower with about 10 % and clay with about 6-9 %. The NA subdomain has the highest amount of clay loam with about 25 % and clay with 11 % in all subdomains but lower amounts of loam (55 %) and sand (3 %).

In the FR subdomain the amount of loam is relatively low compared to the other subdomains with 47 % but this FR has a high amount of sand with 13 % and sandy loam with 17 %. The importance of these regional differences between the soil type distribution is highlighted in the next subsection.

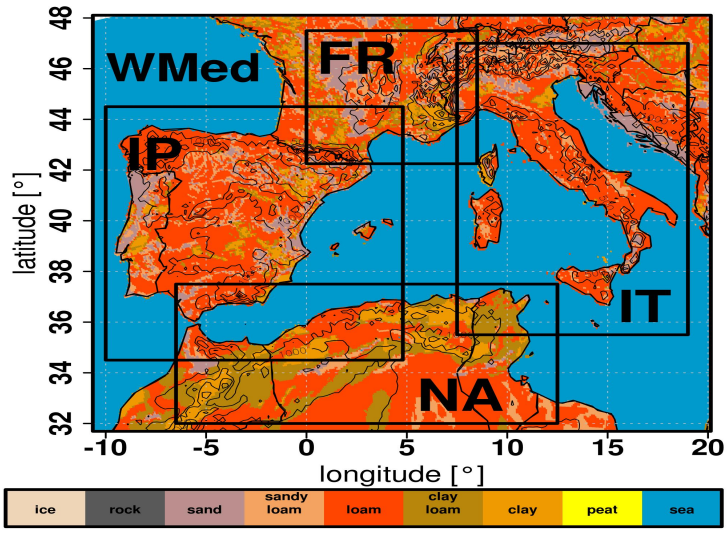

Figure 4.2.: The HWSD soil types considered in the COSMO model in the WMed. The black boxes illustrate the defined subdomains: FR, IT, IP and NA. Eight soil types are distinguished in the COSMO model: Rock, ice, peat, sand, sandy loam, loam clay, loam.

For the WMed region simulations are performed with the COSMO model for two model resolutions: COSMO-7km (convection-parametrised) and COSMO-2.8km (convection-permitting). The characteristics of the two model resolutions (Tab. 3.1) and the downscaling nesting strategy were introduced in the model description in the previous Chapter 3.1.2. In a high-resolution modelling of about 2-3 km deep convection is resolved, whereas in coarser resolutions the convection is parametrised. Studies by Fosser et al. (2015) and Prein et al. (2015) demonstrated an improvement of the representation of convective precipitation on sub-daily scale and over mountain regions as well as of extreme precipitation events. Furthermore, the sign and strength of soil moisture-precipitation feedbacks can depend on simulations with explicit or parametrised convection (Hohenegger et al., 2009). The differences in the representation of SM and atmospheric conditions between COSMO-7km and COSMO-2.8km simulations are considered in Chapter 5. In this comparison of model resolution special attention is paid to the sign and strength of the SM-precipitation feedback. The following Chapters 6-7 focus on the convection-permitting resolution, as some recent studies (e.g. Fosser et al. (2015); Prein et al. (2015); Brisson et al. (2016)) have shown that such high resolution improves the representation of precipitation and the atmospheric fields with respect to convective precipitation formation. An overview about all simulations of the multiscale approach of this thesis with time periods, model resolution and investigation domains is given in Tab. 4.2. The autumn 2012 from the Sep 1, 2012 until Nov 31, 2012 (SON) is chosen to analyse the sensitivity of wet extremes to initial SM conditions because this period includes the HyMeX SOP1 field experiment with its unique observation data set of the WMed. The literature identifies the European summers 2003

and 2015 (Schär et al., 2004; García-Herrera et al., 2010; Ionita et al., 2017) as extreme drought years (see also Chapter 2.4). Therefore, the sensitivity of the representation of heat waves and extreme temperatures to spring soil moisture deficit in the southwestern Mediterranean and continental Europe will be investigated for these years.

Table 4.2.: Overview about the performed simulations of the COSMO multiscale approach.

Performed simulations	Event scale COSMO-NWP	Wet season COSMO-CLM	Dry season COSMO-CLM
Model resolution	2.8 km (CTRL 7 km)	7 km and 2.8 km	2.8 km (CTRL 7 km)
Time period	IOP8, IOP12, IOP15, HPE Sep 9, 2012	SON 2012	JJA 2003 and 2015
Investigation area	Iberian Peninsula (IP)	WMed, FR, IT, IP, NA HyMeX target areas	Continental Europe, IP and ME subdomains
SM sensitivity experiment	Realistic SMO-L4 SM initialisation	Extreme wet and dry SM initialisation	Extreme wet and dry SM initialisation

4.2. Soil Moisture Sensitivity Experiments with the COSMO Model

A fundamental concept of this work is the initialisation of the COSMO model with artificial or realistic initial soil moisture scenarios. The comparison between a reference simulation (CTRL) and the simulations with different initial soil moisture experiments should prove how sensitive the boundary layer conditions and atmospheric processes leading to the development of extreme events react to initial soil moisture conditions.

In the artificial SM sensitivity experiments the model is initialised with extreme wet/dry soil moisture. For an extreme wet soil moisture initial scenario (WET) the initial SM is set to the maximum value of the field capacity and for an extreme dry soil moisture initial scenario (DRY) the initial SM is set to the minimum value of the plant wilting point. These modifications are applied separately for each grid point and model soil level depending on the respective model soil type. The wilting points and field capacities for the different soil types of the soil model TERRA-ML can be found in Tab. 3.2. The SM profile is modified at the model initialisation and these modification evolves freely without any further SM correction or SM assimilation during the simulation.

This kind of physically-based extreme SM initialisation experiment was successfully applied by Kim and Hong (2007) and Jaeger and Seneviratne (2011). These studies evaluated the effects of SM-climate interaction on temperature and precipitation extremes. The approach is extended in this thesis to test the sensitivity of extreme initial SM in convection-resolving modelling on a seasonal scale. This kind of experiment is also sensitive to regional differences of the Mediterranean soil type distribution (Tab. 4.1) due to the strong dependency of wilting points and field capacities to different soil types. The field capacities range from 19.6 % for sand up to 46.3 % for clay and for the wilting points between 4.3 % for sand and 25.7 % for clay. The presented sensitivity scenarios are physically based because wilting point and field capacity are directly connected with plant transpiration and the development of surface and

ground runoff. Therefore, this approach is more realistic to test the impact of extreme SM initialisation than to add or subtract a certain percentage to the reference SM profile (Jaeger and Seneviratne, 2011; Stacke and Hagemann, 2016).

For the initialisation of the model a dry period in the WMed is selected following the result of Khodayar et al. (2015) that SM initialisation during dry periods is more sensitive. In addition, different initialisation strategies are applied taking into account the spin-up time of the seasonal simulations with COSMO-CLM (Chap. 5.2 and Chap. 7.2). The spin-up time is the time period that the model has to reach to achieve an equilibrium state between external forcing and the simulated land surface fluxes (Yang et al., 2011). Khodayar et al. (2015) showed that the spin-up time depends strongly on the initial conditions (dry/wet), the regional characteristic (humid/dry), the soil level depth and the annual period (wet/dry).

Another type of SM sensitivity experiment is the realistic SM initialisation with satellite-derived observations. The benefit to use such SM estimates from remote sensing data for the initialisation and assimilation of the model have been demonstrated in several studies (Bisselink et al., 2011; Brocca et al., 2011; de Lannoy and Reichle, 2016; Blankenship et al., 2016; Kothe et al., 2017). The new aspect of this thesis is to use state-of-the-art 1 km SMOS-L4 3.0 SSM data for the initialisation of convection-permitting modelling of HPEs during the HyMeX SOP1 period. A detail description of the bias correction and processing of SMOS-L4 3.0 SSM data for an SM initialisation in the COSMO model can be found in Chap. 6.1.

4.3. Relevant Indices and Statistical Methods

This section introduces the EDI index to select extreme dry and wet periods and the convective adjustment time-scale τ to distinguish between weak and strong synoptic forcing. On the basis of these indices, the time periods for the SM sensitivity experiments are established which could be favourable for SM-atmosphere interactions. Furthermore, statistical metrics and methods for the evaluation and validation of simulated results or remote sensing observations are presented. The tools are used in the following three analysis Chap. 5-7.

Effective drought index

The effective drought index (EDI) (Byun and Wilhite, 1999) classifies the period of interest in wet and dry periods. This index is used to quantify the drought status of the selected seasons and events (Tab. 4.2) and to prove the representation of major dry and wet periods in the reference simulation and CMORPH observations.

The EDI monitors the duration and severity of droughts. The index is based on the concept of effective

precipitation (EP) that is calculated by a time dependent reduction function on daily precipitation. The following equations describe the derivation of EDI following Byun and Wilhite (1999):

$$EP_i = \sum_{n=1}^{i} [\frac{(\sum_{m=1}^{n} P_m)}{n}] \tag{4.1}$$

EP_i represents the accumulation of precipitation and P_m the precipitation of m days before. The index i indicates the duration of summation. The deviation of EP (DEP) is stated by:

$$DEP = EP - MEP \tag{4.2}$$

where MEP is a mean of EP (total time period). Finally, EDI is calculated as the ratio of DEP and the standard deviation of DEP:

$$EDI = \frac{DEP}{SD(DEP)} \tag{4.3}$$

Several studies (Byun H.R. and Kim D.W., 2010; Jain et al., 2015; Khodayar et al., 2015; Deo et al., 2017) have shown the advantage of EDI in comparison to other drought indices such as the standardised precipitation index (SPI). An advantage to apply EDI is the daily EP concept and the freedom to choose the time step i which represents the days of the weighted precipitation function. Fig. 4.3 illustrates the EDI calculation for the WMed investigation domain for the years 1998-2018. The satellite-derived CMORPH precipitation data are used for the calculation of EDI. CMORPH observations have a spatial resolution of 8 km and are daily accumulated from the originally 1/2 h output. For the time step i 365 days are chosen, so that in the representation of EDI the first year 1998 is missing. Values of EDI between -1 and 1 represent normal conditions for the specific investigated time period and domain. EDI > 1 indicates extreme wet periods and EDI < -1 extreme dry periods.

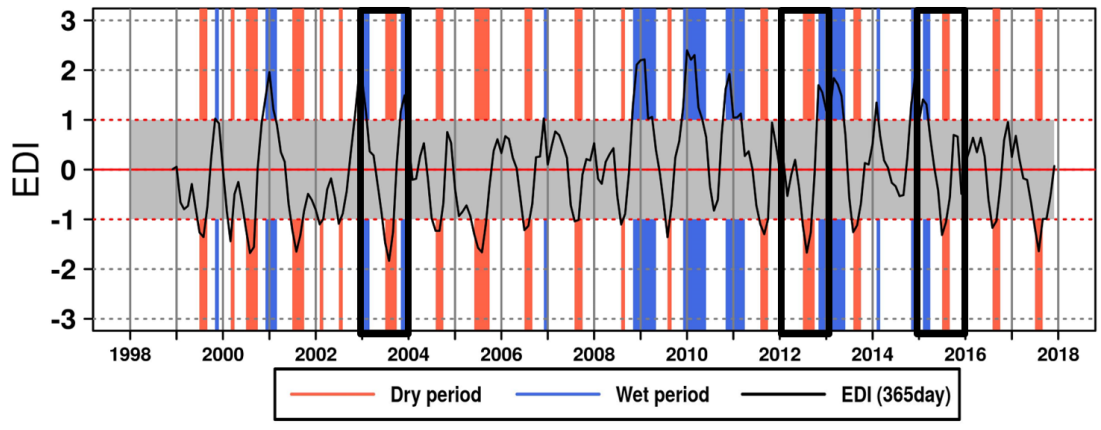

Figure 4.3.: EDI calculation with precipitation from CMORPH (1998-2018) for the WMed domain. Red colours indicate extreme dry periods (EDI< -1) and blue colours show extreme wet periods (EDI > +1). Grey shadow areas present the normal conditions (-1 < EDI <+1). The black boxes illustrate the selected investigation time periods in JJA 2003, SON 2012 and JJA 2015.

The EDI calculation from 20 years of CMORPH data confirms that selected investigation periods in the summer seasons in JJA 2003 and 2015 are extreme dry periods. In particular, summer 2003 is the most extreme dry period in the 20 years of observations in this region corresponding with literature. On the other hand, the autumn period 2012 is identified as a wet extreme period.
Furthermore, the EDI is also calculated from the hourly output of the convection-permitting COSMO simulation on seasonal scale. For this seasonal application the time step i(=15 days) was chosen after testing several possibilities of time duration. With the seasonal EDI calculation the model performance can be proved in the representation of heat waves or wet periods of HPEs in the WMed regional subdomain or the HyMeX target areas.

Convective adjustment time-scale τ

The soil moisture-atmosphere coupling is stronger under weak synoptic conditions where convective precipitation is governed by local-scale flow characteristics and the interaction with the synoptic flow is weak. A physically based quantity to distinguish between strong and weak synoptic-forced precipitation regimes is the convective adjustment time-scale (τ) (Keil et al., 2014). The following equation calculates the convective adjustment time-scale according to Zimmer et al. (2011):

$$\tau = 0.5\left(\frac{\rho_0 c_p T_0}{L_v g}\right)\frac{CAPE}{P} \tag{4.4}$$

where P is the rainfall intensity (mmh^{-1}) and CAPE is the convective available potential energy. c_p is the specific heat of air at constant pressure and T_0 and ρ_0 are reference values of temperature and density respectively. L_v is the latent heat of vaporisation and g the acceleration due to gravity.
In the presence of strong synoptic forcing the amount of convection is determined by the rate at which CAPE is produced by large-scale processes cooling the troposphere. In this case, the convection removes CAPE as fast as it is created and τ values have a time scale of a few hours. Under weak synoptic conditions τ values have a time length of at least 12 h. In this case, convection acts too slowly to remove the CAPE and there must be local factors controlling the rate of creation of CAPE (Keil et al., 2014). The threshold to distinguish between both prevailing regimes is between 3 h and 12 h. In order to ensure a clear separation between both regimes in this study a threshold for τ of 12 h is chosen. The hourly precipitation and CAPE are derived by the COSMO-2.8km simulations. According to Keil et al. (2014) only COSMO grid points with a precipitation rate higher than 1 mm per hour are chosen to exclude dry areas where τ cannot be computed.

Spatial and temporal statistical metrics

Standard statistical metrics are selected to describe the spatial and temporal comparison of two data sets. Following the notation of Taylor (2001) and González-Zamora et al. (2015) x_i and y_i are two variables at

discrete points i (in time or space) and where n stands for the sample size. The average of the two data sets is represented by a bar. The bias between two data sources and standard deviation (std) is given by:

$$bias = \frac{\sum_{i=1}^{n}(x_i - y_i)}{n} \tag{4.5}$$

$$std = \sqrt{\frac{1}{n-1}\sum_{i=1}^{n}(x_1 - \bar{x})^2} \tag{4.6}$$

Furthermore, the quantification of differences in two data sets is given by the root-mean-square difference (RMSD) (Eq. 4.7). The terminology of RMS difference instead of RMS error is selected because the observation data have also instrumental and representative errors.

$$RMSD = \sqrt{\sum_{i=1}^{n}\frac{(x_i - y_i)^2}{n}} \tag{4.7}$$

The centred root mean square differences were introduced by Taylor (2001) to exclude the RMSD amount caused by the bias. The cRMSD describes the differences in the amplitude of the variation and is given by:

$$cRMSD = \sqrt{\frac{\sum_{i=1}^{n}[(x_i - \bar{x}) - (y_i - \bar{y})]^2}{n}} \tag{4.8}$$

The correlation coefficient of Pearson R measures the relationship between two series:

$$R = \frac{\sum_{i=1}^{n}(x_i - \bar{x})(y_i - \bar{y})}{\sqrt{\sum_{i=1}^{n}(x_i - \bar{x})^2}\sqrt{\sum_{i=1}^{n}(y_i - \bar{y})^2}} \tag{4.9}$$

Finally, the agreement index (AI) assesses the accuracy of remotely sensed products (Willmott, 1982). AI is not a measure of correlation in a formal sense but rather a measure of the degree to which model predictions are free of error (González-Zamora et al., 2015):

$$AI = 1 - \frac{\sum_{i=1}^{n}(x_i - y_i)^2}{\sum_{i=1}^{n}(|x_i - \bar{x}| + |y_i - \bar{x}|)^2} \tag{4.10}$$

AI ranges between 0 and 1 where 0 indicates total disagreement between predicted and observed values and 1 demonstrates a perfect agreement.

Taylor diagrams

A statistical quantification of the degree of similarity between two fields is the Taylor diagram (Taylor, 2001). It graphically summarises how closely patterns agree with observations. The Taylor diagram is based on the fact that R, std and cRMSD are complementary but not independent from each other. Therefore, the statistics can be related by the following equation:

$$cRMSD^2 = {std_x}^2 + {std_y}^2 - 2std_x std_y R \tag{4.11}$$

This relationship allows to display the correlation, centred root-mean-square difference and the standard deviations on a two dimensional plot (Taylor, 2001). The standard deviation is illustrated as a radial distance and the correlation with in situ data as an angle in a polar plot. In-situ data are represented by a point located on the x-axis at R=1 and a given standard deviation. The distance to this point indicates the cRMSD.

Box plot

The box plot summarises the distribution of a data set. This visualisation has become a standard technique to present the 5-number summary which consists of the minimum and maximum range values, the upper and lower quartiles and the median (Potter, 2006). The box indicates the position of the upper (75%-quartile) and the lower quartile (25%-quartile), the distance between both quartiles is the interquartile range (IQR) which consists of 50 % of the distribution. The box is intersected by a crossbar that represents the median (50%-quartile). The whiskers connect the box plot with the extreme of the distribution, the minimum and maximum values in a data set. For the representation of whiskers several opportunities could be chosen. One possibility is that the whiskers include the absolute maximum and minimum of a distribution or another common representation is that the whiskers are multiplied by 1.5-fold of the IQR of the lower and upper quartile. Possible outliers are represented individually by symbols.

Nash-Sutcliffe efficiency

Nash-Sutcliffe efficiency (NSE) is a normalised statistic that determines the relative magnitude of the residual variance ("noise") compared to the measured data variance ("information") (Nash and Sutcliffe, 1970). The NSE indicates how well the plot of observed data versus simulated data fits the 1:1 line, where 1 corresponds to a perfect match of modelled data with observed data and can be described by the following equation (Nash and Sutcliffe, 1970; Mauricio Zambrano-Bigiarini, 2017):

$$NSE = 1 - \frac{\sum_{i=1}^{N} (S_i - O_i)^2}{\sum_{i=1}^{N} (O_i - \overline{O})^2} \tag{4.12}$$

S_i presents the simulated values, O_i the observed values and $\overline{O}$ is the mean of the observed values. The NSE is a common method to describe the optimal T_{opt} parameter (timescale of soil moisture variation) of the exponential filter formula (Ford et al., 2014). The highest NS score is considered as the T_{opt} of every soil level (see Chap. 6).

SAL-method

The SAL-method is used to verify the simulated precipitation fields. The SAL-method is a three-component feature-based quality measure considering the structure (S), amplitude (A) and location (L) of precipitation forecast for a predefined region of interest (Wernli et al., 2009). For the structure and location components it is necessary to identify coherent objects in the observed and predicted precip-

itation fields. For this identification a threshold of 1/15 of the 95th percentile of all grid point values in the domain larger than 0.1 mm is selected (Wernli et al., 2009). Due to its high temporal and spatial gridded resolution (8 km, 1/2 h) the satellite measured precipitation observation of CMORPH is the most suitable reference data source that is available for the domains of interest. The amplitude component A indicates an overestimation (underestimation) of total precipitation by positive (negative) values ranging between -2 and +2. The location component L consists of two parts where the first term describes a displacement of the centers of mass of a predicted and an observed precipitation field. The second term measures the error in the weighted-average distance of precipitation objects from the total field's center of mass. The L-component values range between 0 and 2. The structure component S indicates with positive (negative) values that the predicted precipitation objects are too large (small) and/or too flat (peak). A possible range of values extends from -2 to +2. Perfectly simulated precipitation is characterised by zero values for all SAL components. Fig. 4.4a illustrates the different combinations of errors of the three components. In the subfigure (b) and (d) a large displacement in the location L is visible whereas the amplitude A and structure S agree perfectly between forecast and observation. On the contrary, in subfigure (e) the differences in structure S and amount A are large in the forecast compared to the observation and the error in the displacement of L is moderate. In an example of a SAL-diagram in Fig. 4.4b the simulation Sim-1 shows a more worse forecast than Sim-2. The predicted precipitation objects in Sim-1 are too small or peak, the amount of precipitation is underestimated, and the precipitation peak is displaced. In Sim-2 the amount of precipitation is similar between simulation and observation but slightly overestimated whereas the structure is also too small or peak and slightly displaced.

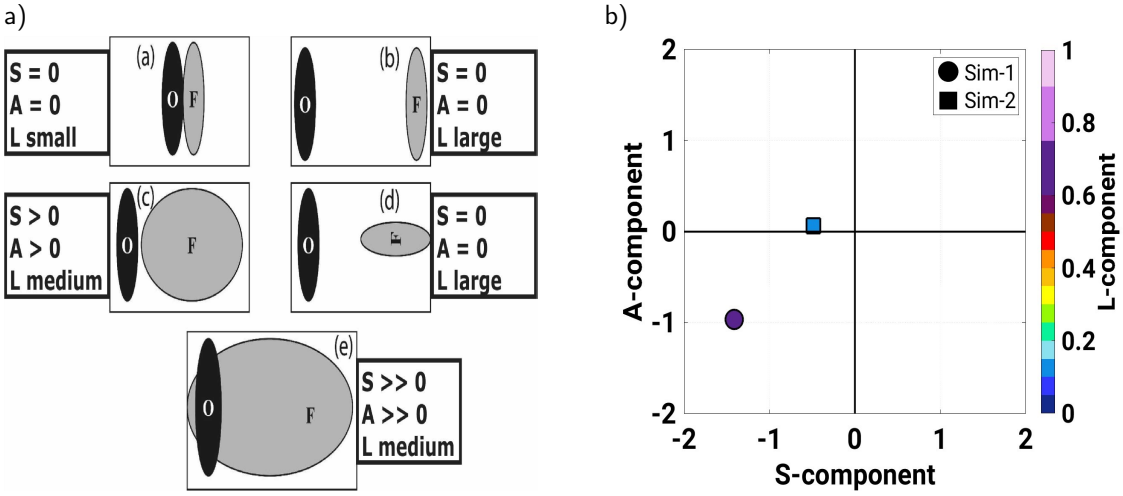

Figure 4.4.: a) A schematic figure (Wernli et al., 2008) to describe the various forecast and observation combination of the three components (S=structure, A=amplitude and L=location) of the SAL-method. O indicates the observation and F the forecast. b) An example of a SAL-diagram with S component on the y-axis [-2;2], the A-component on the x-axis [-2;2] and the coloured scale of the symbols indicate the L-component [0;1]. The different symbols illustrate different COSMO simulations. Values of the components at 0 indicate a perfect agreement between simulations and observations.

5. Sensitivity of Modelled Seasonal Heavy Precipitation to Idealised SM Initialisation in the WMed

This chapter presents a set of experiments regarding the initialisation of soil moisture with the COSMO model. The influence of extremely dry and wet initial soil moisture on the representation of SM-atmosphere interactions leading to wet extreme phenomena in autumn 2012 is investigated. Seasonal COSMO simulations are performed in a resolution of about 7 km (convection-parametrised) and of about 2.8 km (convection-permitting) for the WMed. The modification of atmospheric conditions to the initial soil moisture perturbation and possible SM-precipitation feedbacks are compared between both model resolutions. Sec. 5.1 describes the regional characteristics of the observed and highly resoluted modelled heavy precipitation in the autumn 2012. The concept of the extreme initial SM experiment is introduced in Sec. 5.2. The effects of this SM initialisation on the modification of atmospheric conditions are presented in the following Sec. 5.3. Some insights in feedbacks on soil moisture-precipitation at a seasonal scale and the sensitivity of wet extremes to dry and wet SM initial conditions are contained in Sec. 5.4. Finally, in Sec. 5.5 the dependence of the SM-atmosphere interactions on the model resolution is discussed.

5.1. Regional Characteristics of Precipitation Based on Observations and High-Resolution Modelling

To analyse heavy precipitation (HP) in the WMed (10°W-20°E, 30°N-48°N, Fig. 3.2), the selected wet period of September until November (SON) 2012 is considered. In the included HyMeX SOP1 period daily accumulated rainfall exceeding 100 mm was observed on 20 of 61 days (Ducrocq et al., 2014). Of these 20 days, 16 IOPs are associated with HPEs and 9 IOPs with flash floods. The daily maximum accumulated precipitation at each station from the HyMeX rain gauge data set for SON 2012 is shown in Figure 5.1. Extreme precipitation is related to the orography of the Alps, the Pyrenees and the coastal regions. The HyMeX target areas (Fig. 3.2) are prone to being frequently affected by HPEs and flash floods such as on the eastern Spanish coast (Romero et al., 1998; Llasat et al., 2010), the CV region in southern France (Ricard et al., 2012) and the CI as well as LT areas on the Italian western coast (Romero et al., 1998; Buzzi et al., 2014; Barthlott and Davolio, 2016). The WMed is divided into the four regional subdomains IP, NA, FR and IT (Chap. 4.1) to analyse the regional discrepancy within these region. The heaviest precipitation events with more than 200 mm per day are observed in the subdomain IT and in the south-east part of the Iberian Peninsula (Fig. 5.1). The subdomain FR is mainly affected by HPEs in

the Mediterranean coastal regions and in the Rhone valley (Fig. 2.1) with precipitation between 50 mm and 200 mm. The density of available rain gauge observations in the regional subdomain NA is low, therefore it is difficult to validate this region by rain gauge measurements.

Based on the Köppen-Geiger classification (Kottek et al., 2006), the subdomains IP and NA are classified as dry to warm temperate climates with warm to hot dry summers, while the FR and the IT are categorised as warm temperate climates with fully humid to dry warm summers. In particular, the IT is a complex subregion due to its large north-south elongation which is surrounded by large amounts of the Mediterranean Sea (Tab. 4.1 and Fig. 2.1). Additionally to the complex land-sea distribution, Italy is influenced by several wind systems such as Bora, Mistral and Sirocco. These systems can provide favourable conditions for the initiation of HPEs in this region (Barthlott and Davolio, 2016; Davolio et al., 2017). Moreover, there is a large thermal contrast in the subdomain IT which is characterised by polar frost and snow, full humidity, cold summer climate in the higher altitudes of the Alps in the north and the warm, temperate climate with dry and hot summers in the southern parts of IT.

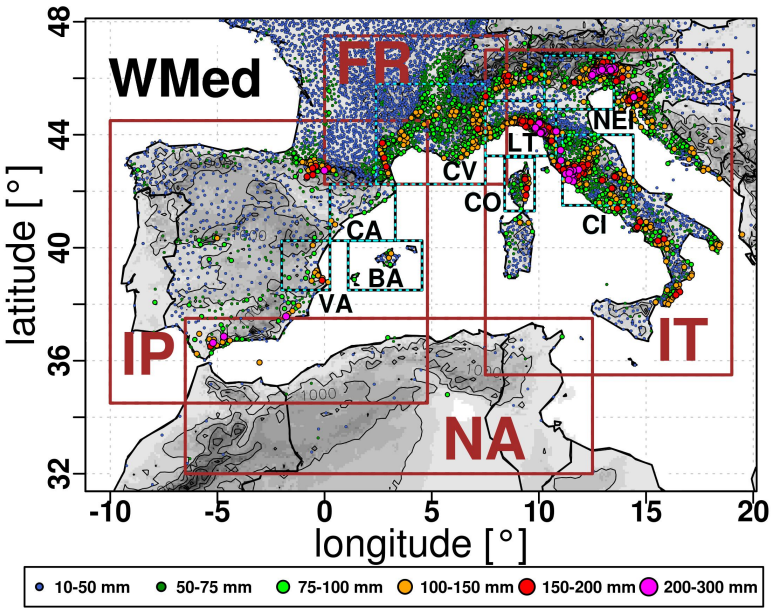

Figure 5.1.: Maximum daily accumulated precipitation (06-06 UTC) at each station in SON 2012 of the HyMeX rain gauge data set Version 4 (Nuret, 2017). The brown boxes indicate the defined regional subdomains and the black boxes show the HyMeX target areas. The grey scale indicates the orography.

In the following the IP and NA are predominantly denoted as semi-arid climate regions, while the regions in IT and FR are classified as humid temperate climate regions. The high-resolution modelling of the Consortium for Small-scale Modeling-CLimate mode (COSMO-CLM)-2.8km reference simulation in this region SON 2012 confirms these two main classifications. The accumulated domain-average precipitation in the SON period for all land grid points varies between 130 mm and 210 mm in the NA/IP regional subdomains and is about 250 mm to 350 mm for the subdomains FR and IT (Tab. 5.3).

The seasonal evolution of the daily-accumulated domain-average precipitation is compared between the

model resolutions of COSMO-CLM and also compared with observations from CMORPH and available rain gauge stations (Fig. 5.2). The validation of the model performance for all regional subdomains shows a good agreement with the observations in terms of time and amount of precipitation. The IOPs given within the subdomains are also well represented in the simulations.

The effective drought index (EDI) and the convective adjustment time-scale (τ) are used to categorise wet and dry periods and the dominant synoptic forcing within the subdomains in SON 2012 (Chap. 4.3). Furthermore, these indices allow not only the identification of interesting periods of HPEs but also the analysis of their preconditions favouring SM-atmosphere interactions. Therefore, the indices are used to select the event periods of the realistic SM initial experiment in Chap. 6.2.

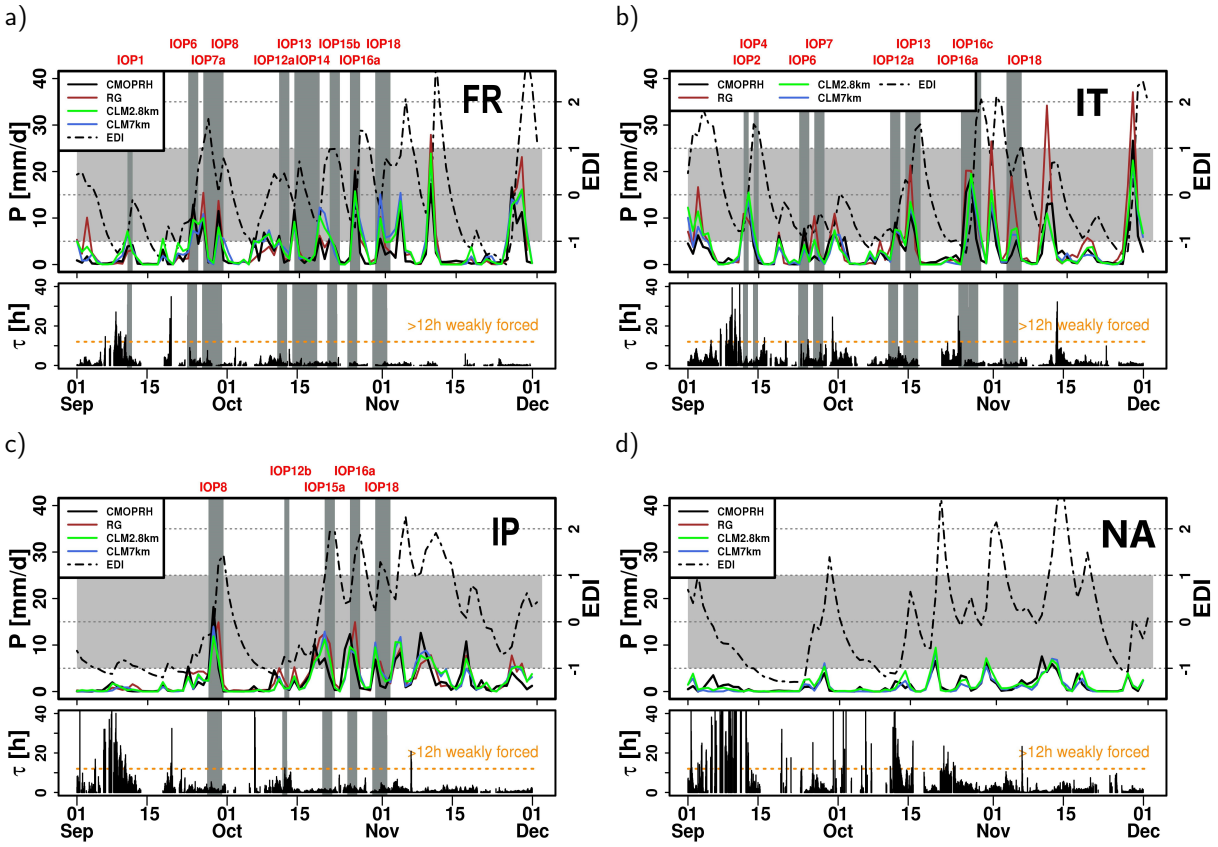

Figure 5.2.: The temporal evolution of the daily accumulated spatial-averaged precipitation is shown both in COSMO resolutions as well as in observations of rain gauges (RG) and CMORPH for the regional subdomains in a) FR, b) IT, c) IP, d) NA. EDI is calculated from the COSMO CLM-2.8km simulation for this period (black dashed-dotted line). Below is the hourly calculation of the convective adjustment time scale for the four subdomains with a threshold of 12 h to distinguish between weak and strong synoptic flow regimes. Darkly shaded areas indicate the IOPs within each subdomain.

The large fluctuation in the calculation of EDI in autumn clearly shows the effects of HPEs. The precipitation signal remains due to the selected time criterion of 15 days in the precipitation weight function of the EDI calculation for some days in the representation of EDI (Chap. 4.3). This tested criterion seems to be suitable for the EDI calculations on seasonal scales. The first half of autumn 2012 is predominately

dry in the semi-arid regions of IP and NA, with the exception of the heavy precipitation of IOP8. In the second half of the period there are more precipitation events in these regions associated with a wet status of EDI. The subdomains FR and IT are more frequently influenced by HPEs during the whole period, with a maximum frequency and intensity from the end of October to the beginning of November. EDI indicates a wet period.

The τ index distinguishes between strong and weak synoptically forced precipitation regimes. In autumn 2012 the largest differences in this quantity exist between the moderate wet climate in the FR subdomain with a predominantly strong large-scale forcing (τ <12 h) and the semi-arid region of NA with a mainly weak synoptically forcing (τ >12 h). In addition, the first half of September is characterised by weak synoptic conditions in all regional subdomains, while in October and November large scale forcing is the dominant factor. Nevertheless, the calculation of τ at regional scale in Fig. 5.2 does not so strongly take into account the effect of single local HPEs and these local effects can play a more important role for precipitation development. Therefore, τ is also calculated for the HyMeX target areas on local scale (Fig. 5.11).

With the high-resolution simulations of COSMO CLM-2.8km regional characteristics of precipitation amount and intensity are analysed (Fig. 5.3). The hourly precipitation rates of the CTRL simulation are used to compare the duration of precipitation with its intensity for the four subdomains. If the intensity exceeds the threshold value of 0.1 mm/h, it is considered as an event until it falls below this value again. Long-lasting precipitation events with a precipitation duration of more than 72 h occur mostly in the humid moderate climate regions of FR and IT. Such events are typically associated with large-scale precipitation which is also reflected in the calculation of the τ index. These results are consistent with those of a previous study by Khodayar et al. (2016a) who investigated similar areas with COSMO CLM-7km simulations in autumn 2011 and 2012. The subregion IP shows only a few of these long-lasting events and the majority of events in the semi-arid regions show a shorter time span than 48 hours. In the subdomain NA the longest duration of precipitation is 48 hours. Convective precipitation dominates in the semi-arid regions. This is in line with the results of Khodayar et al. (2016a). The highest intensities occur on a sub-daily time scale and are associated with convective precipitation. According to rain gauge observations, the strongest events are found in the subdomain IT with a strong intensity caused by convective processes in a time scale of several hours. This result differs from Khodayar et al. (2016a), which found the highest precipitation rates in long-lasting events. In addition, some convective heavy rain events with precipitation up to 400 mm also affect the areas NA and IP. In COSMO CLM-7km simulation of Khodayar et al. (2016a) also this result was not found.

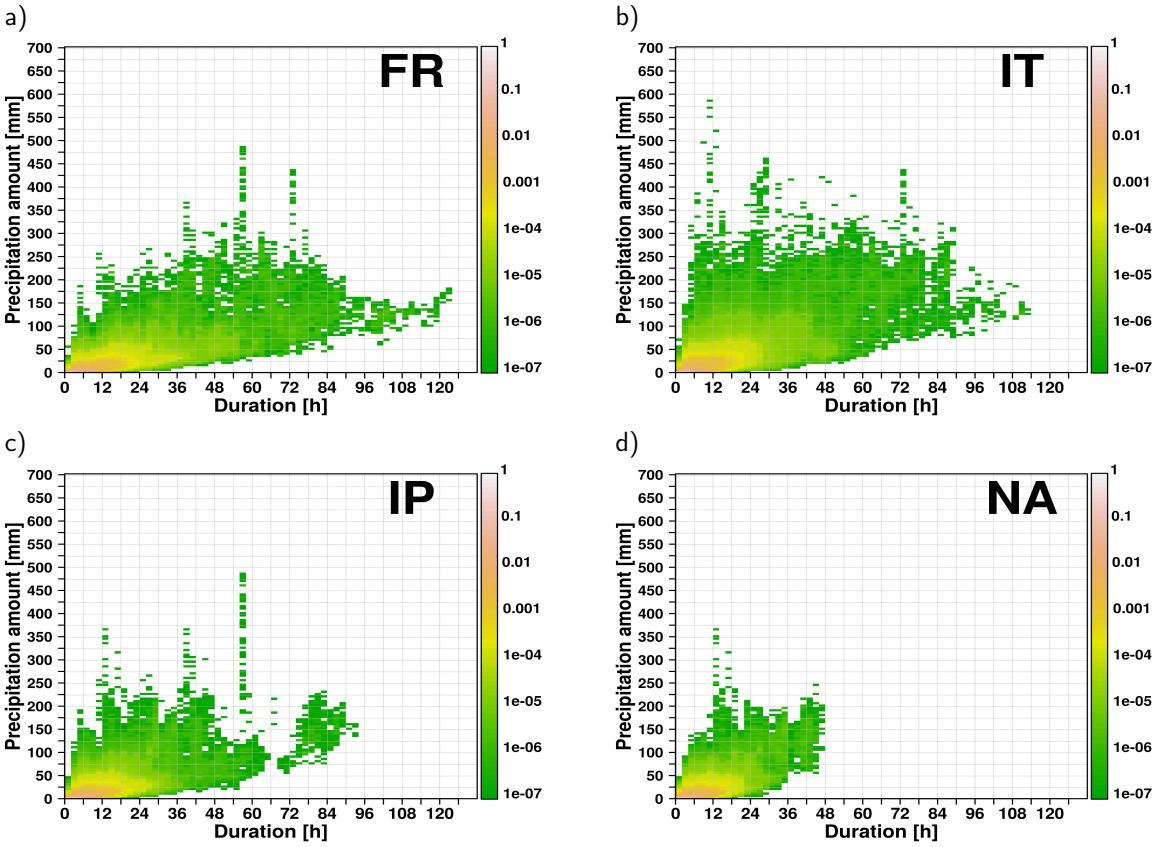

Figure 5.3.: The scatter plots show the hourly COSMO CLM-2.8km modelled precipitation amounts versus duration for the four subdomains a) FR, b) IT, c) IP and d) NA in SON 2012. The colour scale indicates the normalised probability of specific events in the COSMO CLM-2.8km simulation.

5.2. SM Initialisation Sensitivity Experiment for the Autumn Period 2012

A SM sensitivity experiment with COSMO is conducted for the season autumn 2012 to prove whether there is a sensitivity between extreme initial SM conditions and land-atmosphere interactions. As introduced in Chap. 4.2 a wet and dry SM initial scenario at the initialisation time of the COSMO model is applied. At this time, the profile of SM is modified in relation to the corresponding soil type. Afterwards, these modifications evolve freely without further SM correction or SM assimilation in the course of the seasonal simulation. Khodayar et al. (2015) concluded that initialisation during a dry or wet period exerts an important influence on the initial scenario and that soil is more sensitive when initialised during the dry period. For this reason, the initialisation day is chosen within a dry period that is not influenced by large amounts of precipitation in the WMed. This selection criterion guarantees that the initialisation of SM on the following days of the simulation is not distorted by precipitation effects. For a seasonal simulation, a spin-up time of half a month is considered to avoid thermodynamic and dynamic imbalances of the CTRL simulation to its initial conditions, that could persist for the entire duration of the sensitivity simulations and modify the results (Zampieri et al., 2009). However, the exclusion of this spin-up period

also means losing part of the SM-atmosphere interaction signal, especially since the first period after initialisation shows the strongest modification effect. Therefore, a possible modification of SM-atmosphere interactions in the analysis period of SON is more robust, since possible artificial imbalances and the first period of the strongest SM-atmosphere coupling are excluded. With these two selection criteria, August 8, 2012 is identified as a suitable day for the application of the wet and dry SM initialisation scenarios. The initialisation of the seasonal autumn COSMO simulations starts under dry conditions in the summer season (EDI calculation identified dry conditions in summer 2012 as shown in Fig. 4.3).

The initial spatial fields of volumetric soil moisture in the sensitivity studies and the reference simulation (CTRL) are shown in Fig. 5.4. The WMed domain-average of SM in the CTRL is about 13 vol.% and ranges between 8 vol.% in NA and 26 vol.% in FR (Fig. 5.4a).

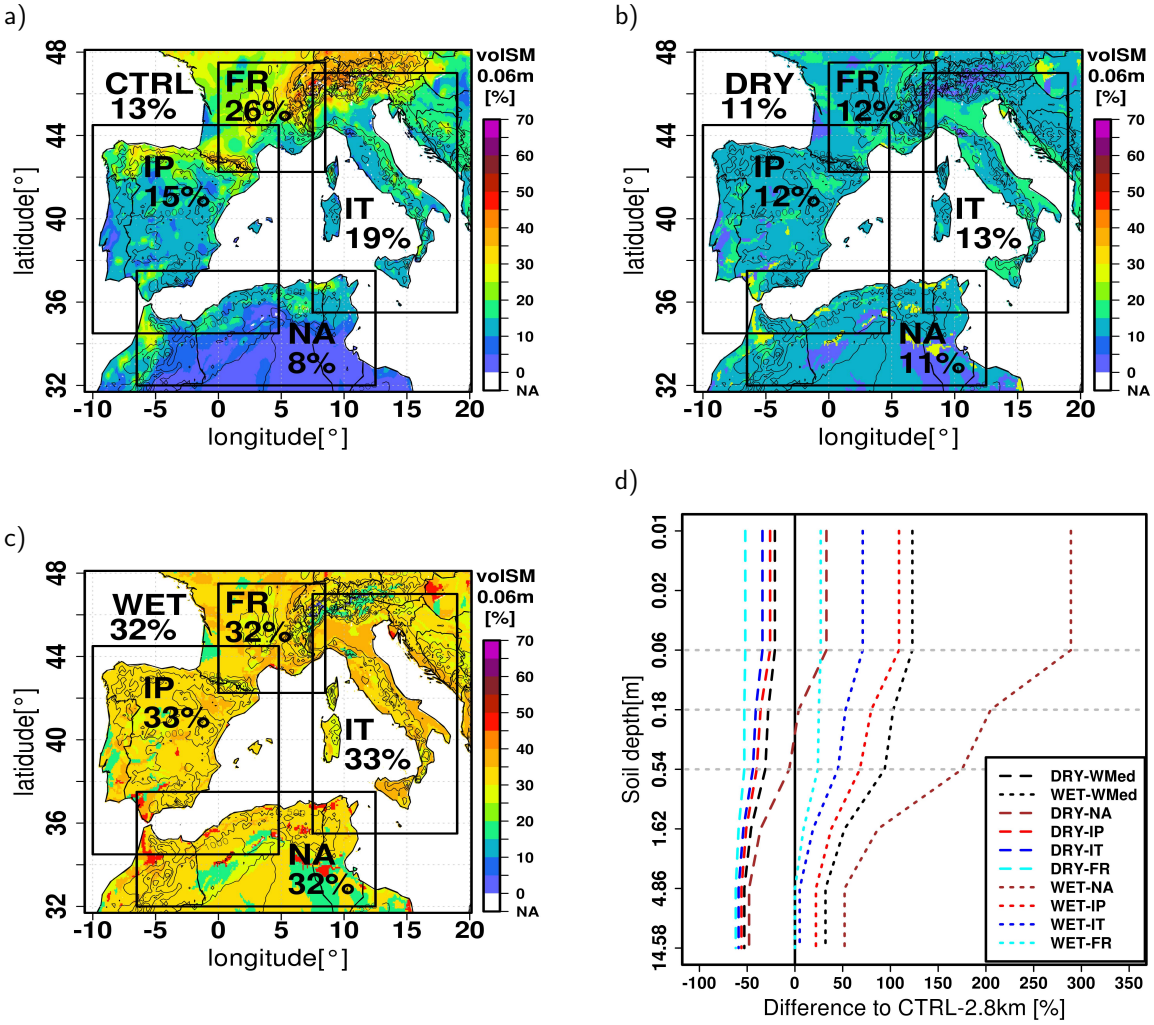

Figure 5.4.: Initial fields of volumetric soil water content at a soil depth of approximately 5 cm in the reference simulation (CTRL) and sensitivity experiments in vol.%. Figure a) shows the initial SM of CTRL and figure b) illustrates the initial SM modification of the DRY-scenario. Figure c) presents the initial SM modification of the WET-scenario. The domain-average values of SM in the WMed and the subdomains are indicated. Figure d) shows the relative changes in SM profile between the DRY- and WET-scenario and the CTRL simulation for the spatial-averages of the whole WMed and each regional subdomain.

In the WMed the SM modification of the WET-scenario with a value of 32 vol.% [+150 % relative change] is higher than the modification of the DRY-scenario with 11 vol.% [-15 % relative change] due to the already prevailing dry conditions on the selected initialisation day in summer 2012. In the dry initial scenario, the surface SM in the subdomains is reduced by -50 % in FR, -30 % in IT and -20 % in IP. In the region NA the spatial-average value of SM is increased because the mean SM value of 8 vol.% in the CTRL is below the wilting point and therefore SM is drier than in the DRY-scenario with 11 vol.%. In deeper soil layers the relative changes are homogeneous and are about -50 %. The relative changes in the WET scenario vary between +25 % in FR and +275 % in NA in near-surface soil layers. In the deeper soil layers SM range between 0 % and +50 % (Fig. 5.4d). Depending on soil type, both initial scenarios can have positive or negative patches, e.g. wet patches in NA in the DRY-scenario or dry patches in the Alps in the WET-scenario. In these cases the CTRL SM is wetter than the field capacity or drier than the wilting point.

Besides the initial modification of SM it is of interest to know how long the perturbation signal remains in the soil. Fig. 5.5 shows the temporal evolution of SM in different soil layers for the CTRL simulation and the sensitivity scenarios for the IP and FR subdomains in comparison to COSMO convection-parametrised and convection-permitting model resolutions. In the following the analysis period of SON 2012 without the spin-up period in August is always considered.

Regional differences in the development of soil moisture in all soil layers can be observed between the subdomain FR and IP. At the beginning of September the volumetric soil water content in the upper soil layers of the region IP is drier with a value of 15 vol.%. In comparison, the value in FR is about 25 vol.%. The upper soil layers indicate a strong response to precipitation events. In the first half of SON the dry soil moisture status in the upper soil layers in the subdomain IP is in accordance with the identified dry period of EDI calculation in this period (cf. Fig. 5.2). Here again, the IOP8 event exhibits a clear response to soil moisture with a lower amount of soil moisture before and after this event. In the second half of autumn 2012 precipitation events occur more frequently and soil moisture increases continuously. In both regions soil moisture in the upper soil layers increases up to 30 vol.% by the end of the autumn 2012 period. Deeper soil layers (>2 m) show smaller soil moisture variations. No significant differences in soil moisture development could be observed between the model resolutions. There are only minor differences in the response to precipitation.

Comparing the SM modification of the sensitivity studies, the semi-arid IP domain is more sensitive to the WET-scenario than the FR subdomain in the upper soil layers. Due to fewer precipitation events in the IP domain, this signal remains longer in the IP domain than in the FR subdomain. The DRY-scenario reveals a higher sensitivity in the FR domain, especially in deeper soil layers. In the near-surface soil layer of the IP domain the wet SM modification remains until the end of the period, but it gets closer to the reference simulation with every precipitation event. The differences of SM between CTRL and DRY-scenario in the IP are smaller. With the occurrence of precipitation, these differences adapt to the value of the CTRL simulation in the uppermost soil layer after one month and in deeper soil layer ($\sim$20 cm)

after 2.5 months. In the FR subdomain the soil moisture differences between the WET-scenario and the CTRL disappear faster due to more frequent precipitation. In this humid region, the impact of the WET-scenario is less than the influence of the DRY-scenario and the dry perturbation remains longer in the soil. If the soil moisture of the sensitivity studies converges in the upper level to the amount of CTRL by the infiltration of water from precipitation, after some time the original perturbation signal appears again. This effect occurs because the original initial disturbance of soil moisture is still present in deeper soil layers and affects the upper soil moisture. This effect is known as the long-term soil moisture memory.

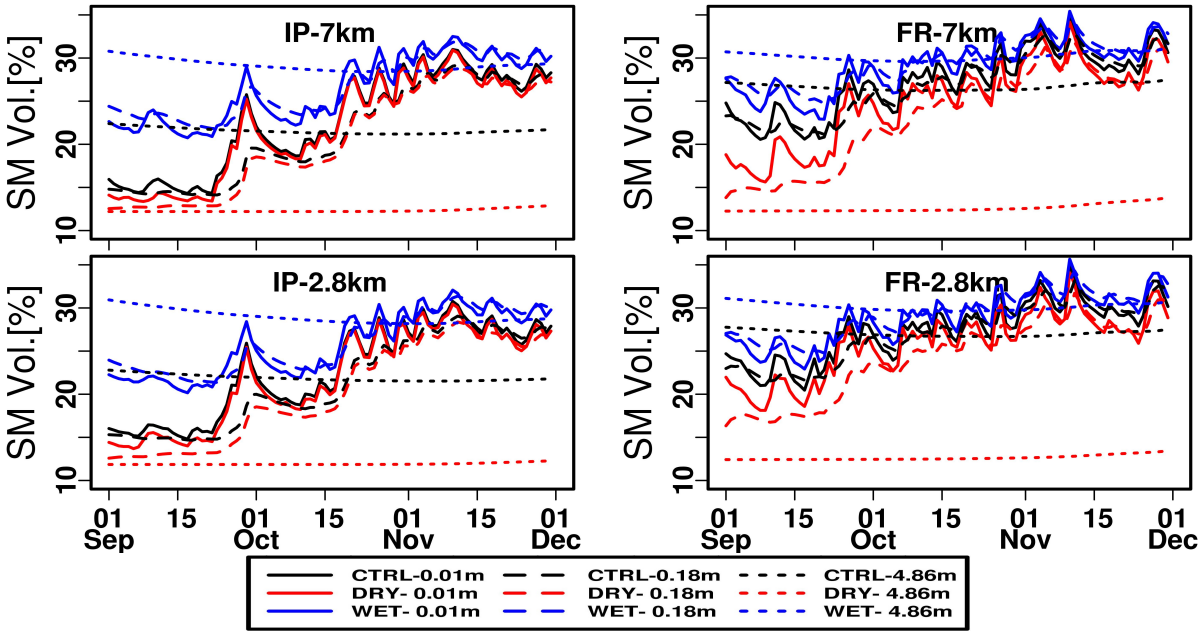

Figure 5.5.: Comparison of temporal evolution of daily volumetric soil water content between COSMO CLM-7km and COSMO CLM-2.8km simulations. The domain-average volumetric soil water content is illustrated for different soil layers of the IP and FR subdomain in the sensitivity scenarios and the CTRL simulation.

5.3. Impact on Atmospheric Conditions

This section examines the effect of the SM initialisation experiment on the seasonal mean conditions of various variables describing the atmospheric state. Fig. 5.6 shows the mean conditions of the COSMO CLM-2.8km CTRL simulation for SON 2012 and the corresponding differences between the extreme SM initial scenarios and the CTRL conditions. In order to achieve a consistent representation of various plots, the red colours always illustrate a positive increase and the blue colours always a negative decrease. Both extreme initialisation scenarios exhibit a positive seasonal SM-atmosphere coupling in most regions of the WMed. In this regard, positive means that a wet/dry SM initialisation leads to an increase/decrease in moisture, instability or cloud cover. The WET-scenario indicates a seasonal mean increase (SON) of all land and sea grid points in latent heat flux (LHFL) and in specific humidity in 2 m (QS2m) due to the initial surplus in SM on Aug 8, 2012 (Fig. 5.4d). The moist signal is transported to the whole

atmospheric column represented by an increase of the integrated water vapour (IWV). Additionally, the atmosphere gets more destabilised which is indicated by higher values of convective available potential energy (CAPE). The higher seasonal mean instability and humidity in the atmosphere induce moist convection which leads to an increase in the total cloud cover (TCC). This increase in total cloud cover is mainly attributed due to an increase in low cloud cover (LCC) and less to middle and high cloud cover. To explain such an increase in moist convection, previous studies have found out that wet soils result in a comparatively shallow boundary layer and a lower level of free convection (e.g. Schär et al. (1999); Hohenegger et al. (2009)). They came to the conclusion that wetter soil conditions are associated with less moist static energy per unit of the planetary boundary layer. In autumn 2012, the wet scenario also implies such a process as a decrease in seasonal mean height of planetary boundary layer (HPBL) is found over land and the surface net radiation flux (Rn) increases (Tab. 5.1). The same positive feedback is shown for the dry initial SM scenario where a reduction of SM leads to less moisture in the atmosphere associated with a more stable atmosphere and less moist convection and TCC. Furthermore, it can be concluded from Fig. 5.6 that the initial SM does not only affect land areas but also the atmospheric conditions above sea areas. The initially perturbed signal over land is also transported during the seasonal simulation to the sea and modifies the conditions over the sea. The changes in pressure at mean sea level (PMSL) (not shown) and the geopotential height at 500 hPa (z500) field reveal that the large-scale conditions are also influenced. The largest modification in the PMSL field can be observed in the inland of the IP and the NA. The strongest modification of the z500 field occurred over the Mediterranean Sea, south of the Balearic Islands. Furthermore, the opposite sign of the modification in LHFL, QS2m, HPBL (not shown) and CAPE over the Mediterranean Sea could be an indication of changes in the mesoscale circulations. Moreover, the sensitivity studies of initial SM reveal that locally seasonal mean near-surface moisture variations of about +1 g/kg over semi-arid land regions (QS2m in Fig. 5.6) could make an important contribution to the initiation of HPEs.

To quantify the positive impacts of initial SM perturbation, Tab. 5.1 shows the seasonal mean changes of various atmospheric variables in the WMed and in the defined subdomains as mean values for all land grid points. The initial modification of SM in upper soil layers is about +130 % and in deeper soil layers of about +30 %. This SM modification causes a seasonal increase of +75 % in evapotranspiration (ET) and LHFL. The QS2m increases by about +10 % and the IWV of about +2 % in the WMed. At the same time the sensible heat flux (SHFL) is reduced by -50 % and the temperature in 2 m (T2m) decreases by about -1 °C. Higher moisture and instability of about +30 % in CAPE lead to more moist convection and low cloud cover (LCC) of about +20 %. The medium cloud cover (MCC) is unvarying and the high cloud cover (HCC) slightly decreases. The increase in LCC affects also short wave radiation at surface (SW) by a mean decrease of -1 % (1 W/m^2). Considering regional differences, the semi-arid regions IP and NA reveal the highest positive effects to SM initialisation in the WET-scenario.

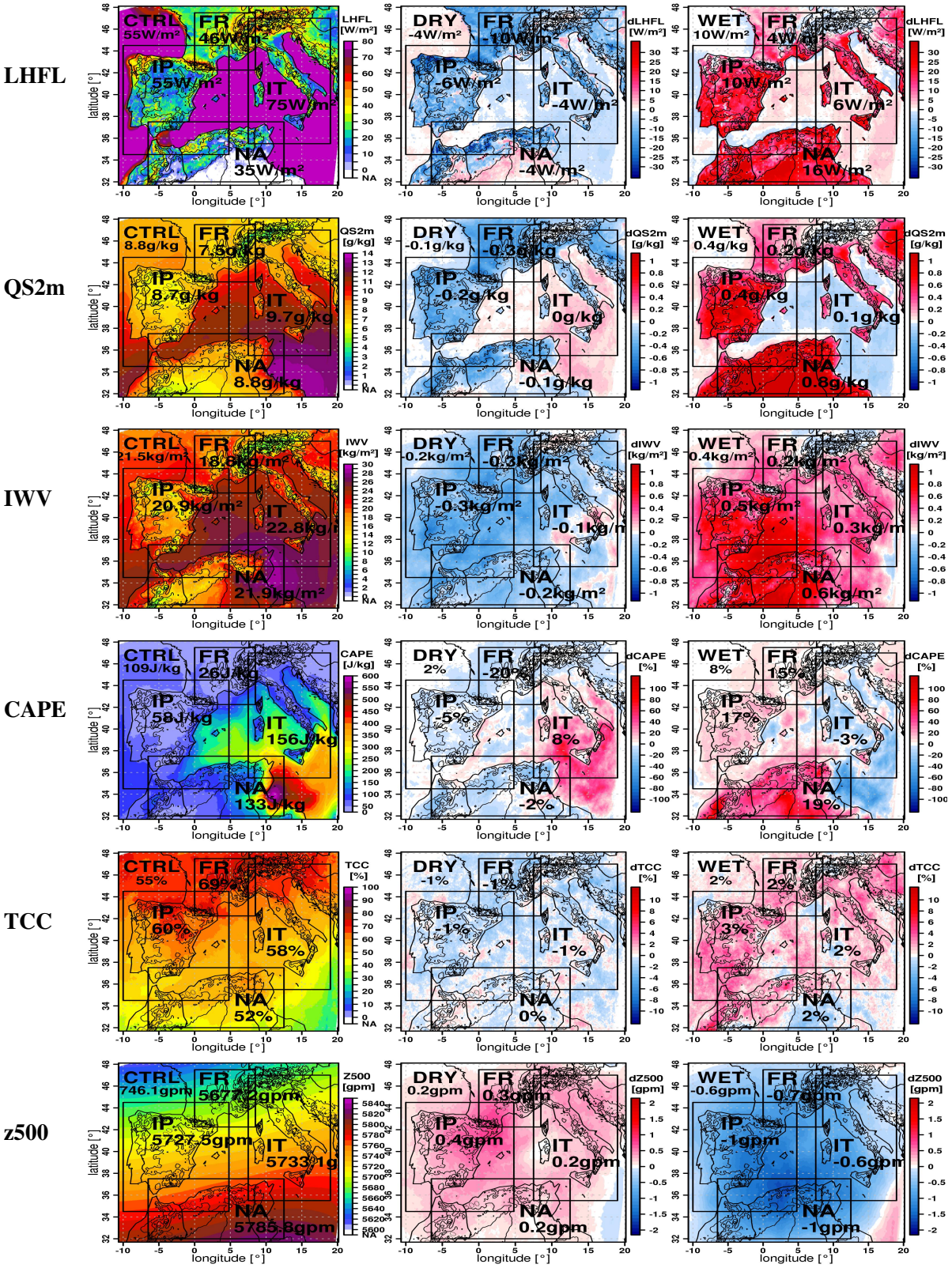

Figure 5.6.: Seasonal atmospheric mean conditions of the reference simulation (CTRL) COSMO CLM-2.8km in autumn 2012 and their seasonal mean differences for the simulation of the SM sensitivity experiment. The first column presents for the CTRL simulation from top to bottom: latent heat flux (LHFL), the specific humidity in 2 m (QS2m), the integrated water vapour (IWV), the total cloud cover (TCC) and the atmospheric stability represented by CAPE. The second column illustrates the modification of these variables as the difference of the DRY-scenario minus the CTRL and the third column as the difference of the WET-scenario minus the CTRL. The four regional subdomains are indicated by black boxes with spatial-mean values of each subdomain.

In the NA region the seasonal mean increase of ET and LHFL is particularly high with +130 % due to the large increase in the initial SM in this region. This higher moisture flux leads to higher mean QS2m of about +15 % and higher seasonal mean instability of about +35 % in CAPE. The decrease in HPBL by about -15 % and the increase in LCC by +40 % induce a stronger moist convection. At the same time, the T2m decreases by about -1.5 °C. The lowest sensitivity in the wet initial scenario shows FR. This subdomain also has the lowest initial modification of SM (Fig. 5.4). In the domain of IP the initial SM perturbation in the surface levels is around +100 %. This soil moisture signal has a higher seasonal mean flux change of about +60 % in ET but the reference values in ET are also higher than in the NA region. Due to higher seasonal mean values in LCC (24 %) and TCC (61 %) in the IP region, the influence on SW is also higher with about -3 % (-3 W/m^2). The SHFL is reduced by about -60 % and the T2m of about -1 °C. In the humid moderate regions of FR and IT the signal is weaker but a positive coupling is also observed.

Table 5.1.: Seasonal changes of mean atmospheric conditions for the WET-2.8km initialisation scenario in SON 2012. Only land grid points are considered. The percentage change is given in % and the absolute mean conditions are described in brackets for the WMed and the regional subdomains.

WET-2.8km	WMed	NA	IP	IT	FR
ET[CTRL]	+75%[68mm]	+130%[51mm]	+60%[90mm]	+40%[99mm]	+15%[116mm]
Rnet[CTRL]	+15%[36W/m^2]	+20%[42W/m^2]	+10%[41W/m^2]	+10%[31W/m^2]	+4%[36W/m^2]
HPBL[CTRL]	-10%[600m]	-15%[650m]	-10%[550m]	-10%[450m]	-5%[500m]
QS2m[CTRL]	+10%[7.4g/kg]	+15%[7.9g/kg]	+10%[7.5g/kg]	+5%[7.8g/kg]	+5%[7.1g/kg]
IWV[CTRL]	+2%[19kg/m^2]	+3%[21kg/m^2]	+3%[19kg/m^2]	+1%[20kg/m^2]	+1%[18kg/m^2]
CAPE[CTRL]	+30%[55J/kg]	+35%[102J/kg]	+40%[33J/kg]	+10%[60J/kg]	+20%[19J/kg]
TCC[CTRL]	+2%[56%]	+2%[52%]	+3%[61%]	+3%[61%]	+2%[70%]
LCC[CTRL]	+20%[19%]	+40%[10%]	+20%[24%]	+15%[28%]	+10%[35%]
SW[CTRL]	-1%[112W/m^2]	-1%[127W/m^2]	-3%[110W/m^2]	-2%[92W/m^2]	-3%[83W/m^2]
SHFL[CTRL]	-50%[21W/m^2]	-40%[33W/m^2]	-60%[20W/m^2]	-150%[6W/m^2]	250%[-2W/m^2]
T2m[CTRL]	-1°C[17.0°C]	-1.5°C[19.8°C]	-1°C[14.8°C]	-0.5°C[13.9°C]	-0.4°C[11.2°C]
PMSL[CTRL]	+0.5hPa[1015]	+0.6hPa[1015]	+0.5hPa[1015]	+0.2hPa[1015]	+0.2hPa[1015]
Z500[CTRL]	-1gpm[5749]	-1.0gpm[5790]	-1.0gpm5724]	-0.5gpm[5714]	-1gpm[5673]

In the dry initial scenario the SM-atmosphere coupling is weaker because the initial SM perturbation is about -50 % smaller (Fig. 5.4d). The SM atmosphere coupling is positive, i.e. a dry initial SM leads to a reduction of ET by about -30 % and a lower QS2m by about -5 % and by about -1 % in IWV (Tab. 5.2). The decrease in surface net radiation flux (Rn) (-5%) and instability (-10 % CAPE) induces less convection and low cloud cover (-10 %). The higher seasonal mean SHFL of about +25 % and the mean T2m of +0.3 °C do not cause a compensatory effect of an increase due to more vigorous thermals as found by Hohenegger et al. (2009) in convection-permitting simulations over the Alps.

The moderate wet FR subdomain is the most affected region in the dry initial scenario. In this region the reduction in the Rn is about -10 %, in QS2m about -5 % and in CAPE about -30 %. In addition,

the HPBL is about +10 % higher and the mean convection is reduced by the reduction of LCC. The SM-temperature feedback is the highest in all subdomains with an increase of +0.6 °C in mean T2m. In the DRY-scenario, the large-scale conditions represented by z500 and PMSL are influenced. The maximum decrease in PMSL is above the Central Massif in the subdomain of FR (not shown) and the local maximum increase of z500 is above the Pyrenees (Fig. 5.6). This modification indicates a stronger anticyclonic large-scale condition. This pattern could explain why the semi-arid IP domain also reveals a strong reduction in ET about -40 % and an increase in SHFL by about +40 % which leads to a stabilisation of atmosphere (CAPE -15 %) and a higher change in mean temperature of about +0.5 °C.

Table 5.2.: Seasonal changes in mean atmospheric conditions for the DRY-2.8km initialisation scenario in SON 2012. Only land grid points are considered. The percentage change is given in % and the absolute mean conditions are described in brackets for the WMed and the regional subdomains.

DRY-2.8km	WMed	NA	IP	IT	FR
ET[CTRL]	-30%[68mm]	-30%[51mm]	-40%[90mm]	-20%[99mm]	-30%[116mm]
Rnet[CTRL]	-5%[36W/m^2]	-5%[42W/m^2]	-5%[41W/m^2]	-5%[31W/m^2]	-10%[36W/m^2]
QS2m[CTRL]	-3%[7g/kg]	-2%[8g/kg]	-4%[7g/kg]	-3%[8g/kg]	-5%[7g/kg]
IWV[CTRL]	-1%[19kg/m^2]	-1%[21kg/m^2]	-2%[19kg/m^2]	-1%[20kg/m^2]	-1%[18kg/m^2]
CAPE[CTRL]	-10%[55J/kg]	-10%[102J/kg]	-15%[33J/kg]	-1%[60J/kg]	-30%[19J/kg]
HPBL[CTRL]	+5%[600m]	+5%[650m]	+5%[550m]	+5%[450m]	+10%[500m]
TCC[CTRL]	-1%[56%]	0%[52%]	-1%[61%]	-1%[61%]	-1%[70%]
LCC[CTRL]	-10%[19%]	-10%[10%]	-10%[24%]	-10%[28%]	-10%[35%]
SW[CTRL]	+1%[112W/m^2]	+1%[127W/m^2]	+1%[110W/m^2]	+1%[92W/m^2]	+1%[83W/m^2]
SHFL[CTRL]	+25%[21W/m^2]	+10%[33W/m^2]	+40%[20W/m^2]	+100%[6W/m^2]	-500%[-2W/m^2
T2m[CTRL]	+0.3°C[17.0°C]	+0.3°C[19.8°C]	+0.5°C[14.8°C]	+0.5°C[13.9°C]	+0.6°C[11.2°C]
PMSL[CTRL]	-0.2hPa[1015]	-0.2hPa[1015]	-0.3hPa[1015]	-0.2hPa[1015]	-0.3hPa[1015]
Z500[CTRL]	+0.2gpm[5749]	+0.2gpm[5790]	+0.4gpm5724]	+0.3gpm[5714]	+0.3gpm[5673]

The seasonal mean modification of the atmospheric profile between CTRL and the two extreme initial scenarios are shown in Fig. 5.7. The Skew-T log-P diagrams indicate the temperature and moisture profiles of the atmosphere at 12 UTC as a spatial-average of the target domains. As an example the subdomains of IP and FR are presented whereby in both regions the wet initial scenarios cause a colder and more humid troposphere up to a height-level of 700 hPa. The dry initial scenarios lead to a warmer and drier troposphere up to 700 hPa pressure level. Comparing the region of IP and FR all simulations show higher temperatures in the IP and a different strength in the modification signal. In the subdomain of the IP the WET-scenario leads to a stronger decrease in the temperature profile and a stronger increase in the dew point profile compared to the FR subdomain. On the other hand, the DRY-scenario in the FR domain causes a stronger increase in the temperature profile curve and a reduction in the humidity profile compared to the IP domain.

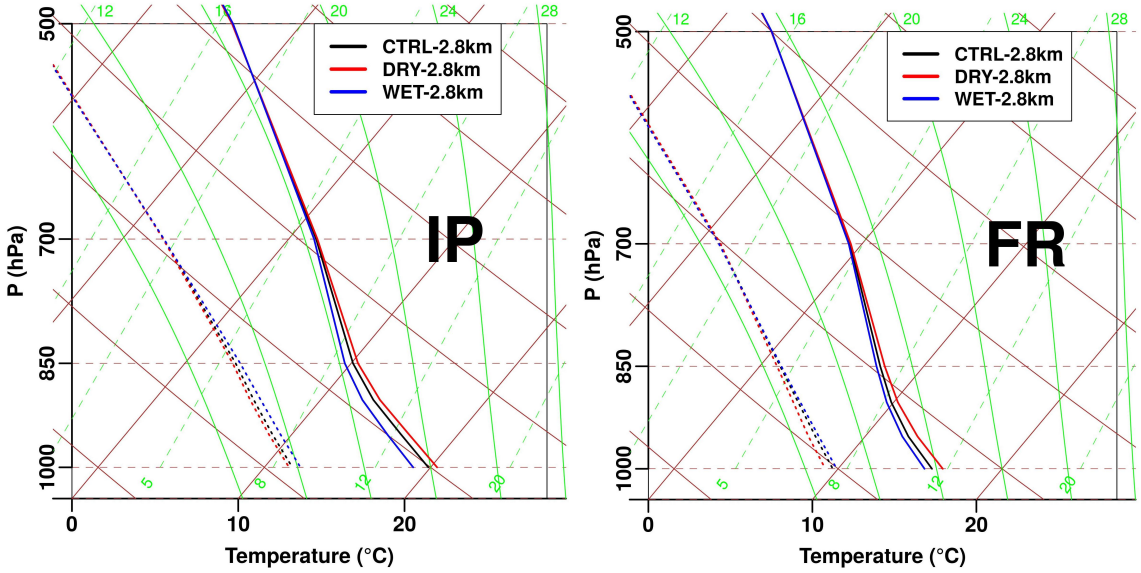

Figure 5.7.: Skew-T log-P diagrams of the atmospheric profile for the seasonal mean conditions of SON 2012 at 12 UTC. The CTRL profile (black) and both DRY (red) and WET (blue) scenarios are shown for the subdomains of IP and FR. The solid lines indicate the temperature profile [°C] and the dotted lines the dew point temperature [°C].

5.4. Soil Moisture-Precipitation Feedback

In the previous section, seasonal soil moisture-atmosphere interactions were found in the WMed due to the SM sensitivity experiment. This section addresses the question whether these SM-atmosphere interactions cause a precipitation feedback and which sign such a SM-precipitation feedback has. Sec. 5.4.1 proves the influence of SM initialisation on the mean seasonal precipitation. Additionally the relation of the SM-precipitation feedback to the model resolution is investigated. The changes in frequency and intensity of extreme precipitation due to wet and dry SM scenarios are considered in Sec. 5.4.2.

5.4.1. SM-Precipitation Feedback on a Seasonal Scale

Fig. 5.8 shows the seasonal accumulated precipitation in the WMed and the percentage changes of this seasonal precipitation both for the two WET- and DRY-scenarios for the COSMO CLM-7km and the COSMO CLM-2.8km model resolution. As discussed in Sec. 5.1, there is a strong north-south gradient in the seasonal mean distribution of precipitation in the WMed with dry conditions in semi-arid regions in the south and wet conditions in the north. When comparing the model resolution between convection-parametrised resolution (∼7 km) and convection-permitting resolution (∼2.8 km), similar seasonal spatial-average rainfall amounts are found which cover all land and sea grid points (Tab. 5.3). Differences are identified in the comparison of spatial distribution and between sea and land (Fig. 5.8, Tab. 5.3).

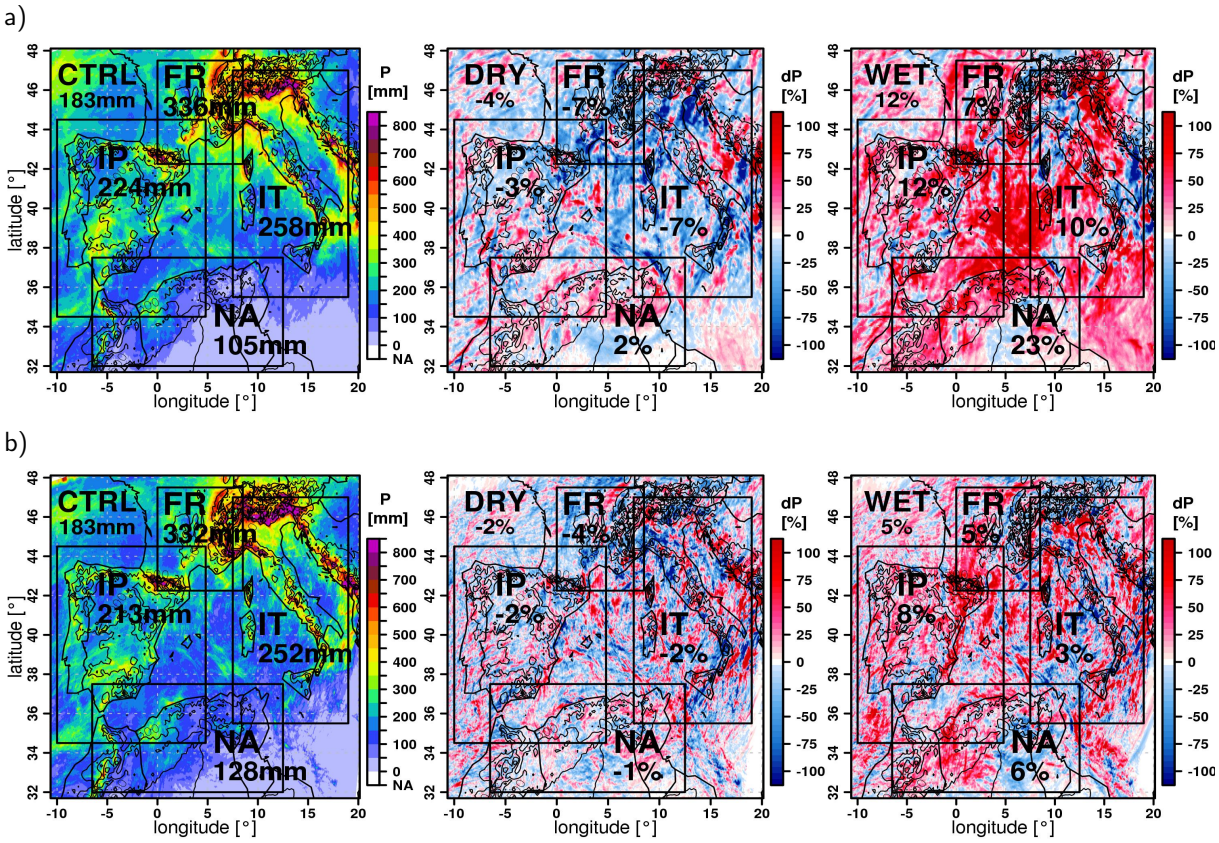

Figure 5.8.: Seasonal mean precipitation in SON 2012 and percentage changes in seasonal mean precipitation between DRY- and WET-scenario minus CTRL. In a) the SM-precipitation feedback is illustrated for COSMO CLM-7km simulation and in b) of COSMO CLM-2.8km. Black boxes indicate the target areas with the spatial-average values of these subdomains.

Relevant changes in the higher resolution of COSMO CLM-2.8km simulation compared to COSMO CLM-7km are the higher number of grid points which better represent the topography and patchiness of precipitation fields (Fig. 5.8). In the spatial fields of seasonally accumulated precipitation in COSMO CLM-2.8km the maxima of precipitation over complex terrain over land are improved. In the COSMO CLM-7km the coastal areas in upstream direction are more affected by strong precipitation (e.g. coast of Corsica, south side of the Alps, Apennines, west side of Italy and east cost of the Adriatic Sea). Furthermore, in North Africa more precipitation is simulated in the COSMO CLM-2.8km (+25 %). If only land grid points are considered, the COSMO CLM-2.8km simulation always shows higher seasonal spatial-average precipitation amounts than COSMO CLM-7km simulation (Tab. 5.3). Semi-arid regions are most strongly affected as convective precipitation occurs predominantly in these regions (cf. τ calculation in Fig. 5.2 and Khodayar et al. (2016a)).

In the WET-scenario the seasonal mean precipitation is increased between +5 % and +15 % in the WMed depending on the model resolution or considering land and/or sea grid points (Tab. 5.3). At the regional scale this SM-atmosphere feedback effect is more pronounced. In the semi-arid region of the WET-scenario the seasonal mean precipitation increase is between +5 % and +25 %. In the DRY-scenario the

seasonal decrease in mean precipitation is up to -5 % in the whole WMed. The regional effect is more pronounced with about -5 % to -10 % in the moderately humid region of FR and IT. In all subdomains SM-precipitation feedback is positive in the sense that more/less soil moisture leads to more/less precipitation (feedback loop of Fig. 2.4). The positive SM-precipitation feedback is stronger over land but also sea areas are affected. Changes in precipitation over the sea are also seen with the same sign in the feedback (Fig. 5.8 and Tab. 5.3).

Table 5.3.: Seasonal accumulated precipitation [mm] and seasonal mean changes in precipitation of the WET- and DRY-scenarios [%] in the different model resolutions. For the entire WMed and the four subdomains a distinction is made between land+sea (All) and only land grid points for the autumn season 2012.

Model run	WMed	NA	IP	FR	IT
CTRL-2.8km All	185 mm	130 mm	225 mm	330 mm	250 mm
CTRL7-km All	185 mm	105 mm	215 mm	335 mm	260 mm
CTRL-2.8km Land	200 mm	130 mm	240 mm	350 mm	355 mm
CTRL-7km Land	180 mm	100 mm	240 mm	340 mm	315 mm
WET-2.8km All	+5%	+6%	+8%	+5%	+3%
WET-7km All	+12%	+23%	+12%	+7%	+10%
WET-2.8km Land	+4%	+6%	+8%	+4%	+2%
WET-7km Land	+9%	+22%	+10%	+7%	+7%
DRY-2.8km All	-2%	-1%	-2%	-4%	-2%
DRY-7km All	-4%	+2%	-3%	-7%	-7%
DRY-2.8km Land	-2%	-1%	-2%	-4%	-2%
DRY-7km Land	-3%	+3%	-3%	-6%	-4%

The box plots in Fig. 5.9 show the distribution of seasonal changes of accumulated precipitation in each grid point of the respective subdomain. In every regional domain the SM-precipitation feedback is positive in both model resolutions. The WET-scenarios of both model resolutions indicate that in the subdomains FR, IP and NA more than 50 % of the data show a positive increase in precipitation. The positive feedback is most pronounced in the FR and the IP region. The whiskers in these regions reveal positive and negative changes due to possible shifts in the location of precipitation between different grid points but even the most extreme changes show the same sign as the SM perturbation. This is not the case for the IT subdomain. In this subdomain, the feedback of seasonal mean precipitation in the interquartile range (IQR) is positive for the sensitivity experiment, whereas the most extreme modification indicates a negative feedback. In these single HPEs, for instance drier soil moisture initial conditions modify the atmospheric conditions (e.g. changes in mesoscale circulation, vigorous thermals) that favour stronger precipitation. A more detailed analysis of the extremes in SON 2012 can be found in the following section.

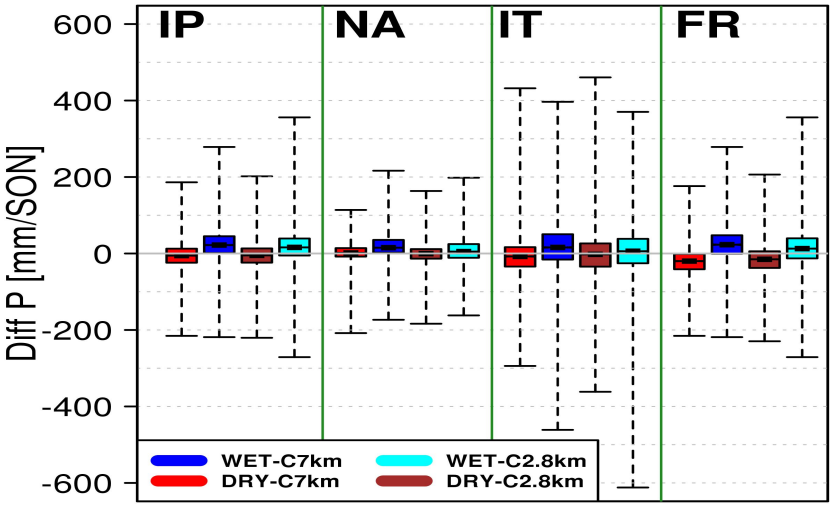

Figure 5.9.: The box plots represent the distribution of changes in the accumulated precipitation of all grid points in the respective subdomain of the WET- and DRY-scenarios in autumn 2012. A comparison between both model resolutions is illustrated. The whiskers show the total distribution of modifications in the precipitation sums.

5.4.2. Impact on the Modelling of Extreme Precipitation

The WMed reveals a positive seasonal mean precipitation SM feedback to the SM sensitivity experiment in autumn, but locally a high variability was found in the changes of seasonal accumulated precipitation (Fig. 5.9). Reasons could be that new HPEs developed or disappeared, that already existing HPEs are strengthened/weakened or that HPEs shift their location. To gain a better insight into these processes, this section examines sensitivity of extreme precipitation to dry and wet initial SM conditions. The probability density functions (PDFs) of the precipitation intensities for different subdomains and the model resolution in comparison to satellite-derived CMORPH are shown in Fig. 5.10. Hourly grid-point precipitation from COSMO-CLM output and CMORPH data are used. Only precipitation events with more than 0.42 mm/hour are counted. The highest frequency and intensity of extreme precipitation events is again observed in the Italian subdomain. Differences in extreme precipitation events appear between the model resolutions, the WET- and DRY-scenarios and between the subdomains. For all subdomains, the frequency of HPEs of the CTRL COSMO CLM-2.8km simulation corresponds better with the observation of CMORPH than these of the CTRL COSMO CLM-7km simulation. However, the highest intensities per hour are not observed in CMORPH observations. In this context, previous studies have demonstrated an underestimation of high precipitation intensities of CMORPH in the WMed (e.g. in Stampoulis et al. (2013)).

In the semi-arid regions of the IP and NA, both SM initial scenarios induce stronger hourly extreme precipitation intensities in the COSMO CLM-2.8km simulations, whereas the frequency of intensities is lower in the subdomains FR and IT. With the exception of the subdomain IT, dry initialisation leads to the most extreme hourly intensities of precipitation in the COSMO CLM-2.8km simulations. In the FR

domain the highest intensities in the COSMO CLM-7km simulations are caused by the WET-scenario whereas in the IP and NA regions the dry scenario indicates higher intensities in this model resolution. The CTRL simulation of the COSMO CLM-2.8km shows the highest intensity and frequency in the IT subdomain.

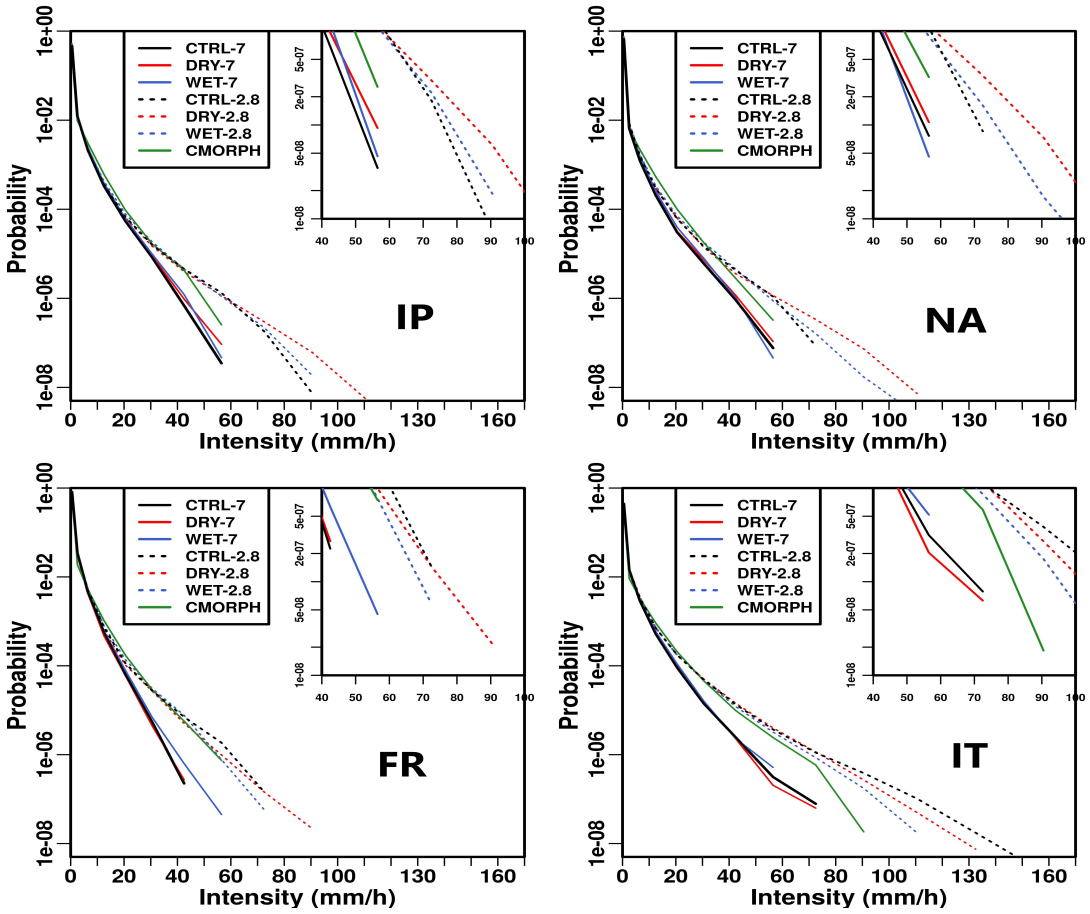

Figure 5.10.: Probability density functions (PDFs) of the hourly precipitation intensities [mm/h] of CMORPH observations, CTRL and the both extreme SM initial scenarios for each subdomain for the SON period 2012. The COSMO CLM-7km simulations are indicated by solid lines and the COSMO CLM-2.8km simulation by dotted lines. The green solid lines represent CMORPH observations. Only land grid points of the target areas are considered. The box in the upper right corner shows a zoom of extreme precipitation between 40 and 100 mm/h.

Tab. 5.4 shows the change in the number of days with precipitation (wet days (RR1)) and the change in the number of days with extreme precipitation. The latter are divided in different categories. The highest frequency of wet days is observed in the FR subdomain with 65 % and the lowest frequency of such days in the NA subdomain with 35 %. In the wet initial scenario of the COSMO CLM-2.8km simulation the number of RR1 in all subdomains increases by 5-10 %. In the dry initial scenario the number of RR1 does not change except for the IT subdomain (-5 %). In the semi-arid regions of NA and IP the number of precipitation days in the DRY-scenario is reduced by up to -25 % compared to the CTRL simulation in the categories of extreme precipitation days between 10 mm up to 150 mm. The reduction in each single precipitation classification varies between -3 % and -25 %. Some of these days with HPEs disappear and

other days become more intense such as days with precipitation between 150 and 200 mm, which occur twice as frequently in the NA subdomain (Tab. 5.4).

Table 5.4.: The number of wet days and the different categories of extreme precipitation days are shown for the CTRL and the WET- and DRY-scenarios of the COSMO CLM-2.8km simulations in the different subdomains. The total number of days is 91 in the autumn period 2012. Wet days (RR1) are days with a spatial-average precipitation amount >1 mm in the subdomain. The days with extreme precipitation are counted if at least one land grid point reaches this daily sum value in the subdomains. An increase in the number of days in the WET- and DRY-scenarios is indicated by green colours and a decrease by red to brown colours.

C2.8km	RR1 >1mm	Days 10-50mm	Days 50-100mm	Days 100-150mm	Days 150-200mm	Days 200-300mm	Days > 300mm
NA-CTRL	**33**	**81**	**49**	**16**	**2**	**1**	**1**
NA-DRY	**33**	**77**	**47**	**12**	**5**	**1**	**1**
NA-WET	**35**	**83**	**51**	**17**	**5**	**1**	**0**
IP-CTRL	**47**	**82**	**59**	**24**	**10**	**4**	**1**
IP-DRY	**47**	**80**	**56**	**24**	**12**	**4**	**1**
IP-WET	**50**	**84**	**64**	**34**	**11**	**6**	**1**
IT-CTRL	**53**	**83**	**63**	**43**	**25**	**17**	**5**
IT-DRY	**51**	**82**	**61**	**44**	**27**	**13**	**3**
IT-WET	**53**	**83**	**65**	**44**	**27**	**16**	**3**
FR-CTRL	**57**	**78**	**42**	**12**	**12**	**4**	**0**
FR-DRY	**57**	**77**	**44**	**13**	**13**	**5**	**0**
FR-WET	**59**	**78**	**46**	**11**	**11**	**6**	**1**

In the semi-arid regions the WET-scenario increases the extreme precipitation days in all categories. The strongest effect is seen in the IP domain where for instance days with extreme daily precipitation of 100 mm to 150 mm show an increase of +10 days (+40 %). For days with extreme precipitation between 200 mm and 300 mm two more days are added (+50 %). In the IT subdomain in both initial scenarios the days with the most extreme events are reduced (>200 mm). In the DRY-scenario the days with precipitation between 10 mm and 100 mm are also reduced. It seems that the most extreme events in this subdomain are weakened by the change of soil moisture conditions, while the days with precipitation between 100 and 200 mm increase in both scenarios. In the WET-scenario the same number of days with intensive precipitation events (>200 mm) is reduced by exactly the same amount as it increases on days with precipitation between 100 mm and 200 mm. The opposite effect occurs in the WET-scenario in the FR subdomain, here the moderate extreme events are intensified. In this region the DRY-scenario leads to an increase in the intensity and frequency of extreme precipitation events in the range of days between 50 mm and 200 mm. Recent studies by Tramblay and Somot (2018) and Drobinski et al. (2018) showed in future projections an increase in intensity and frequency of extreme precipitation in the drier conditions in this FR subdomain. Hereby the increase in evaporation of the Mediterranean Sea, following the Clausius-Clapeyron relation, is the primary source of moisture which counteracts the

drying effect. Nevertheless, in this thesis the detected sensitivity of extreme precipitation to drier soil moisture conditions in moderately humid regions may be an important source of instability, which may trigger more extreme precipitation events under future drier conditions in the Western Mediterranean.

The changes of certain HPEs within the SOP1 period to the sensitivity experiment are presented in Fig. 5.11. The influence of soil moisture initialisation on the temporal development of precipitation and the calculation of τ is shown as an example for various locations of HyMeX target areas in the WMed. The figures give an idea which HPEs are influenced by the WET and DRY initial SM scenarios in terms of the synoptic forcing. Most IOPs of HyMeX are affected by the WET- and DRY-scenarios.

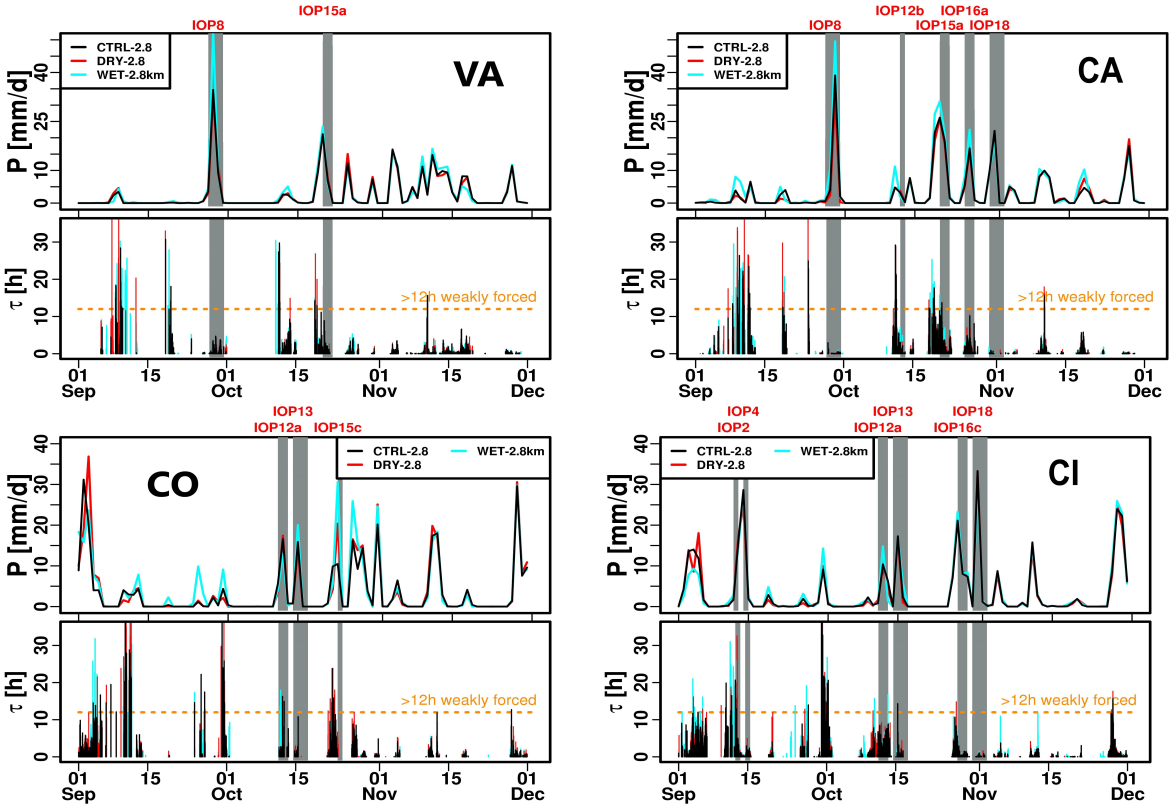

Figure 5.11.: The figures illustrate the changes of the temporal evolution of the spatial-average precipitation of the SM sensitivity experiment (top) for the HyMeX target areas Valencia (VA), Catalonia (CA), Corsica (CO) and Central Italy (CI). At the bottom the changes in the calculation of τ in the WET- and DRY-scenario are shown. The threshold of 12 h distinguishes between weak and strong synoptic flow regimes. The intense observation periods (IOPs) of HPEs in this region are indicated by grey-shadowed colours.

Especially, in the IOP8 in the target areas Valencia (VA) and Catalonia (CA), the maximum precipitation in the WET-scenario is increased even if this case was forced by a large-scale synoptic conditions. The period before the IOP8 was identified in the subdomains IP and NA with EDI as a dry period (Fig. 5.2), which could make this period prone to SM-atmosphere interactions. Central Italy (CI) and Corsica (CO) also show impacts on HPEs in the DRY-scenario. Most of the modified events are associated with high τ values, indicating a weak synoptic influence (Chap. 4.3). The sensitivity of precipitation modification to SM initialisation lasts until the end of the simulation period.

5.5. Discussion and Conclusions

Dependency of SM-precipitation feedback on the spatial model resolution

The validation of the seasonal COSMO CTRL simulations with observations from rain gauges and CMORPH data derived from satellites shows good agreement in intensity of HPEs and in the time of occurrence. Differences in seasonal rainfall sums between both model resolutions are presented in Fig. 5.12 for the autumn season 2012. The convection-permitting simulation resolution increases the precipitation over mountain tops and coastal areas of the IP as well as over North African land. The convection-parametrised simulation reveals high precipitation amounts on the Italian west coast and the islands of Corsica and Sardinia in the south-west upstream flow direction. The comparison between rain gauges and both model resolutions indicates an improvement of the accumulated precipitation in the convection-permitting simulation (Tab. 5.5). The mean deviation of all rain gauge stations in autumn 2012 is improved by 50 % (-2 mm) and the RMSE by about 10 %. The RMSE is high with a value of 120 mm and indicates a high variability of the prediction errors. The result of such a grid-point to grid-point verification must be carefully considered due to the "double penalty problem" (Wernli et al., 2009). In this problem, an incorrectly predicted position of precipitation can lead to poor results even if intensity, size and timing are correct. Nevertheless, the comparison should show a tendency of under- or

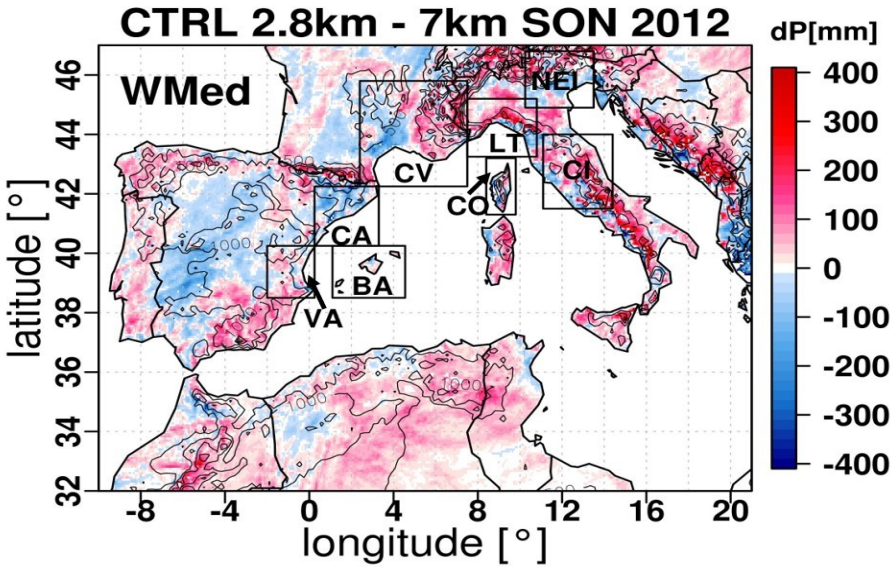

Figure 5.12.: Differences in seasonal accumulated precipitation between COSMO CLM-2.8km minus COSMO CLM-7km CTRL simulations over land in SON 2012. For comparison, the COSMO CLM-2.8km model resolution is upscaled to the model resolution of COSMO CLM-7km. The HyMeX target areas are marked by boxes.

overestimation of the simulations compared to the rain gauge measurements. The differences of the seasonal accumulated precipitation amounts between single rain gauge stations to the next grid point in the COSMO-CLM simulations are shown in App. B.3. A high variability of deviations between the simulated precipitation amounts and the observations of rain gauge stations is observed for the different

investigation domains and the individual measuring stations (Tab. 5.5). The representation of precipitation in the HyMeX target areas along the Spanish and Italian coast is improved in COSMO CLM-2.8km in comparison to COSMO CLM-7km by up to 50 % on average and the root-mean-square error (RMSE) is reduced in the CA domain. In the semi-arid NA subdomain the simulated seasonal mean precipitation is about +25 % higher in the COSMO CLM-2.8km than in the COSMO CLM-7km simulation in SON 2012. In this region the validation with the available rain gauges also indicates an underestimation of the precipitation in both simulation resolutions and a better result in the COSMO CLM-2.8km simulation. In the convection-permitting simulation a higher frequency and intensity of precipitation on a sub-daily time scale is found which is underestimated or missing in the convection-parametrised simulation (Fig. 5.3 and Fig. 5.10). Such high intensity rainfall amounts are observed in autumn 2012 for example in the IOP8 with 200 mm precipitation within 4 hours in Murcia (Khodayar et al., 2016b) or in central Italy in the IOP12 with 150 mm within 6 hours (Khodayar et al., 2018).

Table 5.5.: Differences in seasonal accumulated precipitation amounts between convection-permitting (C2.8km) and convection-parametrised (C.7km) model resolution in validation with rain gauge observations in the different areas of investigations. Only rain gauge stations with daily accumulated precipitation during the entire period of SON 2012 are selected. The nearest grid point of the model simulation to a rain gauge station is used to calculate the differences in the mean value of all stations within an investigation domain and the RMSE between COSMO model resolutions and rain gauges. n is the number of available rain gauge stations.

Domain	n gauges	C2.8km mean	C7km mean	C2.8km RMSE	C7km RMSE
WMed	4367	-2 mm	-4 mm	120 mm	130 mm
NA	22	-23 mm	-25 mm	55 mm	65 mm
IP	784	+25 mm	+38 mm	110 mm	120 mm
IT	1439	-46 mm	-45 mm	160 mm	180 mm
FR	2208	+45 mm	+39 mm	105 mm	95 mm
VA	24	-12 mm	-17 mm	110 mm	120 mm
CA	29	+34 mm	+64 mm	80 mm	130 mm
CO	83	-88 mm	+76 mm	130 mm	230 mm
LT	165	+3 mm	-50 mm	170 mm	180 mm
CI	189	-116 mm	-116 mm	180 mm	200 mm
NEI	42	-15 mm	-80 mm	120 mm	170 mm
CV	969	+53 mm	+38 mm	115 mm	105 mm

The SM experiment with wet and dry initial soil moisture conditions leads to a positive SM-atmosphere coupling in the WMed in both resolutions (Fig. 5.6, App. B.4). A different initial status of SM induces a modification in surface heat fluxes, moisture and instability within the planetary boundary layer and the development of moist convection. The increase/decrease in moist convection and low cloud cover leads to a positive seasonal mean SM-precipitation feedback in both model resolutions. The wet initial SM conditions lead to an increase in seasonal mean precipitation of up to +25 % in semi-arid subdomains and the dry initial SM conditions result in a decrease in seasonal mean precipitation of up to -10 % in moderate humid subdomains. The strength in feedback is stronger in convection-parametrised

simulations. In this regard the seasonal mean in the different atmospheric variables in the WMed and its regional subdomains shows no noticeable differences between the model resolutions (Tab. B.1 and App. B.1). However, the IWV in the atmosphere is higher and the temperature and humidity stratification is more strongly changed up to a height of 700 hPa in the COSMO CLM-7km resolution (Fig. 5.7 and App. B.2). Furthermore, the impact on large-scale conditions in the convection-parametrised resolution is significantly stronger which is indicated by a stronger modification in the geopotential height at 500 hPa (z500) (App. B.1). These stronger features can be caused by the Tiedtke parameterisation scheme as shown in previous investigations by Hohenegger et al. (2009). Moreover, it is known that convective parameterization schemes are a source of errors and uncertainties (e.g. Prein et al. (2015)). On the contrary, in convection-permitting simulations the extreme precipitation is more sensitive to initial SM conditions and leads to stronger changes than in the convection-parametrised simulations (Fig. 5.10). In addition, COSMO CLM-2.8km simulates more wet days and days with extreme precipitation (Fig. 5.10 and App. B.2). In the semi-arid regions wet SM initialisation leads to an increase in the number of days with extreme precipitation in both model resolutions. In dry initialisation the COSMO CLM-7km simulation in the FR subdomain reduces the number of days with moderate extreme events and increases the number of days with the most extreme precipitation events. In contrast, the number of days with extreme precipitation in all categories increases during dry SM initialisation in the convection-permitting model simulation.

General conclusions to research questions (part 1): relevance of SM-atmosphere interactions for the development and occurrence of weather extremes in the WMed

- Initial SM sensitivity studies modify atmospheric conditions in autumn 2012. The wet initial scenario leads to an increase in near-surface humidity by about +10 %, in CAPE by +30 % and +20 % in low cloud cover.
- The found SM-atmosphere interactions in the WMed always induce a positive seasonal mean feedback in both initial SM scenarios as well as in both spatial model resolutions.
- Wet SM initial conditions increase the mean precipitation by up to +25 % in semi-arid regions and the dry SM conditions decrease the mean precipitation by up to -10 % in moderately humid regions.
- The impact of initial SM conditions on extreme precipitation varies and depends on the regional conditions. Extremely wet SM initialisation leads to more frequent and intense daily precipitation in semi-arid regions whereas extreme dry initialisation causes higher hourly precipitation and an increase of extreme precipitation in moderately humid regions.
- Convection-permitting simulations improve the representation of hourly extreme precipitation intensities, the location of the precipitation and the seasonal mean precipitation in semi-arid areas.

6. Impact of Realistic SM Initialisation on Modelling of Heavy Precipitation Events

In the following, the findings from Chap. 5 are now used for the selection of the HPEs. The research question to be answered is whether a better representation of the model initial SM field derived from the satellite measurement improves the modelling of heavy precipitation. Therefore, the impact of realistic SM initialisation on atmospheric conditions leading to HPEs is examined in high-resolution COSMO simulations. A novel 1 km downscaled SMOS-L4 3.0 surface soil moisture (SSM) product is used for this investigation. However, this product only provides SM measurements at a soil depth of up to 5 cm but the COSMO model requires SM information also in deeper soil layers for the initialisation. For this purpose a strategy is introduced in Sec. 6.1 which describes the development of a daily, bias-corrected SMOS-L4 SM profile product. Sec. 6.2 presents the application of this SMOS initialisation for several HPEs in autumn 2012. Furthermore, SM-atmosphere interactions and feedbacks are investigated in a case study. The benefit of a realistic SM initialisation is discussed in Sec. 6.3.

6.1. Strategy for the Preparation of the 1 km-SMOS Product for Model Initialisation

The realistic initialisation of COSMO with the original SMOS-L4 3.0 SSM data from BEC is not possible because the required SMOS-L4 is not available daily and has no information about the SM profile for model initialisation. In addition, the use of satellite-derived information in the model requires a bias correction in order to avoid systematic differences between both data sources. This section describes the development of a strategy for obtaining a daily bias-corrected SM profile product from SMOS-L4 3.0 SSM data that can be applied for realistic SM initialisation. For the WMed, the new SMOS-L4 3.0 SSM data are only available for the Iberian Peninsula (IP) and southern France (Fig. 3.5). Satellite-derived and modelled SM data of one year are required for the bias-correction (Reichle and Koster, 2004). The period from Dec 1, 2011 to Dec 31, 2012 is considered. This year includes the hydrological year 2012 and the HyMeX SOP1 period. SMOS data are available once a day as a descending (L4-D1) and as an ascending (L4-A1) product. Three ground-based in situ networks for the validation of model and satellite-derived SM exist in the investigation domain. The location of the networks and every single station is shown in Fig. 3.5. To compare the different data sets, the nearest grid point of SMOS and COSMO data are chosen for the corresponding ground-based station.

6.1.1. Data Quality and Selection Criteria

The first step is the selection of a SMOS-L4 product that has the highest agreement with the ground-based observations. Besides the SMOS L4-A1 and SMOS L4-D1 products a third merged product was created as the mean of both (L4-M1). The Taylor diagrams in Fig. 6.1 graphically summarise the statistical metrics between the SMOS-L4 products and in-situ measurements of the three networks. The standard deviation, the Pearson correlation R and the unbiased RMSD for the annual mean of 2012 show that for this data set the L4-D1 always has the best agreement with ground-based observations. The L4-D1 RMSD of the REMEDHUS and VAS network is 0.03 m^3/m^3 (cRMSD= 0.02 m^3/m^3) and thus within the desired target accuracy of SMOS (Tab. 6.1). Furthermore, a high agreement index and R with a value of more than 0.8 indicate a good representation of the L4-D1 SSM in these two networks. In the SMOSMANIA network all metrics reveal lower values for all SMOS-L4 products but the L4-D1 still shows the best results. The difference between RMSD (0.07 m^3/m^3) and cRMSD (0.04 m^3/m^3) indicates a systematic dry bias in this network. To sum up, it can be said that the SMOS descending product provides the best agreement with in-situ observations. This conclusion was also found by Piles et al. (2015, 2016). For this reason, the L4-D1 product is selected for the realistic initialisation with SMOS data. A further comparison with ground-based observation in Fig. 6.1d always shows a wet bias in the SSM of the COSMO-2.8km simulation (C2.8km). This bias of COSMO can also be seen in the differences between cRMSD (0.02 m^3/m^3) and RMSD (>0.05 m^3/m^3). A high correlation R >0.9 and low cRMSD indicate a good representation of SSM variability of the model. Contrary to the SMOS-L4 products the C2.8km SM performs best in the SMOSMANIA network, where the climate is moderately wetter than in the other two networks.

Table 6.1.: Comparison of the original SMOS-L4 SSM ascending (L4-A1), descending (L4-D1) product and the merged product of both (L4-M1) with in-situ measurement of the three networks REMEDHUS (REM), SMOSMANIA (SMO) and VAS at a soil depth of 5 cm.

Product	RSMD [m^3/m^3]	cRSMD [m^3/m^3]	AI [0;1]	R [-1;1]
REM L4-A1	0.03	0.03	0.90	0.84
REM L4-D1	0.03	0.02	0.90	0.86
REM L4-M1	0.04	0.04	0.90	0.83
VAS L4-A1	0.04	0.02	0.75	0.78
VAS L4-D1	0.03	0.02	0.87	0.80
VAS L4-M1	0.05	0.04	0.79	0.75
SMO L4-A1	0.10	0.04	0.53	0.64
SMO L4-D1	0.07	0.04	0.59	0.66
SMO L4-M1	0.11	0.04	0.55	0.67

The next step is to prove the data availability of the daily descending product. The selected daily swath product has available data on 385 of 397 days (97 %) but only 179 days (74 days) cover 50 % (75 %) of the investigation domain (Fig. 3.5), as the polar orbiting revisiting time is about 3 days (Kerr et al., 2012). The aim is to create a product for initialisation on a daily basis, therefore the running mean

is derived from that of the current day and the previous day (abbreviated as L4 D2-50%). This two-day running mean increases the days covering 50 % (75 %) of the investigation domain to 382 days (263 days). Consequently, the quality criterion is defined in this way: more than 50 % of the investigation domain of the L4-D2 have to be covered by SMOS data.

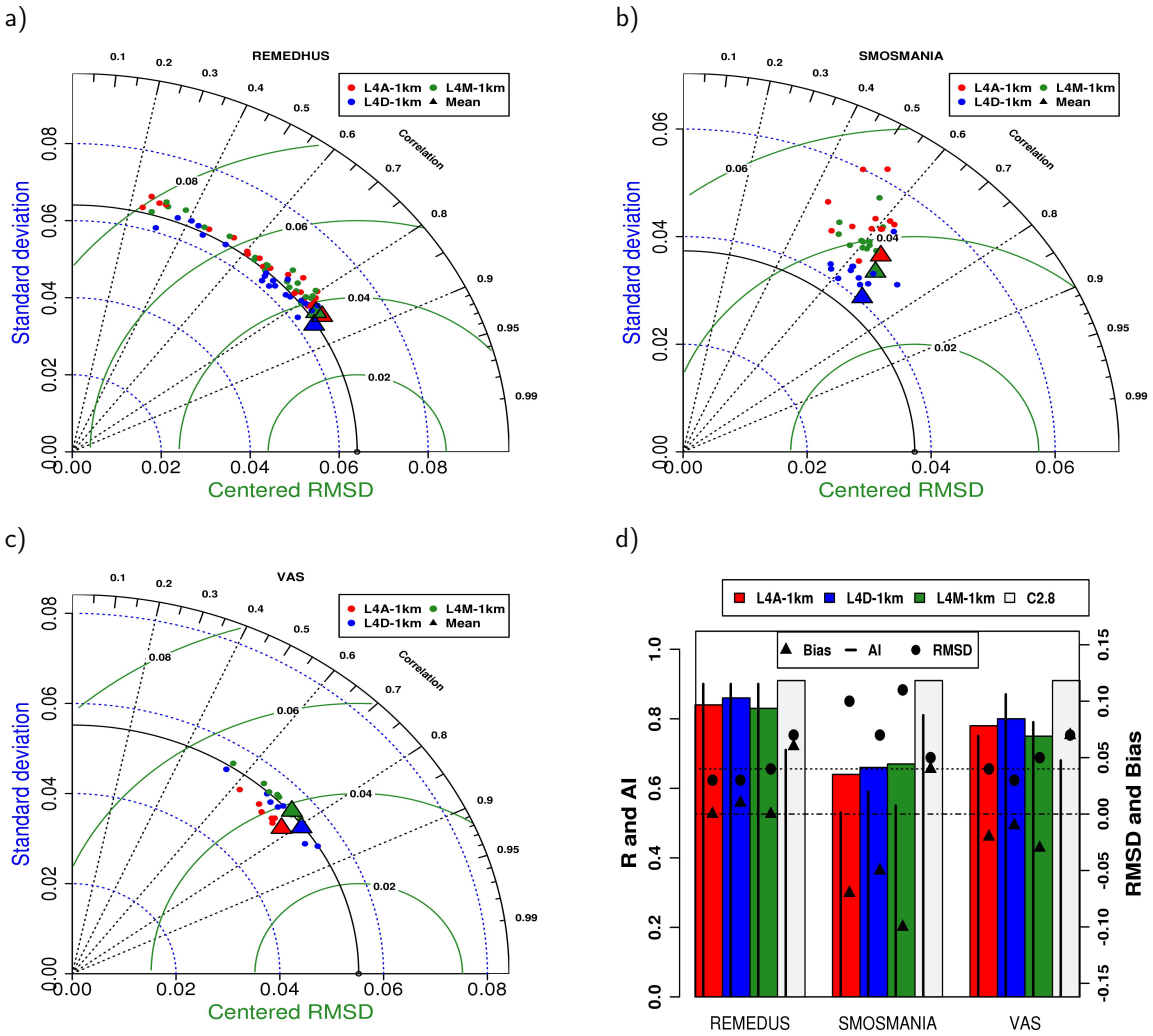

Figure 6.1.: Taylor diagrams of the three 1 km swath products compared to the in-situ measurement of the a) REMEDHUS, b) SMOSMANIA, c) VAS in situ network. Diagram d) shows the correlation (R), the agreement index (AI), the bias and the RMSD of the three swath product and COSMO-2.8km simulation with SM ground measurement of the three in-situ networks. The dotted line indicates the desired target accuracy of SMOS of 0.04 m^3/m^3.

Finally, the remaining grid points in the simulation domain that have missing values are interpolated using the inverse distance weighting method with the 4 nearest neighbours of available data (Ford and Quiring, 2014). The newly created product is named hereafter L4-D2 and provides daily SSM data for the whole investigation domain. An example for Sep 6, 2012 in Fig. 6.2a-c illustrates the improvement in data availability of the L4-D2 compared to the L4-D1 product.

6.1.2. Bias Correction with CDF-Matching

Every soil moisture data set has its own statistical characteristics such as specific mean value, variability and dynamical range (Drusch, 2005). Therefore, systematic differences between model and satellite data can arise due to the model specific soil moisture climatology which results from the model-specific wilting point and the field capacity definitions. Further systematic differences could be caused by different thickness of modelled and measured soil layers. The cumulative density function (CDF)-matching scaling technique is a method to remove these systematic differences between satellite-based and modelled soil moisture. The basic idea introduced by Reichle and Koster (2004) is the conversion ("scale") of the satellite-derived SSM into land surface model consistent SSM. This scaling is done by the following equation:

$$cdf_m(x') = cdf_s(x) \tag{6.1}$$

where cdf_s and cdf_m are the CDFs of the satellite and model soil moisture, respectively, and x and x' are the original and transformed satellite data. For the application of this method the CDFs of both data sets have to be ranked.

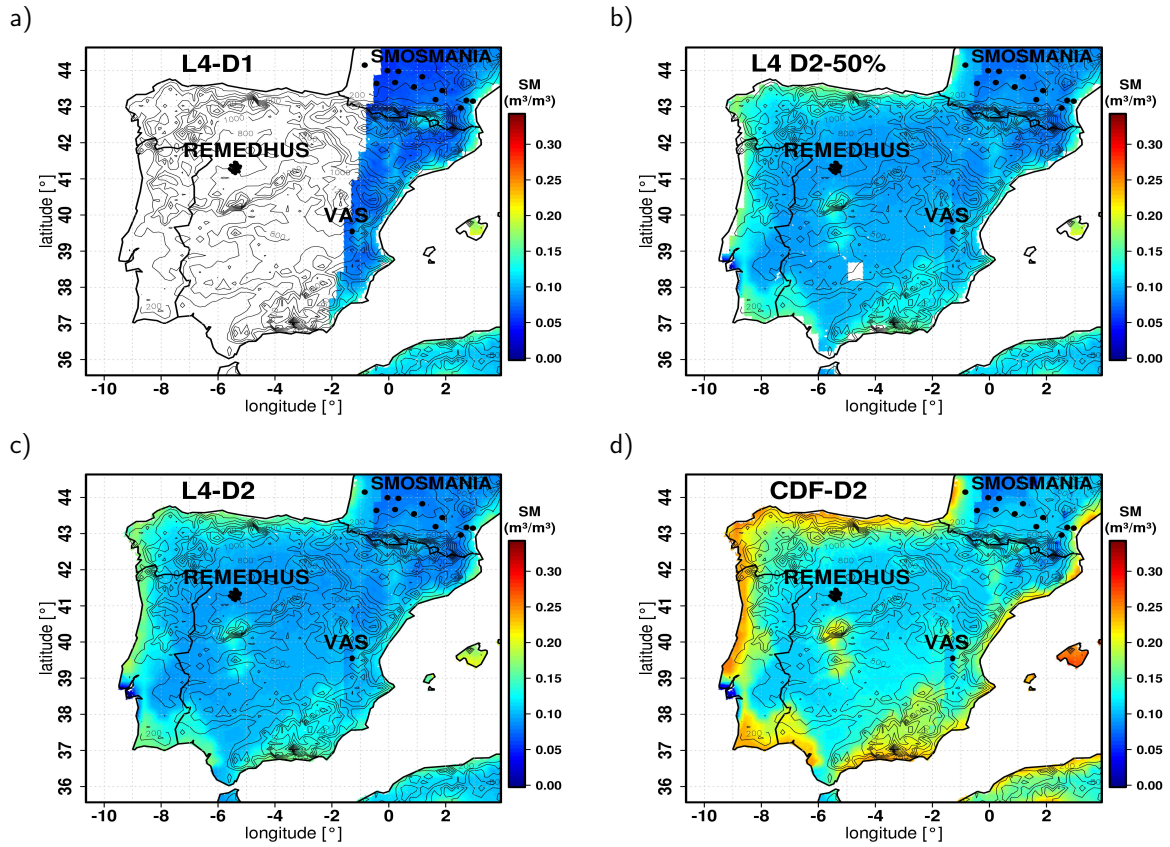

Figure 6.2.: Example for the processing steps of the SMOS-L4 descending product on Sep 6, 2012. The figures show in a) the original 1 km SMOS-L4 product (L4-D1), in b) the two-day running mean of the current and the previous day (L4 D2-50%), in c) the additional missing value interpolation product (L4-D2) and in d) the product with applied bias correction of the CDF-matching.

The differences in SM between the corresponding elements of each ranked data set have to be computed. In order to obtain CDF-corrected SM these differences are adjusted to the modelled data using a fitting function (Brocca et al., 2011) as shown in Fig. 6.3b. CDF-matching avoids the necessity of long satellite data records. Reichle and Koster (2004) concluded that a one-year data record is sufficient to apply the CDF-technique. This application of bias correction ensures that new data records like data from SMOS can be used for initialisation/assimilation of SM in models.

Figure 6.3a shows lower SSM values in the L4-D2 product than for the COSMO-2.8km SM at a soil depth of approximately 5 cm. This selected layer is the maximum soil depth that can be measured by satellite-derived SMOS measurements. Both data sets represent the annual cycle of SSM with low SSM values in summer and high SSM values in winter. In the autumn period, a rapid increase in SSM can be seen in modelled and remotely observed data. The SSM variability in SMOS data is higher, partly due to data gaps in the satellite observations. Especially in the beginning of September such data are missing. The application of the CDF-matching for the year 2012 corrects the mean systematic bias and increases the AI from 0.72 to 0.9 between both data sets.

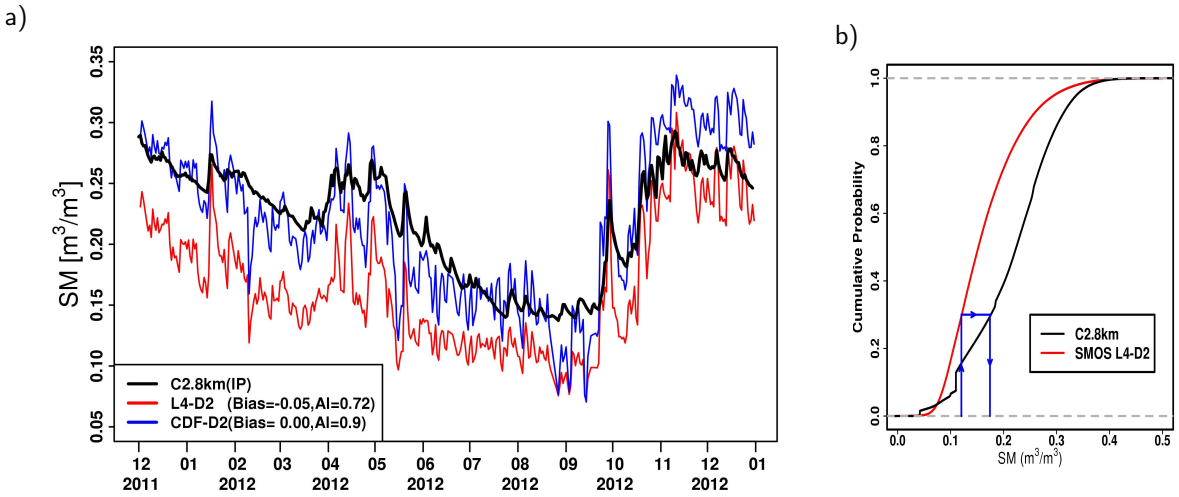

Figure 6.3.: a) Temporal evolution of the spatial-mean near-surface SM (5 cm) for the Iberian Peninsula (IP). The black line shows the COSMO-2.8km SSM (C2.8km), the red line the SMOS L4-D2 SSM product (L4-D2) and the blue line the bias-corrected L4-CDF SSM product (CDF-D2). b) CDFs of L4-D2 (red) and C2.8km (black) are illustrated for the period from Dec 1, 2011 to Dec 31, 2012 for all grid points in the IP-domain. The blue lines with arrows illustrate how L4-D2 data is transferred to a scaled data set.

In contrast to literature the CDF-matching is not only considered for one grid point but for all grid points in the investigation domain. The reason for this choice is that the single grid point (SGP) makes a wet-biased COSMO model representation even wetter as illustrated in Fig. 6.4a-b,e. On the other hand, applying CDF-matching for all grid points (AGP), as shown in Fig. 6.4c-d,f maintains the representation of satellite-observation and increases the SSM of the L4-D2 product (Fig. 6.2c-d). The comparison of the scatter-plots in the SMOSMANIA network reveals that SGP CDF-matching deteriorates the RMSD from 0.08 m^3/m^3 (C2.8km run) to 0.1 m^3/m^3, whereas the AGP approach improves the SSM representa-

tion of the RMSD of 0.06 m^3/m^3. The advantage of using the AGP CDF-matching is also valid for the two other observation networks and it is confirmed for several tested days in 2012.

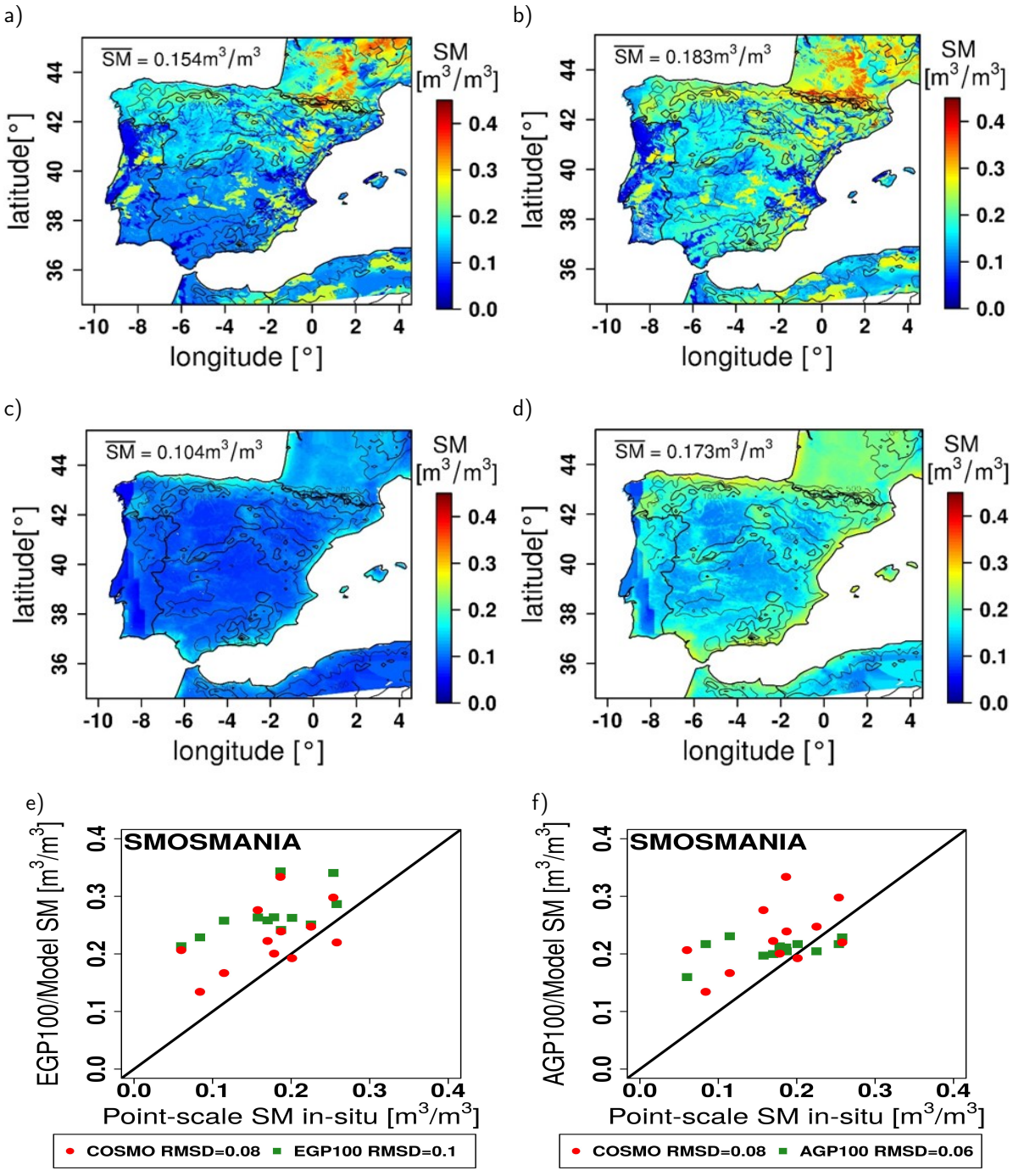

Figure 6.4.: Example for the spatial SSM representation at a soil depth of 5 cm for a) the COSMO-2.8km SSM, b) the SSM after CDF-matching of the single grid point (SGP) approach and e) the validation of the EGP product with SMOSMANIA in-situ stations. In the sub-figures the SSM in c) of the L4-D2 product, d) of the CDF-matching with all grid points (AGP) in the investigation domain and f) the validation with SMOSMANIA observations for the AGP approach is shown.

Furthermore, the AGP CDF-matching improves the SSM representation compared to the original COSMO-2.8km SSM (abbreviated: CDF-D2). Figure 6.5a demonstrates the better accordance of the CDF-D2 for all 38 ground-based observation stations in the year 2012. The new bias corrected product coincides with the temporal development of the in-situ observations. The validation reveals that both the dry bias of the L4-D2 (-0.02 m^3/m^3) as well as the wet bias of the C2.8km (0.05 m^3/m^3) have improved to 0.01 m^3/m^3 (Tab. 6.2). The CDF-D2 product reduces 50 % of the error of the COSMO-2.8km model to 0.03 m^3/m^3, which also proves the highest AI with 0.91.

Fig. 6.5b shows the SSM distribution in the Box-Whisker-Plots for all in-situ observations. The AGP CDF-matching approach increases the SSM variability which is revealed in the higher interquartile range (IQR) of 0.12 m^3/m^3 in the CDF-D2 product compared to 0.08 m^3/m^3 of in situ observations. The same applies for a higher standard deviation of 0.07 m^3/m^3 compared to the L4-D2 and the C2.8km SSM products (both 0.05 m^3m^3). Nevertheless, the CDF-D2 includes the complete range of SSM values of the observations which are not represented by the C2.8km simulation.

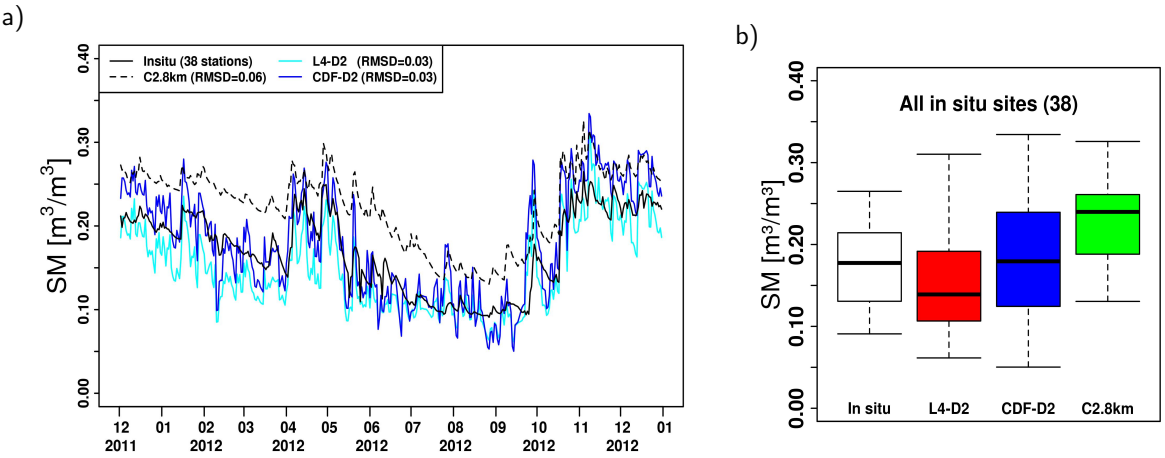

Figure 6.5.: Validation of both L4-D2 products before and after CDF-matching (CDF-D2) with in situ observation for the corresponding 38 stations of the three ground-based networks. a) Temporal evolution of spatial average SSM of L4-D2 (cyan), CDF-D2 (blue), COSMO2.8km (black dashed) and in situ (black solid). b) Box-Whisker-Plots of the SSM distribution. The box borders show the 25-, 50-(black line) and the 75%-quartile. The white box presents the ground-based observation, the red box the the L4-D2 product, the blue box the CDF-D2 product and the green boy the C2.8km modelled data.

Regarding the differences between the distinct SM networks it can be seen that the original L4-D2 product shows the best results for the VAS and REMEDHUS networks (RMSD of 0.04 m^3/m^3, AI of 0.9) and worse results for the SMOSMANIA network (RMSD of 0.1 m^3/m^3 and AI of 0.58). As discussed before the C2.8km SSM performs well for the SMOSMANIA network (RSMD of 0.04 m^3/m^3, AI of 0.81) and worse in the VAS and REMEDHUS networks (RMSD >0.06 m^3/m^3 and AI <0.69). The obtained findings indicate that SSM has a wet bias in C2.8km simulation, especially in semi-arid regions, whereas the product derived from SMOS-L4 3.0 SSM performs well in semi-arid regions but shows dry bias in more moderately wet climate regions.

Table 6.2.: Statistics of the validation between different ground-based observation networks with the SMOS L4-D2 product before (L4-D2) and after bias correction (CDF-L4) and the presentation of the original COSMO-2.8km SSM (C2.8km).

Network	Std [m^3/m^3]	Bias [m^3/m^3]	RSMD [m^3/m^3]	AI [0;1]	R [-1;1]	IQR [m^3/m^3]
All L4-D2	0.05	-0.02	0.03	0.88	0.85	0.08
All CDF-D2	0.07	0.01	0.03	0.91	0.87	0.12
All C2.8km	0.05	0.05	0.06	0.75	0.95	0.07
REM L4-D2	0.06	0.01	0.04	0.90	0.86	0.11
REM CDF-D2	0.08	0.06	0.07	0.75	0.86	0.16
REM C2.8km	0.05	0.06	0.07	0.72	0.91	0.08
SMO L4-D2	0.04	-0.09	0.10	0.58	0.74	0.06
SMO CDF-D2	0.05	-0.03	0.05	0.81	0.76	0.07
SMO C2.8km	0.04	0.03	0.04	0.85	0.91	0.06
VAS L4-D2	0.05	-0.01	0.04	0.87	0.87	0.09
VAS CDF-D2	0.07	0.03	0.05	0.81	0.81	0.14
VAS C2.8km	0.05	0.07	0.07	0.69	0.69	0.06

The performance of the CDF-D2 product is between these two extremes and improves at least one SSM data source. CDF-D2 reduces or maintains the error (bias) compared to the error (bias) of the original L4-D2 product or the modelled C2.8km. Furthermore, the AI(R) is improved for at least one of the two data sources. As before, the IQR and the standard deviation of the CDF-D2 product always show higher values than for the modelled and the SMOS L4-D2 SSM. In conclusion, the presented CDF-D2 product corrects the systematic bias between modelling and satellite-derived data. In addition, validation with ground-based observations shows an improvement in the SSM representation in the new bias-corrected product.

6.1.3. Calculation of the SMOS SM Profile with an Exponential Filter

The exponential filter from Wagner et al. (1999) is used to estimate the whole SM profile from the bias corrected SSM CDF-D2 product. It is a simple and effective empirical method for estimating the profile of soil moisture from surface soil moisture. The exponential filter is based on an analytically solution for differential equation assuming that the temporal variation of the average values of the soil moisture profile is linearly related to the differences between the surface and the profile values (Brocca et al., 2011). Therefore, the exponential filter smoothes the surface SM signal to deeper soil layers using the fact that deeper SM layers exhibit much smaller variations compared to the near-surface soil moisture. The estimation of the root-zone soil moisture with the exponential filter has been successfully applied for in-situ observations (Albergel et al., 2008), model initialisation (Bisselink et al., 2011) and satellite soil moisture data (Brocca et al., 2011; Ford et al., 2014). The recursive formulation of the exponential filter method (Albergel et al., 2008) used in this study is as follows:

$$SWI_{m(n)} = SWI_{m(n-1)} + K_n(ms(t_n) - SWI_{m(n-1)}) \tag{6.2}$$

SWI is the soil water index and $ms(t_n)$ is the surface soil moisture at time t_n. The gain $K_n[0,1]$ is calculated by:

$$K_n = \frac{K_{n-1}}{K_{n-1} + e^{-\frac{(t_n - t_{n-1})}{T}}} \tag{6.3}$$

Thereby T is the characteristic time scale of soil moisture variation in the unit of days. The filter is initialised with $K_1 = 1$ and $SW_{m(1)} = ms(t_1)$. The parameter T is a proxy which represents all processes affecting the temporal dynamics of soil moisture, such as the thickness of the soil layer, the soil hydraulic properties, evaporation, run-off and the vertical gradient of soil properties (texture, density). In order to find the optimal T (T_{opt}), the exponential filter is tested for different T values for every soil layer depth. The T value with the highest prediction accuracy, indicated by the Nash-Sutcliffe efficiency (NSE, Eq. 4.12) score, is chosen as T_{opt} for the corresponding soil layer. Figure 6.6 represents the determination of the T_{opt} of COSMO-2.8km SM profile for every soil layer. T_{opt} ranges from 1 day in the uppermost soil layer to more than 300 days in the deepest layers.

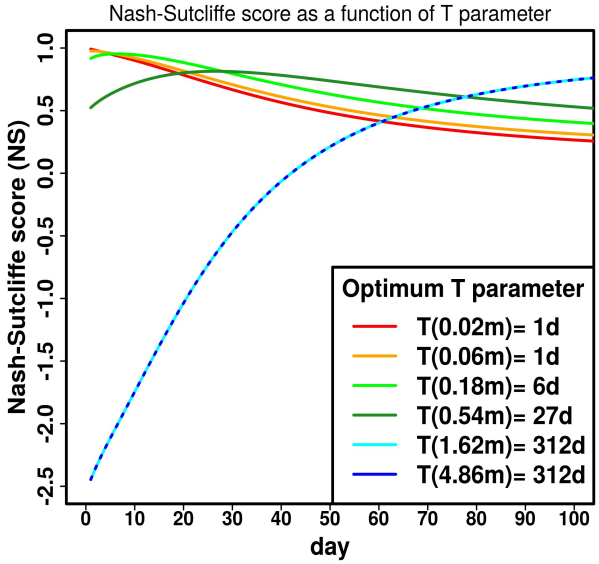

Figure 6.6.: Calculated NSE score for the C2.8km SM profile and corresponding estimated exponential filter T values for every soil layer for the 397 days investigated. T_{opt} is derived as the highest NSE-score for every soil layer.

From these results, it can be concluded that the near-surface COSMO soil layers adapt quickly to soil moisture variation down to a depth of 5 cm on a one-day time scale. Soil layer levels down to a depth of half meter have a SM variation time of about 1 month and deeper soils have a typical time length of about 1 year. These characteristic time scales are used to perform the exponential filter with SSM information of the CDF-D2 product. The SM for the corresponding COSMO soil layer depth is estimated with Eq. 6.2 and the corresponding time scale T. The product created is abbreviated L4-Expo SM.

From the available three ground-based observation networks (Fig. 3.5) only the SMOSMANIA network has measurements in four soil moisture levels of 5-, 10-, 20- and 30 cm. Fig. 6.7 shows an example of

the exponential filter performance for two selected stations, Mouthoumet (MTM) and Condom (CDM), for the year 2012. Considering the depth of 5 cm where the SSM is measured by SMOS, the CDF-D2 product in the MTM station with a RMSD of 0.04 m^3/m^3 performs better than the SSM of C2.8km with a RMSD of 0.06 m^3/m^3. The L4-Expo product improves this SM representation to a RMSD of 0.02 m^3/m^3 (C2.8km=0.07 m^3/m^3). While the daily to monthly SM variability is slightly underestimated, the seasonal and yearly SM variability is more accurate.

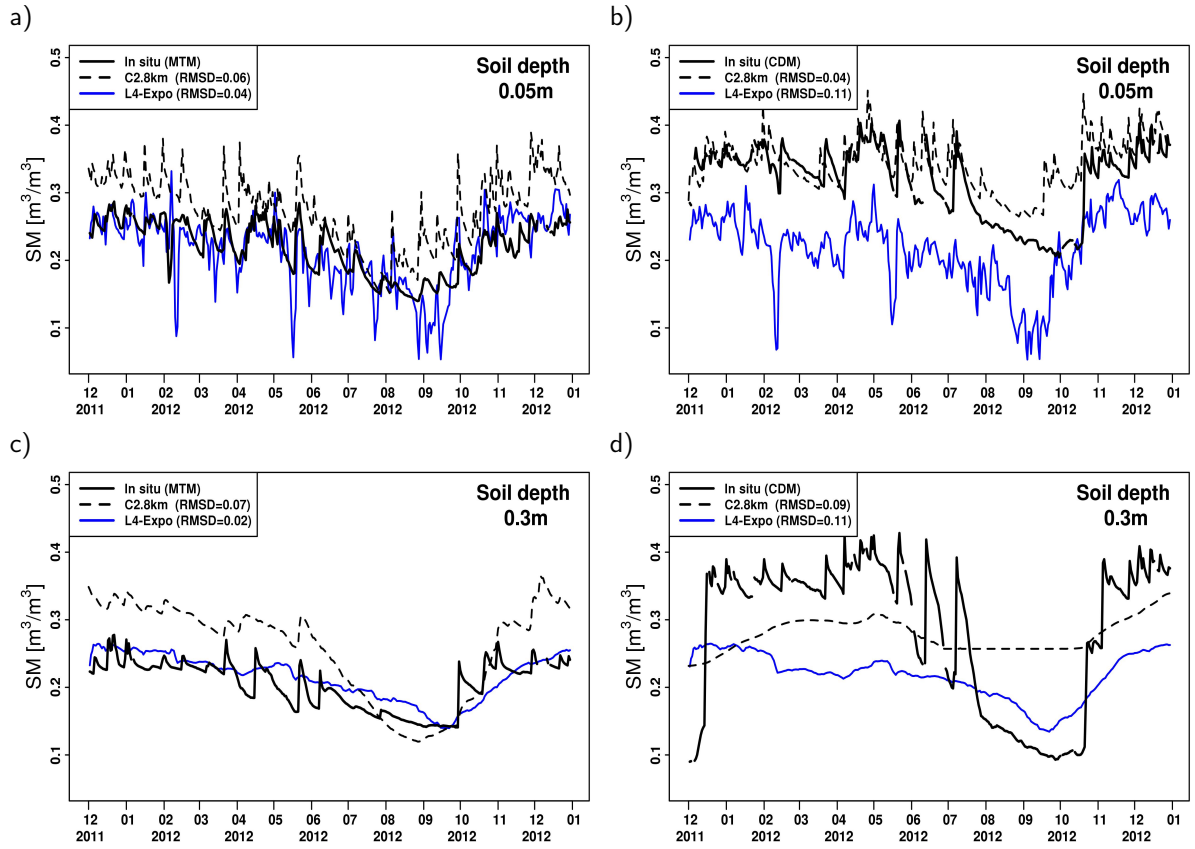

Figure 6.7.: Validation of the SM distribution in the SMOSMANIA stations Mouthoumet (MTM) and Condom (CDM) of the L4-Expo (blue) and C2.8km (black dashed) with ground-based measurements (black solid). Figures a+b show the SM at a depth of 5 cm of the MTM and CDM stations and c+d the SM data at a depth of 30 cm.

The C2.8km SM is too wet from November to June. On the other hand, the CDF-D2 in the CDM station at a depth of 5 cm reveals a too dry representation (RMSD=0.11 m^3/m^3) whereas the C2.8km here performs better (RMSD=0.04 m^3/m^3) (Fig. 6.7c). The underestimation of the CDF-D2 product shown in Fig 6.7d is maintained in L4-Expo SM at a soil depth of 30 cm (RMSD=0.11 m^3/m^3) but in comparison to the upper layer the C2.8km SSM shows a deterioration (RMSD=0.09 m^3/m^3). Especially the seasonal SM variability is poorly represented in the model, whereas the seasonal and yearly variability is well reproduced in the L4-Expo product.

In general, the SM representation varies between the stations because of different soil types, land use and their high variability within a pixel of SMOS or model data. Furthermore, every data source has

its own sources of uncertainty. For example, the comparison between the two stations shows that in the MTM stations the soil type is predominantly sand (42 %), followed by clay (20 %) while in the Condom station clay (49 %) predominates and sand accounts for a smaller proportion (19 %). Land use in CDM is cropland with rain-fed trees and shrubs and in MTM the land use is grassland.

Nevertheless, the L4-Expo product exhibits a good performance (Fig. 6.8) as can be seen from the station-average profile of all stations in the SMOSMANIA network for the autumn period 2012. In order to make the layer structure of ground-based observation comparable with the C2.8km/L4-Expo data, it is assumed that the first three layers up a to soil depth of 6 cm correspond to the in-situ soil moisture measurements at a depth of 5 cm. The model L4-Expo soil level depth up to 18 cm is assigned to SM in-situ measurement at 10 cm. For the fifth model level (up to 54 cm) the corresponding average of 20 cm and 30 cm of the in situ measurements is used. For this time period of SON 2012, the L4-Expo SM profile product is very close to the ground-based observations of SMOSMANIA and corrects the wet bias of the C2.8km simulated SM profile. The error bars depict the standard deviation which varies between 0.08 and 0.09 m^3/m^3 for in situ observation and between 0.02 and 0.07 m^3/m^3 for C2.8km/L4-Expo soil moisture. This indicates a higher SM variability among the single SMOSMANIA stations (as seen in the comparison of MTM and CDM), though the L4-Expo standard deviation in every level is within the standard deviation range of the in-situ measurement.

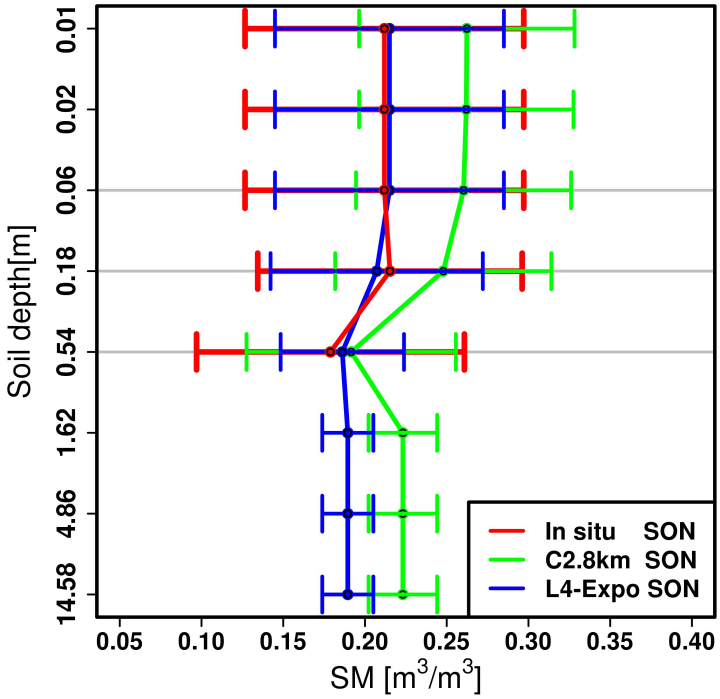

Figure 6.8.: The mean SM profile of SMOSMANIA stations in autumn 2012. The green line shows the profile of COSMO2.8km simulation, the blue line the estimated SM with the exponential filter and the red line the profile of in-situ measured SM. The standard deviations of the ground-based measurements, the SMOS L4-expo product and the C2.8km simulation are indicated by the whiskers in the corresponding colour.

6.2. Model Simulations with SMOS Initialisation

In Sec. 6.1 a daily available, bias corrected SM profile product was created that improves the wet bias between the standard COSMO-2.8km SM profile and the ground-based measurements. In the following, the impact of this realistic soil moisture initialisation on convection processes is proved for various HPEs in the autumn period 2012. Different initialisation times for these events are tested to find the optimal time for realistic SM initialisation. Finally, in a case study the modification of atmospheric conditions leading to a SM-precipitation feedback is analysed.

6.2.1. Effect of SMOS Initialisation on Precipitation Forecast of Four Selected HPEs

HPEs over the IP in autumn 2012

For the season SON 2012 precipitation fields affecting the IP domain are investigated. The knowledge gained in Chap. 5 on heavy precipitation events that are sensitive to initial soil moisture conditions will be taken into account. τ and EDI are used to identify favourable preconditions for SM-atmosphere interactions. The seasonal COSMO CLM-2.8km analysis of the IOPs in the HyMeX target areas VA, BA and CA and the calculation of τ and EDI in autumn 2012 identify the IOP8, IOP12 and IOP15a as suitable events (Fig. 5.11). In addition, the heavy precipitation event on Sep 9, 2012 over the Pyrenees is chosen. All selected events have either dry drought status or/and weak synoptic forcing in their preconditions and they are sensitive to the initial status of soil moisture. The selected events occur in different regions of the IP domain which are marked in Fig. 3.5 by dashed boxes with different acronyms. Maximum daily precipitation reaches sums between 60 mm and more than 200 mm. The first precipitation event on Sep 9, 2012 developed under weak synoptic conditions by orographic lifting in the Pyrenees (PYR) in the late afternoon. IOP8 was initiated by a cut-off low above the IP with ground level convergence leading to deep convection in southern Spain and crossing the Andalusia region (AN) on Sep 28, 2012. Rainfall amounts above 200 mm per day are observed (Röhner et al., 2016; Khodayar et al., 2016b). In the IOP12a a large trough over the Atlantic Ocean induced a south-westerly flow with a low-level convergence zone moving along the eastern Spain coast towards southern France (Khodayar et al., 2018). On Oct 11/12, 2012 a strong convective activity hit the north-eastern Spanish region (CA). Convection was initiated and intensified by a strong increase of atmospheric humidity and the presence of strong instability (Khodayar et al., 2016b). Rain gauges have measured precipitation sums of 75 mm per day on the east coast of Spain. Finally, the IOP15a was initiated by a cut-off low over Gibraltar which was isolated from an elongated trough located near Portugal. This cut-off low propagated towards Catalonia and transported moisture from the tropical North African land region into the WMed (Chazette et al., 2016). On Oct 20, 2012 MCS systems were triggered over Spain, leading to large amount of precipitation from the region around Valencia up to the Pyrenees (VA). Daily accumulated precipitation of more than 100 mm was measured. All four cases encompass a wide range of convective conditions leading to heavy precipitation.

Experiment of SMOS SM initialisation times

The first step of the application of SMOS L4-Expo initialisation in the COSMO model is to find the most promising time of SMOS initialisation related to soil moisture-precipitation coupling. Therefore an ensemble of different initialisation times is developed, ranging from 1 day to 4 days before the HPEs and starting at 00 UTC, 06 UTC and 18 UTC. The time 12 UTC is not chosen because the dependency of SM on the solar radiation is particularly high at this time. A further selection criterion is the exclusion of initial times with a high precipitation amount over the investigation domain or poor SMOS SM data representation. Consequently, 25 initialisation times are considered for the four events (Sep, 5-8; Sep, 25-27; Oct, 8-11; Oct, 16-19) where initial SM is not influenced by precipitation or solar radiation. For every initialisation time, a control simulation (abbreviated: CTRL) and a simulation with the SMOS L4-Exponential filter initialisation (L4-Expo) are performed.

In Fig. 6.9a the modelled precipitation for the initialisation time experiment is verified with the satellite-derived CMORPH precipitation data (Chap. 3.3) using the SAL-method. The mean value of the 25 initialisation times (all events and times) for each SAL-component is determined. Hereby the mean value of the SMOS L4-Expo simulations exhibits an improvement of the A-component of -0.11 compared to -0.23 in the CTRL-simulations. The L-component improves from 0.19 (CTRL) to 0.17 (L4-Expo), whereas the S-component deteriorates slightly from -0.44 (CTRL) to -0.48 (L4-Expo). From these cases it is concluded that the improved representation of SM profile (Fig. 6.8) leads to an improved representation of precipitation. The improved location and amount of precipitation in the realistic SM initialisation could be a result from a better spatial improvement of SMOS SM and the correction of the wet SM bias in the standard model representation.

To find the best initialisation time, the initialisation experiment is divided in two parts. In the first part, different initial days are tested at 00 UTC. Fig. 6.9c illustrates the HPE on Sep 9, 2012 as an example. The temporal evolution reveals an improvement of the simulated precipitation in both runs. SMOS initialised simulations always show better results. The largest sensitivity to improve the precipitation forecast is seen on Sep 6, 2012 (+3 days in advance). In the second part of the experiment, the most sensitive hours for realistic initialisation are tested at 00 UTC, 06 UTC and 18 UTC. Fig. 6.9d shows the results for these three times on Sep 6, 2012. Again the performance in both simulations improves over time and the result in SMOS initialisation is better. Most sensitive is the SMOS initialisation simulation with respect to the CTRL at 00 UTC.

Finally, it can be pointed out that with the SAL analysis the initialisation time of 3 days in advance at 00 UTC is identified as the time in which the SMOS initialisation shows the largest improvement compared to the CTRL simulation. The time-scale of 3 days could be the time period in which remote SM signals are transported at the low-level to contribute to the development of HPEs. Such a time-scale was found by Duffourg and Ducrocq (2011) who stated that a time scale of about 3 days is required for the low-level transport of remote moisture sources feeding HPEs in southeastern France under anticyclonic conditions. The sensitivity to the time 00 UTC may result from the average of the two-day running mean

descending product as a most sensitive time period between both satellite passes at 18 UTC. Fig. 6.9b shows the SAL analysis for the initialisation time where at least one of the SAL-component has improved in all four HPEs.

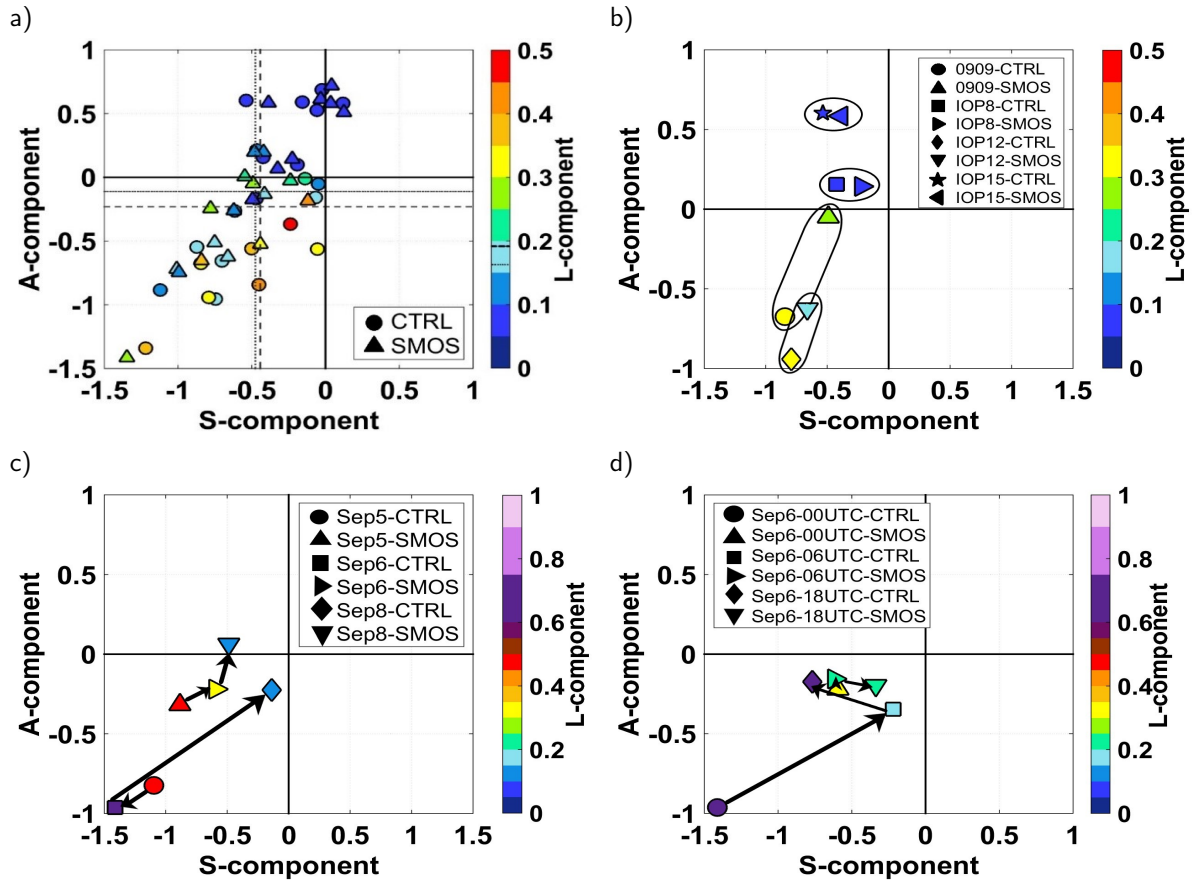

Figure 6.9.: Verification of modelled precipitation with the SAL-method using satellite-derived CMORPH precipitation data as reference a) for all initialisations of the four investigated HPEs between CTRL (circle) and SMOS L4-Expo (triangle). The dotted lines show the mean value of all simulations of the amplitude component A, the structure component S and the location component L for the SMOS simulations. The dashed lines represent the corresponding CTRL components. Figure b) shows SAL results for every IOP initialised 3 days before precipitation at 00 UTC. The CTRL and SMOS pairs of an IOP are indicated by circles. Initial time experiment of the HPE on the Sep 9, 2012 conducted with different c) initial days (at 00 UTC) and d) with different hours on the Sep 6, 2012. The arrows show the temporal evolution of the CTRL and SMOS initialisation.

6.2.2. Case Example: Convective Precipitation Event over the Pyrenees

The convective precipitation event on Sep 9, 2012 is investigated to gain more insights into how realistic initialisation affects atmospheric processes leading to differences in precipitation modelling. This event case reveals the largest improvement between CTRL and SMOS initialised simulation at the four tested HPEs. Figure 6.10 displays the corresponding daily-accumulated precipitation from rain gauges and CMORPH and the simulated COSMO2.8km precipitation fields of the CTRL and SMOS simulation for

the North-East Spain domain (NE-Spain, Fig. 3.5). Both simulations were initialised 3 days in advance on the Sep 6, 2012 at 00 UTC.

a)

b)

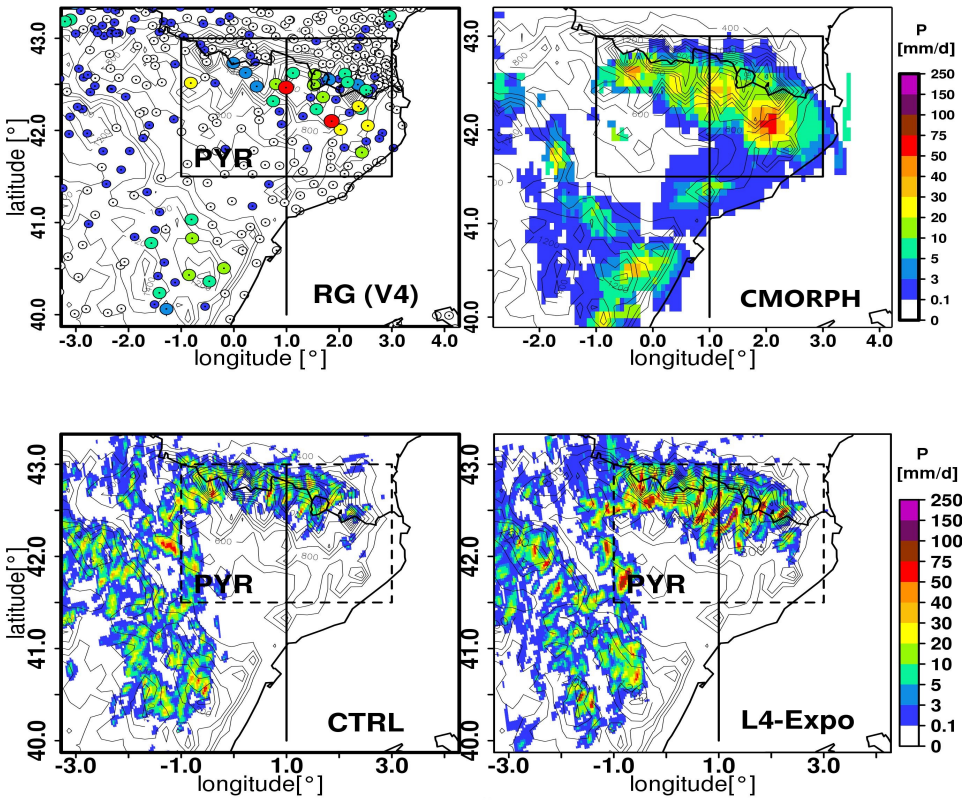

Figure 6.10.: The first row shows the daily accumulated precipitation on Sep 9, 2012 with rain gauges (RG V4) and CMORPH. The simulated daily precipitation of the CTRL and the SMOS L4-Expo initialisation run (L4-Expo) are illustrated in the second row. The target area (PYR) is indicated by a box and the atmospheric cross-section along the latitude of 40° to 43.5°N (longitude 1°E) is represented by a black line.

The Figure 6.11 shows the temporal evolution of domain-average precipitation between rain gauges and the two simulations for the Pyrenees domain (PYR). The timing of the simulated precipitation coincides well with the observations but the amount of precipitation differs. The first larger amount of precipitation occurs in the afternoon of Sep 8, 2012. The predicted maximum is too early and too weak in both simulations, although it is better predicted in the SMOS L4-Expo initialisation. The simulated precipitation maximum on Sep 9, 2012 shows the right timing in CTRL but it is too weak again. The L4-Expo simulation captures the amount of precipitation at 14 UTC well and overestimates a second smaller peak in the late afternoon around 18 UTC. Furthermore, an ensemble of all simulations of the initialisation time experiment for this HPE was created. The ensemble covers 7 initialisation times between Sep 5, 2012 00 UTC and Sep 8, 2012 18 UTC for CTRL and L4-Expo respectively. Fig. 6.9c-d demonstrate an improvement in the forecast in the temporal progress, nevertheless the ensemble spread shown in Fig. 6.11 cannot represent the timing and amount of the first maximum on Sep 8, 2012 . The second maximum

on Sep 9, 2012 is included in both simulations by the spread of the ensemble. Similar to the initialised SMOS run on Sep 6, 2012 at 00 UTC, the SMOS ensemble shows an improved correspondence with observations with regard to the amount and the timing of precipitation compared to the CTRL ensemble. In summary, this precipitation analysis reveals that the SMOS L4-expo initialisation enhances spatial and temporal representation of the amount of precipitation.

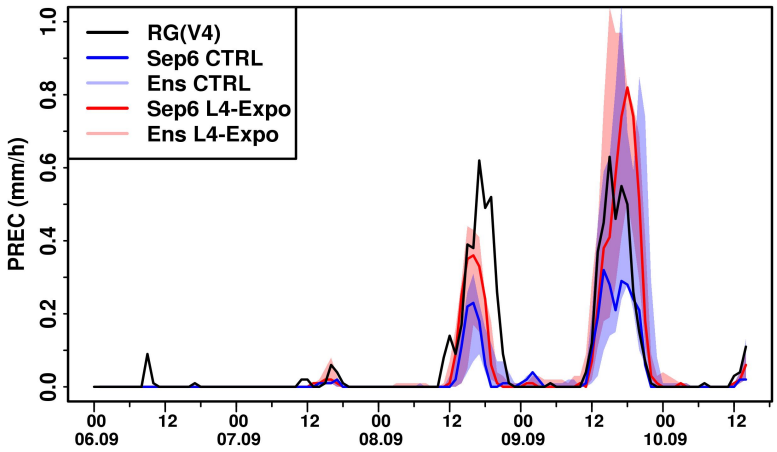

Figure 6.11.: Temporal evolution of domain-averaged precipitation in the PYR region (Fig. 6.10). The domain-average of all rain gauge stations is shown by the solid black line (RG V4), the control COSMO2.8km simulation by the blue line (Sep 6, 2012 CTRL) and the simulation with SMOS-L4-Expo initialisation by the red line (Sep 6, 2012 L4-Expo). The red and blue shaded areas indicate the ensemble of different initialisation times for the L4-Expo (Ens L4-Expo) and CTRL (Ens CTRL).

Soil moisture-atmosphere interactions

In a further step the change in the soil moisture-atmosphere coupling on different spatial scales is investigated to analyse these differences in precipitation representation (Fig. 6.10b). Tab. 6.3 describes the spatial-averaged differences between the L4-Expo minus CTRL simulations in different SM-levels and atmospheric variables as time average from Sep 6, 2012 to Sep 9, 2012. Initialisation with high-resolution SMOS data leads to a mean reduction of SM in the upper soil levels in the IP domain of approx. -10 %. Above the Pyrenees (see Fig. 6.12a) a generally strong mean decline in SM at soil depths of up to 54 cm can be observed but also positive SM patches can be found in inland and coastal areas.

On the regional scale of the IP domain (see Fig. 3.5) the reduction of SM causes a mean decrease in evapotranspiration (ET) and latent heat flux (LHFL) of about -25 %. This reduces the specific humidity in 2 m and the humidity in the lower atmosphere up to 800 hPa (Fig. 6.12b). On the other hand, the mean decrease of SM and moisture at the surface leads to an increase of the sensible heat flux (SHFL) by more than 25 % which raises the temperature in 2 m (T2m) by +0.3 K and the height of planetary boundary layer (HPBL) by about 10 %. Accordingly, the reduction of surface pressure (Fig. 6.12d) and the increase of the geopotential height at 500 hPa (z500) (not shown) point to a stronger development of a thermal heat low in the inland and in the mountains. In addition, Fig. 6.12 also illustrates the SSM anomalous heterogeneity that causes the anomalous heterogeneity of SHFL and QS2m.

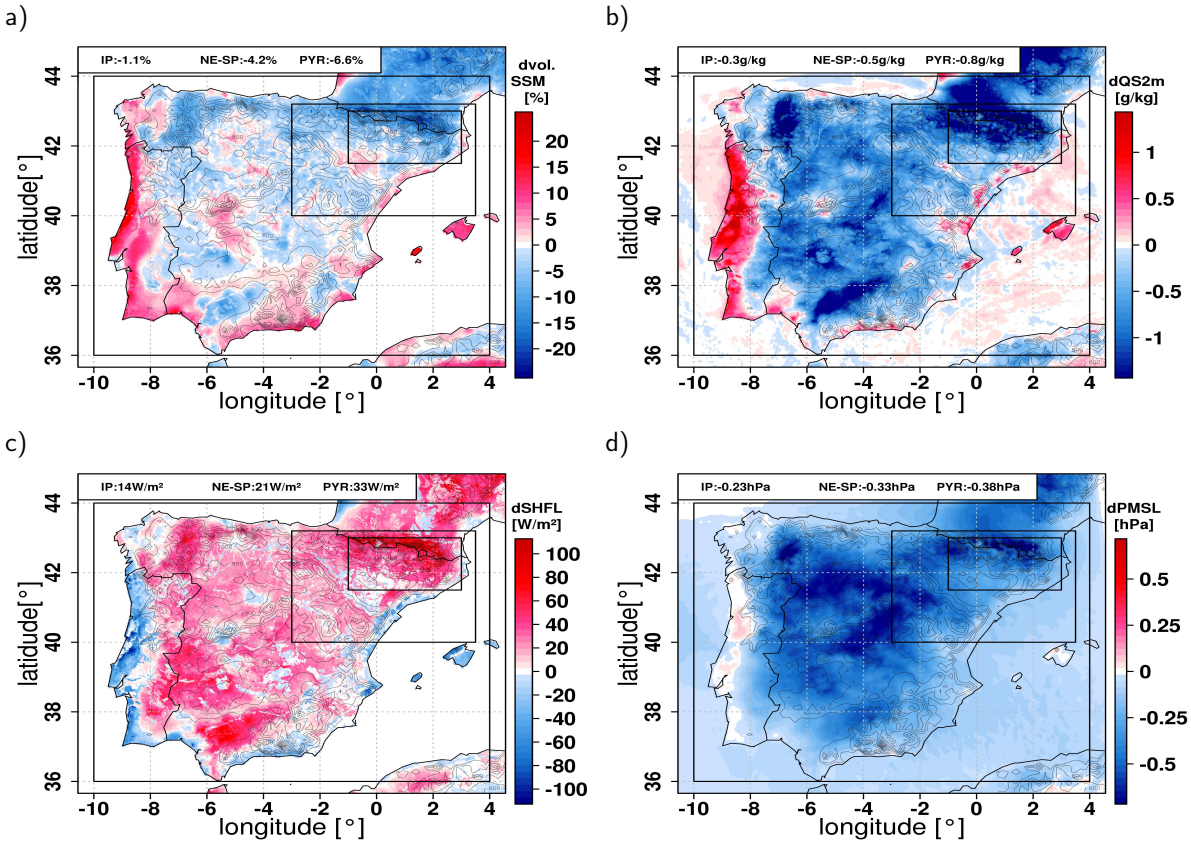

Figure 6.12.: Differences between SMOS L4-Expo minus CTRL simulations for the time average from Sep 6 to Sep 9, 2012. Absolute changes of a) SSM at a soil depth of 5 cm [vol.%], of b) specific humidity in 2 m (QS2m) [g/kg], c) of sensible heat flux (SHFL)[W/m^2] and of d) pressure at mean sea level (PMSL) [hPa]. The spatial mean value for this period in the different target areas IP, NE-Spain and PRY is displayed in the upper legend.

Looking at the hourly change of humidity and wind fields in different atmospheric levels starting from the initialisation on Sep 6, 2012, it can be seen that this thermal low induces a stronger thermal wind circulation during the day. At the same time positive SM anomaly fields lead to an increase in local humidity due to a higher LHFL (Fig. 6.12b). The additional local moisture propagates with the wind circulation towards the inland and forms moisture convergence lines. Positive local moisture anomalies on the coast are also transported to the sea with the land-sea wind circulation and change the atmospheric conditions there. Thus, positive and negative anomalies in the humidity over the sea can also be detected. In particular, the Mediterranean Sea between the Balearic Islands and Catalonia is affected by a positive low-level moisture convergence and a higher atmospheric instability due to higher CAPE values. The advection of convergence lines and additional moisture from the sea as well as locally higher instability lead to a mean increase of the total cloud cover (TCC) of about +5 %. This increase in the TCC is attributed to an increase in middle (+15 %) and high (+10 %) clouds (Tab. 6.3). In summary, it can be said that SMOS initialisation leads to an average reduction of SM and to a higher SM heterogeneity which causes various feedback mechanisms. The mesoscale wind circulations are modified by the development of stronger thermal heat over the mountains and inland of the Iberian Peninsula.

Table 6.3.: Differences in the spatial average between SMOS fields minus CTRL simulation fields for the period from Sep 6 to Sep 9, 2012 00 UTC. The percentage change is the difference between SMOS minus CTRL simulation divided by the spatial average of the CTRL simulation for the period of three days. The different investigation domains from regional to local scale are considered: Iberian Peninsula (IP), North-East Spain (NE-Spain) and the Pyrenees (PYR).

Variable/domain	IP	NE-Spain	PYR
SM5cm	-10%	-25%	-35%
SM18cm	-10%	-30%	-35%
SM54cm	-10%	-30%	-40%
Evapotranspiration (ET)	-25%	-45%	-70%
Latent heat flux(LHFL)	-25%	-45%	-70%
Net radiation surface (Rn)	-3%	-4%	-6%
Specific humidity 2m (QS2m)	-3%	-4%	-8%
Specific humidity 950hPa	-2%	-4%	-7%
Specific humidity 850hPa	-3%	-5%	-7%
Specific humidity 700hPa	+1%	+1%	+2%
CAPE	-5%	-10%	-20%
Integrated water vapour (IWV)	-0.4%	0%	-0.1%
Sensible heat flux (SHFL)	+25%	+45%	+90%
Temperature 2m (T2m)	+1%	+2%	+4%
Height Boundary layer (HPBL)	+10%	+15%	+20%
Total cloud cover	+5%	+10%	+10%
Low clouds	0%	-15%	-20%
Middle clouds	+15%	+30%	+65%
High clouds	+10%	+5%	+10%
Precipitation	+5%	+40%	+120%
Surface pressure	-0.2hPa	-0.3hPa	-0.4hPa
Geopotential height 500hPa	0.5gpm	0.6gpm	0.5gpm

At the local scale of the Pyrenees (PYR) where the main precipitation peak was observed, SM-atmosphere coupling is stronger than at the regional scale of the IP domain. The spatial and temporal average of the SM up to 54 cm is reduced by -40 % (Tab. 6.3). The four times higher soil moisture change in PYR could result from a too wet modelled SM over humid regions in the Pyrenees or from errors in satellite-derived microwave measurements over mountain terrain. Both effects are known problems. The SM modification reduces the mean LHFL by -70 %, the QS2m by -10 % and the mean CAPE by -20% (Tab. 6.3). Less surface moisture and higher SHFL (+90 %) in the SMOS initialisation again increase the mean value of T2m by about +1 K and the HPBL by about +20 % which causes a stronger development of a heat low in the Pyrenees (surface pressure: -0.4 hPa). The higher total cloud cover (+10 %) as well as a larger precipitation amount (+100 %) over the PYR-domain indicates a negative SM-precipitation feedback in the L4-Expo simulation.

In the following, the temporal evolution of atmospheric conditions and the spatial variability of the investigated fields is studied to explain possible differences in the trigger mechanism leading to a better representation of the precipitation peak in the SMOS initialised simulation (Fig. 6.10). Figure 6.13 shows the hourly temporal evolution of the spatial-averaged precipitation, the surface soil moisture in 5 cm, CAPE and the specific humidity in different atmospheric pressure levels. The initial reduction of near-

surface SM (5 cm) in the SMOS simulation remains for the entire simulation time but the differences are reduced after each precipitation event. After a few hours the mean value of the specific moisture in the lower troposphere is already reduced in the SMOS simulation. The opposite effect occurs in the upper tropospheric levels (> 700 hPa) where the SMOS run is more humid than the CTRL because more moisture is advected from the southern part of the IP where positive SM patches have been observed (Fig. 6.12).

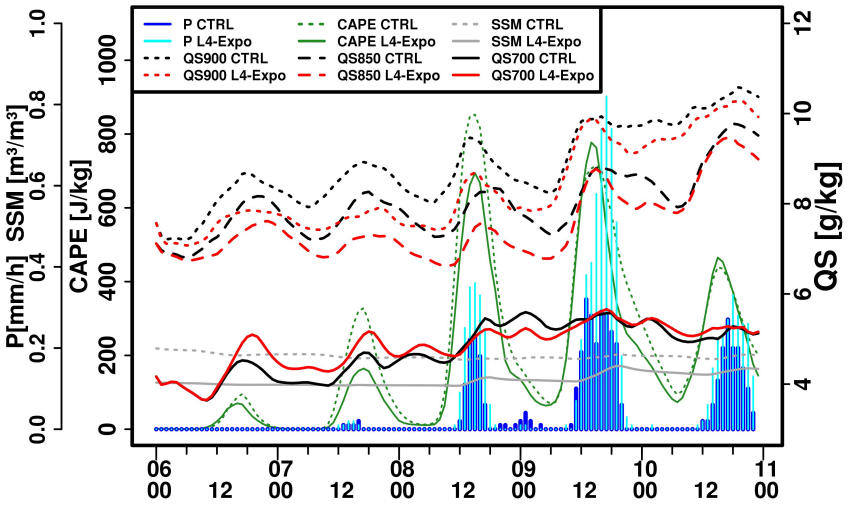

Figure 6.13.: Time series show hourly, spatially averaged surface soil moisture (SSM), precipitation (P), CAPE and specific moisture (QS) at different atmospheric levels averaged for the PYR domain.

One day after initialisation, differences in CAPE appear between both simulations because higher moisture values lead to more instability at lower level in the CTRL simulation. In addition, the general atmospheric conditions in the CTRL run change between the initialisation day and Sep 9, 2012. The surface pressure decreases from 1021 hPa to 1017 hPa, the mean humidity increases from 7 g/kg to 10 g/kg at low level (Fig. 6.13) and the atmosphere becomes more unstable (mean CAPE Sep 9 at 12 UTC >700 J/kg). In the afternoon of Sep 8 and Sep 9, 2012 both simulations show precipitation, whereby the SMOS initialisation exhibits higher hourly precipitation rates. In Fig. 6.13 it can be seen that in the preconditions of the precipitation maximum of the L4-Expo simulation the moisture in the lower troposphere levels rises faster than in the CTRL. This low-level moisture anomaly of the SMOS simulation originates from coastal areas and the sea and is transported to the southern flanks of the Pyrenees in the morning hours with a stronger sea breeze and valley wind (see Fig. 6.14b). In the southern foothills of the Pyrenees moisture converges with higher surface moisture (Fig. 6.14a) and results in near-surface moisture differences of about 2 g/kg. At the same time the low-level humidity in the summits of the Pyrenees is reduced by -2 g/kg and the temperature at 2 m is increased of about 3 K in the SMOS simulation. In the following hours the moisture anomaly in L4-Expo simulation is transported faster to the mountain tops via stronger thermal mountain winds which are caused by this higher warming on the mountain flanks and ridges. In SMOS simulation the higher mountains winds from both sides of the

Pyrenees reach their maximum at around 13 UTC with a mean increase of the low wind speed of about 0.5 m/s (+10-15 %) and maximum differences of 1 m/s in the 99 % quartile (Fig. 6.14c+d). The mean vertical winds in the L4-Expo simulation increase in all atmospheric levels up to 600 hPa (+10 %) for the PYR domain and the 99 % quartile shows up to 24 % stronger vertical winds in 700 hPa for the PYR domain. In the afternoon the stronger winds transport the positive humidity anomaly along the southern flanks to the mountain summits of the Pyrenees. On the mountain summits the convergence of wind and humidity reaches its maximum. The 6 h distribution (12-18 UTC) the 99 % and 90 % quartiles of the L4-Expo simulation reveal a 25 % stronger moisture and wind convergence in 600 hPa and 700 hPa than the CTRL simulation.

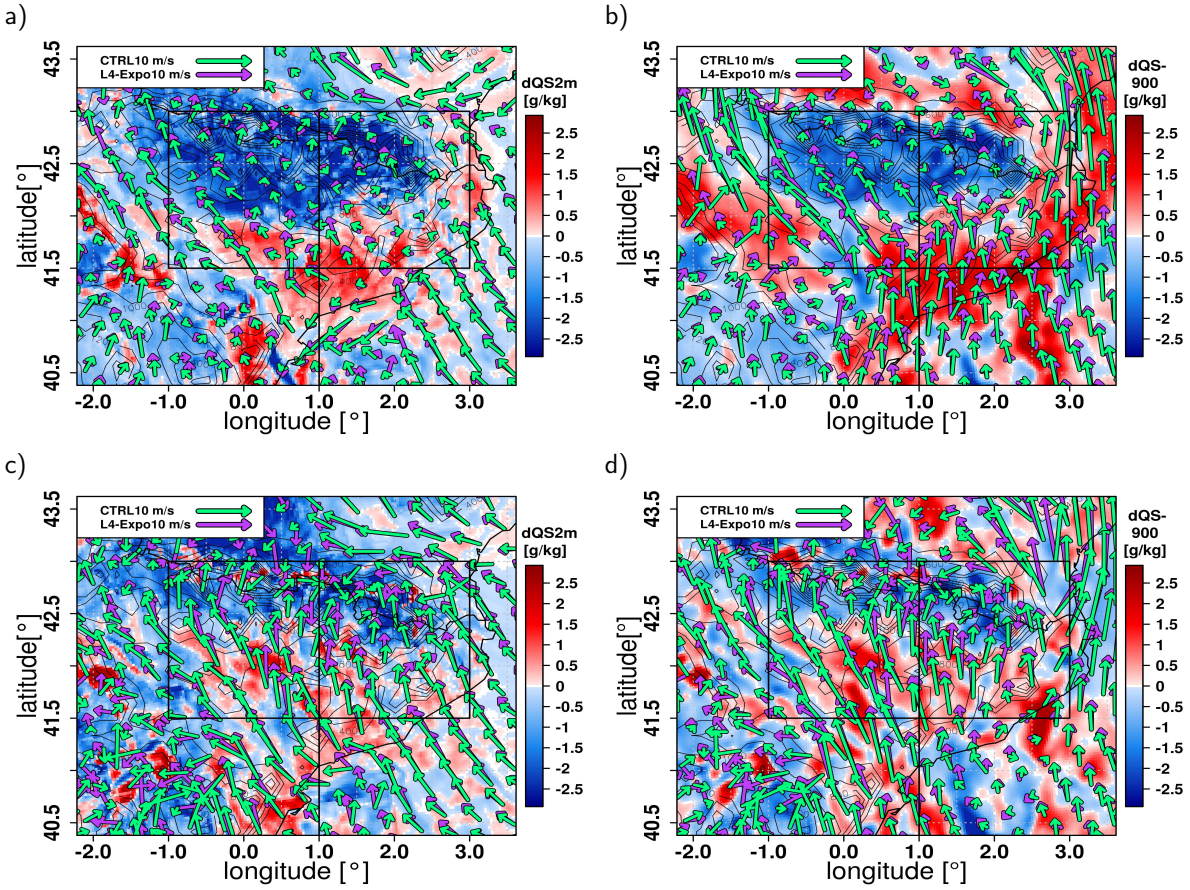

Figure 6.14.: Differences in specific humidity and wind fields between SMOS minus CTRL simulations on Sep 9, 2012 a+b) at 08 UTC and c+d) at 13 UTC. Figures a+c) represent the humidity in 2 m and figures b+d) the humidity in the atmospheric pressure level at 900 hPa. The green arrows indicate winds of the CTRL simulation and the violet arrows show winds of the SMOS simulation at the corresponding height levels.

Fig. 6.15 illustrates how these differences in humidity and wind convergence affect the formation of precipitation. The cross-section at longitude 1°E through the Pyrenees (Fig. 6.10) represents the atmospheric conditions at a specific time. At 13 UTC (Sep 9, 2012) the SMOS initialisation has a higher unstable air mass at 41.7°N ($\theta_e > 2K$, CAPE > 500 J/kg) than in the CTRL run (Fig. 6.10a). At this time the first precipitation occurs in both simulations on the northern side of the Pyrenees.

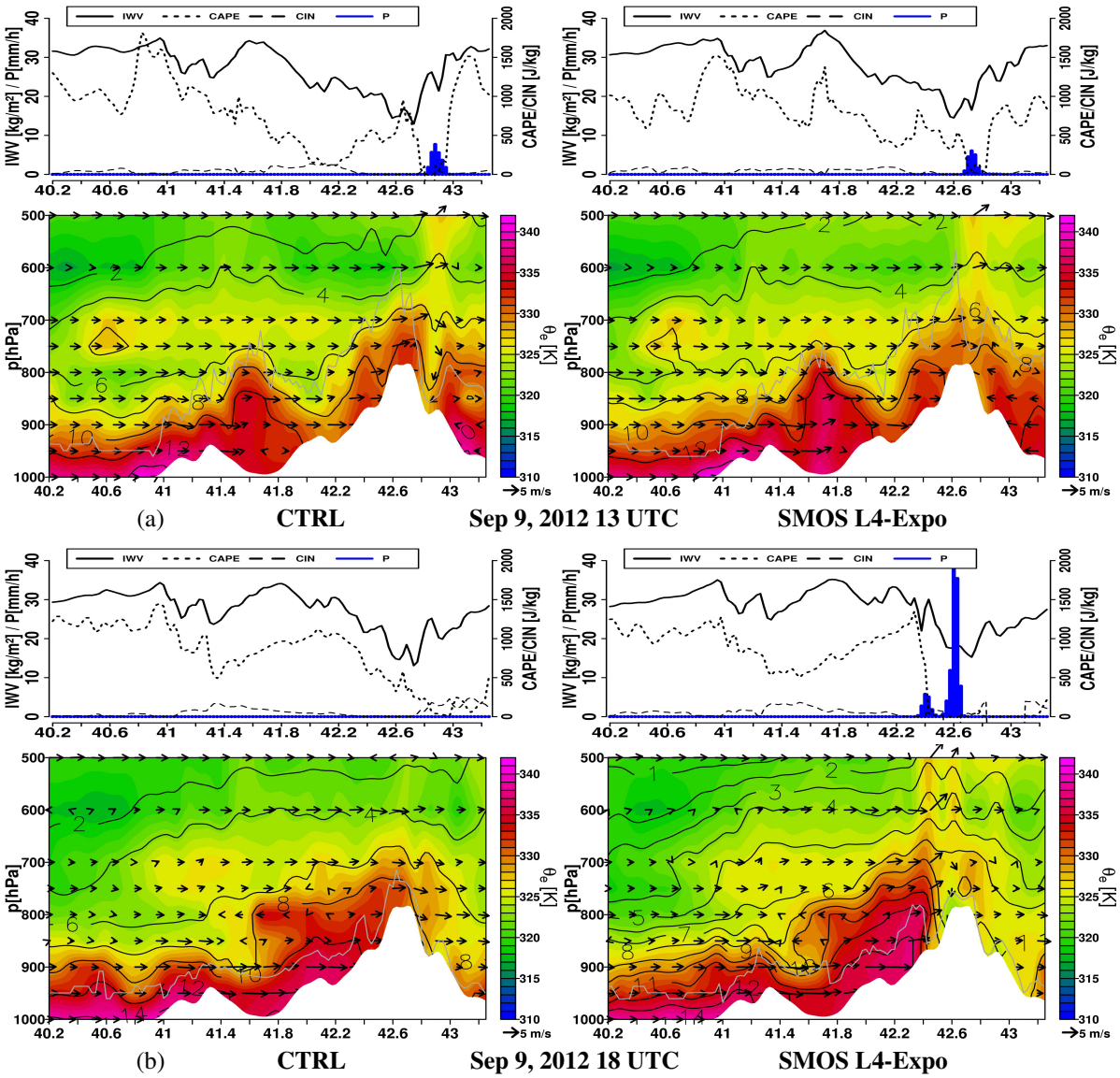

Figure 6.15.: Vertical cross-section of the atmosphere along the latitude 40° to 43.5°N (Fig. 6.10) of the CTRL (left side) and SMOS L4-Expo (right side) simulations. Different time steps are shown in a) Sep 9, 13 UTC and b) Sep 9, 18 UTC. The figures above illustrate the hourly values of IWV, CIN, CAPE and precipitation (histograms). The colour contour diagrams (figures below) show the θ_e values (K), the black solid line the specific humidity (g/kg), the shaded white areas the orography and the arrows the zonal and vertical wind (m/s). The dark grey line indicates the height of the boundary layer.

The SMOS L4-expo simulation shows stronger low-level winds which transport this unstable air mass upwards to the top of the Pyrenees. At 18 UTC in the SMOS L4-Expo simulation the supplied moisture is lifted along the mountain flanks, condensed and leads to heavy precipitation on the mountain ridge. The position of the SMOS-L4 maximum corresponds well to the measured maximum precipitation in ground based measurements (Fig. 6.10 RG(V4)). This precipitation peak is not represented by CTRL simulation (Fig. 6.10b). Furthermore, the simulation initialised with SM of SMOS shows a second precipitation peak at 42.4°N latitude. Strong low moisture convergence at this latitude lifts the unstable air mass of θ_e

$\sim$ 340 K and CAPE $\sim$ 1300 J/kg and intensifies the precipitation in the following hours until 21 UTC. This second precipitation maximum is located on the south flanks of the Pyrenees. At the same time the CTRL run shows neither strong updrafts nor precipitation. Differences between SMOS and CTRL are shown by the stronger vertical gradient with higher specific moisture values above the atmospheric boundary layer in the SMOS run. At the surface the specific humidity in the SMOS L4-Expo simulation is more than 1 g/kg higher than in the CTRL. In summary, it can be concluded that the combination of the convergence of humid unstable air masses and thermally induced wind circulation results in an orographic trigger mechanism for precipitation. Both processes are missing in the CTRL simulation.

6.3. Discussion and Conclusions

Benefit of 1 km SMOS SM initialisation for precipitation modelling

The aim of this part of the work was to assess how 1 km satellite-based SM initialisation in convection-permitting simulation affects the representation of HPEs. A methodology was developed in order to prepare a SM profile product derived from SMOS for initialisation/assimilation in the COSMO 2.8km model. The developed daily SMOS L4-Expo product was tested in the study area of the IP for selected convective HPEs during autumn 2012.

Of the three possible SMOS-L4 3.0 products the descending L4-D1 product shows the best agreement with ground-based observations. This corresponds with results of Piles et al. (2015) and Khodayar et al. (2019). Analogous to the results of Piles et al. (2016) all SMOS-L4 3.0 products show an underestimation of SSM in the moderately humid climate of southern France (SMOSMANIA network). In contrary, the COSMO 2.8km simulation overestimates the SSM in all three networks with the best results achieved in the SMOSMANIA network. Consequently, a large systematic bias between the satellite-based L4-D2 and the simulated C2.8 km SSM was found. An effective way to correct the bias is to apply the CDF-matching technique. The results have shown that not only the systematic bias is corrected but also the CDF-L4 SSM representation is improved compared to ground-based measurements. The RMSD of the model is reduced about 50 % by the bias-corrected CDF-L4 product and the RMSD of the L4-D2 product is also reduced by about 50 % in the SMOSMANIA network. In addition, the exponential filter method was used to estimate the SM profile from the CDF-L4 SSM. Evaluation with the SMOSMANIA SM ground-based observations demonstrates that the developed SMOS L4-Expo product improves the moist SM bias in the standard C2.8km SM profile for the period SON 2012.

The effects of the realistic SM initialisation on the simulated precipitation were assessed on the basis of four selected heavy rainfall events within the HyMeX SOP1 period. An initialisation time experiment was performed to find the most effective time for SMOS initialisation. The component feature-based quality measurement method SAL proves that the advanced SM representation of the SMOS L4-Expo leads to an improvement in precipitation amount and location. The analysis of the individual initialisation time steps showed that the best SMOS initialisation is achieved 3 days in advance at 00 UTC

for all four HPEs. To explain this optimal initialisation time the convective precipitation event on Sep 9, 2012, which revealed the largest improvement between SMOS initialisation and CTRL simulation, was investigated. The transport of humidity and wind field anomalies in the upper tropospheric levels takes 2-3 days and also the development of a thermal low requires about 3 days in SMOS initialisation to reach its maximum. In addition, modifications from remote regions in the IP domain require a time length of about 3 days to contribute to the development of the heavy precipitation in the target area. This is consistent with the results of Duffourg and Ducrocq (2011) who concluded that the transport of remote moisture in the lower troposphere, which feeds the HPEs of the WMed, takes 3-4 days. Further new findings from Dirmeyer and Halder (2016) emphasised the significant positive effects of realistic land surface initialisation on the improvement of near-surface temperature and humidity prediction fpr a time scale of 3 days over land.

Modification of triggering processes of a modelled convective HPE with 1 km SMOS initialisation

In a case study the influence of this realistic SM initialisation on various atmospheric processes leading to precipitation initiation was analysed and is shown in the schematic diagram in Fig. 6.16. The SMOS initialisation reduces the SM over the IP domain accompanied by the improvement of the wet SM bias in the COSMO-2.8 km CTRL SM representation. The reduction of SM leads to a negative soil moisture-precipitation feedback which is caused by a change in boundary layer conditions and induces thermally-driven wind circulation. The physical process behind this is that dry SM reduces the latent heat flux and increases the sensible heat flux which in turn raises the temperature in 2 m by about +1 °C.

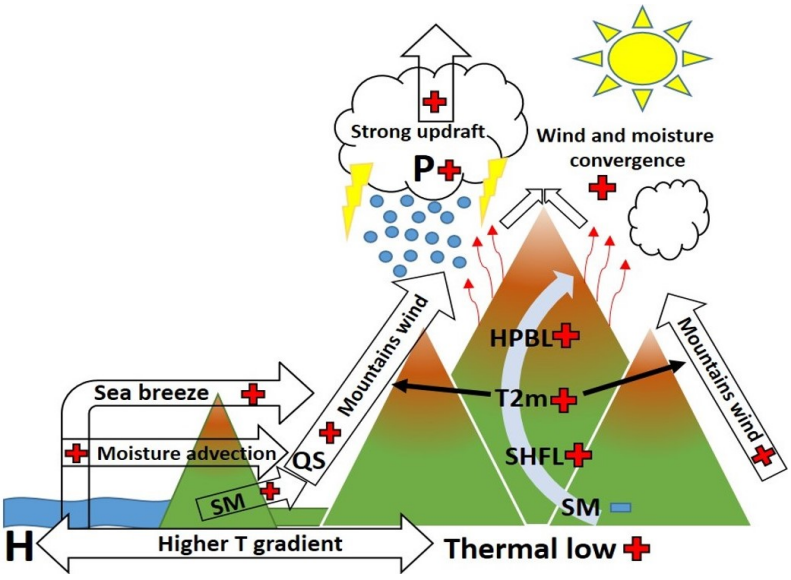

Figure 6.16.: Schematic illustration summarising the modified atmospheric processes of the SMOS-L4 simulation leading to enhanced triggering processes of convective precipitation. The soil moisture (SM) is locally reduced over the mountains (blue minus sign) but increased along the coast (red plus sign). Increases in sensible heat flux (SHFL), specific humidity (QS), temperature in 2 m (T2m), height of planetary boundary layer (HPBL) and finally in precipitation (P) are indicated by red plus signs. The high pressure over the sea is abbreviated by H.

This reduces the pressure (thermal low) and leads to a higher temperature gradient both between sea and land and between foothills and mountain peaks (thermally-driven wind systems). Additional moisture is transported by stronger low-level winds towards the flanks of the Pyrenees resulting in low moisture convergence in this area. In the SMOS simulation precipitation begins at the top of mountains initiated by stronger updrafts due to stronger winds and moisture convergence from both mountain sides. The advected low-level moisture triggers a second precipitation peak by orographic lifting along the southern flanks of the Pyrenees. This second peak moves downhill and brings a high amount of precipitation as moist unstable air masses are lifted by strong low-level convergence. This convergence results from the down-draft of uphill precipitation maximum and supports the upward moisture advection by mountain winds. Similar results of reinforced up-slopes winds over dry soil which produce a strong vertical movement over mountains and favouring convection initiation were also found by Stéfanon et al. (2014). They also showed a strengthening of the circulation of the sea breeze as dry soil improves the thermal contrast between land and sea.

General conclusions to research questions (part 2): impact of realistic initialisation with high-resolution satellite-derived SSM observation on the modelling of extreme precipitation events

- A comprehensive methodology was developed to obtain a daily, bias-corrected SMOS-L4 SM profile product derived from the state-of-the-art 1 km SMOS-L4 SSM product for the initialisation of the COSMO-2.8km model.
- The comparison of this processed satellite-derived product with three ground-based SM networks shows that the application of the CDF-matching improves the mean bias (0.01 m^3/m^3), the root-mean square deviation (0.03 m^3/m^3) and the agreement index (0.91) of the SMOS-L4 SSM of all in-situ observations.
- The constructed SMOS-L4-Expo SM profile product is in good agreement with in-situ observations and successfully corrects the wet bias of the COSMO simulated SM profile.
- The application of realistic SM initialisation using high-resolution SMOS data improves the representation of the selected HPEs in autumn 2012. The optimal initialisation time is 3 days before the event.
- A case study of simulation with SMOS-L4 SM initialisation demonstrated enhanced triggering processes of a convective heavy precipitation event. The realistic SM initialisation induces changes in the pressure field, atmospheric humidity distribution as well as wind circulations. These modifications induced the triggering processes for convective precipitation which are the low-level convergence and the orographic lifting. These processes were not represented by the reference simulation.

7. Contribution of Local and Remote SM-Atmosphere Interactions to European Heat Waves

The focus of this chapter is to quantify the sensitivity of the development of heat waves and extreme temperature to soil moisture initialisation. In particular, the influence of the spring SM deficit for the dry summer periods 2003 and 2015 is analysed. The observed dry anomalies of the two summer periods are described in Sec. 7.1. The simulation strategy for SM initialisation experiments for seasonal convection-permitting simulation is presented in Sec. 7.2. In addition, Sec. 7.3 shows the sensitivity of atmospheric and large-scale conditions to dry and wet spring SM initial scenarios. The response of extreme temperatures to the SM initialisation experiments and their possible effects on the severity of heat waves are investigated in Sec. 7.4. Special attention is given to the local SM-temperature coupling in the WMed and its remote propagation of the heat signal to the surrounding regions of continental Europe. The importance of local and remote SM-feedback mechanisms in dry periods is discussed in Sec. 7.5.

7.1. European Summer Droughts of 2003 and 2015

This section gives an overview of the European drought summer periods 2003 and 2015 and describes the main factors identified as responsible for the occurrence of such events. The summer period June until August (JJA) of the years 2003 and 2015 are the 2nd and 4th warmest summer in Europe since 1910 (NOAA, 2018). Only the summer 2018 was warmer with a temperature anomaly of +2.16 °C in Europe.

In a historical context, the summer of 2003 was the warmest summer in Southwest Europe and Central Europe for at least half a millennium (García-Herrera et al., 2010). Schär et al. (2004) came to the conclusion that in summer 2003 in some regions of Central Europe the temperature anomaly exceeded 5 times the standard deviation. In June and August 2003 two exceptional heat wave periods occurred affecting southwestern Europe in both periods and Central Europe in the first half of August. Daily temperature anomalies were measured up to +12 °C compared to the reference period 1961-1990 and the heat wave period in the first half of August 2003 was the longest observed heat wave in southwestern and Central Europe since 1950 (DWD, 2017). For this reason, record-breaking temperature anomalies were exceeded in many European countries in summer 2003. As mentioned in the introduction, the socio-economic impact was large with 70,000 heat-related deaths in Europe, severe crop and alpine glacier mass losses, record-breaking forest fires in Portugal and threats to water and energy supply systems (García-Herrera et al., 2010).

The climatology of temperature in 2 m (T2m) and precipitation (P) from E-OBS and CMORPH observations (Chap. 3.3) and the anomalies of the seasonal mean temperature and precipitation in the two summers are shown in Fig. 7.1. The observed temperature anomaly in the subdomains Central Europe (ME) and Iberian Peninsula (IP) in 2003 is about +3 °C compared to the reference period 1961-1990. This temperature anomaly is associated with a precipitation deficit of -40 % in the ME subdomain for the period JJA 2003 compared to the CMORPH reference climatology of 1998-2017. In the IP subdomain, the decrease in precipitation is low due to positive anomalies in the northwestern parts of this domain.
In the comparison of the two summers, the JJA 2015 period has a lower mean T2m anomaly of about +2 °C in the two subdomains as shown in Fig. 7.1c. Furthermore, the mean seasonal precipitation anomaly in central Europe is also weaker during this period (Fig. 7.1f). In the ME target region of southern Germany, for example, there is a strongly negative seasonal P anomaly, while in northern Germany there is a positive seasonal P anomaly. In the IP domain, the seasonal mean indicates a positive anomaly due to three strong precipitation events in early June and late July and August (Fig. 7.14a). On the contrary, the first half of July 2015 is identified by EDI as a dry period with almost no precipitation. Thus the seasonal summer average of precipitation is strongly influenced by individual events in semi-arid regions. Nevertheless, summer 2015 was characterised in large parts of Europe by very intense heat episodes with extreme to record-breaking temperatures (Hoy et al., 2017). The main heat wave in Central Europe (2E-24E,45N-55N) with daily temperature anomalies of about +12 °C was observed in July (02-06.07.2015) and August (06-14.08.2015, 29.08-01.09.2015) (DWD, 2017). In these heat wave periods, the temperature record of 40.3 °C in Germany was measured in Kitzingen on Jul 5, 2015 and again on Aug 7, 2015. Heat waves and droughts affected areas from the Iberian Peninsula to Central and Eastern Europe. Over large parts of the Iberian Peninsula May and July 2015 were the hottest months in the records of 1950-2015 (Ionita et al., 2017). In August the peak reached Eastern Europe, with breaking records in Poland, Ukraine and Belarus. In summary, Ionita et al. (2017) showed the years 2003 and 2015 together with the years 1972 and 2010 as the most extreme hot and dry summers in Europe in the last 66 years.
A comparison of the development of both droughts shows that the 2003 drought developed slowly and began at the beginning of the year with a very dry spring season (February and March) over Southern and Central Europe (García-Herrera et al., 2010). The signal persisted and intensified in summer with extreme temperatures in a south-north extension from North Africa to the North Sea. The drought in 2015 developed rapidly over the Iberian Peninsula in the late spring and extended in a west-easterly direction from the Iberian Peninsula via France, Central Europe and Eastern Europe to Ukraine (Ionita et al., 2017).
García-Herrera et al. (2010) pointed out that the main factors for the occurrence and persistence of such extreme dry events are blocking episodes, soil moisture deficit and sea surface temperature. The summer of 2003 was characterised by an intense meridional circulation combined with stationary blocking pat-

terns over Central and Southern Europe. In addition, the displacement of the Atlantic subtropical high contributed to this change in the cycle.

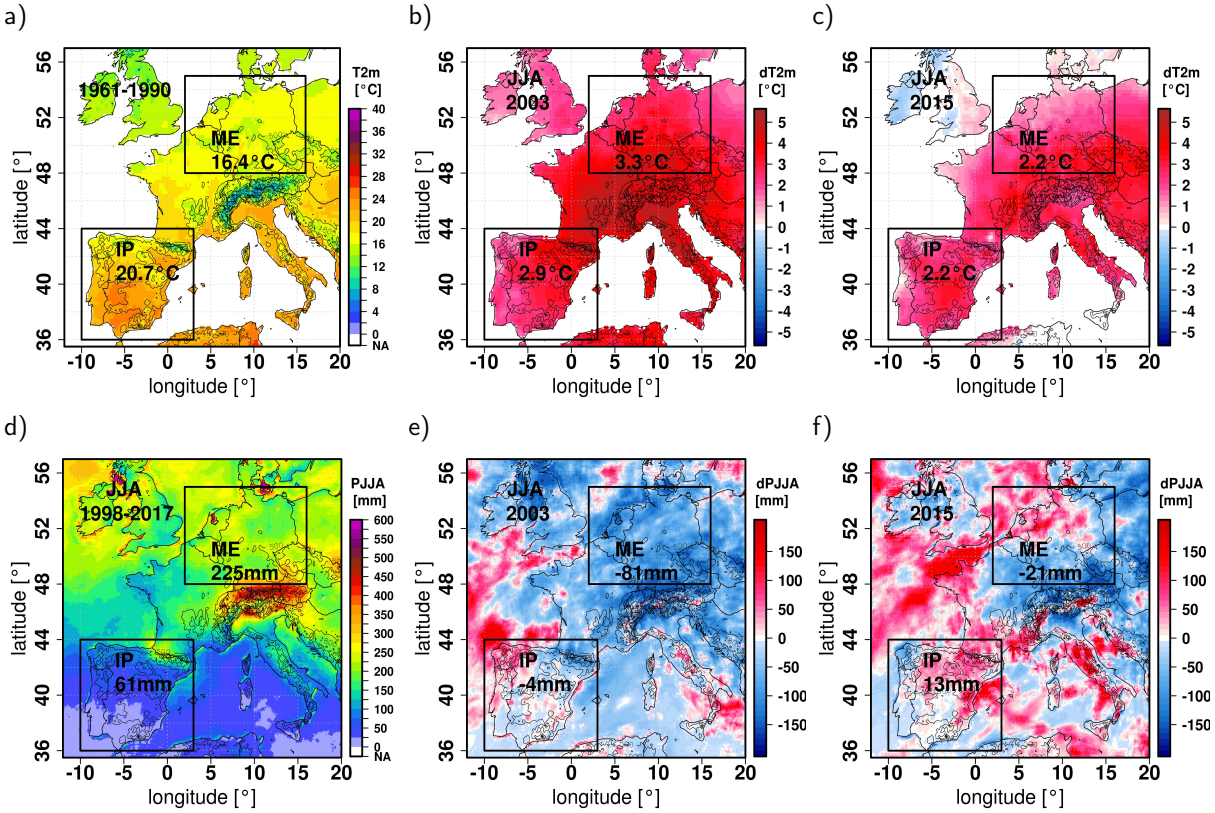

Figure 7.1.: Summer mean temperature and precipitation from E-OBS and CMORPH observations of a reference period and the anomalies in temperature (T2m) and precipitation in JJA 2003 and 2015. Figures a+d) are the available summer climatology of E-OBS T2m (1961-1990) and of CMOPRH (1998-2017). Figures b+c) show the temperature anomalies in summer 2003 and 2015 and figure e+f) the precipitation anomalies for JJA 2003 and 2015.

The heat wave episodes in 2015 were also associated with persistent blocking events and a north deviation of the Atlantic storm track (Ionita et al., 2017). The synoptic weather types (Hess and Brezowsky "Grosswetterlagen") are analysed for these heat wave periods in 2003 and 2015. Both heat wave periods over Central Europe are characterised by four weather types: "Anticyclonic Southwest Regime" (SWa), "High Norwegian Sea, anticyclonic Surface Conditions Central Europe" (HNA), "Bridge Building of the Azores and Russian highs over Central Europe" (BM) and "High Central Europe" (HM). The weather conditions during the heat waves are similar in summer 2003 and 2015 while the seasonal climatology is different between March and August of these years. The analysis of the differences to the climatological mean value of 1881-2008 (Werner and Gerstengarbe, 2010) shows that in 2003 the weather types HM and BM are more frequent with 26 % (1881-2008: 16 %) and SWa with 8.2 % (1.73 %) and the weather type "West Anticyclonic" (WA) with 6.5 % is similar to the climatological mean value of 6.2 %. This corresponds with the results of Fink et al. (2004). In 2015, the weather types HM and BM with 15 %

are similar to the climatological mean. SWa with 5.4 % is slightly more frequent and the WA weather type with 25 % is much more frequent. This could also explain the different precipitation distribution in Fig. 7.1e+f, since the WA weather type, by definition, shows more influence from the west, where the precipitation system affects more frequently Scotland, the British Isles and Baltic Sea (Werner and Gerstengarbe, 2010), while southern Germany is often influenced by high pressure wedges from the Azores. This description fits with the distribution of precipitation and temperature anomalies in Fig. 7.1f.

The role of the sea surface temperature (SST) contribution in respect to the European heat waves is under discussion (García-Herrera et al., 2010). In both summers, the Mediterranean Sea showed an extraordinary positive anomaly of about +3 °C. Black and Sutton (2006) concluded that such anomalies in the Mediterranean have a significant influence on temperature and precipitation and contributed to the heat wave in June 2003. They assumed a significant influence of SST anomalies on large-scale circulation. Additionally, Ionita et al. (2017) showed a strong relationship between the SST in the Western Mediterranean and the occurrence of dry and hot summers. Feudale and Shukla (2007) stated that global SSTs were responsible for the persistence of anticyclonic circulation in Europe. However, Jung et al. (2006) and Ferranti and Viterbo (2006) concluded that in summer 2003 the SSTs played a subordinate role in mid-tropospheric circulation and temperature in Europe. They found that the effect of SST anomalies followed the tropospheric temperature signal rather than vice versa. Ferranti and Viterbo (2006) showed that the response of large initial dry soil anomalies far exceeds the effects of the ocean boundary forcing and they showed that the effect of dry soil initialisation is one order of magnitude larger than the influence of the SST anomalies.

This is the connection to the last main factor for dry summer extremes: the soil moisture deficit. The study of García-Herrera et al. (2010) found that anticyclonic circulation anomalies alone cannot explain the extreme extent of the 2003 summer temperature anomalies. They also suggested that feedback mechanisms between land surface and atmosphere make important contributions to intensify heat wave periods. Fischer et al. (2007b) concluded that a large precipitation deficit between February and May, together with early vegetation greening and strong positive radiation anomalies, contributed to an early and rapid soil moisture loss in 2003. The soil moisture deficit mainly influences the surface temperature by changes in the local surface energy balance. In this context, Fischer et al. (2007a) presented that without the 2003 soil drying anomalies, the maximum temperature is regionally reduced by -1 to -3 °C which corresponds to 50 % of the temperature anomaly. Fischer et al. (2007a) found that this SM amplification effect is even stronger for the development of heat waves at a subseasonal scale. They demonstrated that land-atmosphere interactions account for 50-80 % of the number of hot days during heat wave periods. Moreover, Fischer et al. (2007b) showed that a dry soil also amplifies the anticyclonic circulation anomalies by a positive surface temperature feedback.

In this context, the sensitivity of the dry extreme representation for the SM initialisation for the two extreme summer drought years in 2003 and 2015 is evaluated. From the description of this section it is evident that both years already showed a strong temperature anomaly and therefore it is of interest

assessing whether a further modification of the initial SM via the soil moisture-atmosphere interactions influences the temperature and precipitation response. It is also of interest how the atmosphere is locally and remotely affected by the WMed soil moisture anomaly.

7.2. Soil Moisture Initialisation Strategy

A central idea of this chapter is to discuss the role of the dry initial WMed SM that precedes and contributes to the development of extreme heat in continental Europe. In addition, an open question is whether SM-atmospheric feedbacks exist between the southwestern Mediterranean and Central Europe. In this context, the contribution of the local and remote SM-atmosphere interactions to temperature and precipitation response and a possible amplification of heat waves are assessed. Previous studies by Vautard et al. (2007) and Zampieri et al. (2009) showed a northern progression of heat and drought from late spring to summer from the Mediterranean region by southerly wind episodes for the 10 hottest summers between 1948 and 2005. Their investigations are based on observations as well as on simulations with the 5th generation Penn State mesoscale meteorological model (MM5) with a spatial resolution of about 36 km. Additionally, Zampieri et al. (2009) showed that the transported Mediterranean heat signal established a drier soil in the Western and Central Europe and led to two main feedbacks: higher sensible heat emission and favoured upper-air anticyclonic conditions. This chapter adopts the simulation structure of Zampieri et al. (2009) and extends it by an SM initialisation experiment with convection-permitting simulation on a spatial scale of approx. 3 km for the summers 2003 and 2015.

The domain size of the study is chosen between 30°N-56°N and 10°W-20°E. This area includes the WMed with parts of North Africa, the Alps, Central Europe, large parts of United Kingdom and partly Eastern Europe. Fig. 7.2 shows the investigation domain of the COSMO-CLM convection-permitting sensitivity simulations and the two considered target areas IP and ME. The target regions correspond with the PRUDENCE domains (Christensen and Christensen, 2007) to study local effects of SM-atmosphere coupling in WMed and in Central Europe.

In this thesis a physically-based SM initialisation experiment is performed with one reference simulation (CTRL) and four extreme initial SM scenario simulations. In the first two SM scenarios the initial SM is set to the wilting point (DRY scenario) and the field capacity (WET scenario) for all land grid points south of the dotted line in Fig. 7.2. These modified areas of the Iberian Peninsula and North Africa should represent the effects of WMed SM drying in spring with possible subsequent effects on heat waves in Central Europe. This first SM sensitivity experiment is named after the southwest flow direction (MOD-SW) and the two dry and wet SM scenarios are called DRY-SW and WET-SW.

In the other two initial SM scenarios the initial SM is set to the wilting point and the field capacity for all land grid points for the entire investigation domain of continental Europe. This second SM sensitivity experiment is named MOD-EU and the two dry and wet SM scenarios are called DRY-EU and WET-EU. With the differences between the SM experiments of MOD-EU and MOD-SW the remote effects of SM-

atmosphere interactions between WMed and continental Europe and possible SM feedback mechanisms should be identified and quantified.

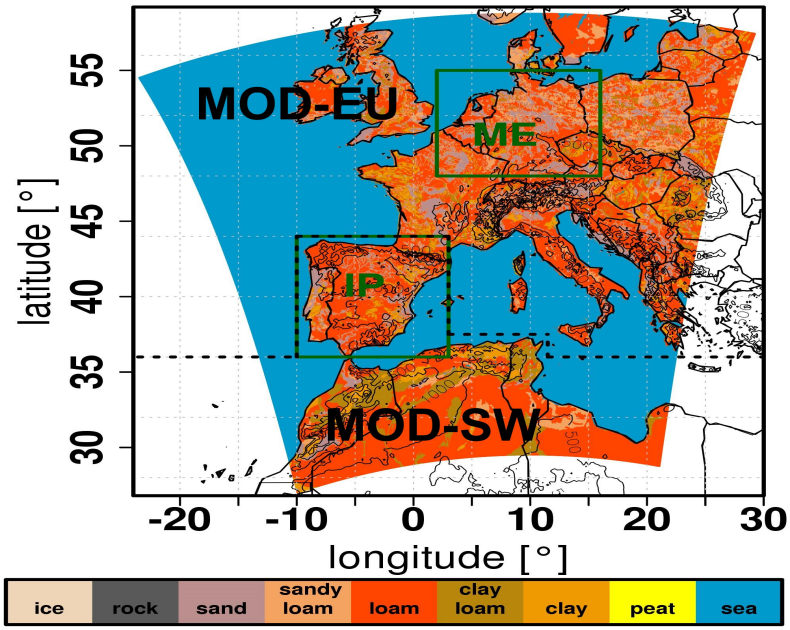

Figure 7.2.: Soil types in the investigation domain of the COSMO-CLM-2.8km simulation for the summer months June-August (JJA) in the years 2003 and 2015. The two PRUDENCE (Christensen and Christensen, 2007) target areas Iberian Peninsula (IP) and Central Europe (ME) are indicated by green boxes. The SM in the land areas south of the dotted line is modified by the initialisation scenarios MOD-SW and in the SM initialisation scenarios of MOD-EU the SM in the whole study area is modified.

The seasonal simulation strategy for this SM initialisation experiment is illustrated in Fig. 7.3 for the year 2015. The first step is to perform an initialisation simulation for the period from 1 April 00 UTC to 15 June 00 UTC to generate SM profile fields for the initial conditions of the SM sensitivity simulations. This initialisation procedure taken from Zampieri et al. (2009) ensures that soil moisture fields are consistent to the parameterisation of the model physics and are in equilibrium with the atmosphere. This initialisation simulation avoids initial transitions which could distort the modification signal of the SM sensitivity simulations and their results. In addition, in this study the initialisation day for the sensitivity studies is selected manually in a time period that is not influenced by large precipitation amounts in the WMed similar to the approach in Chap. 5.2.

In the 2015 example it is stated that the May 26, 2015 fulfils this criterion of the dry initial conditions in the WMed. For this day, the atmospheric boundary and initial conditions are nested in two steps from IFS-0.25° data and the COSMO CLM-7km simulation for the period June-August (JJA). In the initially created conditions the SM profile of this day is replaced by the SM profile of the initialisation simulation for the same day. The differences between this balanced SM profile from the initialisation simulation and the SM profile from the directly nested initial conditions are shown in Fig. 7.4. Finally, the control

simulation is performed with the balance SM profile and the four initial SM scenarios for the period from the initialisation day of May 26, 2015 to September 1, 2015 at 00 UTC.

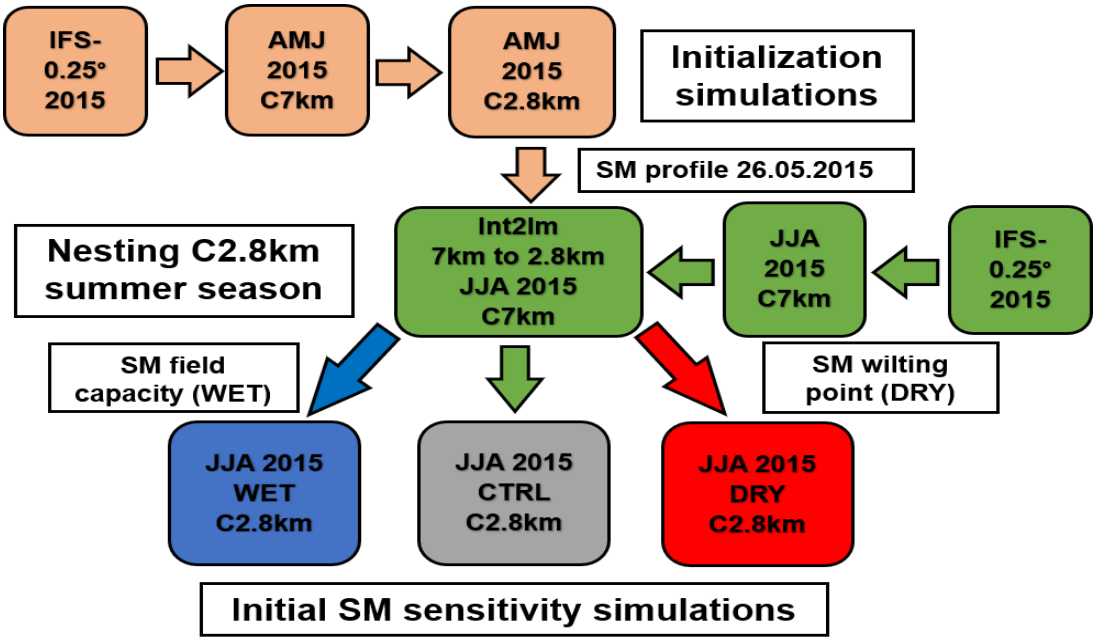

Figure 7.3.: Strategy for a seasonal initialisation experiment in the summer period JJA 2003 and 2015. The salmon-coloured boxes illustrate the initialisation simulations for April to June (AMJ) and the green boxes the nesting steps of initialisation forcing data for the COSMO CLM-2.8km (CLM2.8km) simulation of the summer period JJA. The lowest level illustrates the CTRL simulation with balanced SM profile and the extreme SM physically-based initial scenarios simulation.

For the year 2003 the 11th of May and for the year 2015 the 26th of May are chosen as the days of initialisation which fulfil the selected criterion of dry conditions in the WMed at initialisation ± 2 days. Fig. 7.4 shows the differences between the balance SM field minus the SM field of the directly nested initialisation at a soil depth of 6 cm. In both years there are differences between the SM conditions, with a slight reduction of SM in the balance SM profiles. Locally, the SM fields show differences above $\pm 50\%$. In 2015, the balanced soil moisture at the surface in North Africa shows more wet SM, while the northeastern part of the domain in 2003 shows a higher surface SM at this day (Fig. 7.4). The differences in the SM profile remain up to a soil depth of 54 cm. Below this soil level the differences disappear or become locally slightly positive. The Tab. 7.1 shows the spatial-average volumetric soil moisture of the initialisation days in vol.%. For the years 2003 and 2015 the spatial-average of all modified grid points (MOD-EU, MOD-SW) and the spatial-average of all grid points within the two target areas are presented for all performed simulations. Comparing the late spring conditions in the reference simulations in both years, the year 2015 reveals drier conditions than 2003 with differences between 3 vol.% in the entire MOD-EU domain up to 7 vol.% in the modification domain of MOD-SW. One reason could be that the chosen initialisation day 2015 is half a month later in the calendar year. On the other hand, Ionita et al. (2017) identified May 2015 as the driest and hottest May in the years 1950-2015 over the central and

eastern Iberian Peninsula which would be confirmed by drier soil moisture conditions near the surface in the CTRL simulations.

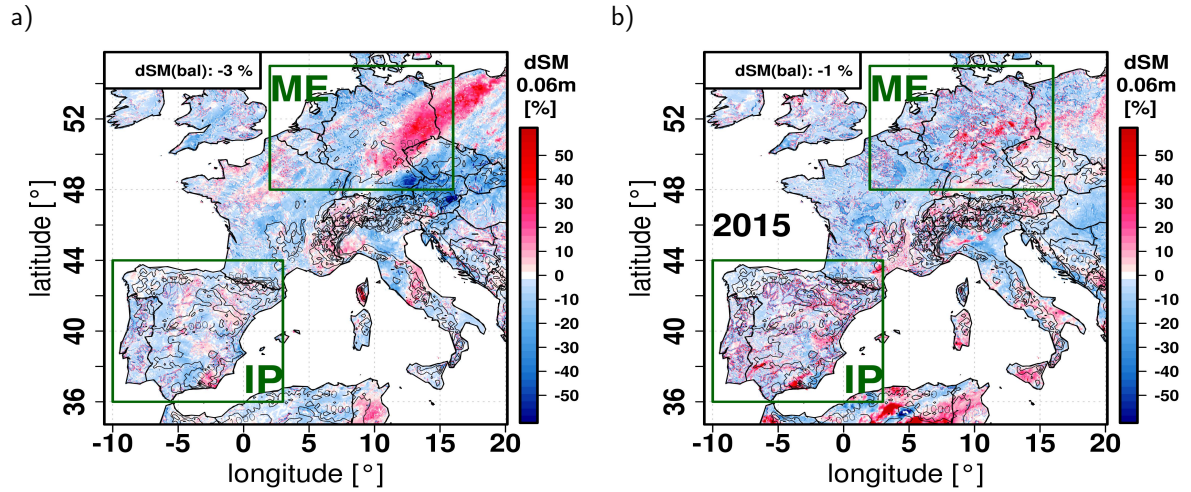

Figure 7.4.: Differences in the SM at a soil depth of 6 cm between the reference simulation (CTRL) of balance SM profile minus the SM profile nested directly on the initialisation day (Fig. 7.3). Both years are shown with the target areas IP and ME in green boxes.

The DRY-scenario of the MOD-SW reduces the SM to 13 vol.% and the WET-scenario increases the SM to 34 vol.% (Tab. 7.1). This modification is comparable to Vautard et al. (2007) and Zampieri et al. (2009) who set the SM in their DRY-scenario to 15 vol.% and the WET-scenario to 30 vol.% in latitudes below 46°N. In the target domain IP the initial SM modification of the MOD-SW and MOD-EU is equal to a reduction in the DRY-scenarios to 11 vol.% and an increase in the WET-scenario of 32 vol.% (Tab. 7.1). The ME region is not modified in the MOD-SW scenario and has the same initial SM as the CTRL simulation in both SW scenarios.

Table 7.1.: Spatial average of the volumetric SM [vol.%] at a soil depth of 6 cm in the domains of the initial SM modification of MOD-SW and MOD-EU and in the corresponding IP and ME subdomains. The volumetric SM values are compared between the CTRL simulation and the four SM initial scenarios.

SM 0.06cm	CTRL-2003	CTRL-2015	DRY-2003	DRY-2015	WET-2003	WET-2015
MOD-SW	20 vol.%	13 vol.%	13 vol.%	13 vol.%	34 vol.%	34 vol.%
SW-IP	25 vol.%	19 vol.%	11 vol.%	11 vol.%	32 vol.%	32 vol.%
SW-ME	26 vol.%	23 vol.%	26 vol.%	23 vol.%	26 vol.%	23 vol.%
MOD-EU	23 vol.%	20 vol.%	12 vol.%	12 vol.%	33 vol.%	33 vol.%
EU-IP	25 vol.%	19 vol.%	11 vol.%	11 vol.%	32 vol.%	32 vol.%
EU-ME	26 vol.%	23 vol.%	10 vol.%	10 vol.%	30 vol.%	30 vol.%

In the target domain ME the SM is reduced to 10 vol.% in the DRY-EU scenario and to 30 vol.% in the WET-EU scenario. Both years are based on the same absolute values of wilting point and field capacity in the SM scenarios but due to the different SM in the CTRL runs the relative changes between the two

years differ as shown in Fig. 7.5. In the dry initial modification of the MOD-EU in Fig. 7.5b+e the year 2003 shows a drier initial SM modification than the year 2015 in the near-surface SM of 6 cm. The differences between the two years in near-surface soil levels are about 8 % for the entire investigation domain and about 14 % in the domain-average of the IP region. The increase in SM in 2015 in North Africa can be explained by the fact that in this region the SM is drier in the CTRL run than the mean SM value of the corresponding wilting points. The opposite effect can be seen in the wet initial modification, where the drier reference soil moisture conditions in 2015 compared to 2003 lead to a larger increase in the WET-EU scenario compared to 2003 (Fig. 7.5c+f).

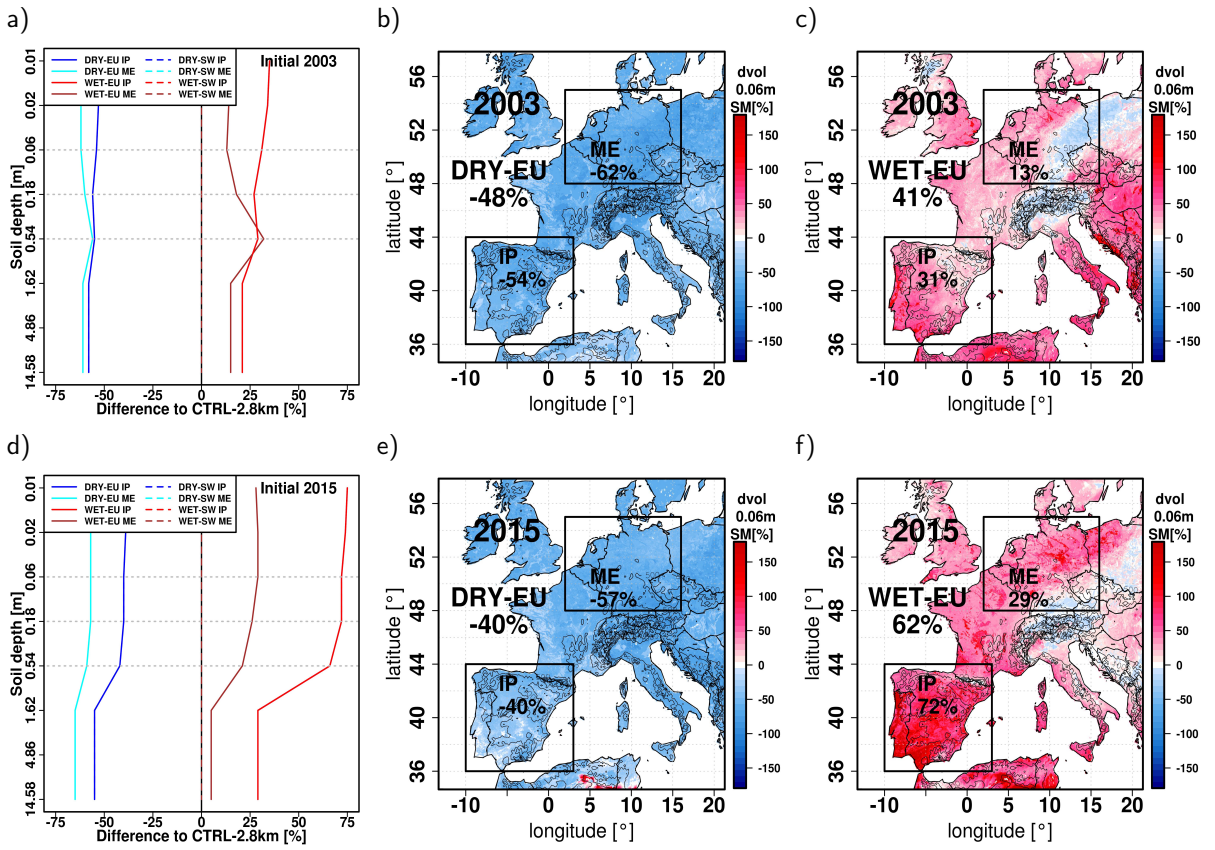

Figure 7.5.: Percentage changes in SM initial scenarios minus CTRL simulations on the initialisation day of the two years 2003 and 2015. The diagrams a+d) indicate the spatial-averaged differences in the SM profile for the four SM initial scenarios. Figures b+e) show the change of SM initialisation in SM at the soil depth of 6 cm of the DRY-EU scenario and in Figures c+f) for the change in the WET-EU scenario.

Fig. 7.5a+d illustrate the percentage changes of the SM profiles between the four scenarios and the CTRL simulation for both years. The strongest signal shows the WET-EU scenario for the IP domain with about +75 % up to a soil depth of 0.54 m and about +25 % in deeper layers. The dry initial signal is about -50 % in both years and becomes stronger with an increasing depth (> 0.54 m) especially in 2015. The modification of the SM profile in the DRY-scenario is stronger in 2003 than in the WET-scenario and the strength of modification is similar in all soil levels. On the other hand the DRY-scenario shows an

increase of the modification signal in the ME region at a soil depth of half a meter which is strongest in 2003 (Fig. 7.5a). These effects on the SM profile are due to a precipitation event that affects the eastern part of the ME domain and reduces the modification signal in the upper soil levels (Fig. 7.4c). In 2015, the change of the WET-scenario SM modification is weaker in deeper soil levels and the signal of the DRY-scenario becomes slightly stronger in deeper soil levels (Fig. 7.5d).

7.3. Sensitivity of Atmospheric Conditions to Extreme Spring SM Initialisation

In this section the contribution of soil moisture anomalies and their interactions with the atmosphere through surface heat fluxes is investigated for the two SM sensitivity experiments of MOD-SW and MOD-EU. In addition, a coupling between these initial SM perturbations and large-scale circulation is studied. For the regional analysis of the local and remote SM-atmosphere interactions both target regions IP and ME are considered. In the following local and remote SM effects are investigated. A local effect is defined as a direct modification of the atmospheric conditions in the regions of the initial SM modification. A remote effect is understood either as a modification of the atmospheric conditions in the surrounding regions without initial SM perturbation (MOD-SW simulations) or the difference between the modification signal of MOD-EU minus MOD-SW SM sensitivity simulations.

7.3.1. MOD-SW SM Experiment

First of all, the soil moisture-atmosphere coupling to the SM initialisation of the southwestern Mediterranean (MOD-SW) which includes the Iberian Peninsula and North Africa is investigated. Fig. 7.6 shows the seasonal change of surface heat fluxes and different atmospheric parameters for the DRY-SW scenario 2003. A clear effect on the distribution of surface heat fluxes can be seen in the dry initial simulation for the whole summer. The additional spring SM deficit leads to a reduction of the latent heat flux (LHFL) while simultaneously the sensible heat flux (SHFL) increases. This land-atmosphere coupling is locally strongest over the areas of SM modification in the MOD-SW regions (Fig. 7.2). The negative anomaly of the latent heat flux reduces the total integrated water vapour (IWV) and leads to a stabilisation of the atmosphere over the Iberian Peninsula.
The initial southwestern Mediterranean SM perturbation has a remote effect on SM-atmosphere coupling to continental Europe (Fig. 7.6). The initial SM anomaly also affects the surface fluxes partitioning in ME regions in an attenuated form due to local SM changes. The remote signal is also apparent in seasonal IWV anomalies, even though a higher destabilisation of the atmosphere is represented by an increase in convective available potential energy (CAPE) in the remote ME region. The dry SM initialisation affects the short-wave radiation and the cloud cover via modification of surface fluxes. The changes are divided into two modified areas. In the northwestern part of the study area, including the northwestern part of the IP and France and the areas north of the Alps, there is a decrease in cloud cover and an increase in short wave radiation at surface (SW). On the contrary, in the southeastern part of the study area, including the

coastal regions and the WMed, the opposite signs of seasonal mean changes in SW and cloud cover can be observed.

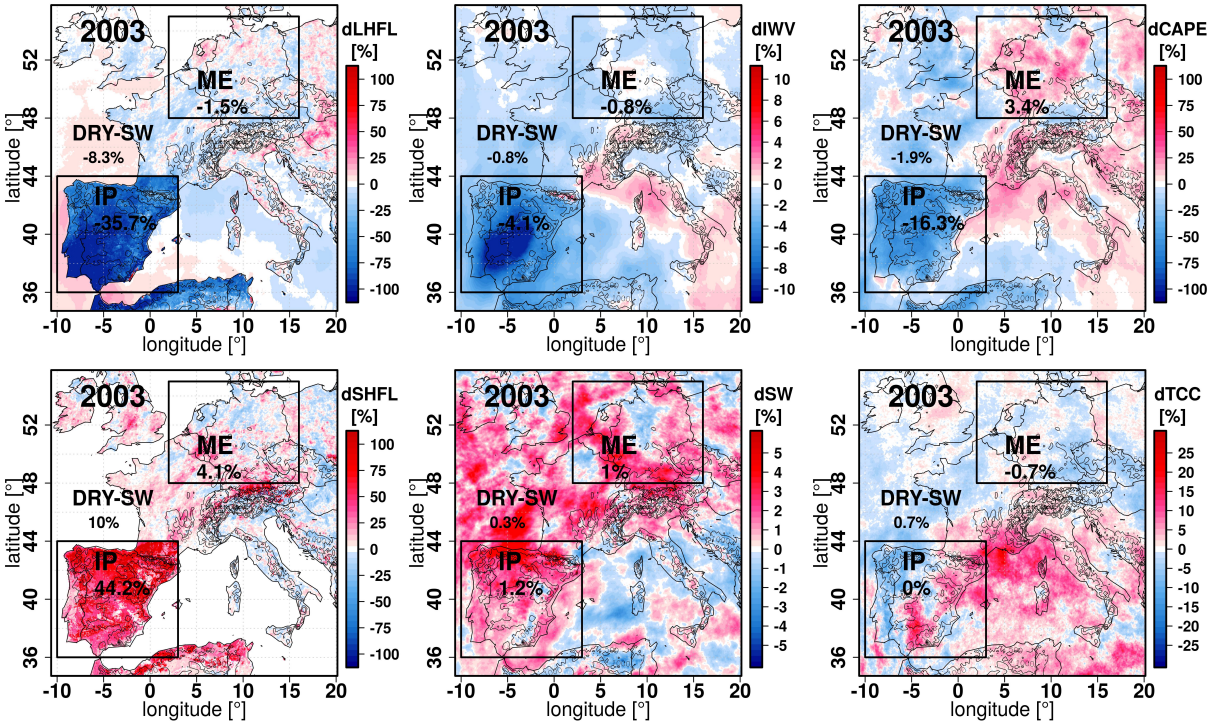

Figure 7.6.: Seasonal mean modification of the atmospheric conditions to dry spring SM initialisation in the south-western Mediterranean scenario (DRY-SW) in JJA 2003. The two target areas are indicated by black boxes with spatial averages of the percentage change within the domain.

Considering the local effect of SM atmosphere coupling in the IP subdomain, the initial SM is reduced by about -50 % in both years leading to a seasonal mean decrease in evapotranspiration (ET) and LHFL of about -75 % with an increase in seasonal SHFL of about +40 % (Tab. 7.2). These changes in surface conditions affect the mean specific humidity in 2 m (QS2m) by about -10 % and the IWV of about -5 %, resulting in a reduction of CAPE by -30 %. In this context it is interesting to see how this affects cloud formation. In both years the seasonal mean of total cloud cover (TCC) increases slightly by +1 %. In the seasonal mean low cloud cover (LCC) is reduced by about -25 % while high cloud cover (HCC) increases by about +10 % (Tab. 7.2). The mean differences in cloud modification are due to the change in spatial distribution (Fig. 7.6). The total effect of the short-wave radiation on the surface is positive with a slight increase of +1 % but as already mentioned, the effects have locally different signs (Fig. 7.6). Finally, the local effect of dry SM initialisation leads to a positive SM-atmosphere coupling with a mean reduction of humidity and low clouds under more stable atmospheric conditions.

The strength and sign of the remote effect found of WMed SM drying on the ME domain depend on the year. In summer 2003 the signal shows the same sign in atmospheric parameters as in the IP region while the signal is indifferent in spatial and seasonal mean in 2015 (Tab. 7.2). In general, the seasonal summer change is weaker in the ME region. In JJA 2003 about 10% of the anomaly signals in SHFL, QS2m,

HCC and about 20 % in IWV and LCC are transported from the original SM initialisation region in the southwestern Mediterranean to the remote ME domain. Differences arise in the representation of CAPE which is positive in the ME region.

Table 7.2.: Seasonal modification of the DRY-SW scenarios in both target areas IP and ME for different atmospheric parameters in JJA 2003 and 2015. The spatial-averages of the changes of all land grid points are given in % and the values in brackets are the corresponding seasonal averages. The acronyms can be taken from the legend A.

DRY-SW	IP 2003	ME 2003	IP 2015	ME 2015
ET[CTRL]	-75%[2mm/d]	-2%[2mm/d]	-70%[2mm/d]	+0.5%[3mm/d]
LHFL[CTRL]	-75%[55W/m^2]	-2%[71W/m^2]	-70%[52W/m^2]	+0.5%[79W/m^2]
SHFL[CTRL]	+45%[80W/m^2]	+5%[47W/m^2]	+35%[85W/m^2]	+0.5%[34W/m^2]
SW[CTRL]	+1%[237W/m^2]	+1%[201W/m^2]	+1%[234W/m^2]	+0.5%[182W/m^2]
Rn[CTRL]	-5%[144W/m^2]	+0.5%[124W/m^2]	-5%[143W/m^2]	+0.5%[119W/m^2]
QS2m[CTRL]	-11%[10g/kg]	-1%[9g/kg]	-10%[9g/kg]	+0.5%[9g/kg]
IWV[CTRL]	-5%[23kg/m^2]	-1%[24kg/m^2]	-5%[23kg/m^2]	+0.5%[25kg/m^2]
CAPE[CTRL]	-30%[153J/kg]	+5%[76J/kg]	-30%[119J/kg]	+15%[95J/kg]
TCC[CTRL]	+1%[36%]	-1%[57%]	+1%[39%]	+0%[70%]
HCC[CTRL]	+11%[23%]	+1%[37%]	+8%[25%]	+3%[46%]
MCC[CTRL]	-1%[18%]	-2%[38%]	+2%[20%]	+0%[48%]
LCC[CTRL]	-26%[10%]	-5%[10%]	-20%[10%]	-2%[20%]

To get more details about the modification ranges within the target domains and also to consider the effects of wet SM initialisation, the Fig. 7.7 illustrates the distribution of the modification of different atmospheric variables for both MOD-SW scenarios. The positive coupling between dry(wet) SM initialisation to a decrease(increase) in LHFL, ET, QS2m, IWV and low cloud cover for more than 50 % (range of boxes) of all grid points in both scenarios is clearly visible in the IP domain in Fig. 7.7a. The effect seems to be stronger in the dry initial scenario due to a stronger initial SM perturbation. The WET-SW scenario reveals a stronger increase in total cloud cover mainly due to an increase in low cloud cover and middle high clouds whereas the sensible heat flux and the short-wave radiation are reduced. In general, the local effect of SM initialisation, e.g. in the IP subdomain, shows a clear SM-atmosphere interaction and locally within this range the modifications are much stronger than in the spatial averages (Fig. 7.7, Tab. 7.2). This is due to the fact that local positive and negative signs compensate each other in the spatial-average. In the remote ME target range this high variability in both signs leads to an even stronger compensation effect. Nevertheless, the median and the different sign directions of wet and dry SM initialisation indicate the same coupling as in the locally modified region of the IP domain, with the exception of CAPE, where the median of both initial scenarios is positive. Within the ME region the remote impact of the DRY-SW scenario leads to a regional seasonal reduction of LHFL/ET by up to -20 %, in QS2m by up to -5 %, in LCC by up to -30 % and an increase in SHFL by up to 30 %.

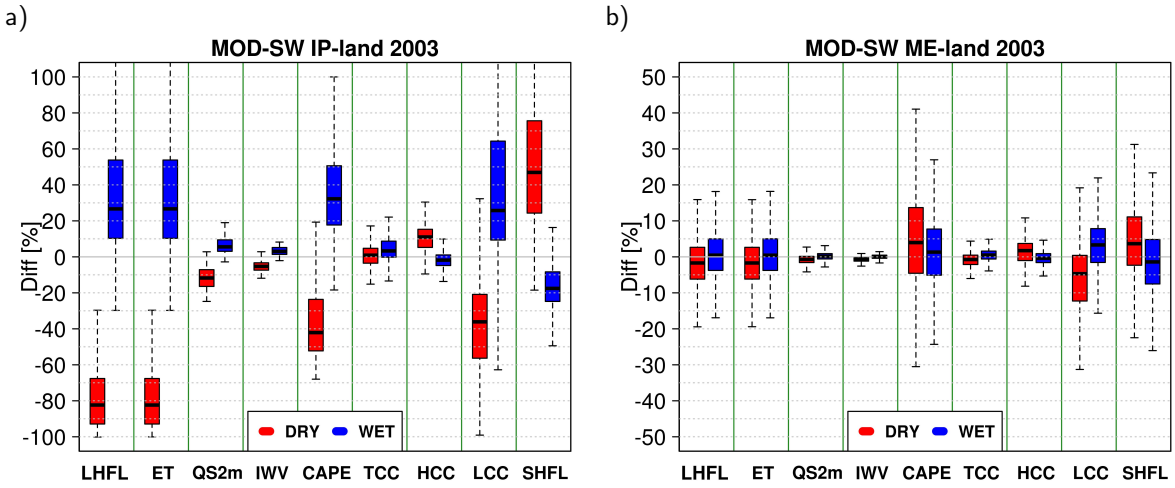

Figure 7.7.: The box plots show the distribution of seasonal mean modifications of both MOD-SW scenarios in the land grid points of both target areas. The boxes indicate the interquartile range of the middle 50% of modification, the black line shows the median and the whiskers illustrate the entire range of modifications. The red boxes represent the result of the dry SM initialisation in the southwest of the WMed (SW-DRY scenario) and the blue boxes of the wet SM initialisation in this region (SW-WET scenario). The following variables are shown: latent heat flux (LHFL), evapotranspiration (ET), specific humidity in 2 m (QS2m), integrated water vapour (IWV), convective available potential energy (CAPE), total cloud cover (TCC), high cloud cover (HCC), low cloud cover (LCC), and sensible heat flux (SHFL).

7.3.2. MOD-EU SM Experiment

In addition to the local and remote effects of the MOD-SW SM initialisation the modifications of the initial SM scenarios of the entire study area are analysed in this section (MOD-EU in Fig. 7.2). With this complementary sensitivity SM experiment the remote effect between Southern Europe and continental Europe can be analysed and quantified in both directions. Tab. 7.3 presents the seasonal modification of the DRY-EU scenario for the spatial-averages of both target areas in JJA 2003 and 2015. In the IP domain, the initial SM modification is the same as in the DRY-SW scenario but the effects on the seasonal average conditions demonstrate stronger anomalies in both years in the DRY-EU. These additional modifications originate from continental regions of Europe and are transported to the Iberian Peninsula. This remote effect in the direction of the WMed can be observed for both summer years. The anomaly of the DRY-SW scenario has increased by 10-15 % for surface heat fluxes, by 30-50 % for QS2m and IWV and by 40 % for CAPE. Furthermore, the DRY-EU scenario shows a reduction of the total cloud cover due to a stronger negative anomaly of the low cloud cover of about 50-70 %. This again leads to a stronger positive seasonal anomaly in the short wave radiation.

In the DRY-EU scenario the initial SM in the ME target area is also modified. In this range, dry initialisation has a total initial SM perturbation of -60 % and is thus about 10 % stronger than in the IP subdomain (see Figure 7.5). Compared to the control values, the changes in both summers are very similar. Tab. 7.3 shows a significant change in all subdomains. In the ME subdomain the absolute mean values of the seasonal mean LHFL are higher than in IP (CTRL values) and vice versa in SHFL. For this reason, the

relative changes in SHFL are higher with +90 % to +140 % and the LHFL is reduced by -70 %. This leads to a positive coupling with the humidity in the atmosphere which is reduced by about -20 to -25 % in QS2m and approx. -10 % in the IWV. Consequently, the reduction of low cloud cover in the ME region is significantly stronger as this region has higher amounts of low cloud cover and a higher negative anomaly of about -60 %. Also in the ME region the high cloud cover increases by about +10 %, the total signal at TCC is negative with about -5 %. On the other hand, there is a strongly positive seasonal mean SW radiation anomaly approx. +10 %.

Table 7.3.: Seasonal modification of the DRY-EU scenarios in both target areas IP and ME for different atmospheric parameters in JJA 2003 and 2015. The spatial-averages of the changes of all land grid points are given in % and the values in brackets are the corresponding seasonal averages. The acronyms can be taken from the legend A.

DRY-EU	IP 2003	ME 2003	IP 2015	ME 2015
ET[CTRL]	-85%[2mm/d]	-70%[2mm/d]	-80%[2mm/d]	-70%[3mm/d]
LHFL[CTRL]	-85%[55W/m^2]	-70%[71W/m^2]	-80%[52W/m^2]	-70%[79W/m^2]
SHFL[CTRL]	+49%[80W/m^2]	+90%[47W/m^2]	+40%[85W/m^2]	+145%[34W/m^2]
SW[CTRL]	+2%[237W/m^2]	+5%[201W/m^2]	+3%[234W/m^2]	+10%[182W/m^2]
Rn[CTRL]	-5%[144W/m^2]	-5%[124W/m^2]	-5%[143W/m^2]	-5%[119W/m^2]
QS2m[CTRL]	-15%[10g/kg]	-20%[9g/kg]	-15%[9g/kg]	-25%[9g/kg]
IWV[CTRL]	-10%[23kg/m^2]	-10%[24kg/m^2]	-10%[23kg/m^2]	-10%[25kg/m^2]
CAPE[CTRL]	-50%[153J/kg]	-65%[76J/kg]	-50%[119J/kg]	-75%[95J/kg]
TCC[CTRL]	-1%[36%]	-5%[57%]	-3%[39%]	-3%[70%]
HCC[CTRL]	+10%[23%]	+10%[37%]	+5%[25%]	+10%[46%]
MCC[CTRL]	-5%[18%]	-10%[38%]	-5%[20%]	-10%[48%]
LCC[CTRL]	-50%[23%]	-60%[37%]	-35%[25%]	-55%[46%]

The distribution of local changes in the seasonal relative modification in JJA 2003 for both MOD-EU scenarios is presented in Fig. 7.8. Comparing the dry initial scenario modifications between DRY-SW (Fig. 7.7a) and the DRY-EU (Fig. 7.8a) in the IP-domain the distribution of the modification also changes to a stronger SM-atmosphere coupling. For the surface fluxes the total ranges do not change but the interquartile (IQ) range of the mean 50 % of the modification is amplified. In the DRY-EU scenario, the total range of moisture and CAPE is negative with anomalies up to -30 % in QS2m and -15 % in IWV and the IQ range of CAPE reduction is -40 to -60 %. CAPE and low cloud cover are more affected in both extreme initial scenarios. Due to this additional strong effect of the SM-atmosphere interactions from outside the IP domain, it can be understood that dry continental European SM conditions can lead to a drying and stabilisation of the WMed atmosphere in summer periods.

In both MOD-EU simulations the ME region reveals the same sign of modification as the IP region (Fig. 7.8b). The variability of the modification is not as high as in the IP domain. There is again an obvious relation between the drying of the spring SM and a reduction of the summer mean values of LHFL, QS2m and IWV which leads to a decrease of the low and medium clouds in the period JJA.

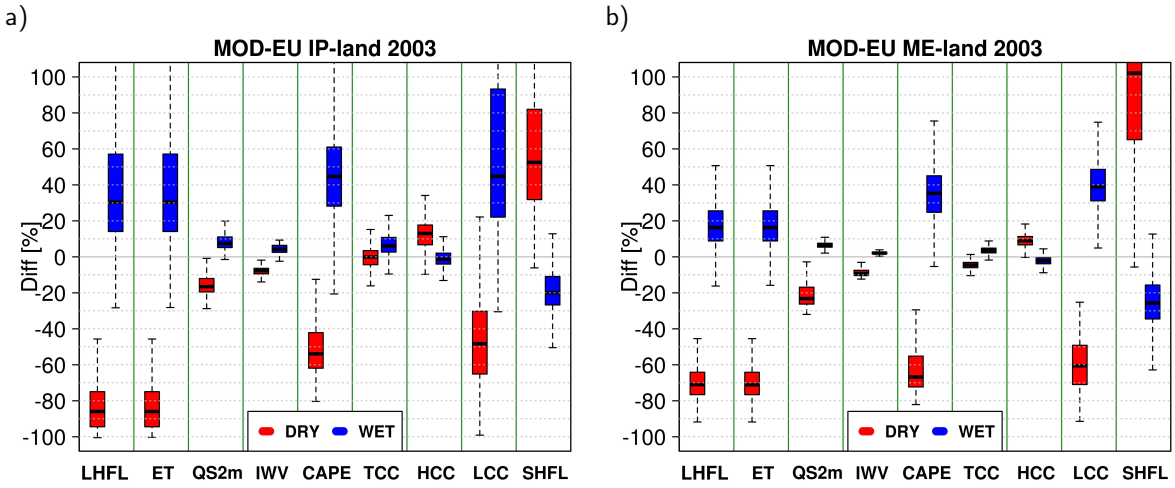

Figure 7.8.: The box plots show the distribution of seasonal mean modifications of both MOD-EU scenarios in the land grid points of both target areas. The boxes indicate the interquartile range of the middle 50 % of modification, the black line shows the median and the whiskers illustrate the entire range of modifications. The red boxes represent the result of the dry SM initialisation in the entire continental Europe area (EU-DRY scenario) and the blue boxes of the wet SM initialisation in this region (EU-WET scenario). The following variables are shown: latent heat flux (LHFL), evapotranspiration (ET), specific humidity in 2 m (QS2m), integrated water vapour (IWV), convective available potential energy (CAPE), total cloud cover (TCC), high cloud cover (HCC), low cloud cover (LCC), and sensible heat flux (SHFL).

7.3.3. SM Feedback to Large-scale Conditions

This subsection deals with the question whether the extreme SM initialisation in the convection-permitting simulations influence the large-scale circulation and could lead to an amplification of already existing circulation patterns. Studies by Fischer et al. (2007a) and Zampieri et al. (2009) found an increase in anticyclonic circulation by drying soil conditions in hot European summers. In this respect, the physical process-chain is that dry soil moisture leads to higher sensible heat fluxes and temperatures above dry soils which lead to a thermal heat low at the surface. In contrast, the geopotential height at 500 hPa (z500) increases which is a proxy for the large-scale conditions (Fischer et al., 2007a). An increase in z500 indicates a strengthening of anticyclonic conditions and thus a positive feedback on surface temperature and soil moisture conditions (Fischer et al., 2007a). Both regional model studies were performed with coarse spatial resolution (>36 km).

In the previous section, an increase in sensible heat fluxes and reduction in moisture and low clouds in both dry initial scenarios were found. Furthermore, a remote effect was shown in the direction of the WMed to continental Europe and the other way round. Fig. 7.9 shows how far such a transport could reach caused by or strengthened by a modification in the large-scale circulation. The seasonal changes of the DRY-SW scenarios are shown for the pressure at mean sea level (PMSL) in Fig. 7.9a+d in the summer periods JJA 2003 and 2015. Both years indicate a seasonal mean decrease of the surface pressure by -1 hPa in the inland of the Iberian Peninsula. The anomaly is strongest above the original areas of SM disturbance but up to 40 % (-0.3 hPa) of the anomaly is seen over remote areas in continental Europe. In

the DRY-EU scenarios the seasonal anomaly of surface pressure is stronger with a maximum in Central and Eastern Europe (> -2 hPa) (not shown).

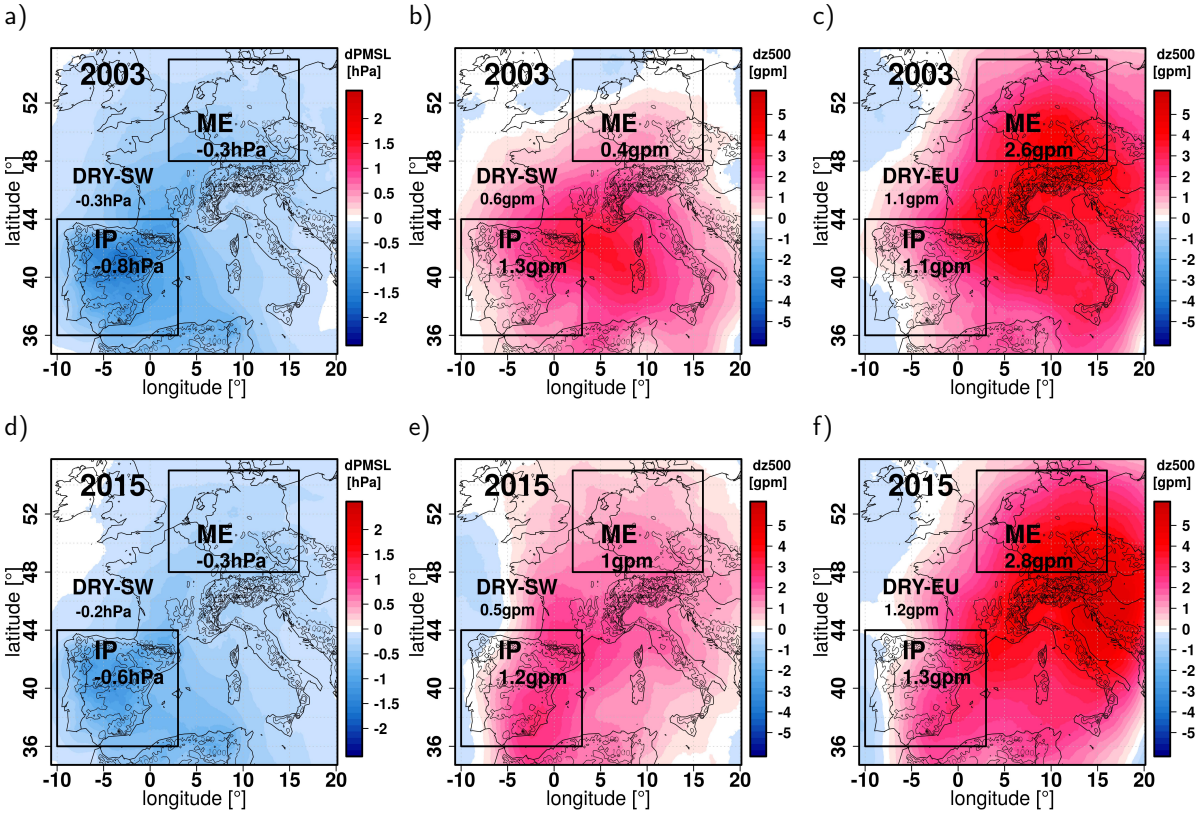

Figure 7.9.: Seasonal mean anomalies of pressure at mean sea level (PMSL) and geopotential height at 500 hPa (z500) of the COSMO CLM-2.8km DRY-scenarios in JJA 2003 and 2015. Figures a+d) show the PMSL for the DRY-SW scenario of the two years and figures b+e) show the corresponding z500 fields. The figures c+f) indicate the z500 of the DRY-EU scenarios in both years.

The response to the geopotential height in the upper troposphere (500hPa) shows a positive seasonal anomaly while differences between the year 2003 in Fig. 7.9b+c and 2015 in Fig. 7.9e+f are shown. The 2003 DRY-SW scenario exhibits the maximum of the z500 anomaly located over the Mediterranean Sea between the Gulf of Leon and Sardinia westward of the PMSL maximum. The remote effect affects areas north to the centre of Germany while a slightly negative anomaly is observed above the North Sea in 2003. In summer 2015, the maximum positive z500 anomaly extends from northern Morocco to southern France and the northern spread of positive anomalies extends through Denmark and the Baltic Sea. A negative anomaly is over the Atlantic Ocean. In the DRY-EU scenarios the anomaly is stronger in z500 with a maximum above Central Europe and the Alps. The position of the maximum is similar in both years with local seasonal anomalies up to +5 gpm (geopotential meters). The Atlantic shows a weaker opposite pole of negative anomalies in z500. In summary, it can be said that apart from a strong SM-atmosphere coupling to the initial SM modification, the local SM modification also influences the

large-scale circulation and strengthens anticyclonic conditions. These results agree with Zampieri et al. (2009) using a coarse resolution and is confirmed in this study for convection-permitting simulations.

7.4. Summer Temperature and Precipitation Response to Initial Spring Soil Moisture

In the previous section, the positive coupling between the initial SM modification on the atmosphere and the influence of SM anomalies on large-scale circulation were demonstrated. In the following a possible subsequent response of extreme temperature in a height of 2m and precipitation will be proved. First, the seasonal influence of the four SM initialisation scenarios on the temperature and precipitation feedback is investigated. In the second part the propagation of the WMed heat signal is discussed in the context of the previous results of Zampieri et al. (2009). In the third part the change of heat wave periods in the target areas is analysed in the different SM sensitivity experiments.

7.4.1. SM-Temperature and SM-Precipitation Feedback in the Summer Season

In this subsection the sensitivity of the summer mean maximum temperature and precipitation to spring SM initialisation is investigated. The mean modification and variability within the two target areas of the SM initialisation experiment are shown in Tab. 7.4 and Fig. 7.10.

The local impact of SM initial perturbation of the MOD-SW scenarios in the IP domain demonstrates a clear SM-temperature and SM-precipitation feedback. The drying of the spring SM leads to a seasonal mean increase of maximum temperature in 2 m (Tmax 2m) of about +2 °C in the IP target region and regional maximum values of about +4.5 °C (Tab. 7.4). At the same time the mean precipitation in JJA is reduced to -25 %. Within the IP region 75 % of all grid points show a precipitation reduction whereas 25 % of the grid points show a decrease larger than -40 % (Fig. 7.10). The seasonal mean Tmax 2m and precipitation response in the DRY-SW scenarios is similar in summer, with a slightly stronger effect in 2003. In the WET-SW scenarios the signals differ for both years as the initial wet perturbation in spring 2015 is twice as high as in 2003. This difference in SM initialisation is also reflected in the seasonal Tmax 2m response which is with -2.1 °C in 2015 twice as high as in 2003 with about -1.1 °C. The regional maximum reduction of Tmax 2m in the year 2015 is -4.5 °C, while for 2003 the maximum seasonal reduction of Tmax 2m is -3.5 °C (Fig. 7.10). This also applies to the precipitation response with a seasonal mean increase of +10 % in 2003 to a mean increase of +25 % in 2015.

The remote feedback of MOD-SW SM initialisation scenarios on temperature and precipitation in the ME target region is shown in Fig. 7.10b. The seasonal mean temperature anomaly of the DRY-SW scenarios is about +0.3 °C and varies between -0.7 °C and +1.6 °C and the seasonal mean temperature anomaly of the WET-SW scenarios is about -0.2 °C and varies between +1 °C and -1.1 °C. In both scenarios, the transported anomaly signal from WMed to Central Europe is of 10-15 %. In JJA the mean precipitation anomaly of -6 %(DRY) and +4 %(WET) in 2003 is stronger than that of -1 %(DRY) and +2 %(WET) in 2015. The anomalies in summer 2015 in the ME region indicate a higher variability in both sign

directions. The comparison with a local anomaly over the initially perturbed region of the IP revealed that 5-40 % of this precipitation (P) anomaly is transported to the ME region in all four SM initialisation scenarios in both summers.

Table 7.4.: Seasonal mean anomaly of Tmax 2m and precipitation (P) of the two SM sensitivity experiments of MOD-SW and MOD-EU in JJA 2003 and 2015. In the corresponding subdomains IP and ME the modification for Tmax 2m is given in °C and for P in %.

Tmax[°C]	DRY03	WET03	DRY15	WET15
IP-SW	+2.1	-1.1	+1.8	-2.1
IP-EU	+2.5	-1.3	+2.4	-2.3
ME-SW	+0.3	-0.1	+0.2	-0.2
ME-EU	+3.8	- 1.2	+4.5	-1.1

P[%]	DRY03	WET03	DRY15	WET15
IP-SW	-24	+10	-19	+25
IP-EU	-38	+17	-42	+20
ME-SW	-6	+4	-1	+2
ME-EU	-42	+20	-38	+8

In the IP domain the SM initialisation for the MOD-SW and MOD-EU scenarios are the same but the influence of remote regions on the SM-atmosphere coupling is presented in Chap. 7.3. In the comparison of the seasonal mean response of temperature and precipitation in Fig. 7.10a+c and Tab. 7.4 even a remote effect from continental Europe to the IP region can be seen. The mean maximum temperature anomaly of the DRY-EU scenarios is +2.5 °C in 2003 and +2.4 °C in 2015 which means an additional increase of the temperature anomaly by 20-30 %. The additionally effects in the WET-EU scenario are slightly lower with an increase in the anomaly of 20 % (-1.3 °C) in 2003 and 10 % (-2.3 °C) in 2015. From the differences between DRY-EU minus DRY-SW, the percentage changes of this remote effect in the IP subdomain are quantified. A larger impact is seen in the amount of precipitation, especially in the DRY-EU scenario. The total decrease in precipitation in both years is about -40 %, with 50 % of this anomaly coming from remote regions and 50 % from local sources in the southwestern Mediterranean. In the WET-EU scenarios the additional remote amount of the precipitation anomaly is 20 % (+30 %) in 2015 and 70 % (+17 %) in 2003 (Table 7.4). The DRY-EU scenarios show the highest temperature anomaly for JJA 2015 with a seasonal mean increase of +4.5 °C which varies regionally between +0.5 °C and +7.5 °C in the ME region. In 2003 the mean anomaly is about +4 °C in the range 0 °C to +6 °C. The differences are caused by a stronger decrease in clouds and precipitation in 2015. Tab. 7.3 and Tab. 7.4 reveal a similar relative mean reduction in low clouds of about -60 % and rainfall of about -40 %, but in JJA 2015 the low clouds and rainfall were higher with 46 % and 200 mm more than JJA 2003 with 37 % (LCC) and about 140 mm in accumulated P.

The stronger total precipitation modification in 2015 is also evident in a lower median and interquartile range (IQR) in Fig. 7.10d. The lower amounts in clouds and precipitation in JJA 2003/2015 agree with CMORPH observations and literature findings (e.g. Ionita et al. (2017)). In the WET-EU scenario the temperature anomaly in both summers is in a similar range between 0 °C and -3 °C with seasonal averages of -1 °C. Relative changes of seasonal precipitation are between +10 % and +20 % with a higher variability also in JJA 2015. The comparison of the remote effect of the DRY-SW scenario modification shows that the transported anomaly of SHFL and Tmax 2m is in a similar order of about 10 %. The

amount of P anomaly is even higher with 10-15 %.

To conclude, it can be assumed that the modification of the physically-based extreme SM initialisation in late spring influences the summer seasonal average conditions for temperature and precipitation. Soil drying induces a Tmax 2m anomaly of about +2.5 °C in the Mediterranean IP subdomain and about +4.0 °C above the ME subdomain in both hot summers. Furthermore, a seasonal mean P anomaly of about -40 % is identified in both regions. The regional change of the maximum temperature exceeds +7.5 °C in JJA 2015. The comparison with the maximum temperature of E-OBS demonstrates that the already existing temperature anomaly of 2003 (E-OBS: +4.1 °C) has doubled and in 2015 there is a 1.5-fold increase in the already existing Tmax 2m anomaly (E-OBS: +2.9 °C) in the ME region. Considering the difference between the modification of MOD-EU minus MOD-SW of the seasonal remote effect from the southwestern Mediterranean to continental Europe and vice versa, 30 % of the temperature anomaly and 50 % of the precipitation anomaly originate from remote regions.

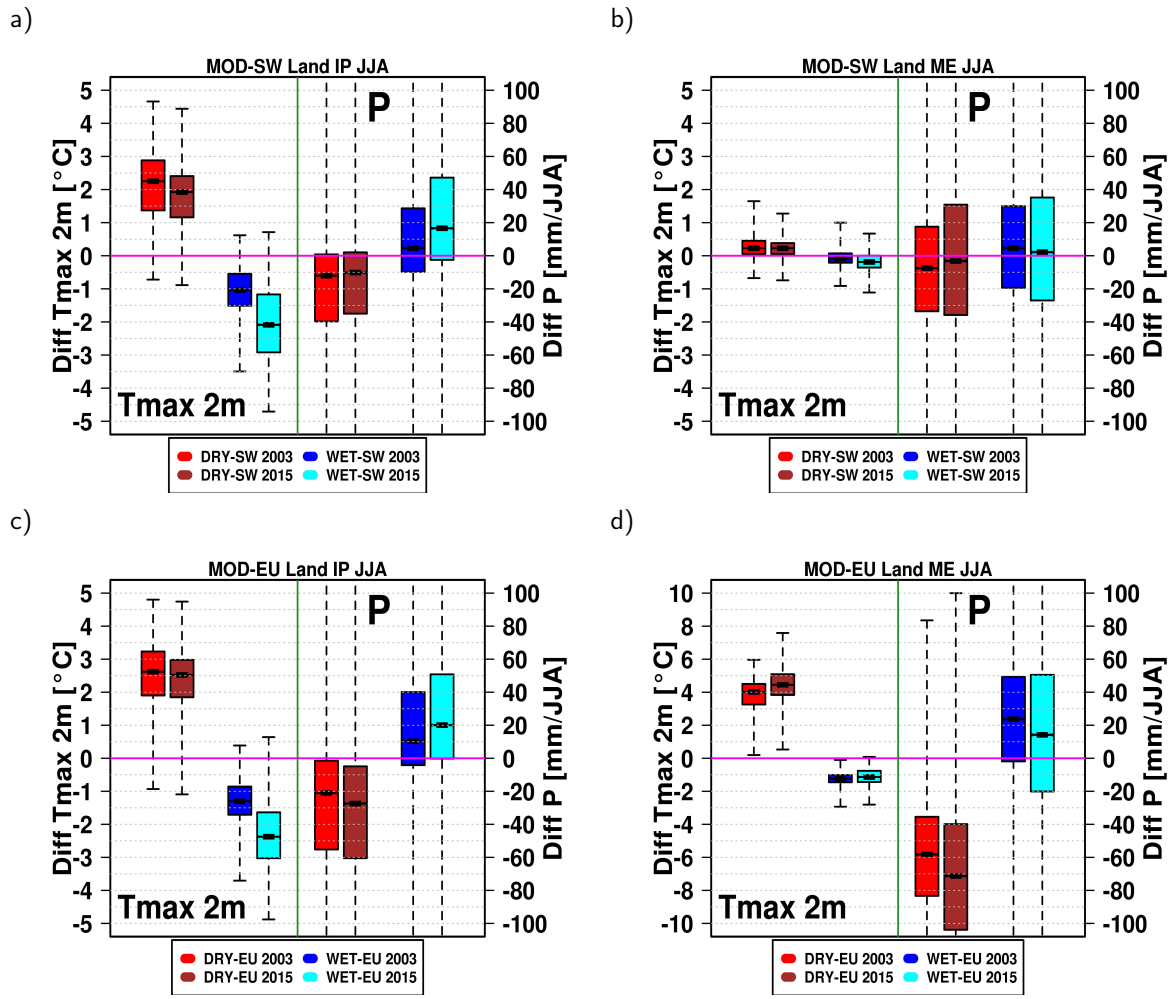

Figure 7.10.: Box-Whisker plots of the total distribution of seasonal modification of the maximum temperature in 2 m (Tmax 2m) and precipitation (P) in the both subdomains IP and ME for the two SM sensitivity experiments of MOD-SW and MOD-EU in JJA 2003 and 2015. Diagrams a+b) show the Tmax 2m and P anomalies of the MOD-SW SM scenarios and diagrams c+d) the anomalies of the MOD-EU scenarios for the both target areas.

7.4.2. Propagation of the WMed Heat Signal to Continental Europe

In this section the differences between the two MOD-SW scenarios are further analysed to understand the northward propagation of the temperature anomaly from the southwestern Mediterranean and its contribution to the continental European hot and dry summer conditions.

The effects of MOD-SW SM initialisation in late spring on the afternoon mean temperature in 2 m (T2m) in July are investigated. In July 2003 the seasonal mean value of T2m at 15 UTC is about 30 °C in the IP region and about 25 °C in the ME region (Fig. 7.11a). July 2015 is in the IP subdomain in the mean T2m at 15 UTC about 1 °C warmer than 2003 (31 °C) and in the ME subdomain about 1 °C colder than 2003 (24 °C). These results agree with the observations by Ionita et al. (2017). The temperature differences between the DRY-SW minus the WET-SW scenario simulation show the maximum range of extreme SM sensitivity in Fig. 7.11b. The differences between July and June of the spread of the scenario DRY-SW minus WET-SW are shown in Figure 7.11c. Zampieri et al. (2009) came to the conclusion that such a consideration isolated the development of the anomaly regardless of the initial conditions (Zampieri et al., 2009). The temperature response in 2 m is strongest over initially drier regions of the IP and North Africa where the mean July anomaly at 15 UTC is about +3 °C and local anomalies reach up to +6 °C. In these regions the drier soil conditions also induce a remote temperature anomaly transport to surrounding Mediterranean areas like Italy and France and farther north to south and eastern Germany, UK and Poland. The mean July temperature anomaly at 15 UTC in ME regions is +0.6 °C and varies between -1 °C and +2.3 °C. Negative temperature anomalies can also be observed in northwestern Germany in particular as well as in Eastern Europe. These temperature anomalies are strongly correlated with positive precipitation anomalies (see App. B.7c).

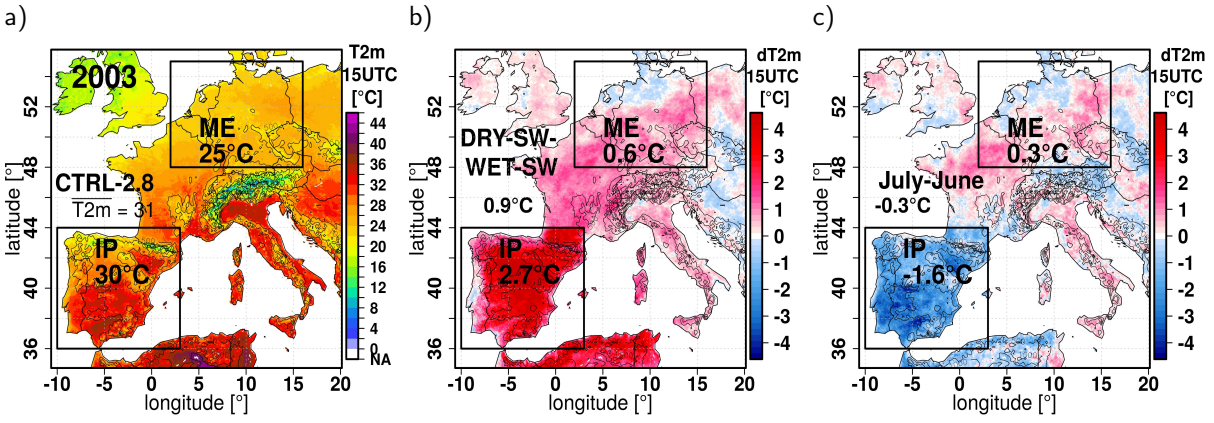

Figure 7.11.: Sensitivity simulation of the MOD-SW scenario for the temperature in 2 m (T2m) at 15 UTC in July 2003. The illustrations show in a) the monthly mean T2m at 15 UTC, in b) the mean July difference between DRY-SW minus WET-SW at this time. Figure c) illustrates the monthly mean differences of July minus June of the DRY-SW minus WET-SW fields at 15 UTC.

The northward propagation of the temperature anomaly of the MOD-SW SM initial areas in Fig. 7.11c reveals a positive temperature anomaly in remote areas and a negative anomaly over the areas of originally perturbed soil moisture. Positive remote T2m anomalies can be found in Northern France, Italy and southern and eastern Germany. The transported signal in mean T2m at 15 UTC is about +0.3 °C but regionally maximum anomalies reach in the monthly mean modification of about +2 °C. Similar results are found for the northward propagation in July 2015 (App. B.6). The mean value of remote propagation is slightly lower with +0.2 °C in 2015 but two remote regions in central France and western Germany also show a stronger peak of the T2m anomaly of about +2 °C. The T2m anomaly is also more pronounced in the west of Germany. In a next step, the remote effect of the found Mediterranean heat progression on local continental Europe surface energy balance and possible feedbacks are examined. The DRY minus WET fields reveal a reduction in total cloud cover and in the incoming surface radiation in App. B.6a+b. In this respect Zampieri et al. (2009) emphasised three mechanism which could be responsible for the reduction of cloudiness. The first local effect induces a lower latent heat flux caused by lower soil moisture. A second transport effect results from the large-scale transport of drier and/or warmer air masses. Finally, a third synoptic effect is caused by an increase in vertical stability with amplification under anticyclonic conditions, resulting in a thicker boundary layer and reduced convection. These effects are demonstrated in the following:

Impact on remote surface energy balance and SM-atmosphere coupling

Fig. 7.12a illustrates the northward progression of the SM anomaly. The signal is positive above the IP domain because the initial perturbation of the WET-scenario leads to a faster drying of the absolute SM than in the DRY-scenario due to higher evapotranspiration rates in the WET-scenario. The negative anomalies in the remote regions are caused by the opposite effect, without initial modification the drier soil of the DRY-scenario leads to a faster loss of soil as evaporation rates are higher in less cloudy conditions with higher incoming solar radiation. In addition, the structure of the remote SM anomalies is more patchy as precipitation anomalies have a high impact on positive SM anomalies, as shown in App. B.7c. In the remote continental regions, the sensible heat signal follows the local SM anomalies, especially in France, Switzerland and southern and eastern Germany (Fig. 7.12b). The signal is predominantly positive and leads to higher sensible heat flux in large parts of Europe. In the ME regions the mean increase is about +8 W/m^2 with local variability between -91 W/m^2 and +102 W/m^2. Similarly, latent heat flux is reduced in remote areas with mean values in the ME subdomain of -8 W/m^2 and local variations between -136 W/m^2 and +93 W/m^2. Finally, a positive coupling with the total incoming surface radiation between the differences of DRY minus WET July-June differences is detected. Positive anomalies are found in northern France, on the east coast of Great Britain, in Italy and Germany. The mean ME value in July is about +3 W/m^2 with a variability between -80 W/m^2 and +115 W/m^2.

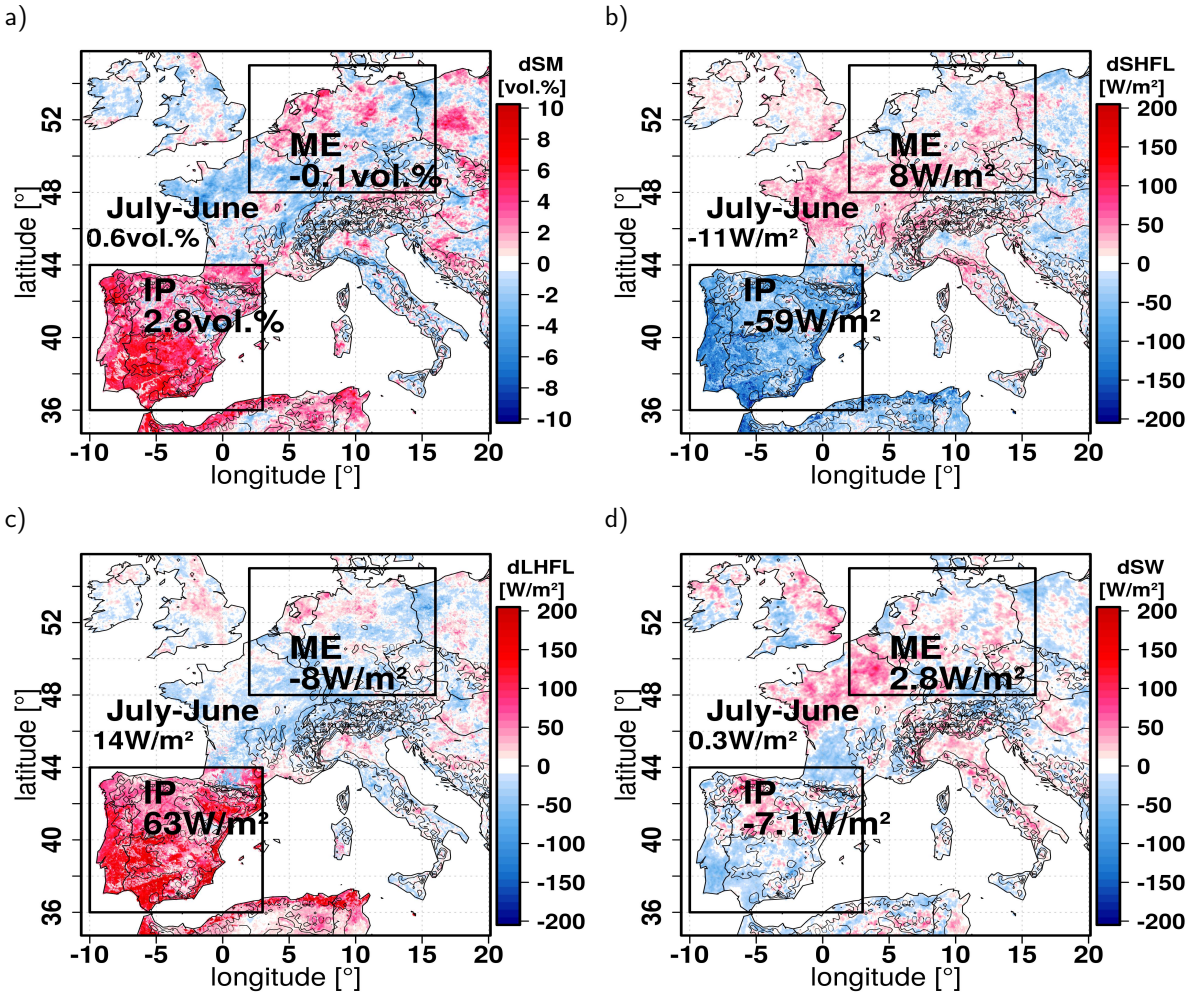

Figure 7.12.: Modification in the surface energy budget of the July minus June differences of the DRY-SW minus WET-SW scenario. In Figure a) the July minus June fields of surface soil moisture in a soil depth of 6 cm are shown (Vol.%). Figures b+c) illustrate the sensible (SHFL) and latent heat flux (LHFL) at 12 UTC (W/m^2) and d) the total short wave radiation at surface (SW) (W/m^2).

Synoptic effect

To get a detailed insight in the change in synoptic conditions due to the southwestern SM spring deficit for July 2003, Fig. 7.13 shows the mean conditions of DRY-SW minus WET-SW differences for pressure at mean sea level (PMSL), geopotential height at 500 hPa (z500) and height of planetary boundary layer (HPBL). Comparable to the results for the JJA 2003 conditions of Chap. 7.3.3 the modification of PMSL in the DRY minus WET scenario in mean July conditions indicate similar affected areas by a negative surface pressure anomaly. The effect is stronger if only July is considered. The high local temperature anomaly above the IP subdomain induces a thermal heat low that lies above dry soils on the Iberian Peninsula inland. The upper troposphere is affected by positive geopotential height differences z500 with the maximum in the northwestern Mediterranean which is also more pronounced (>50 %) than in the whole season. The shape of the z500 anomaly in Fig. 7.13b shows a typical omega block situation over Central Europe. Comparing the differences in DRY-SW minus WET-SW of July 2003 with July

2015 both years show a similar change in the negative PMSL signal (see App. B.5). Differences between the years can be seen in z500 where this amount is more affected in July 2015 with a positive anticyclonic system extending from North Africa to the North Sea and a larger zonal extension from Great Britain to Eastern Europe. Only over the Atlantic a negative anomaly is presented which affects also the northeast of the IP. Another indicator of the change in the troposphere is the increase in the height of the boundary layer shown in Fig. 7.13c. Over the areas of the initial SM perturbation mean HPBL in July increases by +500 m in the IP region and by 80 m in remote areas of ME region with a variability between about -400 m and +650 m. Schär et al. (1999) and Zampieri et al. (2009) concluded that an enhanced Bowen ratio leads to a higher boundary layer and reduced convection. This is also verified in this thesis with convection-permitting simulations in continental Europe.

In summary, a positive feedback could be found in the convection-permitting simulations related to a southwestern spring soil moisture deficit, consistent with earlier results from Zampieri et al. (2009) and Vautard et al. (2007). The dry heat signal is transported in the summer months 2003 and 2015 from the southwestern Mediterranean to continental Europe and intensifies soil drying in remote regions. Locally higher sensible heat fluxes contribute to the local warming signal. The drier air leads to less extensive clouds, which increases solar radiation and then influences soil moisture again. The southwestern Mediterranean soil moisture deficit also implies a strengthening of typical anticyclonic blocking patterns over the western European continent through higher sensible heat flux, temperature anomalies and less convection in a higher planetary boundary layer.

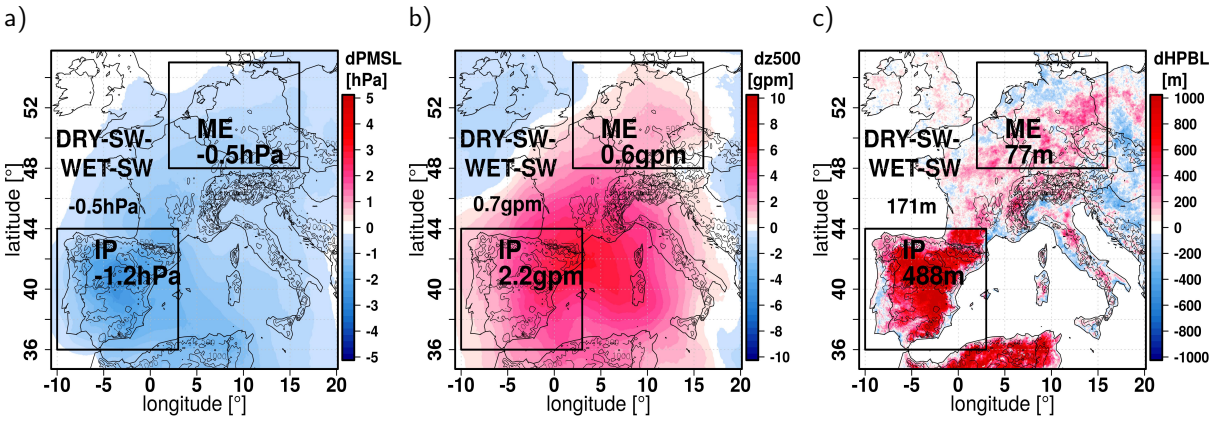

Figure 7.13.: Modification of the large-scale conditions of the DRY-SW minus WET-SW scenario in July 2003. The figures show in a) the anomaly of pressure at mean sea level (PMSL) [hPa], in b) the anomaly of geopotential height z500 [gpm] and in c) the anomaly in the height of planetary boundary layer (HPBL) [m].

7.4.3. Analysis of the Heat Wave Modifications

This subsection analyses the sensitivity of the formation of heat waves to the SM deficit in late spring. In this respect, the temporal model representative of daily precipitation, maximum temperature in 2 m (Tmax 2m) and the heat wave periods are examined. A special attention is given to the summer 2015 because this year is characterised by several intensive heat wave periods which led to record-breaking temperature in many regions in Europe. To validate the model results the observations of CMORPH for precipitation and E-OBS data for Tmax 2m are used. The heat wavelength definition of Jaeger and Seneviratne (2011) is used to identify heat wave periods. This definition selects the duration of heat wave when the daily Tmax 2m is higher than the 90th percentile of a long-term daily Tmax 2m data for two consecutive days. The E-OBS data for the period 1961-1990 are chosen as a long-term data set for Tmax 2m and the 90th percentile of this maximum temperature is shown in Fig. 7.14 by a dashed green line for both target areas.

The Fig. 7.14a+b show the temporal evolution of the daily precipitation and the maximum temperature of the COSMO CLM-2.8km reference simulation and the CMORPH and E-OBS observations. The comparison of the temporal representation of COSMO CLM-2.8km Tmax 2m maxima and precipitation events shows a good agreement with observation in both target areas. The spatial-average precipitation is very consistent between CMORPH and COSMO CLM-2.8km with the same extent of about 0.7 mm/d in the IP subdomain and 2.1 mm/d in the ME subdomain in JJA 2015 (Tab. 7.5). Similar mean precipitation rates are found in the IP subdomain with 0.6 mm/d (0.7 mm/d) for CMORPH (COSMO CLM-2.8km) in summer 2003 (App. B.3). In the ME subdomain lower values with 1.6 mm/d (1.5 mm/d) in CMORPH (COSMO-CLM-2.8km) in summer 2003 are observed in both data sources.

Table 7.5.: Spatial average of observed and modelled precipitation and dry extreme indices in summer 2015. Observations (OBS) of precipitation (P) are from CMORPH (8 km) and for maximum temperature in 2 m (Tmax 2m) from E-OBS (0.25°). Heat wave days are the number of days of a heat wave duration and hot days are days with an average maximum temperature exceeding 30 °C.

ME JJA 2015	OBS	CTRL	DRY-SW	DRY-EU	WET-SW	WET-EU
Tmax mean	24.5°C	23.6°C	23.8°C	28.1°C	23.4°C	22.4°C
Heat wave days	23d	17d	18d	55d	19d	10d
Hot day (>30°C)	13d	5d	6d	32d	3d	1d
P mean	2.1mm/d	2.1mm/d	2.1mm/d	1.3mm/d	2.1mm/d	2.3mm/d

IP JJA 2015	OBS	CTRL	DRY-SW	DRY-EU	WET-SW	WET-EU
Tmax mean	30.0°C	29.7°C	31.5°C	32.1°C	27.6°C	27.4°C
Heat wave days	35d	32d	47d	55d	3d	3d
Hot day (>30°C)	53d	49d	67d	69d	32d	29d
P mean	0.7mm/d	0.7mm/d	0.6mm/d	0.4mm/d	0.8mm/d	0.8mm/d

The comparison of the observed and modelled mean temperature of COSMO CLM-2.8km with 23.6 °C shows lower values than in the E-OBS data with 24.5 °C. Despite a higher mean temperature in the IP

subdomain, the difference is smaller with 0.3 °C in summer 2015. The underestimation in ME Tmax 2m is mainly seen in the hot maxima. One reason for the differences could be the different grid spacing of the two data sources, the COSMO simulation has a spatial resolution of 3 km while the E-OBS has a spatial resolution of about 30 km. In the summer of 2003, the negative bias of COSMO CLM-2.8km simulation is smaller with approx. -0.3 °C in the ME subdomain and slightly higher in the IP subdomain with approx. 0.5 °C (App. B.3). Nevertheless, in both regions the identified heat wave periods of the COSMO reference simulation are consistent with the observations. Such periods are illustrated by red shaded areas in Fig. 7.14a+b. The main heat wave periods in the ME region in early July (02-06.07.2015) and August (06-14.08.2015) are represented. In addition, the dry and hot July 2015 is identified in the IP region. For the quantification of dry extremes in JJA, the total number of days of the heat wave duration fulfilling the criterion of Jaeger and Seneviratne (2011) (hereafter abbreviated as heat day) and the number of hot days with spatial-mean temperature above 30 °C are taken into consideration. Special attention is given to the modification of these days in the MOD-DRY simulations. In the comparison of the heat and hot days in JJA 2015 with E-OBS observation the number of days in the CTRL simulation is again underestimated by 60 % for heat days and by 30 % for hot days (Tab. 7.5). In JJA 2003 the number of hot days and the days of heat wave duration between E-OBS and COSMO CLM-2.8km simulations are more consistent and the model underestimation is about 10 % (App. B.3). In the IP subdomain the hot days in both summers are higher with 53-54 days in the E-OBS data and in the COSMO-CTRL the underestimation of about 10-30 %. The observed days of heat wave duration varies between 32d and 35d with the modelled underestimation is about 10-20 %. In the comparison between observed heat and hot days in both summers a similar number of days could be found in both indices although in summer 2003 the maximum mean temperature was +1.5 °C higher in the ME region and +0.8 °C higher in the IP region than in summer 2015.

In the DRY-SW modification the mean value of Tmax 2m in the IP domain increases by +1.8 °C and the number of hot and heat days increase by +40 % (67d) and +50% (47d). The mean precipitation changes decrease slightly. Fig. 7.14c shows an increase of several heat periods in July 2015, which extends to a long heat wave period and additionally three shorter heat wave periods occur. In the ME region, a remote effect leads to a slight increase in the spatial mean temperature and an increase in the duration of the heat wave by +5 % and on hot days by +15 %. The second heat wave in August 2015 is affected. The effects seem to be small, but it has to be considered that the modification counts for the entire subdomain and from the previous result a high variability of the local modification in the ME subdomain was demonstrated. In the summer of 2003 the remote effect of the DRY-scenario is larger with 3 additional heat days (+15 %) and 4 hot days (+30 %). Both indices are essential extension of the already existing heat wave periods in July and August 2003. The comparison with the results of the MOD-EU simulations shows a further increase of the mean value Tmax 2m for the IP region of about +0.6 °C in JJA 2015 (Tab. 7.5). The days of the duration of the heat wave and the hot days increase further by another 8 days and by another 2 days. The main factor for an extension in heat wave duration is the

reduction in precipitation by -40 %, as shown in the previous section. This decrease in precipitation is also caused by a remote feedback of drying of the continental European soil moisture. Taking into account both local and remote effects the duration of heat waves in the IP subdomain increases by 70 % (factor 1.7) and the hot days by 40 % (factor 1.4) in summer 2015. Similar increase factors are found in the IP subdomain for 2003, with an increase of 1.6 on hot days and 1.7 on the length of heat waves.

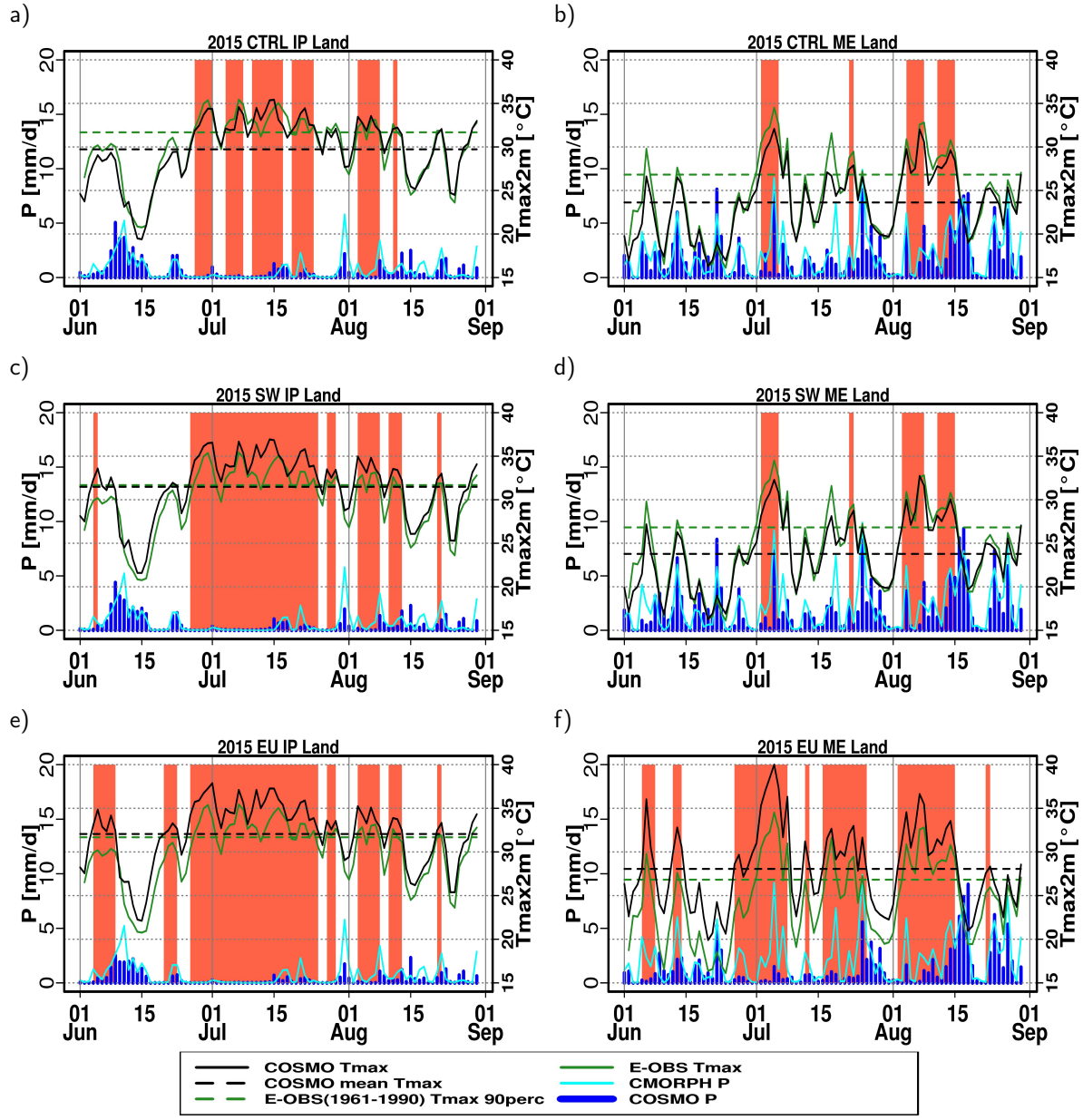

Figure 7.14.: Temporal evolution of the daily spatial-average Tmax 2m and precipitation with the determined heat wave periods in JJA 2015. a+b) show the spatial mean conditions of COSMO CLM-2.8km CTRL simulations, c+d) the simulations of DRY-SW scenarios and e+f) the corresponding simulations of the DRY-EU scenario respectively for the IP and ME regions. The blue colour lines indicate observed and simulated precipitation and the black lines illustrate the simulated Tmax 2m of the respective simulation scenario where solid lines represent the daily values and the dashed lines the mean of JJA. The green line shows daily E-OBS observations and the dashed green line the 90th percentile of E-OBS Tmax in the period 1961-1990.

In the ME subdomain the spring drying in continental soil moisture has a larger effect on temperature of about +4 °C and the heat wave duration extended by a factor 3 and hot days become 6 times more frequently compared with the reference simulation. From Fig. 7.14f the two main heat wave periods are extended and further heat wave periods are generated. Especially already existing heat wave periods become more extreme. An impressive example is the day of temperature recording in Germany on July 5, 2015, when the spatially average maximum temperature in the ME subdomain rises from 32 °C in the CTRL to 40 °C in the MOD-EU (+8 °C). Similar to the IP subdomain the increase in temperature and the reduction of precipitation contribute to an increase in the heat wave signal. In the summer of 2003 similar increasing factors of 3 for the duration of the heat wave and a factor of 4 for hot days were found in the ME subdomain (App. B.3). App. B.9 shows the large extension of the heat wave duration from 25d to 78d (300 %), in which almost the entire summer period 2003 becomes an outstanding heat wave period.

Finally, the effect of the wet SM scenarios on the heat wave duration and hot days is verified. In the WET-EU scenario the mean temperature is reduced by -1.2 °C and the seasonal mean precipitation in the ME region is increased by about +10 %. The resulting effect on the days of heat wave duration is a reduction of about -40 % and on the hot days of about -80 %. In the IP region the mean temperature decrease is about -2.3 °C and the precipitation reduction is -15 %. The MOD-EU wet scenarios lead to a reduction of the hot days of about 40 % and 90 % of the heat wave periods disappear. In summary, it can be said that the modification of the initial spring SM has a large influence on the determination of heat wave periods and extreme temperatures.

7.5. Discussion and Conclusions

Relevance of SM-atmosphere interactions in convection-permitting simulations for the amplification of dry extremes in the WMed

In two SM sensitivity experiments with convection-permitting simulations for continental Europe, the initial spring SM conditions were modified exclusively in the southwestern Mediterranean region (MOD-SW) and throughout continental Europe (MOD-EU) to analyse SM-atmosphere interactions (Fig. 7.2). For each SM sensitivity experiment, the summer periods 2003 and 2015 were initialised with a wet and dry initial scenario. The local and remote effects of SM-atmosphere feedbacks are investigated in the target region of ME and IP. In both summers the dry initial SM perturbation is about +50 % and the wet initial SM modification is between +25 % and +75 % whereby the initialisation signal in 2003 is stronger because the reference soil conditions of 2015 were already drier. The E-OBS and CMORPH observations show for the IP and ME target regions that JJA 2003 was +1 °C warmer in the mean temperature and 25 % drier than 2015. The comparison with the observations shows a good agreement in the temporal evolution of the daily Tmax 2m, the precipitation and the identified heat wave periods with seasonal simulations and thus gives confidence in the performance of COSMO CLM-2.8km.

In the analysis of the initial perturbation of soil moisture a clear SM-atmosphere coupling is found in the summer season. The initial SM modification in late spring influences the partitioning of surface fluxes and atmospheric conditions on a seasonal scale. In the dry initial scenarios the latent heat flux decreases and the sensible heat increase corresponds with an increase of the Bowen ratio. The reduction of the seasonal latent heat flux is directly associated with an average JJA decrease in surface moisture and total integrated water vapor. Due to the absence of moist convection, the atmosphere becomes more stable in the mean JJA conditions as in the CTRL simulation. The total and especially the low cloud cover are reduced which leads to a higher incoming solar radiation.

The dry initial southwestern SM perturbation affects locally and remotely the SM-atmosphere coupling. About 10-20 % of the local seasonal anomaly of SM-atmosphere interactions are transported to the remote region of Central Europe where no SM is disturbed. In the reverse geographic direction the remote effect of dry spring SM initialisation in continental Europe increases the seasonal anomaly of humidity, static stability and cloud cover in the IP by about 30-50 %. Vautard et al. (2007) concluded in their modelling analysis using a convection-parametrised resolution of about 30 km that such a remote drought influence from Northern Europe to the Mediterranean plays a minor role. The results presented in this thesis demonstrate in the convection-permitting simulation of the MOD-EU SM sensitivity experiments also a strong coupling between the SM drying of continental Europe and the change of the Mediterranean atmospheric seasonal conditions.

The response of JJA maximum temperature in 2 m (Tmax 2m) to the dry initial scenario is an increase of about +2.5 °C in the IP region and of about +4.5 °C in the ME region with local seasonal mean Tmax 2m anomalies above +7.5 °C. The future projections of 42 global models of the Coupled Model Intercomparison Project Phase 5 (CMIP5) (Taylor et al., 2012b) indicate in the RCP4.5 scenario the same increase signal of +4.5 °C for Central Europe for the summer season JJA until the end of the 21st century (Christensen et al., 2013). Also for the Mediterranean, half of the increased signal of +5.5 °C in Tmax 2m in JJA is reached only by the dry SM initialisation in late spring. Even though the dry SM initialisation is extreme, it demonstrates the high sensitivity of the maximum temperature to soil moisture conditions and underlines the importance of understanding the feedback mechanism of soil moisture. In addition, the “extreme SM initialisation" demonstrates that the summers could become been even more extreme. The already existing observed anomaly in JJA 2003 is doubled and the anomaly of JJA 2015 is increased by a factor of 1.5. The rise in temperature is accompanied by a decrease in precipitation of about -40 % in the DRY-EU scenarios. On the contrary, in the WET-EU scenarios the seasonal mean of the Tmax 2m is reduced by -1.5 °C with locally negative anomalies down to -4.5 °C. In addition to the temperature rise the mean JJA precipitation increases by +20 %.

Remote SM sources were responsible for 50 % of this precipitation modification and for 30 % of the temperature anomaly. For this reason, the size of the study area must be carefully selected when using high-resolution simulations. In accordance with Vautard et al. (2007) and Zampieri et al. (2009) in coarse model resolution studies, the remote transport of heat signals from the southwestern Mediterranean to

Central Europe could be represented in the performed convection-permitting simulation. Local SM feedback mechanisms in the ME region are induced by the transport of the southwestern Mediterranean heat signal to the ME region, as SM has dried further and sensible heat flux and temperature have increased. Moisture and cloudiness are reduced, which increases incoming solar radiation and affects soil moisture again. The large-scale conditions are influenced by local SM modifications that reinforce the anticyclonic conditions in Southern and Central Europe. The comparison with Zampieri et al. (2009) shows in the COSMO CLM-2.8km simulations a further propagation of the transported heat signal to remote areas of northeastern Europe. The local and remote temperature signal of the DRY-WET range in July is comparable to the local modification of 5-6 °C in 1994 in Vautard et al. (2007) and 2-5 °C in the 10 hottest summers from 1948-2005 in Zampieri et al. (2009) with -1.5 °C to +6 °C in July 2003 and 2015 in the COSMO CLM-2.8km simulation. The found remote signal of about +2 °C in the ME region also agrees with these studies. Differences can be seen in a more patchy structure of anomalies in the high-resolution COSMO CLM-2.8km simulation which are related to different signs of precipitation response which also lead locally to more precipitation associated with higher latent heat flux, soil moisture content and clouds. Such a structure could not be found in coarser resolutions and underlines once more the importance of convection-permitting simulation for the representation of precipitation and the resulting SM-precipitation feedback.

Another result is that the length of the heat wave periods and the number of hot days in the summer season are very sensitive to the modification of late spring SM. In this respect, the feedback signal from SM to Tmax 2m and precipitation are the decisive factors determining the number of hot days and the duration of heat waves. Extreme drying of the SM initial conditions increases the dry extreme indices by a factor of 3 in the ME subdomain and by a factor of 1.5 in the IP subdomain. On the other hand, the wet extreme scenarios reduced the hot days and the duration of the heat wave in the drought summers 2003 and 2015 by -50 %. In summer 2015, the number of hot days in the Mediterranean region is even reduced by 90 %. These results are consistent with the findings of Fischer et al. (2007a,b) who concluded that interactions between soil moisture and temperature increase the duration of the heat waves and account for 50-80 % of hot days. They showed for 2003 that without soil moisture feedback the surface temperature anomalies would have been reduced by 40 % and the JJA 2003 would have been a warm but not an extreme summer. The results of this thesis demonstrate a clearly stronger effect in the impact of dry SM initialisation in convection-permitting simulations to the duration of heat wave and the number of hot days with an increase of +300 % in summer 2003 in the ME subdomain. Moreover, this increase is also higher compared to the results of Jaeger and Seneviratne (2011) who used the same physical method for the SM sensitivity studies and found a doubling of the number of hot days in the heat wave periods of 1976, 1994, 2003 and 2005.

General conclusions to research questions (part 3): contribution of local and remote WMed SM-atmosphere interactions on the development of heat waves in continental Europe considering convection-permitting modelling.

- Summer seasonal mean SM-atmosphere interactions are highly sensitive to the initialisation of spring SM in the WMed and Central Europe in convection-permitting simulations. Drier spring SM conditions reduce the seasonal mean latent heat flux by -80 % and the near-surface moisture by -25 % which leads to a mean stabilisation of the atmosphere (-75 %) and a reduction in the low cloud cover of about -60 %. At the same time the seasonal mean sensible heat flux increases up to +90 % and the incoming solar radiation at surface increases up to +10 % due to less low cloud cover.

- Strong SM-atmosphere coupling leads to SM feedbacks on temperature, precipitation and large-scale circulation. Drier initial SM conditions increase seasonal domain-average maximum temperature in the ME region up to +4.5 °C and up to +2.5 °C in the IP region and precipitation is reduced by about -40 % in both regions.

- The extent of these modifications from non-local sources is 50 % for precipitation and 30 % for temperatures. On the one hand, the changes in southwestern Mediterranean SM conditions induce remote feedbacks to Central Europe, on the other hand, as a new aspect the remote effect of initial spring SM conditions in continental Europe accounts for 50 % of the precipitation reduction and 25 % of the temperature increase in the IP region.

- The main relevant processes for the remote heat propagation from southwestern Mediterranean to Central Europe are: the advection of hot air from the initially modified SM over the Mediterranean region, a local SM-temperature feedback to this advected air masses and the maintenance of anticyclonic blocking due to the initial SM perturbation.

- The initial SM in spring is a key regulator influencing the severity of heat waves in hot summers. In both hot summers of 2003 and 2015 the number of hot days and the duration of heat waves are increased by a factor of 3 (+300 %) in the ME region and by a factor of 1.5 (+150 %) in the IP region. Contrary, the wet initial SM reduces the duration of heat waves in 2015 up to 90 %.

8. Summary and Conclusions

The Western Mediterranean (WMed) is prone to extreme phenomena such as heat waves and heavy precipitation events (HPEs) which lead to hundreds of millions of euros in damage each year and cause a high number of fatalities. Because this region is highly sensitive to climate change, an intensification of dry and wet extremes is expected until the end of the 21st century (Giorgi et al., 2011; Christensen et al., 2013; Tramblay and Somot, 2018). The increase in the severity of extremes will have a crucial socio-economic impact on more than 450 million people living in the Mediterranean countries.

Relevant processes for the prediction of such extreme events are large-scale atmospheric drivers, stochastic processes, local-to-regional feedback mechanisms and the favourable initial state (Sillmann et al., 2017). In the last two processes, soil moisture (SM) plays a central role because it controls the partitioning of surface heat fluxes in transitional climate regions like the WMed. Soil moisture has a long-term memory in regard to forcing atmospheric processes over land. This is why SM can cause feedbacks to the atmosphere on different time scales. Uncertainties in weather and climate models still exist concerning the inadequate spatio-temporal representation of initial SM and the lack of understanding of SM-atmosphere interactions and their feedback mechanisms.

The aim of this work was to enhance knowledge about the impact of SM-atmosphere interactions and feedback mechanisms on the representation of dry and wet extremes in the WMed. To achieve this objective, high-resolution modelling and observations are required for a correct representation of the trigger processes and the development of extreme events. The Special Observation Period 1 (SOP1) campaign of the HYdrological cycle in the Mediterranean EXperiment (HyMeX) collected an unprecedented number of observational data sets focusing on wet extremes within the WMed in autumn 2012. Additionally, the recently released 1 km satellite-derived SSM SMOS-L4 3.0 data give new opportunities to improve the initial conditions of weather and climate models. In this thesis, the state-of-the-art SMOS-L4 SSM data and the HyMeX in-situ observations are combined with high-resolution modelling across temporal and spatial scales. A multi-scale modelling approach with COSMO was developed considering relevant atmospheric processes from sub-daily time scales (for the study of convective precipitation) up to seasonal scales (for the investigation of heat waves). These simulations were performed in convection-permitting resolutions ($\sim$3 km) for the whole WMed up to continental Europe to cover fine-scale and convective processes and to identify local and remote effects of SM-atmosphere interactions. Different sensitivity and realistic SM initialisation experiments were conducted to prove the modification of the atmosphere conditions to changes in the initial SM status. The autumn period 2012 and the summer periods 2003 and 2015 were chosen for these experiments. The effective drought index (EDI) and convective adjustment

time-scale (τ) indicated favourable conditions for SM-atmosphere interactions in these periods. The major conclusions and findings of this thesis on the research questions of the three parts of the analysis can be summarised as follows:

1. To assess the relevance of the SM-atmosphere interactions on the representation of extreme precipitation in the WMed, a sensitivity experiment with extreme initial SM was conducted for the autumn season of 2012. Special attention was given to the comparison of the SM-atmosphere interactions and the sign of SM-precipitation feedback between convection-parametrised and convection-permitting model simulations.

   a) **High-resolution seasonal simulations improve the representation of precipitation over complex terrain in the WMed.** Hourly and sub-daily rainfall intensities in autumn 2012 were better simulated in the convection-permitting control simulation than in the convection-parametrised control simulation in which these precipitation amounts were underestimated. Furthermore, the seasonal representation of convective precipitation over land and above mountain summits was improved in the convection-permitting resolution as the validation with observations has shown.

   b) **Besides the Mediterranean Sea, the initial SM sensitivity studies show that Mediterranean SM variability also contributes to atmospheric conditions leading to heavy precipitation (HP) as an important conditional instability source.** Extreme wet and dry SM initialisation modified the atmospheric conditions. The wet SM initialisation increased the seasonal mean latent heat flux and the near-surface moisture over land by about +10 % in the WMed. This moisture anomaly was transported to the whole troposphere and led to seasonal destabilisation of atmospheric conditions, indicated by an increase of CAPE by about +30 % and a more unstable large-scale condition indicated by a negative geopotential height at 500 hPa (z500). The modified atmospheric conditions induced intensified moist convection which increased the mean low cloud cover by about +20 %. The reduction of the seasonal mean sensible heat flux and the temperature in 2 m (T2m) of about -1 °C did not compensate the increase in instability and convection of additional moisture. This effect is also revealed by an increase of about +15 % in the surface net radiation flux (Rn) which represents a larger total energy flux from surface to atmosphere. The opposite effect was found for the dry SM initialisation in which dry SM initial conditions caused a decrease in R_n, instability and low cloud cover.

   c) **In seasonal mean conditions, the identified SM-atmosphere interactions lead to a positive SM-precipitation feedback in the WMed. This applies to both the convection-permitting and the convection-parametrised model resolution.** The WMed was subdivided into the moderate wet regional domains of FR and IT and into the regional semi-arid domains of IP and NA. The SM-atmosphere interactions found in the wet SM initialisation

showed an increase in seasonal domain-average precipitation in all subdomains up to +25 % in semi-arid regions. Whereas the dry SM initialisation led to a seasonal decrease of precipitation in all subdomains up to -10 % in the FR region. These SM-precipitation feedbacks were positive in both the wet and the dry scenarios. Comparisons between model resolutions revealed a stronger feedback in the convection-parametrised resolution due to a stronger modification of the stratification in the atmosphere (higher IWV amount and stronger negative z500 signal). This more pronounced signal could be a result of the Tiedtke parameterisation as found in a previous study by Hohenegger et al. (2009).

d) **Depending on the regional climate conditions, the effects of the initial SM conditions on extreme precipitation vary. Extreme wet SM initial conditions lead to more frequent and intense extreme precipitation in semi-arid regions while extreme dry SM initial conditions increase the hourly extreme precipitation intensities in autumn 2012.** The wet initial scenario showed in the semi-arid regions an increase of all wet days and extreme wet days with accumulated precipitation up to 300 mm/day. In such regions the modifications of the seasonal atmospheric conditions induced by wet SM initial conditions caused far more extreme events in this period. An increase was found up to +45 % for days with extreme precipitation (between 100 mm and 150 mm). In the dry initial scenario, the modification of seasonal mean atmospheric conditions reduced the frequency of extreme events over semi-arid regions. On the other hand, in the moderately humid FR subdomain extreme events occurred more frequently and were more intense under dry SM initial conditions.

2. The benefit of a realistic SM initialisation with state-of-the-art 1 km satellite-derived SSM SMOS-L4 3.0 data was proved for convection-permitting precipitation modelling of different selected HPEs affecting the IP domain in autumn 2012.

   a) **A strategy was developed to obtain a daily, bias-corrected SMOS soil moisture profile product.** The validation with ground-based measurement exhibited the best agreement of the SSM SMOS-L4 3.0 descending product with the observations. The created two-day running mean L4-D2 product significantly increased the daily data availability in the investigation domain. Furthermore, a systematic bias between COSMO modelled and satellite-derived SMOS-L4 SSM data was corrected with the CDF-matching method. An adapted version of the CDF-matching method kept the SMOS-L4 SSM representation and improved 50 % of the RMSD of each ground-based network. Finally, a well-established exponential filter method was used to derive SM profiles from SMOS CDF-D2 SSM. Validation with ground-based observations demonstrated that the created SMOS L4-Expo product improves the wet bias of the COSMO-2.8km standard SM profile.

b) **Realistic SM initialisation with high-resolution SMOS data improves the representation of HPEs in autumn 2012.** An ensemble of 25 runs with different initial times of the four selected HPEs showed that the bias-corrected SMOS L4-Expo SM enhanced the amount and the spatial accuracy of simulated precipitation fields in the selected HPEs. The initial time experiment revealed an optimal time of realistic SMOS initialisation of 3 days in advance. This result is in accordance with findings of Duffourg and Ducrocq (2011) who stated that a time scale of about 3 days is required for the low-level transport of remote moisture sources feeding HPEs in southeastern France under anticyclonic conditions.

c) **The simulation with SMOS-L4 SM initialisation demonstrates in a case study an enhanced representation of the triggering processes of a convective heavy precipitation event.** A heavy precipitation event under weak synoptic conditions in the Pyrenees on September 9, 2012 was selected. On this day, the control simulation did not correctly represent the precipitation peak. In this specific case the SMOS L4-Expo SM initialisation locally reduced the SM at the summit of the mountains. As a consequence, the atmospheric conditions were modified by higher sensible heat fluxes, near-surface temperature and boundary layer height. A stronger temperature gradient between summits and foreland as well as between land and sea induced a stronger thermally-driven wind circulation. Additional unstable moist air masses from remote sources reached the investigation area 3 days after the SMOS L4-Expo SM initialisation with modified wind circulation and converged with local near-surface moisture at the foothills of the mountains. The combination of additional moisture and a stronger thermally-driven wind circulation led to strong moisture convergence and orographic lifting, which were the required missing triggering mechanisms for convective precipitation in this case study. These trigger mechanisms of convective precipitation were not represented by the reference COSMO-2.8km simulation.

3. The impact of SM-atmosphere interactions on extreme temperatures and heat waves was investigated for the WMed and Central Europe in the summers of 2003 and 2015. Two SM sensitivity experiments with extreme initial SM modification in spring in the southwestern Mediterranean (MOD-SW) and in the whole investigation domain of continental Europe (MOD-EU) were performed. This was conducted to analyse local and remote SM-atmosphere interactions in seasonal convection-permitting simulations. A local effect is defined as a direct modification of atmospheric conditions in the regions of the initial SM modification. Remote effect is understood either as a modification of the atmospheric conditions in the surrounding regions without initial SM perturbation (SW-simulations) or the difference between the modification signal of MOD-EU minus MOD-SW (signal of continental Europe towards southwestern Mediterranean).

a) **Strong local and remote SM-atmosphere couplings with feedbacks on temperature, precipitation and large-scale circulation are identified. Drying of initial spring SM increases seasonal domain-average maximum temperatures up to +4 °C and reduces seasonal mean precipitation by about -40 %.** Local drier spring SM conditions reduced the seasonal domain-average latent heat flux by -80 % and near-surface moisture by -25 % which led to a mean stabilisation of the atmosphere (-75 % in CAPE) and a reduction in low cloud cover of -60 %. At the same time, the drying of initial SM increased the seasonal domain-average sensible heat fluxes up to +90 % and the incoming solar radiation up to +10 % due to the reduction in the low cloud cover. The wet initial scenarios indicated the same couplings with opposite signs. The drying of initial SM conditions in the MOD-EU domain induced a seasonal mean maximum temperature anomaly of about +2.5 °C in the Iberian Peninsula (IP) region and about +4 °C in the Central Europe (ME) region in both summers. This modification doubled the already existing observed extreme temperature anomaly in both years. In addition, the dry initial scenarios caused a reduction of precipitation by -40 %. The wet initial scenarios showed once again the opposite effect with an increase in mean precipitation and a reduction in mean maximum temperatures. Remote SM sources were responsible for 50 % of this precipitation modification and for 30 % of the temperature anomaly. A novel aspect found in this thesis is that the initial SM drying in continental Europe has a remote effect on the WMed, which accounts for -20 % of the precipitation reduction in the IP region (50 % of the total modification). At the same time, remote feedbacks from the southwestern Mediterranean in the direction to Central Europe were found.

   There were three main relevant processes to explain a remote heat propagation from the southwestern Mediterranean to Central Europe: First, the advection of hot air from the initially modified SM over the Mediterranean regions; second, a local SM-temperature feedback to this advected air masses; and third, the maintenance of an anticyclone blocking situation due to the initial SM perturbation. These three processes agree with previous findings from coarser limited-area modelling studies. In addition, a stronger propagation of heat and remote effects to farther regions in the north and the east of Europe were found. Thereby, the remote signal was strongly influenced by the modification of precipitation structures arising from the use of convection-permitting models which were not found in previous studies using models with coarse resolution.

b) **Soil moisture is a key regulator influencing the severity of heat waves in hot summers.** The extreme dry spring SM initialisation scenarios in continental Europe demonstrated an increase in the number of hot days and the duration of heat waves by a factor of 3 in the ME subdomain and by a factor of 1.5 in the IP subdomain. With a wet spring initialisation the opposite effect was observed. There was a reduction of both dry extreme indices of about -50 %.

Several previous research studies, e.g. Prein et al. (2015); Dirmeyer and Halder (2016); Sillmann et al. (2017), emphasised in their outlook the necessity to represent fine-scale processes and SM-atmosphere interactions in convection-permitting model resolutions to enhance the process understanding and avoid misrepresentation of SM feedbacks. The presented study highlights that it is very important to consider large domains in seasonal convection-permitting simulations. The relevance of using large domains is that in addition to the local SM feedbacks, non-local feedbacks must also be taken into account. The evidence of this are the anomalies of precipitation (50 %) and of temperature (30 %) explained by remote effects. In accordance with the previous results of Fosser et al. (2015) and Prein et al. (2015), an improvement in the representation of convective precipitation in such convection-permitting resolutions on the sub-daily scale has been demonstrated.

The main findings regarding SM-atmosphere interactions and feedback mechanisms in convection-permitting simulations in the WMed are summarised in Fig. 8.1. Extreme dry and wet soil moisture initialisations exhibit positive seasonal feedbacks. Higher/lower initial SM leads to higher/lower moisture and instability in the atmosphere by the partitioning of the surface fluxes. These modifications strengthen/inhibit moist convection which results in a higher/lower amount of cloud cover and precipitation. Positive SM-precipitation feedback means that the wet/dry SM initialisation leads to an increase/decrease in mean precipitation. Furthermore, wet/dry SM initialisation induces a decrease/increase in temperature via lower/higher sensible heat fluxes. This modification intensifies the effect of the original SM anomaly (SM-temperature feedback). On the event scale, single HPE may also show negative SM-precipitation feedback to dry SM initialisation (cf. Chapter 6.3). In such cases, local factors like thermal wind circulation induced by SM drying and/or the advection of moisture convergence lines can cause more precipitation over dry soils (purple arrow in Fig. 8.1). Additionally, SM initialisation can strengthen/weaken the summer anticyclonic blocking conditions indicated by the modification of geopotential height at 500 hPa (z500) as a proxy for large-scale conditions. Therefore, the local initial SM perturbation in the WMed remotely modifies the seasonal large-scale conditions in continental Europe (SM-large scale feedback).

The achieved results of this thesis can be summarised to the general conclusion that soil moisture plays a relevant role for the occurrence of both dry and wet extreme phenomena in the WMed. The sensitivity experiments for the summer and autumn periods demonstrated that SM induces changes in mean atmospheric conditions which lead to seasonal changes in domain-average precipitation between -40 % and +25 % and temperature between -2 °C and +4 °C. In autumn, the wet SM initialisation increases the number of days with extreme precipitation up to +50 %. In summer the soil moisture can act as a strong regulator for the severity of heat waves. In this season dry spring initialisation increases the number of hot days and the duration of heat waves in Central Europe by a factor of three. For the first time, high-resolution realistic SM initialisation was carried out with SMOS-L4 3.0 data revealing that this improved the representation of four simulated HPEs within the WMed.

This study demonstrates that the combination of high-resolution modelling and state-of-the-art observations advance the understanding of SM-atmosphere interactions and feedbacks. These results are assumed to have real applicability for the climate and weather prediction modelling. In a next step, long-term convection-permitting simulations in the WMed can be extended over several years to gain further information about all seasonal and the interannual variability. In order to further improve the future projections of extremes in the WMed, the described realistic SMOS-L4 SM initialisation can be used for high-resolution climate-scale simulations.

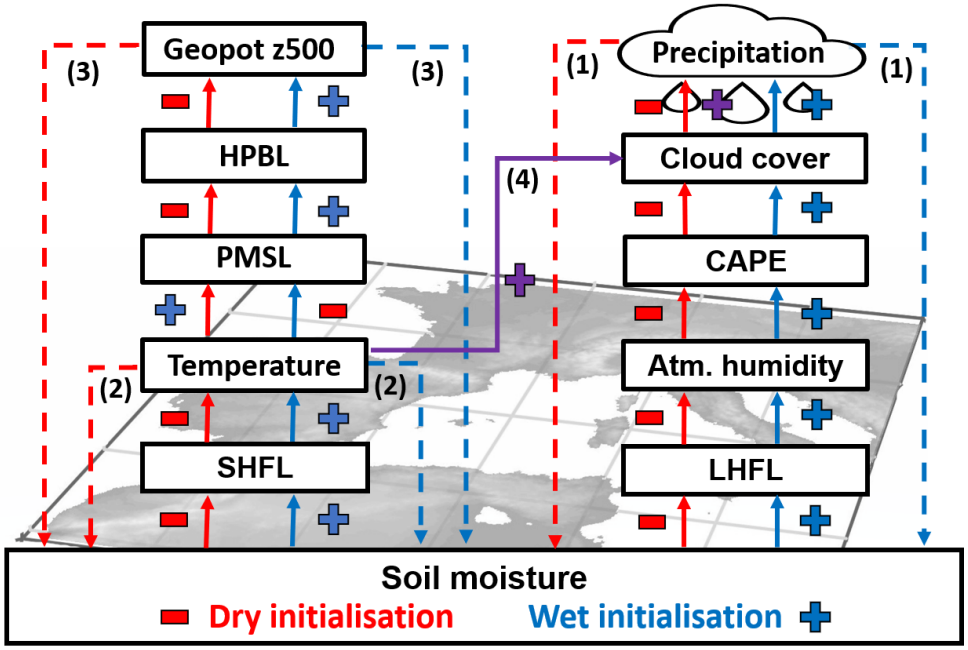

Figure 8.1.: Schematic summary of the seasonal SM-atmosphere interactions and feedback mechanisms which were found in convection-permitting simulations of the WMed in this PhD thesis. The positive signs (blue colours) indicate an increase and the negative signs (red colours) a decrease in the modification of the respective variables. The following variables describe the stability, moisture and heat fluxes: convective available potential energy (CAPE), latent heat flux (LHFL), sensible heat flux (SHFL), pressure at mean sea level (PMSL), height of planetary boundary layer (HPBL) and the geopotential height at 500 hPa (z500). The numbers indicate the most relevant SM feedback mechanisms: (1) Positive SM-precipitation feedback on a seasonal scale (cf. Chap. 5.4 and Chap. 7.3); (2) SM-temperature feedback (Chap. 7.4); (3) SM-large scale feedback (cf. Chap. 7.3.3); (4) On event scale, the impact of regional factors like the thermal wind circulation can also lead to a negative SM-precipitation feedback (cf. Chap. 6.3) which is represented by the purple arrow and positive signs (purple colour).

A. Acronyms

AI Agreement index 48
AMSR-E Advanced Microwave Scanning Radiometer - Earth Observing System 33
AR5 Fifth Assessment Report 2
ASCAT Advanced SCATterometer 33
BA Baleric Islands 42
BEC Barcelona Expert Center 36
CA Catalonia 42
CAPE Convective available potential energy 19
CCI Climate Change Initiative 33
CDF Cumulative density function ii
CI Central Italy 42
CIN Convective inhibition 19
CMIP3 Coupled Model Intercomparison Project Phase 3 9
CMIP5 Coupled Model Intercomparison Project Phase 5 124
CMORPH Climate prediction center MORPHing technique 39
CO Corsica 42
COSMO Consortium for Small-scale Modeling i
COSMO-CLM Consortium for Small-scale Modeling-CLimate mode 52
CTRL Reference simulation 44
CV Cévennes-Vivarais 42
DRY Dry soil moisture initial scenario 44
ECV Essential climate variable 33
EDI Effective drought index 20
EP Effective precipitation 45
ET Evapotranspiration 59
ESA European Space Agency's 33
FR France 42
HCC High cloud cover 59
HP Heavy precipitation 41
HPBL Height of planetary boundary layer 59

B. Appendix

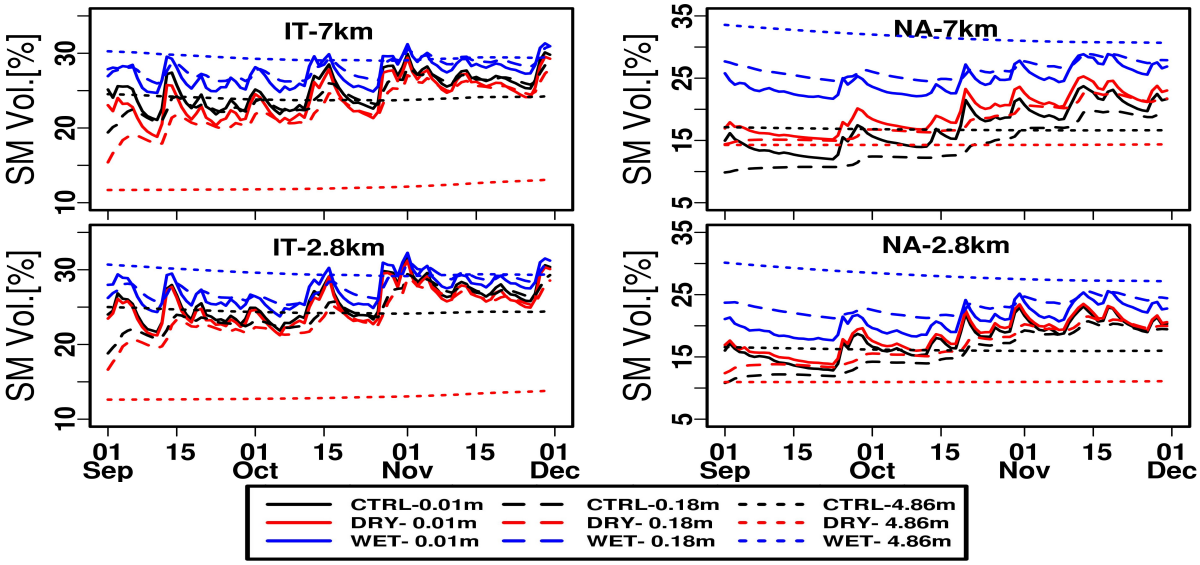

Figure B.1.: Comparison of temporal evolution of daily volumetric soil water content between COSMO CLM-7km and COSMO CLM-2.8km simulations. The domain-average volumetric soil water content is illustrated for different soil layers of the IT and NA subdomain in the sensitivity scenarios and the CTRL simulation.

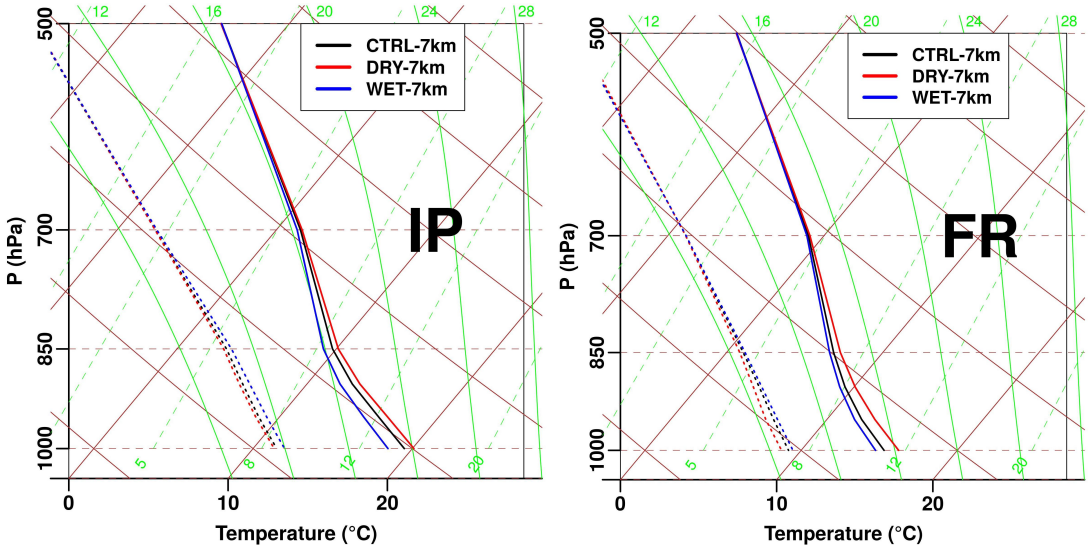

Figure B.2.: Skew-T log-P diagrams of the atmospheric profile for the seasonal mean conditions in COSMO CLM-7km of SON 2012 at 12 UTC. The CTRL profile (black) and both SM DRY (red) and WET (blue) scenarios are shown for the IP and FR subdomain. The solid lines indicate the temperature profile [°C] and the dotted lines the dew point temperature [°C].

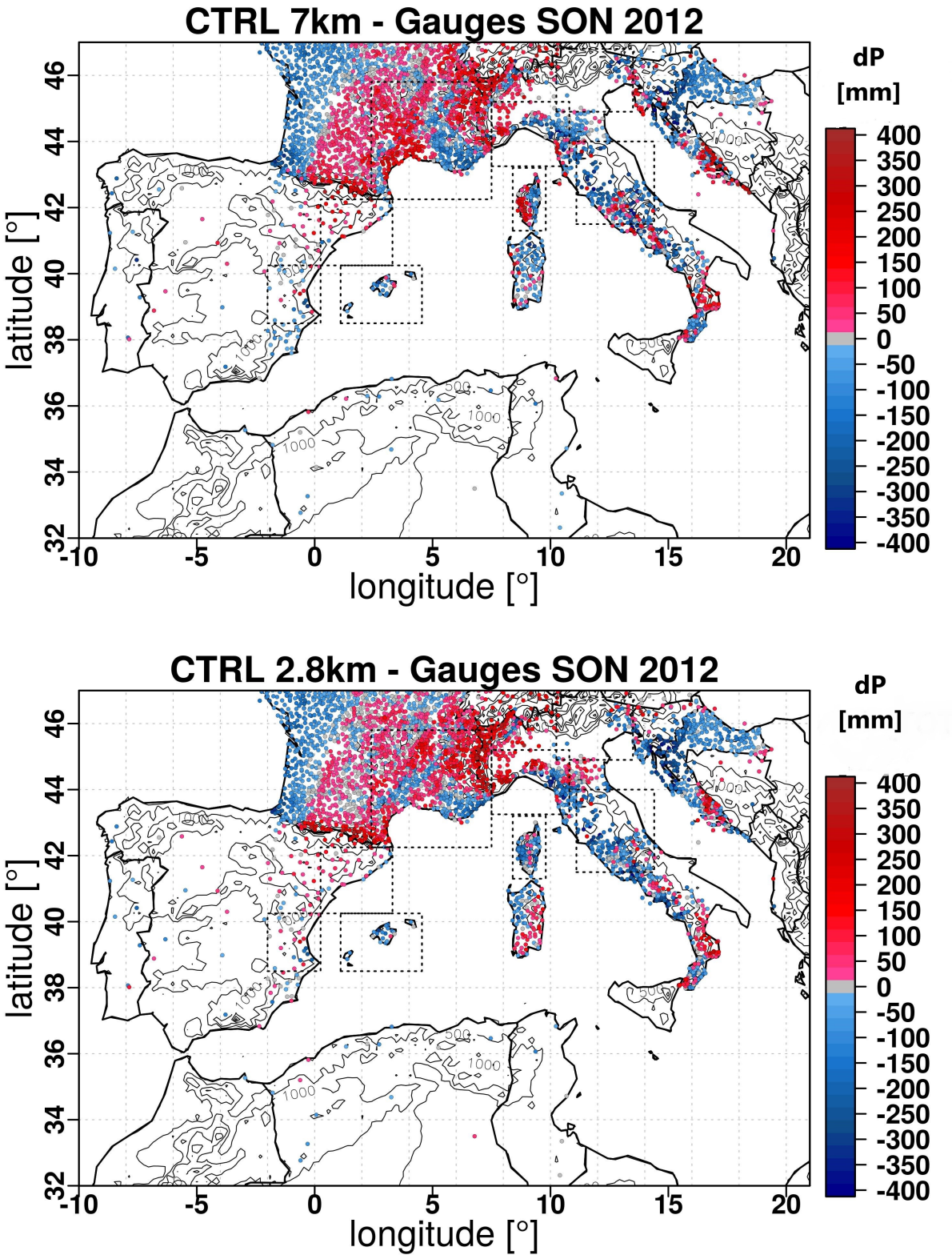

Figure B.3.: Validation of COSMO CLM-7km and COSMO CLM-2.8km simulations with rain gauges. Only rain gauge stations with daily accumulated precipitation in the whole SON 2012 period are selected. The nearest grid point of the model simulation to a rain gauge station is used to calculate the differences in accumulated precipitation in SON 2012.

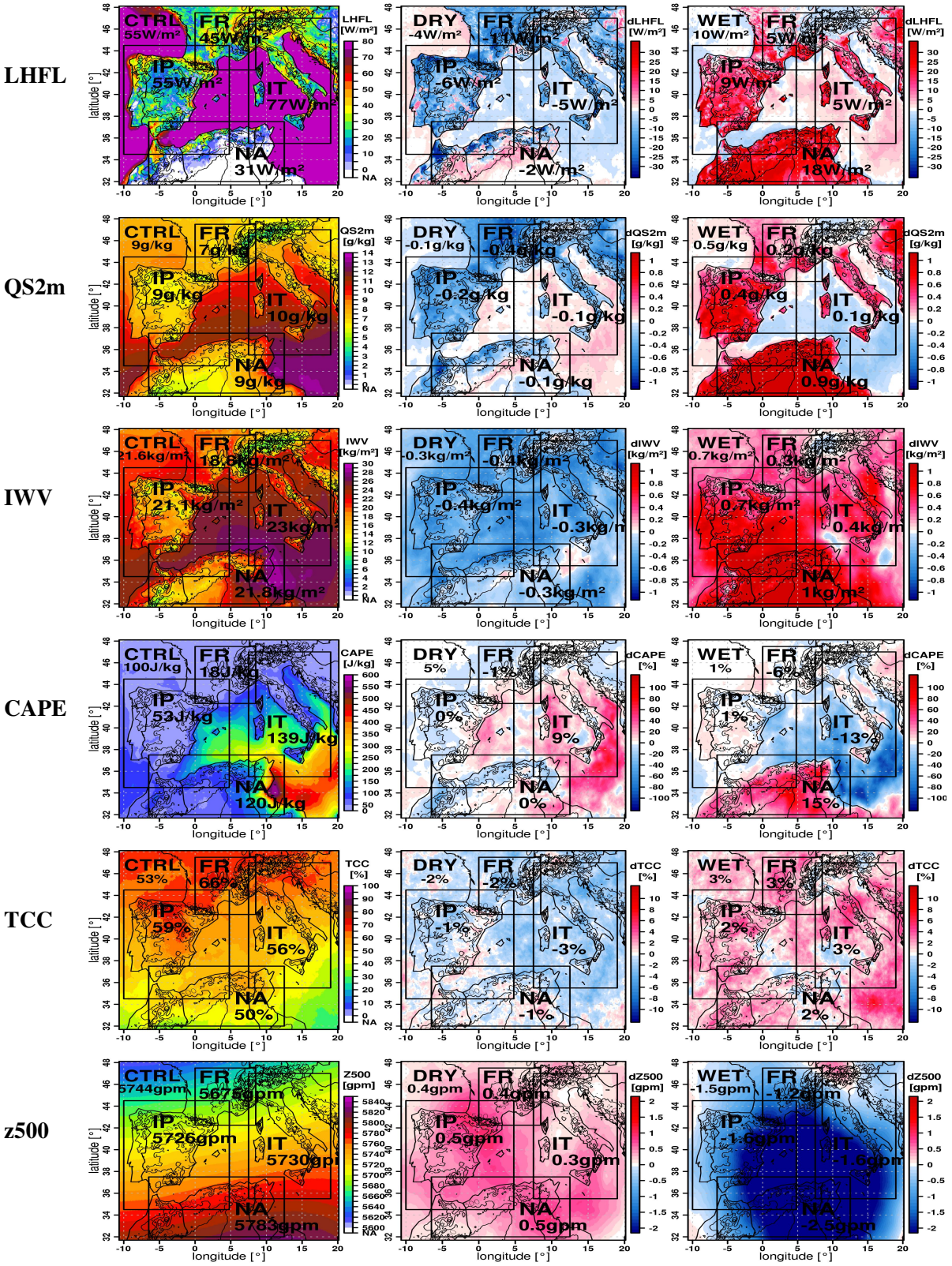

Figure B.4.: Seasonal atmospheric mean conditions of the reference simulation (CTRL) COSMO CLM-7km in autumn 2012 and their seasonal mean differences for the simulation of the SM sensitivity experiment. The first column presents for the CTRL simulation from top to bottom: latent heat flux (LHFL), the specific humidity in 2 m (QS2m), the integrated water vapour (IWV), the total cloud cover (TCC) and the atmospheric stability represented by CAPE. The second column illustrates the modification of these variables as the difference of the DRY-scenario minus the CTRL and the third column as the difference of the WET-scenario minus the CTRL. The four regional subdomains are indicated by black boxes with spatial-mean values of each subdomain.

Table B.1.: Seasonal changes of mean atmospheric conditions for the WET-2.8km initialisation scenario in SON 2012. Only land grid points are considered. The percentage change is given in % and the absolute mean conditions are described in brackets for the WMed and the regional subdomains.

WET-2.8km	WMed	NA	IP	IT	FR
ET[CTRL]	+85%[61mm]	+240%[31mm]	+60%[85mm]	+35%[99mm]	+20%[108mm]
Rnet[CTRL]	+20%[34W/m^2]	+25%[38W/m^2]	+10%[39W/m^2]	+10%[29W/m^2]	+2%[27W/m^2]
QS2m[CTRL]	+10%[7.2g/kg]	+15%[7.6g/kg]	+10%[7.4g/kg]	+5%[7.6g/kg]	+5%[6.9g/kg]
IWV[CTRL]	+5%[19kg/m^2]	+5%[21kg/m^2]	+5%[19kg/m^2]	+2%[20kg/m^2]	+1%[18kg/m^2]
CAPE[CTRL]	+40%[45J/kg]	+40%[87J/kg]	+25%[28J/kg]	+5%[46J/kg]	-2%[12J/kg]
TCC[CTRL]	+3%[54%]	+2%[49%]	+3%[60%]	+2%[61%]	+3%[67%]
LCC[CTRL]	+20%[18%]	+40%[10%]	+20%[24%]	+10%[25%]	+10%[33%]
SW[CTRL]	-1%[111W/m^2]	-1%[127W/m^2]	-4%[108W/m^2]	-2%[91W/m^2]	-4%[82W/m^2]
SHFL[CTRL]	-45%[22W/m^2]	-40%[36W/m^2]	-70%[20W/m^2]	-175%[5W/m^2]	370%[-1W/m^2]
T2m[CTRL]	-1°C[16.8°C]	-1.5°C[19.8°C]	-1°C[14.5°C]	-0.5°C[13.4°C]	-0.5°C[10.7°C]
PS[CTRL]	+0.5hPa[1016]	+1hPa[1016]	+0.5hPa[1016]	+0.3hPa[1016]	+0.2hPa[1016]
Z500[CTRL]	-1.5gpm[5747]	-2.5gpm[5787]	-1.5gpm[5722]	-1gpm[5711]	-1gpm[5671]

Table B.2.: The number of wet days and the different categories of extreme precipitation days are shown for the CTRL and the WET- and DRY-scenarios of the COSMO CLM-7km simulations in the different subdomains. The total number of days is 91 in the autumn period 2012. Wet days (RR1) are days with a spatial-average precipitation amount >1mm in the subdomain. The days with extreme precipitation are counted if at least one land grid point reaches this daily sum value in the subdomains. An increase in the number of days in the WET- and DRY-scenarios is indicated by green colours and a decrease by red-brown colours.

C2.8km	Wet days >1mm	Days 10-50mm	Days 50-100mm	Days 100-150mm	Days 150-200mm	Days 200-300mm	Days > 300mm
NA-CTRL	**30**	**55**	**31**	**13**	**5**	**2**	**0**
NA-DRY	**30**	**57**	**31**	**11**	**5**	**3**	**0**
NA-WET	**32**	**67**	**37**	**15**	**3**	**1**	**0**
IP-CTRL	**44**	**74**	**47**	**19**	**8**	**5**	**1**
IP-DRY	**44**	**70**	**42**	**16**	**8**	**7**	**2**
IP-WET	**51**	**79**	**53**	**28**	**8**	**2**	**1**
IT-CTRL	**51**	**72**	**57**	**39**	**22**	**8**	**2**
IT-DRY	**50**	**74**	**53**	**32**	**17**	**9**	**2**
IT-WET	**54**	**75**	**59**	**36**	**20**	**13**	**3**
FR-CTRL	**54**	**72**	**40**	**16**	**8**	**3**	**0**
FR-DRY	**50**	**70**	**36**	**11**	**6**	**4**	**1**
FR-WET	**57**	**71**	**47**	**17**	**7**	**2**	**0**

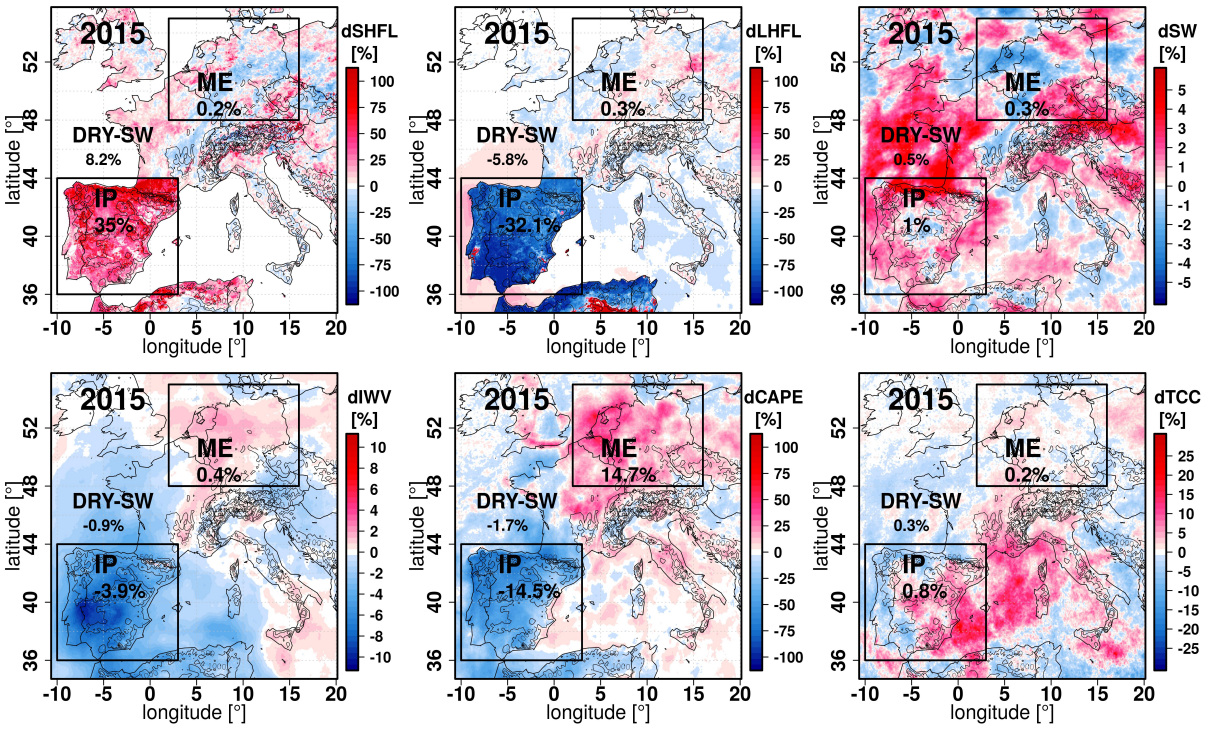

Figure B.5.: Seasonal mean modification of the atmospheric conditions to dry spring SM initialisation in the south-western Mediterranean scenario (DRY-SW) in JJA 2015. The two target areas are indicated by black boxes with spatial averages of the percentage change within the domain.

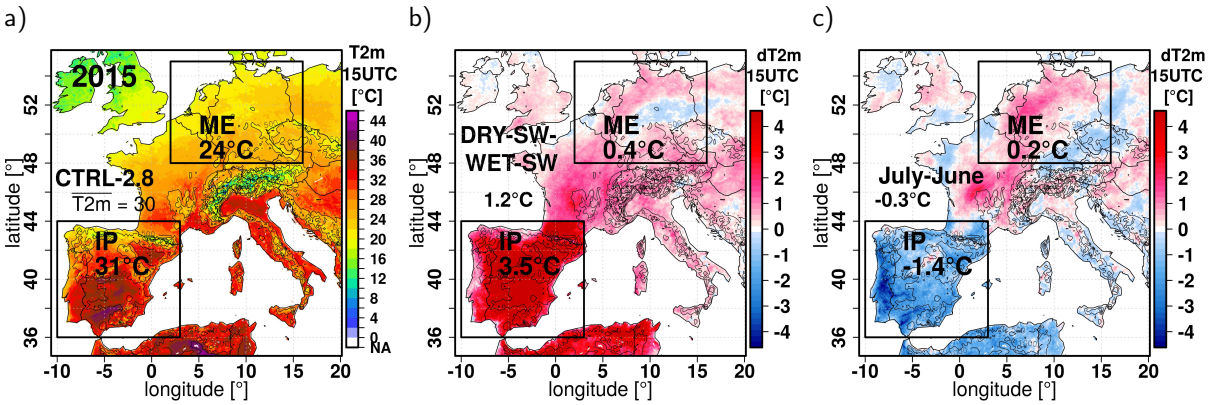

Figure B.6.: Sensitivity simulation of MOD-SW scenario for the temperature in 2 m (T2m) at 15 UTC in July 2015. The illustrations show in a) the monthly mean T2m at 15 UTC, in b) the mean July difference between DRY-SW minus WET-SW at this time. Figure c) illustrates the monthly mean differences of July minus June of the DRY-SW minus WET-SW fields at 15 UTC.

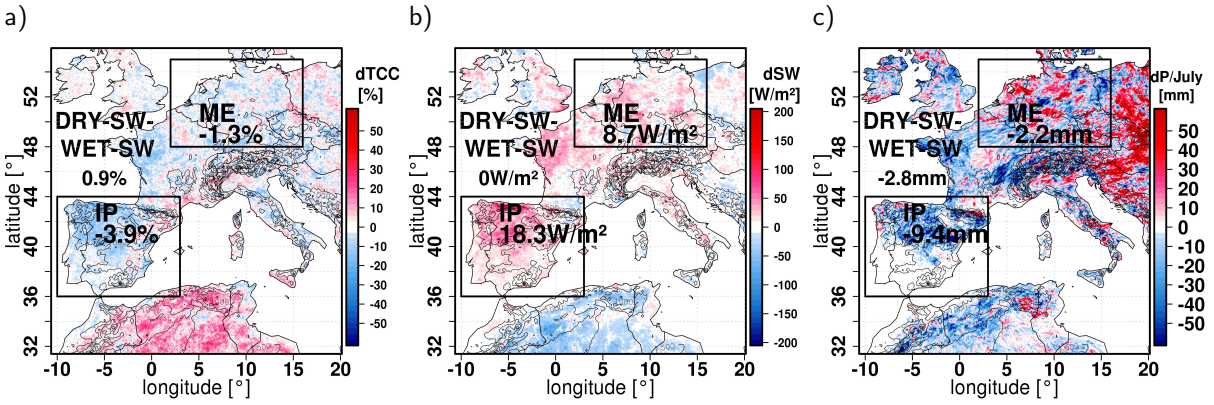

Figure B.7.: Modification of clouds, short-wave radiation and precipitation of the DRY-SW minus WET-SW scenario in July 2003. The figures show in a) the anomaly of total cloud cover (TCC) [%], in b) the anomaly of SW [W/m^2] and in c) the anomaly in the precipitation [mm].

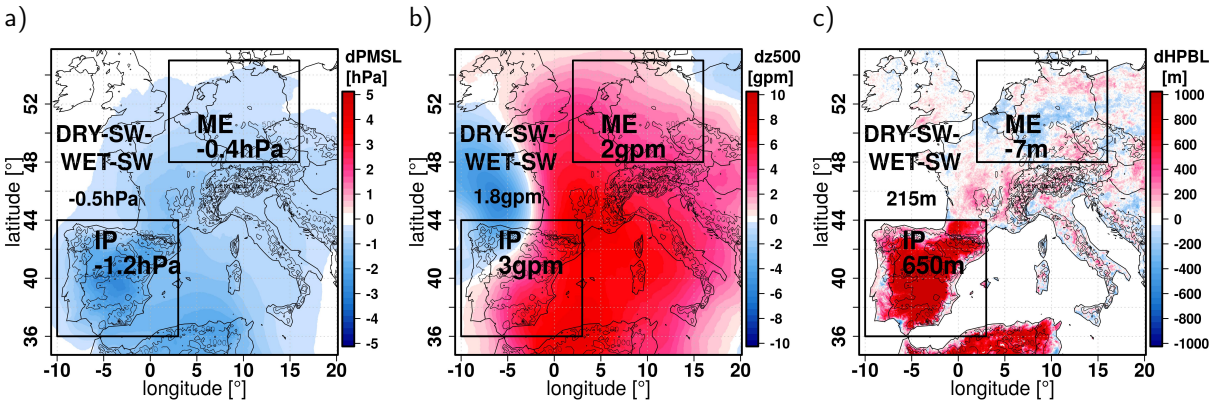

Figure B.8.: Modification of the large-scale conditions of the DRY-SW minus WET-SW scenario in July 2015. The figures show in a) the anomaly of pressure at mean sea level (PMSL) [hPa], in b) the anomaly of geopotential height at 500 hPa [gpm] and in c) the anomaly in the height of planetary boundary layer (HPBL) [m].

Table B.3.: Spatial average of observed and modelled precipitation and dry extreme indices in summer 2003. Observations (OBS) of precipitation (P) are from CMORPH (8 km) and for maximum temperature in 2 m (Tmax 2m) from E-OBS (0.25°). Heat wave days are the number of days of a heat wave duration and hot days are days with an average maximum temperature exceeding 30 °C.

ME JJA 2003	OBS	CTRL	DRY-SW	DRY-EU	WET-SW	WET-EU
Tmax mean	26.0°C	26.3°C	26.5°C	30.1°C	26.2°C	25.0°C
Heat wave days	25d	26d	29d	78d	26d	19d
Hot day (>30°C)	13d	14d	18d	47d	14d	9d
P mean	1.6mm/d	1.5mm/d	1.4mm/d	0.9mm/d	1.6mm/d	1.7mm/d
IP JJA 2003	OBS	CTRL	DRY-SW	DRY-EU	WET-SW	WET-EU
Tmax mean	30.8°C	30.3°C	32.4°C	32.8°C	29.2°C	29.0°C
Heat wave days	32d	26d	52d	54d	21d	17d
Hot day (>30°C)	54d	46d	70d	73d	35d	32d
P mean	0.6mm/d	0.7mm/d	0.5mm/d	0.4mm/d	0.8mm/d	0.8mm/d

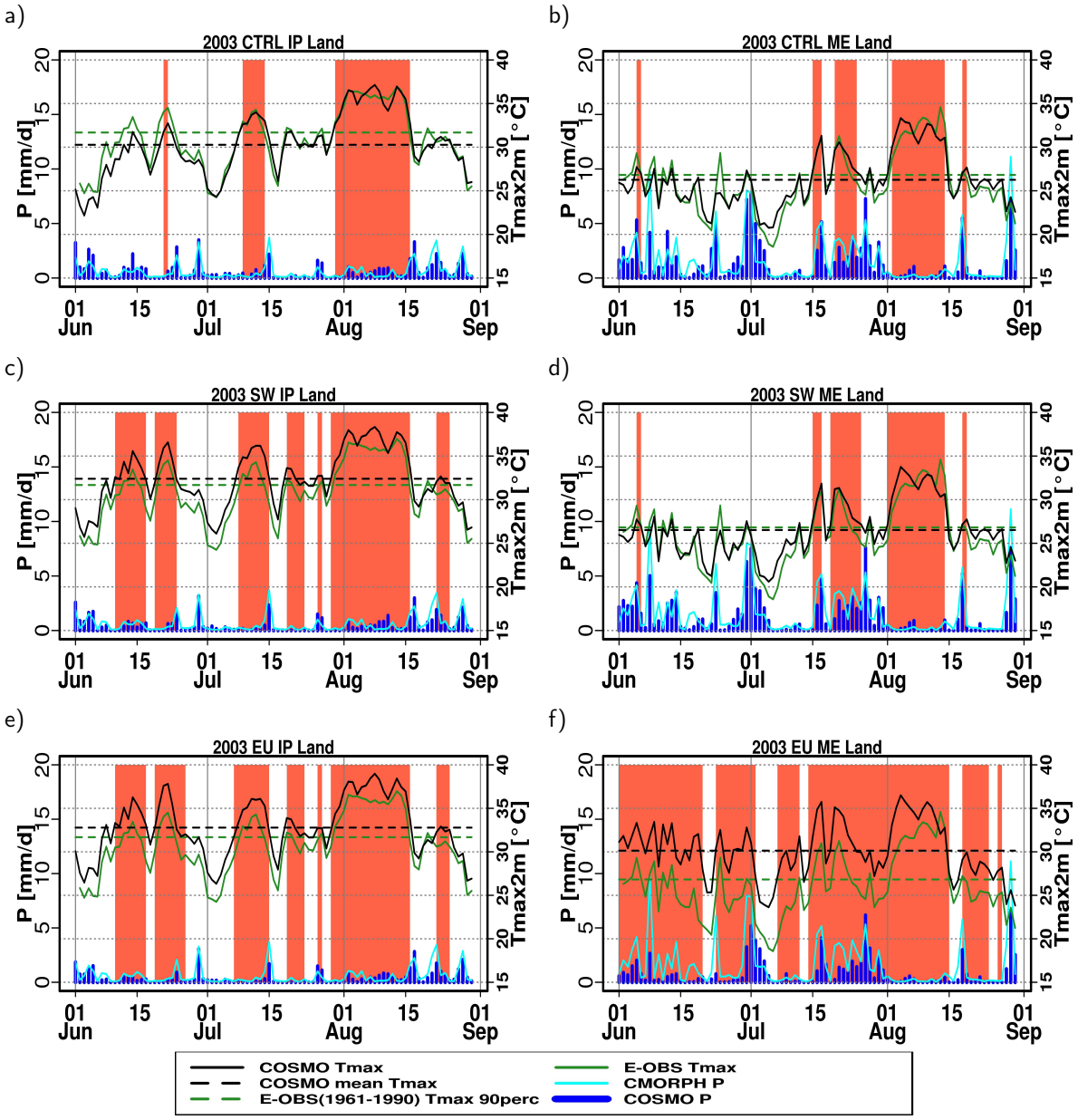

Figure B.9.: Temporal evolution of the daily spatial-average Tmax 2m and precipitation with the determined heat wave periods in JJA 2003. a+b) show the spatial mean conditions of COSMO CLM-2.8km CTRL simulation, c+d) the simulations of DRY-SW scenarios and e+f) the corresponding simulations of the DRY-EU scenario respectively for the IP and ME regions. The blue colour lines indicate observed and simulated precipitation and the black lines illustrate the simulated Tmax 2m of the respective simulation scenario where solid lines represent the daily values and the dashed lines the mean of JJA. The green line shows daily E-OBS observation and the dashed green line the 90th percentile of E-OBS Tmax in the period 1961-1990.

C. Danksagung

Zum Schluss möchte ich mich bei allen Beteiligten ganz herzlich bedanken, die zum guten Gelingen dieser Doktorarbeit beitragen haben.
Allen voran gilt mein Dank Herrn Prof. Dr. Christoph Kottmeier, der als Referent und Institutsleiter meine Dissertation maßgeblich betreut und ermöglicht hat. Die persönlichen Gespräche, die Unterstützung und die inhaltlichen Nachfragen waren während meiner Promotionszeit sehr hilfreich. Herrn Prof. Dr. Joaquim Pinto danke ich für die Übernahme des Korreferats und die engagierte Betreuung meiner Arbeit. Der regelmäßige Austausch, eine jederzeit offene Tür bei Fragen und neue Impulse sowie Anregungen haben mich sehr unterstützt und in meiner Arbeit vorangebracht.
Ein besonders großer Dank geht an meine Betreuerin und Projektleiterin Dr. Samiro Khodayar. Sie hat ermöglicht, dass ich diese Doktorarbeit am IMK-TRO schreiben konnte. Samiros wissenschaftliche Erfahrung und ihre Ratschläge bei gemeinsamen Besprechungen und Arbeitsgruppenmeetings, auf Konferenzen oder auch per Skype und E-Mail haben mich in meiner wissenschaftlichen Karriere am IMK geprägt und sowohl fachlich als auch persönlich weitergebracht. Durch ihre persönliche, herzliche und engagierte Art war die Arbeit während der Promotionszeit immer angenehm und produktiv. Sie hat mich stets gefördert und auch gefordert und so dafür gesorgt, dass der „rote Faden“ dieser Arbeit nie verloren gegangen ist. Vielen Dank Samiro für deinen Einsatz und ganz besonders auch für das Korrekturlesen meiner Arbeit. Ich war immer gern ein Teil deiner Arbeitsgruppe.
Des Weiteren möchte ich mich bei allen bedanken, die mich durch fachliche Diskussionen, Verbesserungsvorschläge und Anregungen unterstützt haben. Namentlich erwähnen möchte ich an dieser Stelle Nicole Albern, Karmen Babic, Marcus Breil, Dominik Büeler und Susanna Mohr sowie mein Studienfreund Tobias Heppelmann. Besonders möchte ich mich auch bei Heike Vogel und Hans-Jürgen Panitz für die technische Unterstützung im Umgang mit dem COSMO-CLM Model bedanken. Für die Weitergabe seiner Erfahrungen rund ums Thema Promotion und Doktorprüfung möchte ich Manuel Schmidberger danken. Mein herzlicher Dank geht ebenso an Johannes Hörner, der mir mit seiner Arbeit als Hiwi in unserer Arbeitsgruppe eine große Hilfe war und mir besonders in der stressigen Endphase der Arbeit sehr geholfen hat. Für sprachliche Korrekturen danke ich außerdem Breandán Ó Corráin.
Vielen Dank auch an alle, die mich während meiner Promotionszeit am IMK begleitet haben. Danke für inspirierende und abwechslungsreiche Gespräche in den Mittagspausen, die oft ein Highlight des Tages waren und für lustige Gespräche am Kaffeeautomaten oder in der Kaffeerunde. Besonders möchte ich auch meinem zuverlässigen Laufpartner Bernhard Vogel für die Joggingtouren rund ums KIT danken, die mir sehr dabei geholfen haben, wieder mit klarem Kopf an den Schreibtisch zurückzukehren. Ich

habe mich am IMK immer als Teil einer großen Familie gefühlt, viele nette Menschen kennengelernt und neue Freunde gewonnen.
Ganz besonders möchte ich mich bei Alberto Caldas-Álvarez bedanken. Wir haben gemeinsam mit der Promotion angefangen und uns auf Anhieb sehr gut verstanden. Wir haben nicht nur fachliche Themen diskutiert, sondern vor allem auch viel gemeinsam gelacht. Alberto, du warst nicht nur der beste Kollege, den ich mir hätte vorstellen können, sondern bist auch ein sehr guter Freund geworden. Vielen Dank für deine zahlreichen inhaltlichen und sprachlichen Anregungen zu meiner Arbeit, für deine mentale Unterstützung und deine Freundschaft.
Meiner Familie danke ich für die Unterstützung, die mich überhaupt erst so weit gebracht hat. Vor allem möchte ich meiner Mutter, Helga Helgert-Hock, danke sagen für die sprachlichen Korrekturen, die wir an vielen Tagen gemeinsam erarbeitet haben. Meiner Mutter hat das Korrigieren dabei zumeist mehr Spaß gemacht als mir selbst. Zu guter Letzt möchte ich mich bei meiner Frau Jasmin bedanken. Du warst für mich die größte Unterstützung während meiner gesamten Promotionszeit. Du hast mich immer wieder ermutigt, motiviert und mich besonders in der Endphase auch mit Korrekturen unterstützt. Vielen Dank auch dafür, dass du mir immer den Rücken freigehalten hast. Das alles bedeutet mir sehr viel.

D. Bibliography

Albergel, C., C. Rüdiger, T. Pellarin, J.-C. Calvet, N. Fritz, F. Froissard, D. Suquia, A. Petitpa, B. Piguet, and E. Martin, 2008: From near-surface to root-zone soil moisture using an exponential filter: an assessment of the method based on in-situ observations and model simulations. *Hydrology and Earth System Sciences Discussions*, **5 (3)**, 1603–1640.

Alpert, P., 2002: The paradoxical increase of Mediterranean extreme daily rainfall in spite of decrease in total values. *Geophysical Research Letters*, **29 (11)**, 2996.

Alpert, P., D. Hemming, F. Jin, G. Kay, A. Kitoh, and A. Mariotti, 2013: The Hydrological Cycle of the Mediterranean. *Regional assessment of climate change in the Mediterranean*, Navarra, A., Ed., Springer, Dordrecht, Advances in Global Change Research, Vol. 50, 201–239.

American Meteorological Society (AMS), 2019: Drought: An Information Statement of the American Meteorological Society (Adopted by AMS Council on 19 September 2013). URL `https://www.ametsoc.org/ams/index.cfm/about-ams/ams-statements/statements-of-the-ams-in-force/drought/`, visited on 31.01.2019.

Barthlott, C. and S. Davolio, 2016: Mechanisms initiating heavy precipitation over Italy during HyMeX Special Observation Period 1: a numerical case study using two mesoscale models. *Quarterly Journal of the Royal Meteorological Society*, **142**, 238–258.

Beaulant, A.-L., B. Joly, O. Nuissier, S. Somot, V. Ducrocq, A. Joly, F. Sevault, M. Deque, and D. Ricard, 2011: Statistico-dynamical downscaling for Mediterranean heavy precipitation. *Quarterly Journal of the Royal Meteorological Society*, **137 (656)**, 736–748.

Beljaars, A. C. M., P. Viterbo, M. J. Miller, and A. K. Betts, 1996: The Anomalous Rainfall over the United States during July 1993: Sensitivity to Land Surface Parameterization and Soil Moisture Anomalies. *Monthly Weather Review*, **124 (3)**, 362–383.

Bisselink, B. and A. J. Dolman, 2008: Precipitation Recycling: Moisture Sources over Europe using ERA-40 Data. *Journal of Hydrometeorology*, **9 (5)**, 1073–1083.

Bisselink, B., E. van Meijgaard, A. J. Dolman, and R. A. M. de Jeu, 2011: Initializing a regional climate model with satellite-derived soil moisture. *Journal of Geophysical Research*, **116 (D2)**, 1323.

Black, E. and R. Sutton, 2006: The influence of oceanic conditions on the hot European summer of 2003. *Climate Dynamics*, **28 (1)**, 53–66.

Blanchet, J., G. Molinié, and J. Touati, 2018: Spatial analysis of trend in extreme daily rainfall in southern France. *Climate Dynamics*, **51 (3)**, 799–812.

Blankenship, C. B., J. L. Case, B. T. Zavodsky, and W. L. Crosson, 2016: Assimilation of SMOS Retrievals in the Land Information System. *IEEE transactions on geoscience and remote sensing : a publication of the IEEE Geoscience and Remote Sensing Society*, **54 (11)**, 6320–6332.

Bluestein, H. B. and M. H. Jain, 1985: Formation of Mesoscale Lines of Pirecipitation: Severe Squall Lines in Oklahoma during the Spring. *Journal of the Atmospheric Sciences*, **42 (16)**, 1711–1732.

Boberg, F. and J. H. Christensen, 2012: Overestimation of Mediterranean summer temperature projections due to model deficiencies. *Nature Climate Change*, **2 (6)**, 433–436.

Bolle, H.-J., 2003: *Mediterranean Climate: Variability and Trends*. Regional Climate Studies, Springer, Berlin and New York.

Breil, M. and G. Schädler, 2017: Quantification of the Uncertainties in Soil and Vegetation Parameterizations for Regional Climate Simulations in Europe. *Journal of Hydrometeorology*, **18 (5)**, 1535–1548.

Brisson, E., K. van Weverberg, M. Demuzere, A. Devis, S. Saeed, M. Stengel, and N. P. M. van Lipzig, 2016: How well can a convection-permitting climate model reproduce decadal statistics of precipitation, temperature and cloud characteristics? *Climate Dynamics*, **47 (9-10)**, 3043–3061.

Brocca, L., S. Hasenauer, T. Lacava, F. Melone, T. Moramarco, W. Wagner, W. Dorigo, P. Matgen, J. Martínez-Fernández, P. Llorens, J. Latron, C. Martin, and M. Bittelli, 2011: Soil moisture estimation through ASCAT and AMSR-E sensors: An intercomparison and validation study across Europe. *Remote Sensing of Environment*, **115 (12)**, 3390–3408.

Buzzi, A., S. Davolio, P. Malguzzi, O. Drofa, and D. Mastrangelo, 2014: Heavy rainfall episodes over Liguria in autumn 2011: numerical forecasting experiments. *Natural Hazards and Earth System Sciences*, **14 (5)**, 1325–1340.

Byun, H.-R. and D. A. Wilhite, 1999: Objective Quantification of Drought Severity and Duration. *Journal of Climate*, **12 (9)**, 2747–2756.

Byun H.R. and Kim D.W., 2010: Comparing the Effective Drought Index and the Standardized Precipitation Index. *Economics of drought and drought preparedness in a climate change context*, López-Francos A, Ed., Zaragoza : CIHEAM / FAO / ICARDA / GDAR / CEIGRAM / MARM, Options Méditerranéennes : Série A. Séminaires Méditerranéens, Vol. 95, 85–89, URL `http://om.ciheam.org/om/pdf/a95/00801330.pdf`, visited on 11.04.2019.

Calvet, J.-C., N. Fritz, F. Froissard, D. Suquia, A. Petitpa, and B. Piguet, 2007: In situ soil moisture observations for the CAL/VAL of SMOS: the SMOSMANIA network. *IEEE International Geoscience and Remote Sensing Symposium, 2007*, IEEE Service Center, Piscataway, NJ, 1196–1199.

Chazette, P., C. Flamant, J.-C. Raut, J. Totems, and X. Shang, 2016: Tropical moisture enriched storm tracks over the Mediterranean and their link with intense rainfall in the Cevennes-Vivarais area during HyMeX. *Quarterly Journal of the Royal Meteorological Society*, **142**, 320–334.

Christensen, J. H. and O. B. Christensen, 2007: A summary of the PRUDENCE model projections of changes in European climate by the end of this century. *Climatic Change*, **81 (S1)**, 7–30.

Christensen, J. H., K. Krishna Kumar, E. Aldrian, S.-I. An, I.F.A. Cavalcanti, M. de Castro, W. Dong, P. Goswami, A. Hall, J.K. Kanyanga, A. Kitoh, J. KossinN.-C. Lau, J. Renwick, D.B. Stephenson, and S.-P. 0Xie and T. Zhou, (Eds.) , 2013: *Climate Phenomena and their Relevance for Future Regional Climate Change. In: Climate Change 2013: The Physical Science Basis. Contribution of Working Group I to the Fifth Assessment Report of the Intergovernmental Panel on Climate Change [Stocker, T.F., D. Qin, G.-K. Plattner, M. Tignor, S.K. Allen, J. Boschung, A. Nauels, Y. Xia, V. Bex and P.M. Midgley (eds.)].* Cambridge University Press, Cambridge, United Kingdom and New York, NY, USA.

Davies, H. C., 1976: A lateral boundary formulation for multi-level prediction models. *Quarterly Journal of the Royal Meteorological Society*, **102 (432)**, 405–418.

Davolio, S., R. Henin, P. Stocchi, and A. Buzzi, 2017: Bora wind and heavy persistent precipitation: atmospheric water balance and role of air-sea fluxes over the Adriatic Sea. *Quarterly Journal of the Royal Meteorological Society*, **143 (703)**, 1165–1177.

Dayan, U., K. Nissen, and U. Ulbrich, 2015: Review Article: Atmospheric conditions inducing extreme precipitation over the eastern and western Mediterranean. *Natural Hazards and Earth System Science*, **15 (11)**, 2525–2544.

de Lannoy, G. J. M. and R. H. Reichle, 2016: Assimilation of SMOS Brightness Temperatures or Soil Moisture Retrievals into a Land Surface Model. *Hydrology and Earth System Sciences Discussions*, 1–27.

Deo, R. C., H.-R. Byun, J. F. Adamowski, and K. Begum, 2017: Application of effective drought index for quantification of meteorological drought events: a case study in Australia. *Theoretical and Applied Climatology*, **128 (1-2)**, 359–379.

Dickinson, R. E., 1984: Modeling evapotranspiration for three-dimensional global climate models. *Climate processes and climate sensitivity*, Symposium, M. E., J. E. Hansen, and T. Takahashi, Eds., American Geophysical Union, Washington, D.C., Maurice Ewing series, Vol. 29, 58–72.

Dirmeyer, P. A. and S. Halder, 2016: Sensitivity of Numerical Weather Forecasts to Initial Soil Moisture Variations in CFSv2. *Weather and Forecasting*, **31 (6)**, 1973–1983.

Doms, G. and M. Baldauf, 2018: A Description of the Nonhydrostatic Regional COSMO-Model: Part I: Dynamics and Numerics. *Deutscher Wetterdienst, P.O. Box 100465, 63004 Offenbach, Germany*, URL `http://www.cosmo-model.org/`, visited on 11.04.2019.

Doms, G., J. Förstner, H.-J. H. E. Heise, M. R. D. Mironov, T. Reinhardt, B. Ritter, R. Schrodin, and J.-P. Schulz, and G. Vogel, 2011: Part II : Physical Parameterization. *Deutscher Wetterdienst, P.O. Box 100465, 63004 Offenbach, Germany*, URL `availableat:http://www.cosmo-model.org`.

Dorigo, W., W. Wagner, C. Albergel, F. Albrecht, G. Balsamo, L. Brocca, D. Chung, M. Ertl, M. Forkel, A. Gruber, E. Haas, P. D. Hamer, M. Hirschi, J. Ikonen, R. de Jeu, R. Kidd, W. Lahoz, Y. Y. Liu, D. Miralles, T. Mistelbauer, N. Nicolai-Shaw, R. Parinussa, C. Pratola, C. Reimer, R. van der Schalie, S. I. Seneviratne, T. Smolander, and P. Lecomte, 2017: ESA CCI Soil Moisture for improved Earth system understanding: State-of-the art and future directions. *Remote Sensing of Environment*, **203**, 185–215.

Doswell, C. A., C. Ramis, R. Romero, and S. Alonso, 1998: A Diagnostic Study of Three Heavy Precipitation Episodes in the Western Mediterranean Region. *Weather and Forecasting*, **13 (1)**, 102–124.

Drobinski, P. and V. Ducrocq, 2008: Hydrological cycle in Mediterranean experiment (HyMeX) : Towards a major field experiment in 2010-2020 : white book, draft 1.3.2, URL `http://www.hymex.org/public/documents/WB_1.3.2.pdf`, visited on 11.04.2019.

Drobinski, P., V. Ducrocq, P. Alpert, E. Anagnostou, K. Béranger, M. Borga, I. Braud, A. Chanzy, S. Davolio, G. Delrieu, C. Estournel, N. F. Boubrahmi, J. Font, V. Grubišić, S. Gualdi, V. Homar, B. Ivančan-Picek, C. Kottmeier, V. Kotroni, K. Lagouvardos, P. Lionello, M. C. Llasat, W. Ludwig, C. Lutoff, A. Mariotti, E. Richard, R. Romero, R. Rotunno, O. Roussot, I. Ruin, S. Somot, I. Taupier-Letage, J. Tintore, R. Uijlenhoet, and H. Wernli, 2014: HyMeX: A 10-Year Multidisciplinary Program on the Mediterranean Water Cycle. *Bulletin of the American Meteorological Society*, **95 (7)**, 1063–1082.

Drobinski, P., N. D. Silva, G. Panthou, S. Bastin, C. Muller, B. Ahrens, M. Borga, D. Conte, G. Fosser, F. Giorgi, I. Güttler, V. Kotroni, L. Li, E. Morin, B. Önol, P. Quintana-Segui, R. Romera, and C. Z. Torma, 2018: Scaling precipitation extremes with temperature in the Mediterranean: past climate assessment and projection in anthropogenic scenarios. *Climate Dynamics*, **51 (3)**, 1237–1257.

Drusch, M., 2005: Observation operators for the direct assimilation of TRMM microwave imager retrieved soil moisture. *Geophysical Research Letters*, **32 (15)**, 269.

Ducrocq, V., I. Braud, S. Davolio, R. Ferretti, C. Flamant, A. Jansa, N. Kalthoff, E. Richard, I. Taupier-Letage, P.-A. Ayral, S. Belamari, A. Berne, M. Borga, B. Boudevillain, O. Bock, J.-L. Boichard, M.-N. Bouin, O. Bousquet, C. Bouvier, J. Chiggiato, D. Cimini, U. Corsmeier, L. Coppola, P. Cocquerez, E. Defer, J. Delanoë, P. Di Girolamo, A. Doerenbecher, P. Drobinski, Y. Dufournet, N. Fourrié, J. J. Gourley, L. Labatut, D. Lambert, J. Le Coz, F. S. Marzano, G. Molinié, A. Montani, G. Nord, M. Nuret, K. Ramage, W. Rison, O. Roussot, F. Said, A. Schwarzenboeck, P. Testor, J. van Baelen, B. Vincendon, M. Aran, and J. Tamayo, 2014: HyMeX-SOP1: The Field Campaign Dedicated to Heavy Precipitation and Flash Flooding in the Northwestern Mediterranean. *Bulletin of the American Meteorological Society*, **95 (7)**, 1083–1100.

Ducrocq, V., O. Roussot, K. Béranger, I. Braud, G. D. A. Chanzy, P. Drobinski, C. Estournel, B. Ivancan-Picek, S. Josey, K. Lagouvardos, P. Lionello, M.C. Llasat, W. Ludwig, C. Lutoff, A. Mariotti, A. Montanari, E. Richard, R. Romero, I. Ruin, and S. Somot, 2010: HyMeX Science Plan Version 2.3.2: September 2010, URL `https://www.hymex.org/public/documents/HyMeX_Science_Plan.pdf`, visited on 11.04.2019.

Duffourg, F. and V. Ducrocq, 2011: Origin of the moisture feeding the Heavy Precipitating Systems over Southeastern France. *Natural Hazards and Earth System Science*, **11 (4)**, 1163–1178.

———, 2013: Assessment of the water supply to Mediterranean heavy precipitation: a method based on finely designed water budgets. *Atmospheric Science Letters*, **14 (3)**, 133–138.

DWD, 2017: Long-Term Records of Heat and Cold Waves (Bubble Diagram): RCC Node-CM Product Description Product descriptions: Version 1.1 (June 2017). URL `https://www.dwd.de`, visited on 11.04.2019.

Eltahir, E. A. B., 1998: A Soil Moisture-Rainfall Feedback Mechanism: 1. Theory and observations. *Water Resources Research*, **34 (4)**, 765–776.

Eltahir, E. A. B. and R. L. Bras, 1996: Precipitation recycling. *Reviews of Geophysics*, **34 (3)**, 367–378.

Emanuel, K. A., 1994: *Atmospheric convection*. Oxford Univ. Press, New York.

Entekhabi, D., I. Rodriguez-Iturbe, and R. L. Bras, 1992: Variability in Large-Scale Water Balance with Land Surface-Atmosphere Interaction. *Journal of Climate*, **5 (8)**, 798–813.

Entekhabi, D., S. Yueh, P. O'Neill, and K. Kellogg et al., 2014: SMAP Handbook. *JPL Publication*.

Ferranti, L. and P. Viterbo, 2006: The European Summer of 2003: Sensitivity to Soil Water Initial Conditions. *Journal of Climate*, **19 (15)**, 3659–3680.

Feudale, L. and J. Shukla, 2007: Role of Mediterranean SST in enhancing the European heat wave of summer 2003. *Geophysical Research Letters*, **34 (3)**, 217.

Fink, A. H., T. Brücher, A. Krüger, G. C. Leckebusch, J. G. Pinto, and U. Ulbrich, 2004: The 2003 European summer heatwaves and drought -synoptic diagnosis and impacts. *Weather*, **59 (8)**, 209–216.

Fischer, E. M. and C. Schär, 2010: Consistent geographical patterns of changes in high-impact European heatwaves. *Nature Geoscience*, **3 (6)**, 398–403.

Fischer, E. M., S. I. Seneviratne, D. Lüthi, and C. Schär, 2007a: Contribution of land-atmosphere coupling to recent European summer heat waves. *Geophysical Research Letters*, **34 (6)**, L02 202.

Fischer, E. M., S. I. Seneviratne, P. L. Vidale, D. Lüthi, and C. Schär, 2007b: Soil Moisture–Atmosphere Interactions during the 2003 European Summer Heat Wave. *Journal of Climate*, **20 (20)**, 5081–5099.

Ford, T. W., E. Harris, and S. M. Quiring, 2014: Estimating root zone soil moisture using near-surface observations from SMOS. *Hydrology and Earth System Sciences*, **18 (1)**, 139–154.

Ford, T. W. and S. M. Quiring, 2014: Comparison and application of multiple methods for temporal interpolation of daily soil moisture. *International Journal of Climatology*, **34 (8)**, 2604–2621.

Fosser, G., S. Khodayar, and P. Berg, 2015: Benefit of convection permitting climate model simulations in the representation of convective precipitation. *Climate Dynamics*, **44 (1-2)**, 45–60.

Furl, C., D. Ghebreyesus, and H. Sharif, 2018: Assessment of the Performance of Satellite-Based Precipitation Products for Flood Events across Diverse Spatial Scales Using GSSHA Modeling System. *Geosciences*, **8 (6)**, 191.

García-Herrera, R., J. Díaz, R. M. Trigo, J. Luterbacher, and E. M. Fischer, 2010: A Review of the European Summer Heat Wave of 2003. *Critical Reviews in Environmental Science and Technology*, **40 (4)**, 267–306.

Gaume, E., M. Borga, Llassat Maria Carmen Llassat, Maouche Said, and Lang, Michel Lang: et al., 2016: Mediterranean extreme floods and flash floods: The Mediterranean Region under Climate Change. A Scientific Update. *Coll. Synthèses*, pp.133–144, URL `http://www.editions.ird.fr/produit/433/9782709922210/The%20Mediterranean%20Region%20under%20Climate%25`, visited on 11.04.2019.

Giorgi, F., 2006: Climate change hot-spots. *Geophysical Research Letters*, **33 (8)**, 89.

Giorgi, F., E.-S. Im, E. Coppola, N. S. Diffenbaugh, X. J. Gao, L. Mariotti, and Y. Shi, 2011: Higher Hydroclimatic Intensity with Global Warming. *Journal of Climate*, **24 (20)**, 5309–5324.

González-Zamora, Á., N. Sánchez, J. Martínez-Fernández, Á. Gumuzzio, M. Piles, and E. Olmedo, 2015: Long-term SMOS soil moisture products: A comprehensive evaluation across scales and methods in the Duero Basin (Spain). *Physics and Chemistry of the Earth, Parts A/B/C*, **83-84**, 123–136.

GOSIC, 2018: Global Observing Systems Information Center (GOSIC): National Centers for Environmental Information (NCEI) formerly known as National Climatic Data Center (NCDC). URL `https://www.ncdc.noaa.gov/gosic`, visited on 05.08.2018.

Grasselt, R., D. Schüttemeyer, K. Warrach-Sagi, F. Ament, and C. Simmer, 2008: Validation of TERRA-ML with discharge measurements. *Meteorologische Zeitschrift*, **17 (6)**, 763–773.

Guillod, B. P., B. Orlowsky, D. G. Miralles, A. J. Teuling, and S. I. Seneviratne, 2015: Reconciling spatial and temporal soil moisture effects on afternoon rainfall. *Nature communications*, **6**, 6443.

Habib, E., A. T. Haile, Y. Tian, and R. J. Joyce, 2012: Evaluation of the High-Resolution CMORPH Satellite Rainfall Product Using Dense Rain Gauge Observations and Radar-Based Estimates. *Journal of Hydrometeorology*, **13 (6)**, 1784–1798.

Hartmann, D. L., A.M.G. Klein Tank, M. Rusticucci, L.V. Alexander, S. Brönnimann, Y. Charabi, F.J. Dentener, E.J. Dlugokencky, D.R. Easterling, A. Kaplan, B.J. Soden, P.W. Thorne, and M. Wild and P.M. Zhai, (Eds.) , 2013: *Observations: Atmosphere and Surface. In: Climate Change 2013: The Physical Science Basis. Contribution of Working Group I to the Fifth Assessment Report of the Intergovernmental Panel on Climate Change [Stocker, T.F., D. Qin, G.-K. Plattner, M. Tignor, S.K. Allen, J. Boschung, A. Nauels, Y. Xia, V. Bex and P.M. Midgley (eds.)].* Cambridge University Press, Cambridge, United Kingdom and New York, NY, USA.

Haylock, M. R., N. Hofstra, A. M. G. Klein Tank, E. J. Klok, P. D. Jones, and M. New, 2008: A European daily high-resolution gridded data set of surface temperature and precipitation for 1950–2006. *Journal of Geophysical Research*, **113 (D20)**, 1691.

Heise, E., 2002: Parametrisierungen. URL `https://www.dwd.de/`, visited on 11.04.2019.

Hertig, E., S. Seubert, A. Paxian, G. Vogt, H. Paeth, and J. Jacobeit, 2014: Statistical modelling of extreme precipitation indices for the Mediterranean area under future climate change. *International Journal of Climatology*, **34 (4)**, 1132–1156.

Hillel, D., 1980: *Applications of soil physics*. Academic Pr, New York, NY.

Hirschi, M., B. Mueller, W. Dorigo, and S. I. Seneviratne, 2014: Using remotely sensed soil moisture for land–atmosphere coupling diagnostics: The role of surface vs. root-zone soil moisture variability. *Remote Sensing of Environment*, **154**, 246–252.

Hohenegger, C., P. Brockhaus, C. S. Bretherton, and C. Schär, 2009: The Soil Moisture–Precipitation Feedback in Simulations with Explicit and Parameterized Convection. *Journal of Climate*, **22 (19)**, 5003–5020.

Hoinka, K. P. and M. D. E. Castro, 2003: The Iberian Peninsula thermal low. *Quarterly Journal of the Royal Meteorological Society*, **129 (590)**, 1491–1511.

Holton, J. R. and G. J. Hakim, 2013: *An introduction to dynamic meteorology*. 5th ed., Elsevier Academic Press, Amsterdam and Heidelberg.

Houze, R. A., 2004: Mesoscale convective systems. *Reviews of Geophysics*, **42 (4)**, 86.

Hoy, A., S. Hänsel, P. Skalak, Z. Ustrnul, and O. Bochníček, 2017: The extreme European summer of 2015 in a long-term perspective. *International Journal of Climatology*, **37 (2)**, 943–962.

Ionita, M., L. M. Tallaksen, D. G. Kingston, J. H. Stagge, G. Laaha, H. A. J. van Lanen, P. Scholz, S. M. Chelcea, and K. Haslinger, 2017: The European 2015 drought from a climatological perspective. *Hydrology and Earth System Sciences*, **21 (3)**, 1397–1419.

Jaeger, E. B. and S. I. Seneviratne, 2011: Impact of soil moisture–atmosphere coupling on European climate extremes and trends in a regional climate model. *Climate Dynamics*, **36 (9-10)**, 1919–1939.

Jain, V. K., R. P. Pandey, M. K. Jain, and H.-R. Byun, 2015: Comparison of drought indices for appraisal of drought characteristics in the Ken River Basin. *Weather and Climate Extremes*, **8**, 1–11.

Jansa, A., P. Alpert, P. Arbogast, A. Buzzi, B. Ivancan-Picek, V. Kotroni, M. C. Llasat, C. Ramis, E. Richard, R. Romero, and A. Speranza, 2014: MEDEX: a general overview. *Natural Hazards and Earth System Sciences*, **14 (8)**, 1965–1984.

Joyce, R. J., J. E. Janowiak, P. A. Arkin, and P. Xie, 2004: CMORPH: A Method that Produces Global Precipitation Estimates from Passive Microwave and Infrared Data at High Spatial and Temporal Resolution. *Journal of Hydrometeorology*, **5 (3)**, 487–503.

Juglea, S., Y. Kerr, A. Mialon, J.-P. Wigneron, E. Lopez-Baeza, A. Cano, A. Albitar, C. Millan-Scheiding, M. Carmen Antolin, and S. Delwart, 2010: Modelling soil moisture at SMOS scale by use of a SVAT model over the Valencia Anchor Station. *Hydrology and Earth System Sciences*, **14 (5)**, 831–846.

Jung, T., L. Ferranti, and A. M. Tompkins, 2006: Response to the Summer of 2003 Mediterranean SST Anomalies over Europe and Africa. *Journal of Climate*, **19 (20)**, 5439–5454.

Keil, C., F. Heinlein, and G. C. Craig, 2014: The convective adjustment time-scale as indicator of predictability of convective precipitation. *Quarterly Journal of the Royal Meteorological Society*, **140 (679)**, 480–490.

Kerr, Y. H., P. Waldteufel, P. Richaume, J. P. Wigneron, P. Ferrazzoli, A. Mahmoodi, A. Al Bitar, F. Cabot, C. Gruhier, S. E. Juglea, D. Leroux, A. Mialon, and S. Delwart, 2012: The SMOS Soil Moisture Retrieval Algorithm. *IEEE Transactions on Geoscience and Remote Sensing*, **50 (5)**, 1384–1403.

Kerr, Y. H., P. Waldteufel, J.-P. Wigneron, S. Delwart, F. Cabot, J. Boutin, M.-J. Escorihuela, J. Font, N. Reul, C. Gruhier, S. E. Juglea, M. R. Drinkwater, A. Hahne, M. Martín-Neira, and S. Mecklenburg, 2010: The SMOS Mission: New Tool for Monitoring Key Elements ofthe Global Water Cycle. *Proceedings of the IEEE*, **98 (5)**, 666–687.

Khodayar, S., A. Coll, and E. Lopez-Baeza, 2019: An improved perspective in the spatial representation of soil moisture: potential added value of SMOS disaggregated 1 km resolution "all weather" product. *Hydrology and Earth System Sciences*, **23 (1)**, 255–275.

Khodayar, S., B. Czajka, A. Caldas-Alvarez, S. Helgert, C. Flamant, P. Di Girolamo, O. Bock, and P. Chazette, 2018: Multi-scale observations of atmospheric moisture variability in relation to heavy precipitating systems in the northwestern Mediterranean during HyMeX IOP12. *Quarterly Journal of the Royal Meteorological Society*, **144 (717)**, 2761–2780.

Khodayar, S., N. Kalthoff, and C. Kottmeier, 2016a: Atmospheric conditions associated with heavy precipitation events in comparison to seasonal means in the western mediterranean region. *Climate Dynamics*, **51 (3)**, 951–967.

Khodayar, S., F. Raff, N. Kalthoff, and O. Bock, 2016b: Diagnostic study of a high-precipitation event in the Western Mediterranean: adequacy of current operational networks. *Quarterly Journal of the Royal Meteorological Society*, **142**, 72–85.

Khodayar, S., A. Sehlinger, H. Feldmann, and C. Kottmeier, 2015: Sensitivity of soil moisture initialization for decadal predictions under different regional climatic conditions in Europe. *International Journal of Climatology*, **35 (8)**, 1899–1915.

Kim, J.-E. and S.-Y. Hong, 2007: Impact of Soil Moisture Anomalies on Summer Rainfall over East Asia: A Regional Climate Model Study. *Journal of Climate*, **20 (23)**, 5732–5743.

Kirshbaum, D., B. Adler, N. Kalthoff, C. Barthlott, and S. Serafin, 2018: Moist Orographic Convection: Physical Mechanisms and Links to Surface-Exchange Processes. *Atmosphere*, **9 (3)**, 80.

Koster, R. D., P. A. Dirmeyer, Z. Guo, G. Bonan, E. Chan, P. Cox, C. T. Gordon, S. Kanae, E. Kowalczyk, D. Lawrence, P. Liu, C.-H. Lu, S. Malyshev, B. McAvaney, K. Mitchell, D. Mocko, T. Oki, K. Oleson, A. Pitman, Y. C. Sud, C. M. Taylor, D. Verseghy, R. Vasic, Y. Xue, and T. Yamada, 2004: Regions of strong coupling between soil moisture and precipitation. *Science (New York, N.Y.)*, **305 (5687)**, 1138–1140.

Koster, R. D. and M. J. Suarez, 2001: Soil Moisture Memory in Climate Models. *Journal of Hydrometeorology*, **2 (6)**, 558–570.

Kothe, S., J. Tödter, and B. Ahrens, 2017: Strategies for soil initialization of regional decadal climate predictions. *Meteorologische Zeitschrift*, **25 (6)**, 775–794.

Kottek, M., J. Grieser, C. Beck, B. Rudolf, and F. Rubel, 2006: World Map of the Köppen-Geiger climate classification updated. *Meteorologische Zeitschrift*, **15 (3)**, 259–263.

Lionello, P., (Ed.) , 2006: *Mediterranean climate variability*, Developments in earth & environmental sciences, Vol. 4. Elsevier, Amsterdam and Heidelberg.

Llasat, M. C., M. Llasat-Botija, M. A. Prat, F. Porcú, C. Price, A. Mugnai, K. Lagouvardos, V. Kotroni, D. Katsanos, S. Michaelides, Y. Yair, K. Savvidou, and K. Nicolaides, 2010: High-impact floods and flash floods in Mediterranean countries: the FLASH preliminary database. *Advances in Geosciences*, **23**, 47–55.

López-Baeza, E., A. Velázquez, C. Antolín, A. Bodas, J. F. Gimeno, K. Saleh, and M. A. Sánchez, 2003: The Valencia Anchor Station, a Cal/Val reference area for largescale low spatial resolution remote sensing missions. *Proc. 3rd International Conference on Experiences with Automatic Weather Stations, pp.19-21*.

Lorenz, R., D. Argüeso, M. G. Donat, A. J. Pitman, B. van den Hurk, A. Berg, D. M. Lawrence, F. Chéruy, A. Ducharne, S. Hagemann, A. Meier, P. C. D. Milly, and S. I. Seneviratne, 2016: Influence of land-atmosphere feedbacks on temperature and precipitation extremes in the GLACE-CMIP5 ensemble. *Journal of Geophysical Research: Atmospheres*, **121 (2)**, 607–623.

Lorenz, R., E. B. Jaeger, and S. I. Seneviratne, 2010: Persistence of heat waves and its link to soil moisture memory. *Geophysical Research Letters*, **37 (9)**, n/a–n/a.

Mariotti, A., Y. Pan, N. Zeng, and A. Alessandri, 2015: Long-term climate change in the Mediterranean region in the midst of decadal variability. *Climate Dynamics*, **44 (5-6)**, 1437–1456.

Mariotti, A., M. V. Struglia, N. Zeng, and K.-M. Lau, 2002: The Hydrological Cycle in the Mediterranean Region and Implications for the Water Budget of the Mediterranean Sea. *Journal of Climate*, **15 (13)**, 1674–1690.

Mariotti, A., N. Zeng, J.-H. Yoon, V. Artale, A. Navarra, P. Alpert, and L. Z. X. Li, 2008: Mediterranean water cycle changes: transition to drier 21st century conditions in observations and CMIP3 simulations. *Environmental Research Letters*, **3 (4)**, 044 001.

Markowski, P. and Y. Richardson, 2010: *Mesoscale Meteorology in Midlatitudes*. John Wiley & Sons, Ltd, Chichester, UK.

Martínez-Fernández, J. and A. Ceballos, 2005: Mean soil moisture estimation using temporal stability analysis. *Journal of Hydrology*, **312 (1-4)**, 28–38.

Mauricio Zambrano-Bigiarini, 2017: hydrogof: Goodness-of-fit functions for comparison of simulated and observed hydrological time series. URL `http://hzambran.github.io/hydroGOF/`, r package version 0.3-10, visited on 11.04.2019.

Mellor, G. L. and T. Yamada, 1982: Development of a turbulence closure model for geophysical fluid problems. *Reviews of Geophysics*, **20 (4)**, 851.

Miralles, D. G., P. Gentine, S. I. Seneviratne, and A. J. Teuling, 2018: Land-atmospheric feedbacks during droughts and heatwaves: state of the science and current challenges. *Annals of the New York Academy of Sciences*.

Mohanty, B. P., M. H. Cosh, V. Lakshmi, and C. Montzka, 2017: Soil Moisture Remote Sensing: State-of-the-Science. *Vadose Zone Journal*, **16 (1)**, 0.

Munich RE NatCatSERVICE, 2019: Heatwave / wildfire events worldwide 2003. URL `https://natcatservice.munichre.com/`, visited on 11.04.2019.

Naeimi, V., K. Scipal, Z. Bartalis, S. Hasenauer, and W. Wagner, 2009: An Improved Soil Moisture Retrieval Algorithm for ERS and METOP Scatterometer Observations. *IEEE Transactions on Geoscience and Remote Sensing*, **47 (7)**, 1999–2013.

Nash, J. E. and J. V. Sutcliffe, 1970: River flow forecasting through conceptual models part I — A discussion of principles. *Journal of Hydrology*, **10 (3)**, 282–290.

NOAA, 2018: Climate at a Glance: Global Time Series, published October 2018: retrieved on November 19. URL `https://www.ncdc.noaa.gov/cag/`, visited on 11.04.2019.

Nuret, M., 2017: Mediterranean Database: Rain gauges from HyMeX domain precipitation amount. URL `http://mistrals.sedoo.fr/?editDatsId=904&datsId=904&project_name=HyMeX`, visited on 11.04.2019.

Orlowsky, B. and S. I. Seneviratne, 2012: Global changes in extreme events: regional and seasonal dimension. *Climatic Change*, **110 (3-4)**, 669–696.

Owe, M., R. de Jeu, and T. Holmes, 2008: Multisensor historical climatology of satellite-derived global land surface moisture. *Journal of Geophysical Research*, **113 (F1)**, 687.

Owens, R. and T. Hewson, 2018: ECMWF Forecast User Guide. URL `https://www.ecmwf.int/`, visited on 11.04.2019.

Panciera, R., J. P. Walker, T. J. Jackson, D. A. Gray, M. A. Tanase, D. Ryu, A. Monerris, H. Yardley, C. Rudiger, X. Wu, Y. Gao, and J. M. Hacker, 2014: The Soil Moisture Active Passive Experiments (SMAPEx): Toward Soil Moisture Retrieval From the SMAP Mission. *IEEE Transactions on Geoscience and Remote Sensing*, **52 (1)**, 490–507.

Paxian, A., E. Hertig, S. Seubert, G. Vogt, J. Jacobeit, and H. Paeth, 2015: Present-day and future mediterranean precipitation extremes assessed by different statistical approaches. *Climate Dynamics*, **44 (3-4)**, 845–860.

Petropoulos, G., P. Srivastava, M. Piles, and S. Pearson, 2018: Earth Observation-Based Operational Estimation of Soil Moisture and Evapotranspiration for Agricultural Crops in Support of Sustainable Water Management. *Sustainability*, **10 (2)**, 181.

Petropoulos, G. P., G. Ireland, P. K. Srivastava, and P. Ioannou-Katidis, 2014: An appraisal of the accuracy of operational soil moisture estimates from SMOS MIRAS using validated in situ observations acquired in a Mediterranean environment. *International Journal of Remote Sensing*, **35 (13)**, 5239–5250.

Pfahl, S., P. A. O'Gorman, and E. M. Fischer, 2017: Understanding the regional pattern of projected future changes in extreme precipitation. *Nature Climate Change*, **7**, 423 EP –, URL `https://doi.org/10.1038/nclimate3287`, visited on 11.04.2019.

Piles, M., A. Camps, M. Vall-llossera, I. Corbella, R. Panciera, C. Rudiger, Y. H. Kerr, and J. Walker, 2011: Downscaling SMOS-Derived Soil Moisture Using MODIS Visible/Infrared Data. *IEEE Transactions on Geoscience and Remote Sensing*, **49 (9)**, 3156–3166.

Piles, M., G. P. Petropoulos, N. Sánchez, Á. González-Zamora, and G. Ireland, 2016: Towards improved spatio-temporal resolution soil moisture retrievals from the synergy of SMOS and MSG SEVIRI spaceborne observations. *Remote Sensing of Environment*, **180**, 403–417.

Piles, M., X. Pou, Camps A., and Vall-IIosera, M. and the SMOS-BEC team, 2015: Quality report: Validation of SMOS - BEC L4 high resolution soil moisture products, version 3.0 or "all-weather". *Technical Report*.

Piles, M., N. Sanchez, M. Vall-llossera, A. Camps, J. Martinez-Fernandez, J. Martinez, and V. Gonzalez-Gambau, 2014: A Downscaling Approach for SMOS Land Observations: Evaluation of High-Resolution Soil Moisture Maps Over the Iberian Peninsula. *IEEE Journal of Selected Topics in Applied Earth Observations and Remote Sensing*, **7 (9)**, 3845–3857.

Pinto, J. G., S. Ulbrich, A. Parodi, R. Rudari, G. Boni, and U. Ulbrich, 2013: Identification and ranking of extraordinary rainfall events over Northwest Italy: The role of Atlantic moisture. *Journal of Geophysical Research: Atmospheres*, **118 (5)**, 2085–2097.

Potter, K., 2006: Methods for Presenting Statistical Information: The Box Plot. *Hans Hagen, Andreas Kerren, and Peter Dannenmann(Eds.), Visualization of Large and Unstructured Data Sets, GI-Edition Lecture Notes in Informatics (LNI)*.

Prein, A. F., W. Langhans, G. Fosser, A. Ferrone, N. Ban, K. Goergen, M. Keller, M. Tölle, O. Gutjahr, F. Feser, E. Brisson, S. Kollet, J. Schmidli, N. P. M. van Lipzig, and R. Leung, 2015: A review on regional convection-permitting climate modeling: Demonstrations, prospects, and challenges. *Reviews of geophysics (Washington, D.C. : 1985)*, **53 (2)**, 323–361.

Rajczak, J. and C. Schär, 2017: Projections of Future Precipitation Extremes Over Europe: A Multi-model Assessment of Climate Simulations. *Journal of Geophysical Research: Atmospheres*, **122 (20)**, 10,773–10,800.

Rebora, N., L. Molini, E. Casella, A. Comellas, E. Fiori, F. Pignone, F. Siccardi, F. Silvestro, S. Tanelli, and A. Parodi, 2013: Extreme Rainfall in the Mediterranean: What Can We Learn from Observations? *Journal of Hydrometeorology*, **14 (3)**, 906–922.

Reichle, R. H. and R. D. Koster, 2004: Bias reduction in short records of satellite soil moisture. *Geophysical Research Letters*, **31 (19)**, 1590.

Ribes, A., S. Thao, R. Vautard, B. Dubuisson, S. Somot, J. Colin, S. Planton, and J.-M. Soubeyroux, 2018: Observed increase in extreme daily rainfall in the French Mediterranean. *Climate Dynamics*, **29 (11)**, 31.

Ricard, D., V. Ducrocq, and L. Auger, 2012: A Climatology of the Mesoscale Environment Associated with Heavily Precipitating Events over a Northwestern Mediterranean Area. *Journal of Applied Meteorology and Climatology*, **51 (3)**, 468–488.

Rijtema, P. E., 1969: Soil moisture forecasting. URL `http://library.wur.nl/WebQuery/wurpubs/422161`, visited on 11.04.2019.

Rios-Entenza, A. and G. Miguez-Macho, 2014: Moisture recycling and the maximum of precipitation in spring in the Iberian Peninsula. *Climate Dynamics*, **42 (11-12)**, 3207–3231.

Ritter, B. and J.-F. Geleyn, 1992: A Comprehensive Radiation Scheme for Numerical Weather Prediction Models with Potential Applications in Climate Simulations. *Monthly Weather Review*, **120 (2)**, 303–325.

Röhner, L., K.-U. Nerding, and U. Corsmeier, 2016: Diagnostic study of a HyMeX heavy precipitation event over Spain by investigation of moisture trajectories. *Quarterly Journal of the Royal Meteorological Society*, **142**, 287–297.

Romero, R., C. A. Doswell, and C. Ramis, 2000: Mesoscale Numerical Study of Two Cases of Long-Lived Quasi-Stationary Convective Systems over Eastern Spain. *Monthly Weather Review*, **128 (11)**, 3731–3751.

Romero, R., C. Ramis, S. Alonso, C. A. Doswell, and D. J. Stensrud, 1998: Mesoscale Model Simulations of Three Heavy Precipitation Events in the Western Mediterranean Region. *Monthly Weather Review*, **126 (7)**, 1859–1881.

Saini, R., G. Wang, and J. S. Pal, 2016: Role of Soil Moisture Feedback in the Development of Extreme Summer Drought and Flood in the United States. *Journal of Hydrometeorology*, **17 (8)**, 2191–2207.

Sanchez, N., J. Martinez-Fernandez, A. Scaini, and C. Perez-Gutierrez, 2012: Validation of the SMOS L2 Soil Moisture Data in the REMEDHUS Network (Spain). *IEEE Transactions on Geoscience and Remote Sensing*, **50 (5)**, 1602–1611.

Schaettler, U., G. Doms, and C. Schraff, 2014: COSMO Documentation Part VII: User's Guide: COSMO V5.1. *Tech. rep. , Deutscher Wetterdienst, P.O. Box 100465, 63004 Offenbach*, URL `www.cosmo-model.org`, visited on 11.04.2019.

Schär, C., D. Lüthi, U. Beyerle, and E. Heise, 1999: The Soil–Precipitation Feedback: A Process Study with a Regional Climate Model. *Journal of Climate*, **12 (3)**, 722–741.

Schär, C., P. L. Vidale, D. Lüthi, C. Frei, C. Häberli, M. A. Liniger, and C. Appenzeller, 2004: The role of increasing temperature variability in European summer heatwaves. *Nature*, **427 (6972)**, 332–336.

Schwingshackl, C., M. Hirschi, and S. I. Seneviratne, 2017: Quantifying Spatiotemporal Variations of Soil Moisture Control on Surface Energy Balance and Near-Surface Air Temperature. *Journal of Climate*, **30 (18)**, 7105–7124.

Sénési, S., P. Bougeault, J.-L. Chèze, P. Cosentino, and R.-M. Thepenier, 1996: The Vaison-La-Romaine Flash Flood: Mesoscale Analysis and Predictability Issues. *Weather and Forecasting*, **11 (4)**, 417–442.

Seneviratne, S. I., T. Corti, E. L. Davin, M. Hirschi, E. B. Jaeger, I. Lehner, B. Orlowsky, and A. J. Teuling, 2010: Investigating soil moisture–climate interactions in a changing climate: A review. *Earth-Science Reviews*, **99 (3-4)**, 125–161.

Seneviratne, S. I., R. D. Koster, Z. Guo, P. A. Dirmeyer, E. Kowalczyk, D. Lawrence, P. Liu, D. Mocko, C.-H. Lu, K. W. Oleson, and D. Verseghy, 2006a: Soil Moisture Memory in AGCM Simulations: Analysis of Global Land–Atmosphere Coupling Experiment (GLACE) Data. *Journal of Hydrometeorology*, **7 (5)**, 1090–1112.

Seneviratne, S. I., D. Lüthi, M. Litschi, and C. Schär, 2006b: Land-atmosphere coupling and climate change in Europe. *Nature*, **443 (7108)**, 205–209.

Seneviratne, S. I. and R. Stöckli, 2008: The Role of Land-Atmosphere Interactions for Climate Variability in Europe. *Climate variability and extremes during the past 100 years*, Brönnimann, S., J. Luterbacher, and T. Ewen, Eds., Springer Science + Business Media, [Dordrecht], Advances in Global Change Research, Vol. 432, 179–193.

Seneviratne, S. I., M. Wilhelm, T. Stanelle, B. van den Hurk, S. Hagemann, A. Berg, F. Cheruy, M. E. Higgins, A. Meier, V. Brovkin, M. Claussen, A. Ducharne, J.-L. Dufresne, K. L. Findell, J. Ghattas, D. M. Lawrence, S. Malyshev, M. Rummukainen, and B. Smith, 2013: Impact of soil moisture-climate feedbacks on CMIP5 projections: First results from the GLACE-CMIP5 experiment. *Geophysical Research Letters*, **40 (19)**, 5212–5217.

Sillmann, J., V. V. Kharin, F. W. Zwiers, X. Zhang, and D. Bronaugh, 2013: Climate extremes indices in the CMIP5 multimodel ensemble: Part 2. Future climate projections. *Journal of Geophysical Research: Atmospheres*, **118 (6)**, 2473–2493.

Sillmann, J., T. Thorarinsdottir, N. Keenlyside, N. Schaller, L. V. Alexander, G. Hegerl, S. I. Seneviratne, R. Vautard, X. Zhang, and F. W. Zwiers, 2017: Understanding, modeling and predicting weather and climate extremes: Challenges and opportunities. *Weather and Climate Extremes*, **18**, 65–74.

Silvestro, F., S. Gabellani, F. Giannoni, A. Parodi, N. Rebora, R. Rudari, and F. Siccardi, 2012: A hydrological analysis of the 4 November 2011 event in Genoa. *Natural Hazards and Earth System Sciences*, **12 (9)**, 2743–2752.

Spinoni, J., G. Naumann, J. V. Vogt, and P. Barbosa, 2015: The biggest drought events in Europe from 1950 to 2012. *Journal of Hydrology: Regional Studies*, **3**, 509–524.

Srivastava, P., G. Petropoulos, and Y. H. Kerr, 2016: *Satellite soil moisture retrieval: Techniques and applications*. Elsevier, Amsterdam, Netherlands.

Stacke, T. and S. Hagemann, 2016: Lifetime of soil moisture perturbations in a coupled land–atmosphere simulation. *Earth System Dynamics*, **7 (1)**, 1–19.

Stampoulis, D., E. N. Anagnostou, and E. I. Nikolopoulos, 2013: Assessment of High-Resolution Satellite-Based Rainfall Estimates over the Mediterranean during Heavy Precipitation Events. *Journal of Hydrometeorology*, **14 (5)**, 1500–1514.

Stefanon, M., F. D'Andrea, and P. Drobinski, 2012: Heatwave classification over Europe and the Mediterranean region. *Environmental Research Letters*, **7 (1)**, 014 023.

Stéfanon, M., P. Drobinski, F. D'Andrea, C. Lebeaupin-Brossier, and S. Bastin, 2014: Soil moisture-temperature feedbacks at meso-scale during summer heat waves over Western Europe. *Climate Dynamics*, **42 (5-6)**, 1309–1324.

Taylor, C. M., R. A. M. de Jeu, F. Guichard, P. P. Harris, and W. A. Dorigo, 2012a: Afternoon rain more likely over drier soils. *Nature*, **489 (7416)**, 423–426.

Taylor, C. M., A. Gounou, F. Guichard, P. P. Harris, R. J. Ellis, F. Couvreux, and M. de Kauwe, 2011: Frequency of Sahelian storm initiation enhanced over mesoscale soil-moisture patterns. *Nature Geoscience*, **4 (7)**, 430–433.

Taylor, K. E., 2001: Summarizing multiple aspects of model performance in a single diagram. *Journal of Geophysical Research: Atmospheres*, **106 (D7)**, 7183–7192.

Taylor, K. E., R. J. Stouffer, and G. A. Meehl, 2012b: An Overview of CMIP5 and the Experiment Design. *Bulletin of the American Meteorological Society*, **93 (4)**, 485–498.

Thiébault, S., J.-P. Moatti, Thiébault, Ducrocq, V, E. Gaume, F. Dulac, E. Hamonou, Y.-J. Shin, G. Joel, G. Boulet, J.-F. Guégan, R. Barouki, I. Annesi-Mae, P. Marty, E. Torquebiau, J.-F. Sou, Y. Aumeeruddy-Thomas, J.-L. Chotte, and D. Lacroix, 2016: *The Mediterranean Region under Climate Change. A Scientific Update: Abridged English/French Version: and Sou, Jean-François and Aumeeruddy-Thomas, Yildiz and Chotte, Jean-Luc and Lacroix, Denis)*. IRD éditions.

Tiedtke, M., 1989: A Comprehensive Mass Flux Scheme for Cumulus Parameterization in Large-Scale Models. *Monthly Weather Review*, **117 (8)**, 1779–1800.

Tramblay, Y., C. Bouvier, P.-A. Ayral, and A. Marchandise, 2011: Impact of rainfall spatial distribution on rainfall-runoff modelling efficiency and initial soil moisture conditions estimation. *Natural Hazards and Earth System Science*, **11 (1)**, 157–170.

Tramblay, Y. and S. Somot, 2018: Future evolution of extreme precipitation in the Mediterranean. *Climatic Change*, **29 (11)**, 31–1.

Trigo, I. F., G. R. Bigg, and T. D. Davies, 2002: Climatology of Cyclogenesis Mechanisms in the Mediterranean. *Monthly Weather Review*, **130 (3)**, 549–569.

van den Besselaar, E. J. M., A. M. G. Klein Tank, and T. A. Buishand, 2012: Trends in European precipitation extremes over 1951-2010. *International Journal of Climatology*, **111**, n/a–n/a.

van der Ent, R. J., H. H. G. Savenije, B. Schaefli, and S. C. Steele-Dunne, 2010: Origin and fate of atmospheric moisture over continents. *Water Resources Research*, **46 (9)**, 61.

Vautard, R., P. Yiou, F. D'Andrea, N. de Noblet, N. Viovy, C. Cassou, J. Polcher, P. Ciais, M. Kageyama, and Y. Fan, 2007: Summertime European heat and drought waves induced by wintertime Mediterranean rainfall deficit. *Geophysical Research Letters*, **34 (7)**, 3661.

Wagner, W., G. Lemoine, and H. Rott, 1999: A Method for Estimating Soil Moisture from ERS Scatterometer and Soil Data. *Remote Sensing of Environment*, **70 (2)**, 191–207.

Wang, G., A. J. Dolman, R. Blender, and K. Fraedrich, 2010: Fluctuation regimes of soil moisture in ERA-40 re-analysis data. *Theoretical and Applied Climatology*, **99 (1-2)**, 1–8.

Werner, P. C. and F.-W. Gerstengarbe, 2010: Katalog der Grosswetterlagen Euroas (1881-2009): Nach Paul Hess und Helmug Brezowsky: 7., Verbesserte und ergänzte Auflage. *Postdam-Institut für Klimafolgenforeschung e. V.*, **No. 119**.

Wernli, H., C. Hofmann, and M. Zimmer, 2009: Spatial Forecast Verification Methods Intercomparison Project: Application of the SAL Technique. *Weather and Forecasting*, **24 (6)**, 1472–1484.

Wernli, H., M. Paulat, M. Hagen, and C. Frei, 2008: SAL—A Novel Quality Measure for the Verification of Quantitative Precipitation Forecasts. *Monthly Weather Review*, **136 (11)**, 4470–4487.

Wicker, L. J. and W. C. Skamarock, 2002: Time-Splitting Methods for Elastic Models Using Forward Time Schemes. *Monthly Weather Review*, **130 (8)**, 2088–2097.

Willmott, C. J., 1982: Some Comments on the Evaluation of Model Performance. *Bulletin of the American Meteorological Society*, **63 (11)**, 1309–1313.

Winschall, A., H. Sodemann, S. Pfahl, and H. Wernli, 2014: How important is intensified evaporation for Mediterranean precipitation extremes? *Journal of Geophysical Research: Atmospheres*, **119 (9)**, 5240–5256.

Xoplaki, E., J. F. González-Rouco, J. Luterbacher, and H. Wanner, 2004: Wet season Mediterranean precipitation variability: influence of large-scale dynamics and trends. *Climate Dynamics*, **23 (1)**, 63–78.

Yang, L., G. Sun, L. Zhi, and J. Zhao, 2018: Negative soil moisture-precipitation feedback in dry and wet regions. *Scientific reports*, **8 (1)**, 4026.

Yang, Y., M. Uddstrom, and M. Duncan, 2011: Effects of short spin-up periods on soil moisture simulation and the causes over New Zealand. *Journal of Geophysical Research: Atmospheres*, **116 (D24)**.

ZAMG, 2007: MANUAL OF SYNOPTIC SATELLITE METEOROLOGY: CONVECTION AND INSTABILITY. URL `http://www.zamg.ac.at/docu/Manual/SatManu/main.htm?/docu/Manual/SatManu/Basic/Convection/Stability.htm`, visited on 11.04.2019.

Zampieri, M., F. D'Andrea, R. Vautard, P. Ciais, N. de Noblet-Ducoudré, and P. Yiou, 2009: Hot European Summers and the Role of Soil Moisture in the Propagation of Mediterranean Drought. *Journal of Climate*, **22 (18)**, 4747–4758.

Zdruli, P., S. Kapur, and I. Çelik, 2011: Soils of the Mediterranean Region, Their Characteristics, Management and Sustainable Use. *Sustainable land management*, Kapur, S., Ed., Springer, Berlin and Heidelberg, 125–142.

Zhou, X. and B. Geerts, 2013: The Influence of Soil Moisture on the Planetary Boundary Layer and on Cumulus Convection over an Isolated Mountain. Part I: Observations. *Monthly Weather Review*, **141 (3)**, 1061–1078.

Zimmer, M., G. C. Craig, C. Keil, and H. Wernli, 2011: Classification of precipitation events with a convective response timescale and their forecasting characteristics. *Geophysical Research Letters*, **38 (5)**.